Imperial College London

SOLUTION-PROCESSED METAL OXIDE INTERLAYERS FOR HYBRID ORGANIC:INORGANIC OPTOELECTRONIC DEVICES

Maurizio Morbidoni

Department of Materials and Centre for Plastic Electronics

Imperial College London

June 2017

A thesis submitted in partial fulfilment of the requirements for the degree of

Doctor of Philosophy

"Tarapia tapioca come se fosse antani con la supercazzola prematurata, ha lo scappellamento a destra."

(Conte Raffaello Mascetti)

DECLARATION OF ORIGINALITY

I declare that the work contained in this thesis is my own unless stated otherwise or referenced specifically in-text. Where work was done in collaboration with others, the contribution and the persons who carried it out are stated. The copyright of this thesis rests with the author and is made available under a Creative Commons Attribution Non-Commercial No Derivatives licence. Researchers are free to copy, distribute or transmit the thesis on the condition that they attribute it, that they do not use it for commercial purposes and that they do not alter, transform or build upon it. For any reuse or redistribution, researchers must make clear to others the licence terms of this work.

ABSTRACT

Research on optoelectronic devices based on organic semiconductors has seen a steady rise in the last 20 years. Recently the incorporation of inorganic materials such as transition metal oxides as charge transport layers in these devices was found to be highly beneficial in terms of energy level alignment, stability and lifetime. Roll-to-roll processing of organic electronics and the use of flexible plastic substrates poses some limitations on the deposition of these oxides: they should be processed using solution-based methods and not require high temperature post-deposition treatments.

In this work, thin films of four different transition metal oxides (MoO_{3-x}, V_2O_{5-x}, WO_{3-x}, CoO_x) were deposited using facile solution processes. The chemistry of the precursor solutions was carefully chosen to ensure the formation of the oxide of interest without the need for high temperature post-deposition treatments (i.e. <150 °C). The oxides were incorporated in organic solar cells and light-emitting diodes as hole transport layers and the effect of the solvo-thermal processing conditions of the oxides on the behaviour of the devices was studied. All performance metrics were compared with those of poly(3,4-ethylenedioxythiophene) polystyrene sulfonate (PEDOT:PSS), a widely adopted hole transport material. Great improvements in both types of devices were recorded: in solar cells, the power conversion efficiency was up to 22% higher with a WO_{3-x} interlayer when compared with devices incorporating PEDOT:PSS; in light-emitting diodes, the luminous efficacy was 24% higher using a MoO_{3-x} interlayer instead of a PEDOT:PSS one. In addition to this, the possibility of improving the characteristics and performances of PEDOT:PSS by blending it with MoO_{3-x} was explored. Different degrees of mixing were investigated, and the effect of increasing MoO_{3-x} percentage in the PEDOT:PSS/MoO_{3-x} hybrid on the behaviour of optoelectronic devices was studied. When compared to simple PEDOT:PSS, the hybrid produced an increase of 10% in the power conversion efficiency of solar cells and of 23% in the luminous efficacy of light-emitting diodes.

This thesis is divided into six chapters. Chapter 1 provides an insight into the underlying principles of device operation together with a review of the main characteristics of transition metal oxides and their incorporation in organic electronic devices. Moreover, a detailed analysis of different solution-based methods that can be utilised for their deposition is given. Chapter 2 lists the different materials, recipes, and characterisation techniques used in this work. Chapters 3-5 contain the results obtained in this research: Chapter 3 focuses on MoO_{3-x} and V_2O_{5-x} oxides, Chapter 4 deals with the PEDOT:PSS/MoO_{3-x} hybrids and finally Chapter 5 contains results from WO_{3-x} and CoO_x. Conclusions are laid out in Chapter 6, together with ideas and prompts for future expansions of this work.

ACKNOWLEDGEMENTS

First and foremost, I will always be grateful to my supervisor, Dr Martyn McLachlan. He was a constant source of support and advice, and he left me the freedom I needed to work at the best of my abilities. He also gave me the possibility to present my work at many different conferences, which really helped my growth as a researcher. Thank you.

Among all the people I have worked with during my PhD, special thanks go to Dr David Payne and Dr Anna Regoutz. Their help with XPS measurements was invaluable, as were their advice and feedback on the topic. Also, I will be eternally grateful to Dr Xuhua Wang for her help and discussion on hyPV and hyLED devices, and to Dr Victoria Bemmer for help on AFM measurements. Soon-to-be-Dr Luca Occhi deserves the credit for the optical measurements carried out in Chapter 4, I could not have done it without him.

People in the McLachlan group (present and past) deserve a special mention. Discussions with them and the advice they provided were always very useful; in particular, thanks to Dr Claire Burgess for the TEM measurements in Chapter 4, to Dr Jorge Costa Faria for initial training and constant advice, and finally to Rebecca Kilmurray and Jiaqi Zhang, for being my sounding boards.

Finally, the most important acknowledgement of all: to my family, mum dad and my sister, for always believing in me and for being there for me whenever I needed them; as they say, home is where your heart is, and my heart will always be with them. Speaking of heart, I would not have lasted this long away from home if I had not met my girlfriend Alice; she is simply the best thing that ever happened to me.

FOREWORD

This work was carried out at Imperial College London between October 2014 and June 2017. All the results were obtained by me except for the TEM images and EDX results in Chapter 4, which were taken by Dr Claire Burgess, and the refractive index measurements in the same Chapter, which were carried out by Dr Luca Occhi using a procedure proposed by Dr Paul Stavrinou.

Parts of Chapter 1 are included in a review paper currently being prepared with the help of Jonathan Ngiam and Dr Martyn McLachlan.

Two more papers are currently being written, one on the MoO_{3-x} results from Chapter 3 and one based on the results in Chapter 4.

Oral presentations on the results obtained in this work were or will be given at the following conferences:

- 13th Int. Conference on Materials Chemistry, Liverpool (UK) July 2017;
- 14th Int. Conference on Nanosciences and Nanotechnologies, Thessaloniki (GR) July 2017;
- 10th Int. Symposium on Flexible Organic Electronics, Thessaloniki (GR) July 2017;
- XXV Int. Materials Research Congress, Cancun (MX) August 2016
- 9th Int. Symposium on Flexible Organic Electronics, Thessaloniki (GR) July 2016.

While not discusse here, a collaboration with Dr Jiaqi Zhang resulted in the following publication:

> Zhang, J.; Faria, J. C. D.; Morbidoni, M.; Porte, Y.; Harrabi, K.; and McLachlan, M. A. "Low Temperature Solution Porcessed ZnO Interlayers ZnO as a Cathodic Interlayer for Inverted Polymer Solar Cells" Adv. En. Mater. 2016.

Three more papers based on this collaboration have been submitted or will be submitted shortly.

CONTENTS

LIST OF FIGURES

LIST OF TABLES

SCOPE

In this work, the possibility of substituting PEDOT:PSS with transition metal oxides (TMOs) films was explored. The recipes used for TMOs synthesis and deposition were conceived keeping in mind two key requirements:

- Post-deposition temperatures below 150 °C;
- Mild chemistry of the solvent systems.

These requirements are of paramount importance to ensure that the recipes are readily transferable to fabrication of inverted structure devices and/or fabrication of devices on flexible substrates. They put many limitations on the transition metal precursors that can be used, especially because of the limitation on post-deposition temperature.

The first route identified was a variation of the hydrogen bronze route, starting from metal powder and involving only H_2O_2 as additive. It was noted that previous formulations of this recipe did not explore the effects of different solvents on the performances of the films as hole transport layer (HTL). Therefore, in this work three different solvents (methanol, ethanol and isopropanol) were considered as possible candidates and their effect on device performances were analysed. This was carried out for MoO_{3-x} and V_2O_{5-x} films, with three solvents and three low temperature post-deposition treatments analysed in detail.

Then, two parallel directions were followed: first, the possibility of improving the characteristics of PEDOT:PSS through blending with an oxide component (MoO_{3-x}) was explored; secondly, more oxides were studied, this time deposited from routes that involved organometallic precursors.

The process of blending PEDOT:PSS with MoO_{3-x} was investigated in a few previous works found in the literature, and MoO_{3-x} was chosen as the oxide candidate because of this possibility to have a benchmark for comparison.

Concerning the second path, the study of more oxide systems, WO_{3-x} was synthesised from an already known route, and the effects of different solvo-thermal processing conditions on the performances on devices were investigated as before. Also, a completely novel route with a new material (CoO) was explored to begin to understand whether less investigated oxide systems could be suitable candidates as PEDOT:PSS replacements.

1 INTRODUCTION

In the last 30 years, the field of organic electronics has risen to the forefront of scientific research. The first report of electrical conductivity in polymers in 1977[1] gained the Nobel Prize for the authors[2], a testimony to the importance of the discovery that spawned the plastic electronics field. The pioneering papers from Tang, where he reported the first organic photovoltaic device[3] and the first organic light-emitting diode[4] demonstrated how organic materials could substitute silicon and other inorganic semiconductors in optoelectronic devices. In these works, small molecules were used, but it was not long before light-emitting diodes were realised using a polymeric material[5]. The organic electronic field was born, and since then organic materials have been successfully employed in efficient organic solar cells (OSC), organic field-effect transistors (OFET) and, perhaps the most striking breakthrough of all, in display technology, with organic-light emitting diodes (OLEDs)-based displays which have already reached the market[6–8]. Despite the nomenclature "organic electronics", devices do not exclusively employ organic materials. The best example is provided by the electrodes, which can be either opaque or transparent depending on whether their role in a device is simply to conduct electricity or also to let light pass through to reach or leave the active layer. Opaque electrodes are common metals such as calcium, aluminium, gold, silver. Transparent electrodes, however, can be realised using different materials, the most common one being ITO[a]. Electrodes are an example of how common inorganic materials can be used in conjunction with organics to fabricate working devices. Apart from ITO, other metal oxides, in particular transition metal oxides (TMOs), can be inserted in organic devices as charge selective layers, to improve performances. Devices employing these TMOs as electrode interlayers are often referred to as *hybrid organic:inorganic devices* (hyPV[b] and hyLEDs[c], for instance). Depending on the nature of these oxides and on the electronic configuration and properties, they can be used as either electron-transporting or hole-transporting materials. Specifically, this work deals with TMOs acting as hole-transporting layer, to either extract carriers from the active layer (in hyPV) or inject them in the organic (in hyLEDs).

The need for interlayers was identified as it was noticed that charge transport within the devices was affected by many loss mechanisms. Interlayers are nowadays a fundamental component of organic electronic devices:

[a] Indium-tin oxide
[b] Hybrid photovoltaics
[c] Hybrid light-emitting diodes

- in photovoltaic devices, they ensure charge selectivity by preferentially extracting holes at the anode and electrons at the cathode;
- in light-emitting diodes, the previous point holds true but charge carriers are injected into the devices rather than extracted.

The charge transport mechanisms are connected with the electronic structure and behaviour of the materials composing the interlayers. Therefore, a full understanding of their role will comprise both an analysis of the energetics and operation of devices and a study of the physico-chemical properties of the interlayer materials.

The general performance metrics and electrical characteristics of optoelectronic devices will be covered in the Materials & Methods chapter, in the section dealing with the characterisation of devices. In the following discussion, details on the working principles of organic devices incorporating selective charge transport interlayer will be given. This will be followed by a section detailing the properties of transition metal oxides and the mechanism through which energy level alignment with the organic materials occurs. Finally, the last part will describe the theory and practical details of solution processing of metal oxides, identifying different possible routes to the synthesis of these materials.

1.1 Organic Electronics

The semiconducting behaviour in organic materials comes from the delocalisation of electrons due to the hybridisation of *2s*- and *2p*-orbitals of carbon atoms. These orbitals can hybridise in two ways: if all four have the same final energy, there is sp^3 hybridisation (carbon atoms in diamond are sp^3, for instance); if only two of the *2p* orbitals and the *2s* are involved, with the third *2p* one lying at higher energy compared to them, there is sp^2 hybridisation (an example is graphite). The latter is the one of interest for the semiconducting behaviour of organic materials. In this configuration, the three hybridised orbitals lie on the same plane at angles of 120° between each other. The lobes of the non-hybridised *2p* orbital are perpendicular to the other three.

When two sp^2 carbon atoms combine, they can form a molecule of ethylene (C_2H_4, Figure 1.1a). Of the three sp^2 orbitals present on each carbon (in yellow in Figure 1.1), one bonds with the other carbon atom and two bond with two hydrogen atoms (not shown): these are all σ bonds. The electron densities of the out-of-plane *2p* orbitals from both carbons (in green in Figure 1.1), sitting above and below the C-C bond plane, can overlap, forming a π bond parallel to the C-C σ bond and resulting in a C=C double bond.

When two ethylene molecules are combined (Figure 1.1b), forming a molecule of butadiene, the backbone is again composed of σ bonds between carbon atoms. Even though nominally

only two of the three carbon-carbon bonds can be double bonds, the out-of-plane orbitals can overlap along the whole length of the molecule. This process, which delocalises the π electrons across the molecule, is called *conjugation* and only occurs in molecules with alternating single and double bonds. More ethylene molecules can be added to form longer chains such as 1, 3, 5, 7-octatetraedene (Figure 1.1c), with even greater delocalisation of the π electrons. For very long molecules, e.g. polyacetylene[d], the π electrons are fully delocalised along the backbone of the molecules and the π orbitals overlap into energy bands (Figure 1.1d).

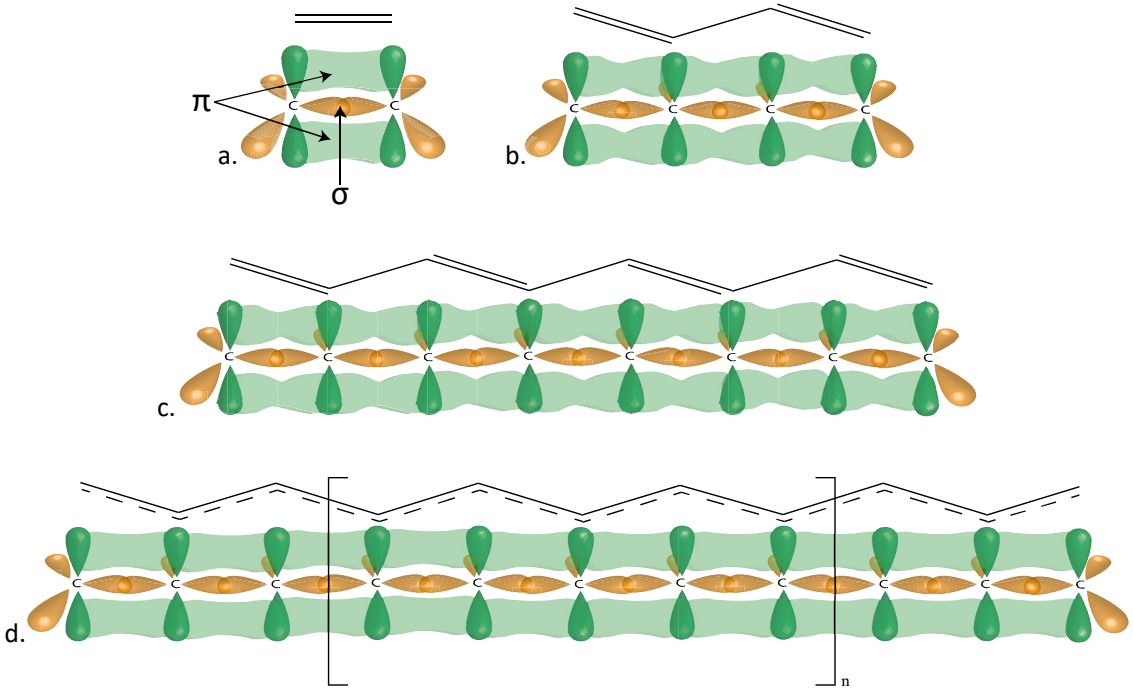

Figure 1.1: Formation of σ and π bonds in conjugated organic molecules. a. Ethylene molecule showing the double bond resulting from a σ and a π orbital. b. butadiene molecule. c. 1, 3, 5, 7-octatetraene molecule. d. polyacetylene, where π orbitals are fully delocalised along the aliphatic chain. This leads to the formation of a so-called π-band, extending above and below the C-C plane. In all subfigures, yellow orbitals not connecting two carbon atoms are C-H bonds (hydrogen not shown for clarity).

The overlapping of the atomic orbitals can be modelled using a *linear combination of atomic orbitals* approach. Bonding and antibonding orbitals arise from the combination of both sp^2 and single *2p* orbitals. sp^2 orbitals produce σ (bonding) and σ^* (antibonding) molecular orbitals, while out-of-plane *2p* orbitals produce π (bonding) and π^* (antibonding) molecular orbitals. The stronger overlap of sp^2 orbitals with respect to *2p* orbitals implies that σ orbitals have higher energies than π orbitals (i.e. they are more stable, more "bonding"), while σ^* have less energy than π^* (they are more reactive). Therefore, the smallest possible electronic excitation will be the promotion of an electron from the highest occupied π orbital (the HOMO[e]) to the lowest

[d] n.b.: polymerisation of ethylene would lead to a polymeric chain of single C-C bonds, which do not have π electrons. Hence, polyacetylene is taken as an example of a polymeric material with a π band.
[e] Highest Occupied Molecular Orbital

unoccupied π^* orbital (the LUMO[f]). The HOMO-LUMO gap is analogous to the direct band gap in inorganic semiconductors, and the delocalised π electrons can be used for electrical conduction. The magnitude of the HOMO-LUMO gap is larger for systems with only a few overlapping orbitals, and it becomes smaller as more and more units are added to the chain. Therefore, for very long chains the gap should close and the material should become a metallic conductor. However, the difference in length between single and double bonds, impurities along the polymeric chain backbone, lattice vibrations, are all factors that limit the distance an electron can travel freely along the chain; this results in a finite HOMO-LUMO gap which converge to a minimum value. The length of the segments of the chain over which hybridisation is not broken by the aforementioned factors is called the *conjugation length*. A detailed explanation on these phenomena can be found in the book written by Geoghegan and Hadziioannou[9].

Polarons

The HOMO-LUMO gap of organic semiconductors is usually quite large (> 1.5 eV), therefore charge carriers are not able to conduct electricity unless the material is doped. Doping processes in organic materials are very different than those in inorganic semiconductors; they involve reduction or oxidation of the material, which is then in an excited state:

- Oxidation of the molecule, produced by electron accepting groups bound on the chain, leaves positive charges on the C-C backbone (e.g. oxygen, iodine, chlorine);
- Reduction of the molecule, produced by electron donating groups bound on the chain, leaves negative charges on the C-C backbone (e.g. lithium, caesium).

The charges left on the backbone counterbalance the presence of the electron

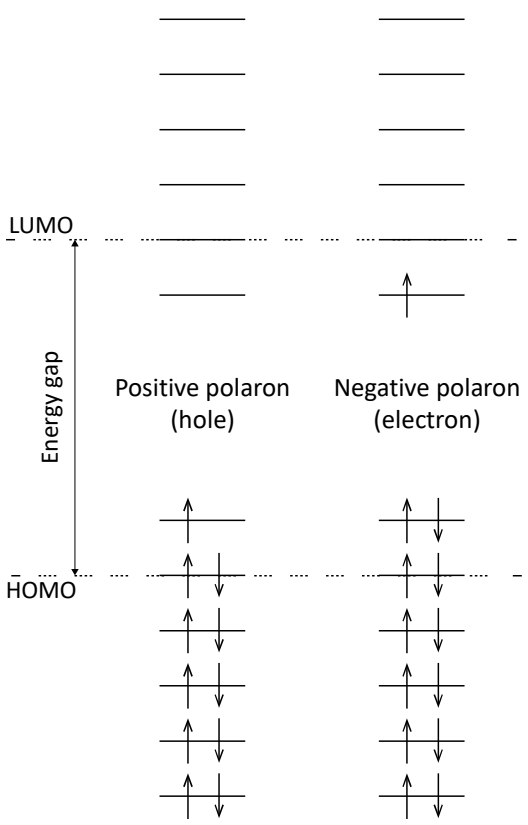

Figure 1.2: Formation and occupancy of intragap states in a positive and a negative polaron.

[f] Lowest Unoccupied Molecular Orbital

acceptor/donor to ensure the charge neutrality of the system; however, they are delocalised over the distance of a few molecules from the site where the dopant is bound to the chain. These charges interact with the electronic distortion that their presence produces on the backbone: this interaction can be modelled as a quasiparticle called a *polaron*. The electronic distortion induced by the charge produces a local polarisation of the chain and a shifting in the energy level aimed at minimising the energy of the system. Intragap levels are formed, and their occupancy depends on the type of polaron (positive or negative). The situation is shown in Figure 1.2 for both types of polarons. The charges created by functional groups (donors or acceptors) can move along the chain thanks to the delocalisation brought by the conjugation of π orbitals. Polarons themselves can aid the conduction process by hopping between adjacent chains.

Excitons

Another quasiparticle that plays a fundamental role in organic semiconductors is the *exciton*. An exciton is formed by the interaction between an electron that has been excited into a higher energy state and the hole it has left in the ground state[g]. The exciton formation is the reason behind the difference between the electronic and the optical band gap. When the material absorbs a photon, an electron from the HOMO level is excited into the LUMO. However, the electron and the hole are attracted to each other by Coulomb force which leads to the formation of the exciton; this Coulombic attraction is the *exciton binding energy*, which in organic materials is in the range 0.3-0.5 eV[10]. The effect of the exciton binding energy leads to a situation similar to that of a polaron, with the appearance of two intragap energy levels, one just above the HOMO and the other just below the LUMO. The former will host the hole left behind by the electron, which will occupy the latter. Because of this, the material effectively need to absorb a photon whose energy is only equal to the difference between the two intragap levels. To summarise, the electronic energy gap is equal in magnitude to the HOMO-LUMO gap, while the optical band gap is the HOMO-LUMO gap minus the exciton binding energy, and is thus smaller than the electronic gap.

Excitons are not only formed by absorbing light, but also when charges are injected into an organic material and come into close proximity within it; the first process is important in light-absorbing devices (solar cells), while the second is fundamental in light-emitting devices. When formed, an exciton involves a few adjacent monomers along the chain, depending on its radius. Exploiting the hydrogen atom analogy, an exciton radius can be modelled as an atomic radius

[g] The quantomechanical behaviour of the hole-electron pair is similar to that of a hydrogen atom and can be modelled following the same line of reasoning, which will not be covered here.

in a simple atom made by a negative charge moving around a positive one. Because of the attractive Coulombic force between the electron and its hole, an exciton has a finite lifetime, usually on the orders of nanoseconds. Hence, before recombining, it can travel along the chain for a few nanometres: this distance is the *exciton diffusion length* and it is usually around 10 nm, with larger values achievable in highly crystalline organic materials[11]. The exciton diffusion length is very important in photovoltaic devices, as it will be shown in the following section that the exciton need to reach an interface before recombining in order for a solar cell to generate current. Its recombination or decay mechanism is important in light-emitting applications instead, where radiative decay, called *luminescence*[h], leads to emission of a photon.

1.1.1 Photovoltaic devices

Because of the high binding energy of the excitons formed in organic materials, light absorption alone does not yield photogenerated carriers. As discussed above, when a photon is absorbed and an exciton is formed, this will hop along the chain (or between chains) for a short distance before recombining. If on its hopping path the exciton reaches an interface between the photoactive material and a second component, the energy offset at the interface of the two materials could provide enough energy to separate the electron and the hole.

1.1.1.1 Working Principles

The splitting of the exciton is usually achieved in organic photovoltaic devices by blending the photoactive material (in this work, P3HT[i]), with materials that have a deeper LUMO level that can accept the electron and leave behind the hole; these acceptor materials are usually fullerene derivative (in this work ICBA[j]). Details and structures of the materials will be provided in the Materials & Methods section. It is generally accepted that a difference of 0.3 eV between the two LUMO levels is sufficient for exciton separation[12,13]. The exciton splitting is performed on two levels at the same time: from an electronic point of view, the electron jumps into a more stable state; from a physical point of view, the electron and the hole are now located on different molecules, which means that they are spatially separated. While this separation lowers the chances of recombination, the hole and the electron travel close to each other along the interface for a short time, which means that recombination across the two molecules can still happen. When it does, it is termed *bimolecular recombination* to distinguish it from the

[h] The process is called photoluminescence if the exciton was formed following the absorption of a photon, electroluminescence if the carriers were injected into the organic. The latter is the process at the core of light-emitting devices.

[i] Poly(3-hexylthiophene-2,5-diyl)

[j] Indene-C_{60} bisadduct

regular *geminate recombination*. It is interesting to note that bimolecular recombination can occur between an electron and a hole which were not originally parts of the same exciton.

A schematic of the energetics involved in a solar cell employing an organic material as active layer is shown in Figure 1.14. A photon is absorbed by the P3HT; it diffuses through the polymer until it either decades or reaches an interface with ICBA, where the electron jumps into the LUMO of the acceptor, while the hole remains in the polymeric material (both carriers are found in the form of polarons[10]). They travel alongside each other for a short distance, still attracted by a now-reduced Coulomb force. If bimolecular recombination does not occur, they can travel across the respective donor or acceptor phases and eventually reach the electrode bilayers. On the right-hand side in Figure 1.3, the electron is extracted to the Al cathode through the ZrO_2 cathode interlayer. ZrO_2, because of its low-lying Fermi level, provides an excellent energy level alignment[k] with the LUMO of the ICBA molecules[14]. On the left-hand side, MoO_3 was instead chosen because of its deep Fermi level, which allows for efficient energy level alignment with the P3HT HOMO level[14]: the hole is extracted through the interlayer to the ITO anode.

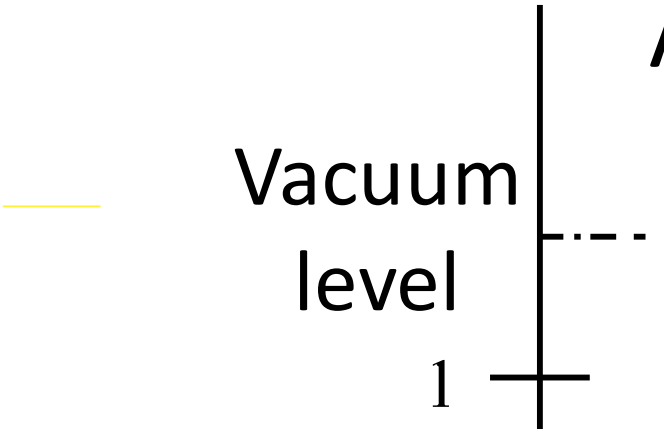

Figure 1.3 Working principle of an organic photovoltaic device using a P3HT:ICBA bulk heterojunction active layer.

In p-n junction solar cells, the built-in voltage at the interface between the p and n layers provides the driving force to separate the carriers and drive them towards the electrodes. In organic photovoltaic devices, interfaces are used to split the exciton, but there is no built-in field to then guide them towards the respective electrode to be collected. There is only a small

[k] The energy level alignment process will be discussed in the section dealing with Transition Metal Oxides.

electric field that appears when the cathode and the anode are put in electrical contact; this is because their Fermi level must equalise and therefore there is a net flux of electrons from the cathode to the anode. This electric field can help drive the charges to the respective electrode. Because of these reasons, device architecture plays a very important role in organic solar cells.

Structure

The simplest structure is a bilayer device where the acceptor is deposited on top of the donor (or vice versa)[15–17]; modelling of device behaviour is often carried out on bilayer devices[9,18]. Having only a single interface, the biggest issue with bilayer device is that the active layer stack must be thin; otherwise, the majority of the excitons will form in the bulk of one of the two components and will recombine before it can reach the interface. To overcome this limitation, small organic molecules can replace polymers: their higher crystallinity can increase the exciton diffusion length, allowing for thicker devices to be fabricated. The advantage of bilayer devices is that they provide a continuous path towards the electrode for the carrier of choice.

The bulk heterojunction concept[19,20] overcomes the limitation on thickness brought about by the lack of interfaces. By intimately mixing the donor and the acceptor, a favourable morphology can be realised, where an exciton will always find an interface within its diffusion length, no matter where it was created in the active layer; this has quickly become the most popular structure in organic photovoltaic devices[21]. The hyPV devices fabricated in this work are structured in this way, with the ICBA acceptor dispersed within the P3HT donor matrix. However, bulk heterojunctions require a finer level of control on the morphology when compared to bilayer devices. Unfavourable intermixing may result in non-continuous pathways to the electrodes, producing isolated regions in the acceptor phase which can trap electrons rather than extracting them to the cathode. Hole passing near these regions can undergo bimolecular recombination with these electrons. Moreover, the high density of interfaces implies that spatial separation of holes and electrons is more difficult to achieve, and this again increases the likelihood of bimolecular recombination.

1.1.1.2 Optimisation of Device Performance

The equivalent circuit of a solar cell, together with the performance metrics and the equations from which they are derived, are discussed in the Materials & Methods chapter, in the part dedicated to the devices' characterisation and testing. In this section, only basic definitions of the parameters will be given, while the discussion will focus on how the peculiarities of organic-based devices affect them.

Open circuit voltage

When the electrodes are not connected through an external circuit, the device is in *open circuit* conditions. As the Fermi levels of the cathode and the anode cannot equalise, a potential arises within the device: this potential is the *open circuit voltage* V_{oc}. In bulk heterojunction solar cells, the V_{oc} depends on the energy levels of the donor and the acceptor[22]:

$$V_{oc} = \frac{1}{e}(\left|E_{HOMO}^{DONOR}\right| - \left|E_{LUMO}^{ACCEPTOR}\right| - \Delta)$$

Equation 1.1

The Δ value is in the range 0.3-0.6 eV; it is commonly ascribed to compensating effects produced by dark currents and the field-driven nature of the photocurrent in bulk heterojunction devices[23,24]. The value can be seen as the separation in energy at which the electron and the hole polaritons are formed, as opposed to the optical band gap which is the separation in energy between the bound hole and electron. In a parallel with inorganic semiconductor physics, the V_{oc} can be treated as the difference in the quasi-Fermi level of the hole and the electron[25].

The V_{oc} can be optimised by tuning the energy levels of either the acceptor or the donor material, in order to maximise the HOMO-LUMO difference in Equation 1.1[23,26]. This can have an impact on the photocurrent generation, if the offset between the LUMO of the donor and that of the acceptor is reduced to values that do not ensure efficient exciton splitting. Also, tuning of the LUMO of the acceptor molecules usually requires the introduction of new functional groups, which may negatively affect the morphology of the active layer[27,28]. Other factors that influence the V_{oc} are the temperature, the film morphology, and the illumination intensity; their effect on the V_{oc}, of little interest to this work, have been extensively dealt with in refs [9,10,21].

The maximum values of V_{oc} can only be obtained if the carriers can be extracted at the electrodes without any voltage drop along their path. Therefore, interfaces with the cathode and the anode must provide Ohmic contacts with the organic active layer. This is achieved with the use of appropriate charge transport interlayers, which through efficient energy level alignment with the organic materials provide a lossless contact between them and the respective electrode.

Photocurrent

When the device is in short-circuit conditions, meaning that the electrodes are in electrical contact and their Fermi levels are equalised, upon illumination a current is generated through the device. To facilitate comparison of data obtained from devices of different sizes, this current is usually reported as a current density value. It is, unsurprisingly, called the *short circuit current*

J_{sc}. Its magnitude strongly depends on the number of photogenerated charges, and it is therefore influenced by a number of factors:

- The light absorption efficiency in the active layer materials;
- The efficiency of the dissociation process;
- The efficiency of charge transport across the layers to the electrodes.

Organic semiconductors have high absorption coefficients, which means that devices incorporating these materials as active component can be much thinner than, for instance, silicon photovoltaic devices. However, unlike inorganic semiconductors, the absorption only occurs over a small range of wavelengths, due to the very localised nature of the energy levels which do not broaden into large energy bands. Because of the photon flux distribution of light coming from the sun, the largest number of photons per wavelength is found at values around 600 nm[29]; for this reason and from thermodynamic considerations on charge-transfer states, organic materials which have band gaps in the orange-infrared region will produce devices with the highest efficiencies[12,30].

The optical path within the active layer is not limited by its thickness: non-absorbed light will be reflected by the back electrode and will therefore pass through the device again, increasing the chances for the photons to be absorbed. Furthermore, the electrodes can be patterned to exploit the beneficial effects of surface plasmons[31,32]. Also, the use of transparent interlayers with high refractive index (transition metal oxides are an example of this) can redistribute the light intensity within the device so that it peaks close to the centre of the active layer, thus maximising light collection[33–35]. It is worth noting that the benefits of optical spacing are greatly reduced if the active layer thickness is already optimised[36]; nevertheless, in devices with thicknesses away from the ideal value, for example in a semi-transparent cell, it could prove very useful.

After the photogeneration of the exciton, the electron and the hole must be efficiently separated if they are to be used to do work. It was already discussed how interfaces between materials showing LUMO offset can be used to split the exciton. As observed above, a bulk heterojunction is the morphology that yield the best results for low mobility polymers and small molecules, while highly crystalline organic materials, showing high delocalisation and carrier mobility, can be deposited in bilayer structures.

The morphology of a bulk heterojunction architecture is also a key factor in regulating charge transport to the electrodes. Percolative paths of both donor and acceptor phases are necessary to extract the separate charge carriers, and isolated areas or dead-ends must be avoided if

possible. The analysis and modelling of the intermixing process is beyond the scope of this work: a detailed discussion can be found in the book from Koehler and Baessler[21].

Electrical Losses

Electrical losses have a major effect on the *fill factor*, which is commonly defined as a measure of the 'squareness' of the J-V plot; following the very clear explanation from Koehler and Baessler[21]: the horizontal section of the curve should be as horizontal as possible, and the same holds true for the vertical one. This implies that the forward current is highly dependent on the applied voltage and increases exponentially with it, while the photocurrent does not depend on the applied bias (and on the electric field it generates). The two sections of the curve originate from the dark current and the photocurrent, respectively.

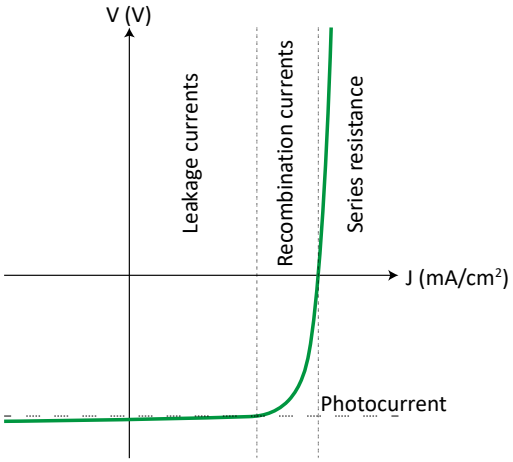

Figure 1.4: J-V of a typical solar cell, with the different loss regions highlighted.

In a typical J-V plot, three regions can be isolated, each with a dominant loss mechanism[37] (Figure 1.4). Leakage currents are responsible for losses in the first region, positioned at low, positive biases. Leakage currents can originate from pinholes in the active layer: such defects, if they manage to connect the two electrodes, will produce parasitic currents within the device. A second region is identified at moderate, positive biases; here, recombination currents are the major issue. Recombination currents can be ascribed to the two processes, geminate pair and bimolecular recombination, described above; both are responsible for the dependence of the photocurrent on the device bias[38]. To reduce these losses, both types of recombination must be field-independent; for geminate pair recombination, the active layer materials properties can be tuned to ensure energetic separation of the exciton after it has formed. For bimolecular recombination, field-independency can be achieved by using selective charge transport layers to reduce charge recombination at the electrode interfaces, i.e. by introducing electron blocking layers at the anode and hole blocking layers at the cathode.

The interfaces with the electrodes are critical points because there are many carriers and therefore bimolecular recombination can easily take place, especially for excitons formed near the interface. Blocking layers prevent the carriers from reaching the wrong electrons, where they would recombine and reduce the photogenerated current[21,38,39]. Both contributions (leakage and recombination currents) result in a S-shape in the fourth quadrant, reducing the

fill factor of a device. If the exciton separation process is field-dependent, at low electric fields[I] (near the V_{oc}), the photocurrent contribution to the total current will be depleted because only a few excitons will be separated. At the same time, if the recombination processes are field-dependent, their effect will be stronger near the V_{oc} and the photocurrent can be further reduced. Leakage currents can introduce a slope in the J_{sc} region, but they are mostly related to non-uniform morphology or non-selective interlayers; they can be greatly reduced by choosing appropriate charge transport interlayers and ensuring that the active layer is compact and pinhole-free. Finally, the third region, at high positive biases, is the region governed by the internal resistance of the device and its components, summed up in a value termed *series resistance*. A large series resistance will induce a deviation from the vertical direction in the J-V curve at voltages higher than V_{oc}. In the limit of a very high value, it will affect both the fill factor and the J_{sc} value[29,37]. Control over the electronic properties of all the layers in a device is fundamental to ensure that the series resistance is kept to a minimum. When this is achieved, the device area becomes the major contribution to the series resistance efficiency losses; this is ascribed to the resistivity of the transparent electrode, which is commonly ~100 times more resistive than the metal electrode[40].

1.1.2 Light-emitting diodes

An exciton in an organic material can be formed not only via light absorption, but also through carriers' injection when the active material is sandwiched between two electrodes. If the carriers can travel and meet within the organic layer, they can form an exciton which, after diffusing for a short time, can decay radiatively. Organic light-emitting diodes exploit this process, called electroluminescence, for lighting and display purposes.

1.1.2.1 Working Principles

The energetics of a simplified single layer OLED, consisting of a light-emitting polymer (poly(*p*-phenylene vinylene), PPV) sandwiched between two electrodes, is summarised in Figure 1.5. The effect of an applied bias of varying magnitude is also shown. Before contact, the two electrodes and the active layer are at rest and they share the same vacuum level. After contact, in the short-circuit condition, there is a flow of electrons from the calcium to the ITO in order to establish an equal Fermi level across the structure. A potential difference arises, resulting in

[I] The internal electric field of a device is $F = \frac{(V_{applied} - V_{oc})}{d}$.

a displacement of the vacuum level equal to the difference between the work functions of the electrodes[41]:

$$\frac{1}{e}(WF_{ITO} - WF_{Ca}) = V_{turn-on}$$

Equation 1.2[m]

When a reverse bias is applied, the Fermi level of the cathode is pushed further down in energy with respect to the ITO one. In this situation, holes would be injected into the active layer from the cathode, but the very high energy barrier between its Fermi level and the HOMO of the organic precludes this possibility. Similarly, electrons cannot be injected from the anode into the LUMO of the polymer. In reverse bias, like in a diode, there is no current flow through the device; in real devices, pinholes or other shunt current processes can produce small leakage currents.

The reverse bias condition, where no charge injection from the electrode can occur, lasts until the applied bias reaches the turn-on value defined by Equation 1.2: here, the so-called *flat band situation* is recovered, where the energy bands and levels mirror those of the materials when they are not in contact. As soon as the applied voltage exceeds this threshold value, hole injection from the anode into the HOMO and electron injection from the cathode into the LUMO is promoted[21,41]. Carriers are injected on both sides into the active layer, and if they meet they can pair in an exciton and decay radiatively, emitting light.

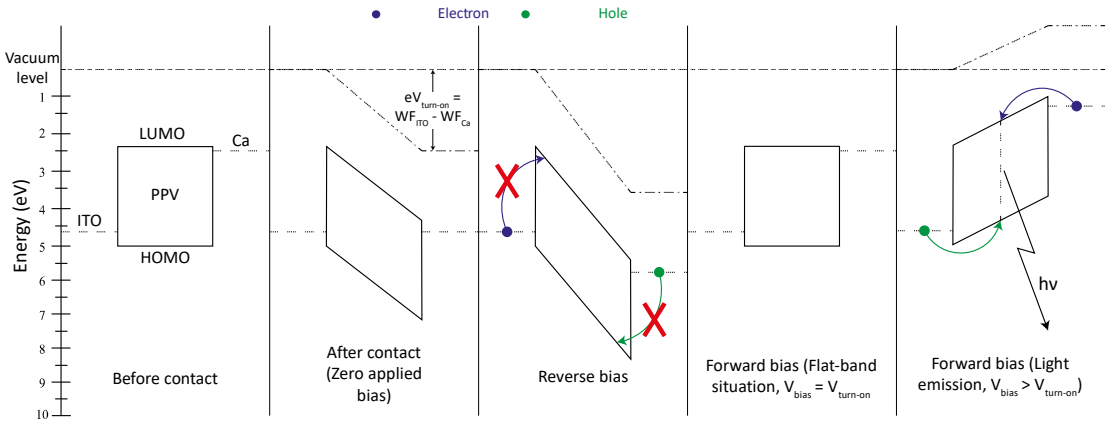

Figure 1.5: Energetics and effect of an applied bias on a simple metal-organic-metal OLED device.

From these considerations, the importance of Ohmic contacts can be quickly understood: the light emission process can start at voltages just above the turn-on only if the electrical contacts between the active layer and the electrodes are Ohmic. If non-Ohmic interfaces are present, energy barriers to injection must be overcome before light emission takes place; this means

[m] Another denomination for $V_{turn-on}$ is built-in voltage V_{bi}

that, at voltages just above the flat band situation, light emission still does not happen and higher biases are required to turn on the device[42].

To ensure Ohmic contacts with the electrodes, interlayers are often used, with TMOs being one of the most common materials[43–49]. Anode and cathode interlayers ensure that charge alignment at the electrodes' interfaces are favourable and that charge injection is efficient[50,51]. The energetics diagram in a real device, incorporating MoO_3 as hole transport layer and ZrO_2 as electron transport layer is shown in Figure 1.6. The favourable energy level alignment between the oxides and the organic active layer result in the formation of Ohmic contacts on both electrodes.

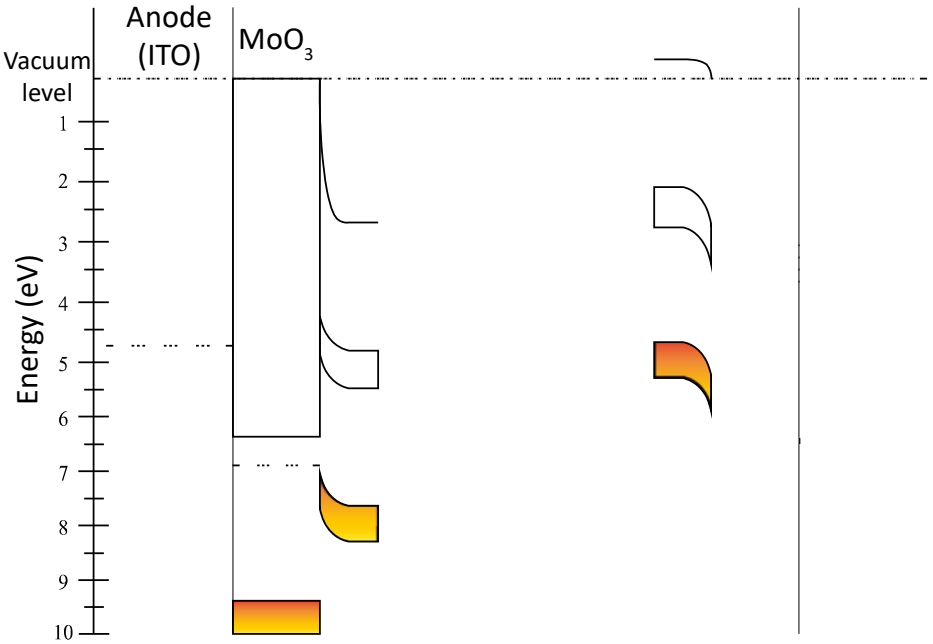

Figure 1.6: Band structure situation in a real OLED device, incorporating TMOs as anode and cathode interlayer.

The situation summarised here is for the flat band situation: band bending produces p-doping of the polymer on the anode side and n-doping on the cathode side[50]; charge accumulates at the interface and can flow through the device following the gradient in the energy levels as soon as the applied voltage exceeds the turn-on voltage. It is worth noting that the width of the band bending region has been exaggerated in Figure 1.6 for clarity, whereas in reality it is no larger than 10 nm, depending on the dielectric constant of the organic.

1.1.2.2 Optimisation of Device Performance

The performance of an organic light-emitting device is usually quantified by its luminous power efficiency PE, which is expressed in lumens/watt. As with solar cells, general equations to derive the various device metrics will be provided in the Materials & Methods chapter.

The key factor in obtaining high efficiencies in OLEDs is that a large majority of the carriers injected pair up in excitons and decay radiatively; the emitted photons must of course be extracted from the device. This can be done by optimising four processes within a device:

- Limiting the number of carriers that reach the opposite electrode without undergoing radiative recombination;
- Maximising the number of excitons formed in a singlet spin state, as this is the situation leading to radiative recombination;
- Maximising the luminescence quantum yield of the emitting material;
- Ensuring high outcoupling of the generated photons.

Blocking Layers

Carriers travelling through the active layer, which do not combine with the opposite carrier to form an exciton, can reach the counter electrode where they will recombine non-radiatively. This is often the case in organic light emitting diodes where charge transport is not completely ambipolar (usually the hole mobility is much larger than the electron mobility). The difference in charge transport may shift the recombination zone (the area where the majority of the excitons are formed and decay) from the centre of the device towards one of the electrodes, usually the cathode. Here, the radiative recombination process is in competition with non-radiative charge recombination at the interface between the active layer and the cathodic bilayer, leading to losses in efficiency. To overcome this, blocking layers are used[21], at the interface between the active layer and the charge transport interlayers. A good electron blocking layer will have a LUMO (or a conduction band edge) at energies closer to vacuum than the LUMO of the emissive material: this will introduce an energy barrier for electrons moving through the emissive layer into the anodic bilayer, where they would recombine non-radiatively. Similarly, a material with a very deep HOMO (or valence band edge) can be introduced between the active layer and the electron transport layer: this will prevent holes from reaching the cathode bilayer and recombine non-radiatively. When blocking layers are used, holes and electrons are effectively confined within the emissive layer, thus maximising the chances of exciton formation and radiative decay. As seen in Figure 1.6, ZrO_2 itself can act as both electron injecting and hole blocking layer: in fact, its valence band edge is far from the HOMO of the light-emitting polymer, preventing holes from reaching the cathode. On the

contrary, MoO_3 by itself can easily inject holes into the HOMO level of the polymer, but cannot block electrons from the LUMO from reaching the ITO through its conduction band.

Spin Statistics

According to the spin statistics, when a recombination event takes place between an electron and a hole there is a 75% chance that this will lead to the formation of a spin-1 species (a triplet state)[52]. In conventional emitting organic materials, the triplet state does not lead to light emission as a result of the recombination process.

Exploiting the high spin-orbit coupling of materials containing heavy metals such as iridium is one way of overcoming the problem: the presence of the heavy atom increases the possibility of singlet-triplet mixing via inter-system crossing, therefore recovering emission from the triplet state[53]. Therefore, complexes of heavy metals can be used to dope the active layer materials; however, the use of these triplet emitters is not as straightforward as one would hope, as they have strict requirements on the host materials in terms of suitable energy levels[54].

Another way of reducing losses due to spin statistics is to increase the singlet-to-triplet ratio in the active layer material. This can be done by reducing the energy gap between the triplet and the singlet states[n] to a value close to k_BT at room temperature (0.025 eV). If this happens, thermally activated intersystem crossing from the triplet into the singlet state increases the number of emissive singlet states that can contribute to light emission. This process is called *thermally activated delayed fluorescence TADF*[55].

Quantum Yield

The luminescence quantum yield can be increased by reducing the rate of non-radiative recombination as compared to that of radiative recombination. This can be obtained by reducing vibrations in the polymeric chains, as vibronic transitions regulate intersystem crossing from the singlet into the non-radiative triplet. Stiffer polymeric chains can be designed to reduce these vibrations, especially those leading to the mixing of σ and π orbitals. Another way is to suppress the formation of excimers, which can be achieved by using side chains that can effectively separate the chromophores[21].

Light Outcoupling

The difference in refractive index between the organic and the ITO-coated glass substrate and between the latter and air is a major source of optical losses because of total internal reflection, and only photons emitted within a 40° aperture cone can leave the device. Common strategies

[n] The triplet state T_1 has lower energy than the singlet S_1, so usually transfers from T_1 to S_1 do not happen at RT.

adopted to maximise photon outcoupling aim to reduce light trapping: roughening of the glass or corrugating the emissive layer are two examples[41]. Also, different substrates can be used, such as high-refractive index glasses or polymeric substrates covered by an oxide-metal-oxide multilayer which also have the advantage of flexibility[21].

1.2 Transition Metal Oxides

Transition metal oxides (TMOs) are a very interesting family of materials, and arguably one of the most widely employed across all areas of engineering. Their uses range from optoelectronic devices to energy generation and storage (e.g. fuel cells) to memory and data storage application[14,56–59]. It may seem counterintuitive to incorporate them in organic electronic devices, but some of their unique properties make them ideal to fully complement those of the organic active layer materials. The first property that makes them so appealing in optoelectronic applications is certainly their transparency across the visible range. The use of wide band gap TMOs ensures that no light is absorbed in its path to/from the organic materials. The best example of the importance of transparency is ITO: transparent electrodes are fundamental in organic optoelectronic applications and ITO, with its wide band gap and its excellent conductivity, has been of paramount importance in the progress of the organic electronics field. Other TMOs can be used as transparent electrodes: some examples include FTO (fluorine-doped tin oxide) and AZO (aluminium-doped zinc oxide)[60–63], state-of-the-art materials such as IGZO (indium-gallium-zinc oxide) or even a combination of TMOs such as MoO_{3-x} and silver nanowires[64]. Another very important feature that has proven extremely useful in devices is the huge range over which their work functions are distributed, extending from the very deep value of ~7 eV for MoO_3[65]to the quite shallow values of 3.5-4 eV reported for ZnO and ZrO[66–68]. This range covers the whole distribution of HOMO-LUMO levels of the organic materials employed in devices; therefore, TMOs can be incorporated as selective charge transport layers. Those with a very high work function are commonly employed as hole transport layers (HTL), because their deep work function ensures pinning to the HOMO level of the organics. Conversely, the ones with a low work function easily pin to the LUMO level of organics and are thus employed as electron transport layers (ETL).

1.2.1 Overview

IUPAC defines transition metals as “an element whose atom has an incomplete *d* sub-shell, or which can give rise to cations with an incomplete *d* sub-shell”[69]. Even though elements of the 12th group falls outside of this definition, ZnO is commonly considered a TMO and treated as such in organic electronics. Table 1.1 lists the TM as they appear in the periodic table, together with Group 12 elements (shaded in yellow).

Group	3	4	5	6	7	8	9	10	11	12
Period 4	Sc	Ti	V	Cr	Mn	Fe	Co	Ni	Cu	Zn
Period 5	Y	Zr	Nb	Mo	Tc	Ru	Rh	Pd	Ag	Cd
Period 6		Hf	Ta	W	Re	Os	Ir	Pt	Au	Hg
Period 7		Rf	Db	Sg	Bh	Hs	Mt	Ds	Rg	Cn

Table 1.1: Transition metals as they are positioned in the periodic table. Highlighted in orange are the metals whose oxides were used in this work; highlighted in yellow are the metals of the 12th group which are not included in the IUPAC definition of TM.

The electronic configurations of TM are complex and widespread as two shells (*d* and *s*) are involved when the metal is ionised. When the oxide is formed, the outer *s* electrons are the first to be used to form bonds, leaving the cation in a d^n configuration. The electronic configurations of the TM whose oxides were used in this work are shown in Table 1.2, together with the oxides that were used and their band gap and work function values.

Metal	Electronic Configuration (in metal)	Oxidation states (in oxides)	Oxide	Band Gap (eV)	Work Function (eV)	Ref
V	$[Ar]3d^34s^2$	**5**, 4, 3, 2, 1	V_2O_5	2.7	7.0	[70]
Mo	$[Kr]4d^55s^1$	**6**, 5, 4, 3, 2, 1	MoO_3	3.0	6.7-7.0	[50,71,72]
W	$[Xe]4f^{14}5d^46s^2$	**6**, 5, 4, 3, 2, 1	WO_3	3.0	6.5-6.7	[73–75]
Co	$[Ar]3d^74s^2$	5, 4, 3, **2**, 1	CoO	2.4	4.7-4.8	[14,76]

Table 1.2: Information on the metals and their oxides used in this work. The oxidation states in bold are those found in the oxides in the 4th column, which were used in this work. Band gap and work function values refer to these oxides.

The values of band gap shown are quite large and ensure transparency over the visible range. The work function values are deep enough to ensure good alignment with the HOMO of most photoactive organic materials, which are usually in the range 4.5-6.5 eV[77–79]. An interesting feature of TMOs is that, even though the wide band gap suggests an insulating nature for them, the presence of native defects such as oxygen/metal vacancies and metal interstitials induce various levels of doping. Depending on the type of defect that is thermodynamically favoured, TMOs can be n-type (mostly because of oxygen vacancies) or p-type (mostly because of metal vacancies). A few examples of this include MoO_3, V_2O_5 (both included in this work), and ZnO as n-type materials and CoO (included in this work), NiO, and Cu_2O as p-type materials. Interestingly, the intrinsic n- or p-type nature of the TMOs does not directly affect their suitability as either HTL or ETL; that is, n-type TMOs such as MoO_3 and V_2O_5 can be and are used as hole transport layer, for instance. This is because, as will be shown in the following discussion, the work function is the major factor involved in the energy level alignment processes that determine whether a TMO can be used as a HTL or an ETL. In the following sections, TMOs will be dealt with both from the point of view of solid state physics (their band structure, defects and semiconducting behaviour) and from the one of organic optoelectronic devices (energy

level alignment and charge injection/extraction). For this last part, the focus will be mainly on anode interlayers, but the same principles hold true for ETL, too.

1.2.2 Chemical Properties

A detailed study of the electronic structure cannot ignore a chemical understanding of the different TMOs. The solid-state chemistry influences their electrical and magnetic behaviour, with defect states dictating the nature of their semiconducting behaviour and the position of their work function.

Oxygen content

One of the first parameters to evaluate is the oxygen content, fundamental in determining the n- or p-type nature of the oxide, and how it can be influenced (e.g. how reduction of an oxide can be induced or prevented). Taking an oxide with general formula MO_m, reduction can take place as detailed in Equation 1.3:

$$MO_m \rightarrow MO_{m-n} + \frac{n}{2} O_2$$

Equation 1.3

Thermodynamically, it is known that reduction is spontaneous if ΔG (Equation 1.4) is negative.

$$\Delta G = \Delta H - T\Delta S$$

Equation 1.4

Concerning Equation 1.3, the change in enthalpy does not depend on the oxygen pressure, but the change in entropy does (Equation 1.5), as gas evolves from the solid.

$$\Delta S = \Delta S^0 - \left(\frac{nR}{2}\right) \ln p_{O_2}$$

Equation 1.5

Therefore, ΔG can be expressed in terms of the partial pressure of O_2 (Equation 1.6)

$$\Delta G = \Delta G^0 - \left(\frac{nRT}{2}\right) \ln p_{O_2}$$

Equation 1.6

From the above, it can be inferred that the reduction reaction is spontaneous if:

$$p_{O_2} < e^{\frac{-2\Delta G^0}{nRT}}$$

Equation 1.7

In the limit of very high T the reduction reaction will take place anyway. From the Gibbs-Helmholtz equation:

$$\frac{d\left(\frac{\Delta G}{T}\right)}{dT} = -\frac{\Delta H}{T^2}$$

Equation 1.8

From Equation 1.7 a threshold value can be defined:

$$\ln p_d = -\frac{2\Delta G^0}{nRT}$$

Equation 1.9

Substituting Equation 1.9 in Equation 1.8, one obtains:

$$\frac{d(\ln p_d)}{dT} = \frac{2\Delta H}{nRT^2}$$

Equation 1.10

Equation 1.10 states that above a certain temperature, reduction will happen regardless of the oxygen pressure, because an increase in T results in an increase in the threshold pressure defined in Equation 1.7 and Equation 1.9. The thermodynamic considerations made above hold true not only for reduction of an oxide to one with less oxygen content, but also for reduction to the parent metal. The threshold pressure expressed in Equation 1.7 can be therefore called *decomposition pressure*[77]. Phase diagrams can be calculated, as shown in Figure 1.7 for cobalt: at different temperature and pressure values, either the metal or one of the two oxides can be stable. The stability is of course thermodynamic in nature, and is related to equilibrium conditions. Kinetic considerations must be taken into account, making the study and calculation of phase diagrams much more complicated.

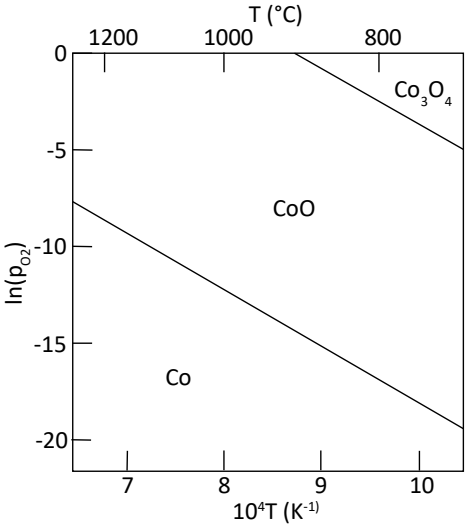

Figure 1.7: Phase diagram of cobalt oxide, showing the different regions where either one of the oxide or the metal is stable. (Adapted from [77])

Defects

Thermodynamics considerations similar to those detailed above imply that all solids (at T>0 °K) will contain defects; the most elementary ones are vacancies, where a lattice site is empty, and interstitial, where a non-lattice site is occupied by an extra atom. In TMOs, the formation of defects is usually related to the various oxidation states; for example, oxygen vacancies in MoO_3 are connected to the presence of Mo(V) cations in the lattice. The energy of formation of a

defect can be quantified using Equation 1.4, where ΔH is the energy needed to form a defect and ΔS is the increase in entropy due to the disorder created by it. The presence of defects perturbs the electronic structure of the material by creating an extra hole or electron; however, the overall electroneutrality of the oxide should be maintained. There are a few different processes through which this can happen:

- Compensating defects (Frenkel[o] or Schottky[p]) can be created;
- The electronic structure in neighbouring lattice sites can be altered;
- Defects due to impurities introduce new levels that can be occupied by the extra carrier;
- An ion charge can change (e.g. when different oxidation states are present).

Usually in TMOs one kind of defect is predominant, causing non-stoichiometry of the material. An excellent example is again MoO_3: oxygen vacancies, being far more frequent than other defects, result in the oxygen-deficient MoO_{3-x}; a similar behaviour occurs for V_2O_5 and WO_3. On the other hand, metal vacancies are the cause of the substoichiometry of oxides such as CuO and NiO. These defects can interact with each other through Coulomb forces and can disrupt the local electronic structure. When their number is very high, they can interact and order themselves in clusters, both electronically and structurally. Intragap defects states can combine and defect bands can form within the band gap of the oxide which, albeit maintaining its transparency, can become semiconducting or even conducting. Defects can also be eliminated from the material: if the defects align, a shear in the structure can effectively remove them. This process occurs through the formation of what are called *crystallographic shear phases*.

Defects and Semiconductivity

Trends in defects are dictated by the oxidation states. For instance, d^0 oxides cannot be oxidised but are easily reduced through formation of oxygen vacancies. Conversely, oxidation of monooxides such as NiO or CuO is favoured via formation of oxygen interstitials or, more commonly, metal vacancies.

The type of defect that is thermodynamically favoured determines the semiconducting nature of non-stoichiometric oxides:

- Oxygen vacancies and metal interstitials donate extra electrons to the lattice;
- Metal vacancies and oxygen interstitials remove electrons from the lattice.

In the first case, the extra electrons are situated in defect states close to the conduction band edge, hence inducing n-type semiconductivity; the most common examples are substoichiometric MoO_{3-x}, WO_{3-x} and V_2O_{5-x}, all of them covered in this work. The other

[o] When a vacancy is formed, it is compensated by the creation of an interstitial of the same ion.
[p] When a vacancy is formed, it is compensated by the creation of a vacancy of its counterion.

situation, where defects remove electrons from the material, produces p-type semiconductivity because they introduce empty defect states close to the valence band edge: electrons from the valence band can be thermally excited into these defects states, leaving behind an electron hole; examples of this are $Co_{1-x}O$ and $Cu_{1-x}O$.

Another cause of semiconducting behaviour is the presence of impurities, which can act as dopants: adding a second cation into a d^0 oxide introduces extra electrons (n-type doping), while replacing the metal ion in the lattice with a cation with lower oxidation state removes electrons (p-type doping).

The Kröger-Vink notation can be used to describe defects. For example:

$$\frac{1}{2}O_2 = \square_M'' + O_O^x + 2h^{\cdot}$$

Equation 1.11

The oxidation of an oxide MO produces $M_{1-x}O$ through formation of a metal vacancy $\square_M''$ and two holes. One hole can be tightly bound to the metal site:

$$\frac{1}{2}O_2 = \square_M' + O_O^x + h^{\cdot}$$

Equation 1.12

In the case described by Equation 1.12, only one free carrier (hole in this case) is generated and available for electrical conduction.

Similarly, in the case of n-type oxides:

$$O_O^x = \square_{\ddot{O}} + \frac{1}{2}O_2 + 2e'$$

Equation 1.13

Oxygen vacancies are formed through evolution of gaseous oxygen and production of two electrons. As before, one carrier can be strongly tied to the vacancy:

$$O_O^x = \square_{\dot{O}} + \frac{1}{2}O_2 + e'$$

Equation 1.14

In this case, only one electron is available for conduction.

Structure and Coordination

Electronic and crystallographic structures are vastly influences by near-neighbour interactions. As the nature of bonds in TMOs is mostly ionic, metal-oxygen interactions are of the utmost importance; coordination of metal cations by oxygen anions can be described in terms of:

- Bond lengths;
- Coordination number;
- Geometry.

The distance between the atoms can be estimated using ionic radii. The ionic radius depends on the oxidation state of the ion: the fewer electrons are present, the smaller the radius.

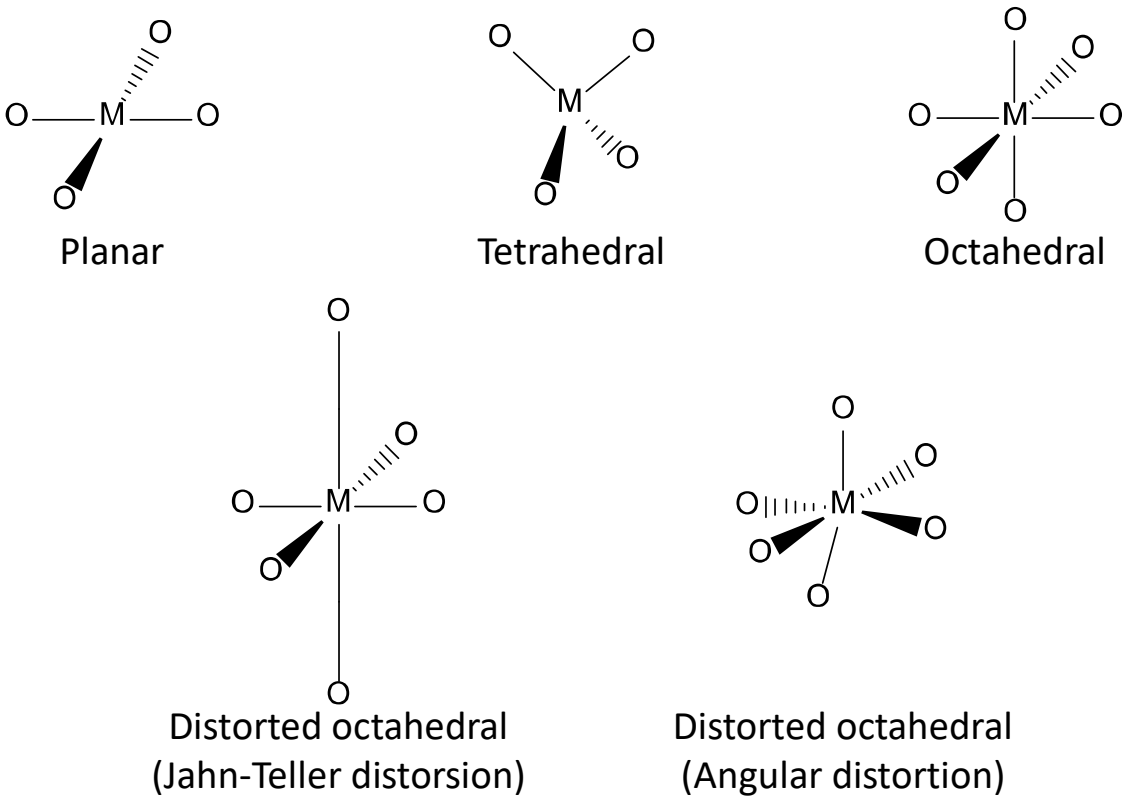

Figure 1.8: Most common coordination geometries for TMOs. Planar and tetrahedral geometries have a coordination number of 4, while the octahedral geometry has a coordination of 6. The latter can present two types of bond distortion, one regarding its length (also known as Jahn-Teller distorsion) and one regarding the bond angle.

Moreover, in the same group on the periodic table, ion sizes increase when moving down through the different periods: for instance, by looking at Table 1.1, tungsten ions are larger than molybdenum ions (considering the same oxidation state for both). While moving through groups within the same period, thus increasing the atomic number, ion radii get smaller, albeit this trend is not always regular. This radius reduction is caused by the greater nuclear charge; the higher number of electrons due to *d*-shell filling can only partly counterbalance this effect.

Figure 1.8 shows the coordination geometries usually found in TMOs; coordination numbers of 8 or greater can be found in oxide with very large cations (not shown here). The most common geometry is octahedral; however, it is often distorted in one of two ways: either two opposite bonds are lengthened, shifting the symmetry to tetragonal, or one or two bonds are shortened as compared to the others. The former situation is usually found in d^4 and d^9 electron configurations. The latter is very common in d^0 systems like V_2O_5 and MoO_3. In Table 1.3 some parameters for the oxide considered in this work are listed; namely, the coordination geometry and the crystal symmetry and structure. All four of them arranged the metal cation in an octahedral coordination: each octahedron has the metal in the centre and six oxygens at the

corners of the octahedrons (as seen in Figure 1.8). The octahedra can arrange themselves by sharing corners, edges, or faces. Of particular interest in this work is the distribution where corners are shared, as it is commonly found in TMOs *bronzes*[80]. These are binary oxides that accommodate a third, electropositive atom[q] in the interstices formed by the structural corner sharing; this third component can provide the oxide with interesting electronic properties.

Oxide	Coordination	Symmetry	Structure
CoO	Octahedral (6)	Cubic	Rock-salt
MoO_3	Distorted octahedral (6)	Monoclinic	MoO_3
V_2O_5	Distorted octahedral (6)	Orthorombic	V_2O_5
WO_3	Octahedral (6)	Cubic	ReO_3

Table 1.3: Coordination, symmetry and crystal structure of the oxides studied in this work. Information taken from [78].

1.2.3 Electronic Structure

Several theories can be used to describe the electronic structure of TMOs; this is because the wide variety of properties makes it difficult to find a unique model to describe them. A few approaches have been explored, which can be broadly divided into theories describing either *localised* or *partially delocalised* electron states[r]. An ionic model like the *crystal field theory* is the perfect example of a localised approach; instead, a molecular orbitals approach based on hybridisation of orbitals (such as *ligand field theory*) falls into the second category.

1.2.3.1 Crystal field theory

The ionic model is a simplified approach that excludes any hybridisation between oxygen and metal orbitals. Therefore, oxygen atoms are treated as O^{2-} ions and metal atoms are treated as M^{x+} cations, where x is the oxidation state of the metal. As seen above, in TMOs the oxygen atoms are arranged around the metal in different coordination geometries. The oxides considered in this work all show an octahedral configuration; hence the following discussion will be focused on that geometry. When the metal atom is in a spherical symmetry environment, the five *d*-orbitals are degenerate. However, when the metal ion is placed in an octahedral coordination, with six ligands (oxygen atoms in TMOs) at the corners of the octahedron, the *d*-orbitals are no longer degenerate. The two whose lobes are aligned with the oxygen atoms are destabilised (termed e_g orbitals); the other three, termed t_{2g} orbitals, are stabilised instead, because their maximum amplitude points away from the oxygen atoms. The situation is shown in Figure 1.9 for both cases. At the centre of the octahedra is the metal cation (not labelled for clarity). The two e_g orbitals are degenerate, as are the three t_{2g}. The presence of oxygen atoms

[q] Either an alkali metal like Na, or hydrogen.
[r] Fully delocalised approach such as band theory have vast limitations because of the highly ionic character of the M-O bond, and therefore were not dealt with in this work.

in a specific coordination geometry (octahedral in this case) induces a splitting between the two sets of *d*-orbitals called the *crystal field splitting* Δ_O[s]; this is shown in Figure 1.10a. As the total energy of the system must be maintained, the change in energy for the two sets of orbitals is different, as highlighted in the picture.

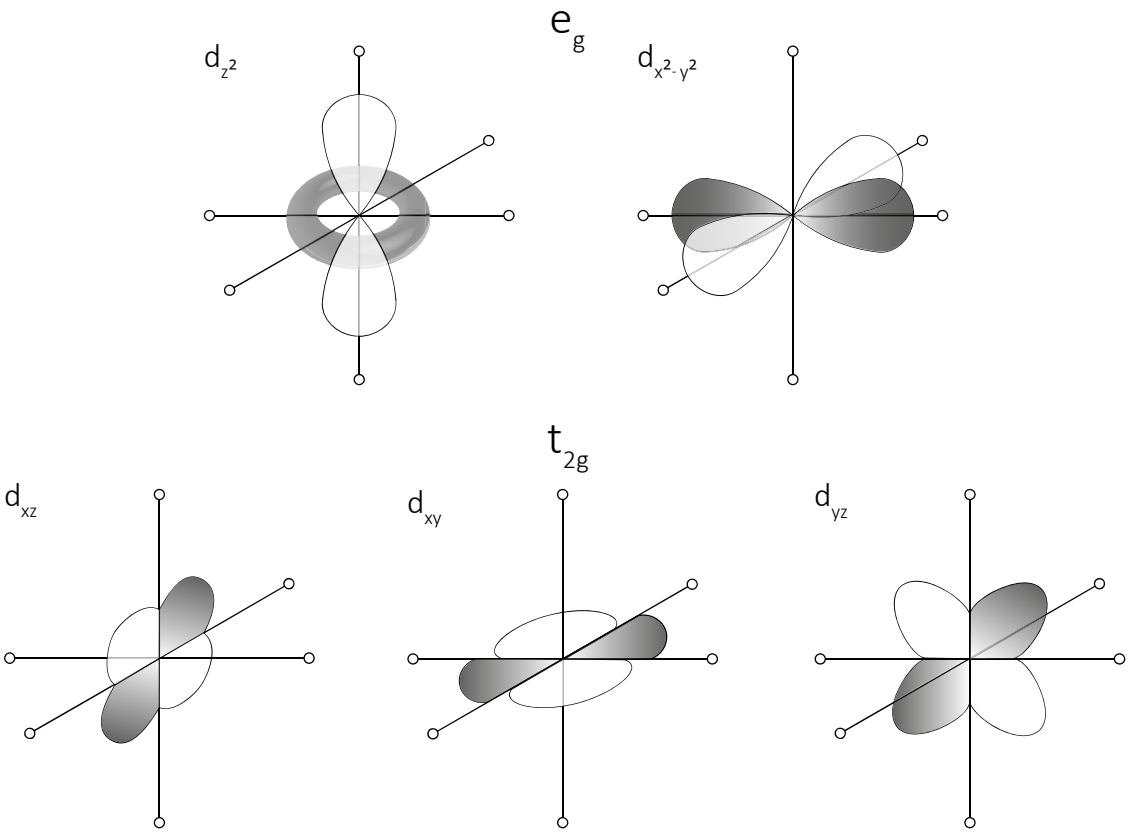

Figure 1.9: *d*-orbitals of the metal ion of a TMO arranged in an octahedral coordination.

It is worth noting that the absolute value of Δ_O depends on the ligands that surround the metal atoms: in TMOs oxygen is considered, but crystal field splitting occurs in all the coordination complexes. Filling of split *d*-orbitals is influenced both by the magnitude of Δ_O and by Hund's first rule when more than three electrons are present[t]. The former would favour double occupation of the t_{2g} orbitals, with any electrons after the third distributed with opposite spins. Instead, Hund's first rule would minimise the electrostatic repulsion between electrons filling the same orbital by arranging the electrons one for each orbital with parallel spins. Therefore, if the pairing energy (the electron-electron repulsion energy) is smaller than Δ_O, the electrons will fill the t_{2g} with opposite spins first, and only after all the six available states are occupied will start filling the e_g set. On the other hand, if Δ_O is small, it becomes favourable to distribute the electrons with parallel spins across all available orbitals first. This situation has the highest

[s] The 'o' denotes the octahedral coordination.
[t] The first three electrons will occupy the three t_{2g} states with parallel spins.

number of unpaired spins, and is therefore termed a *high spin* configuration, as opposed to the former being referred to as *low spin*; the different configurations are pictured in Figure 1.10b.

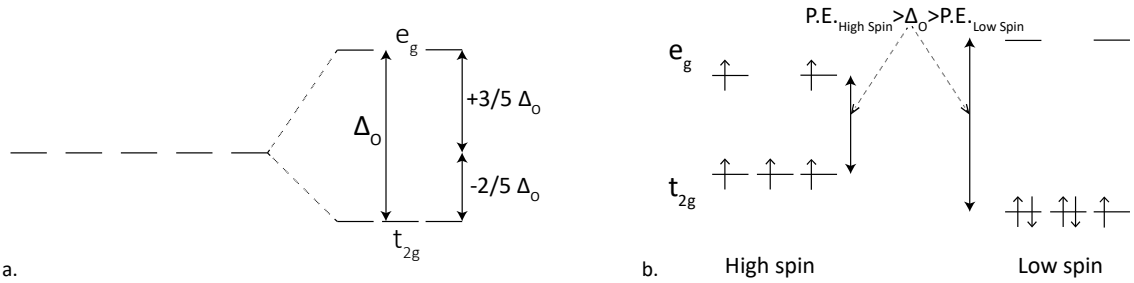

Figure 1.10: a. The splitting of *d*-orbitals induced by an octahedral coordination (Δ_O). The conservation of energy dictates the change in energy of the two sets of orbitals. b. High and low spin configurations based on the relative magnitudes of the pairing energy P.E. and Δ_O.

Generally, 3d orbitals result in high spin configurations, while 4d and 5d orbitals favour low spin. The stabilisation obtained by arranging electrons in a certain configuration can be calculated (in units of Δ_O): for an octahedral geometry, electrons occupying t_{2g} orbitals each contribute an energy $-^2/_5\ \Delta_O$, while electrons occupying e_g orbitals each contribute an energy $^3/_5\ \Delta_O$. The *crystal field stabilisation energy* (CFSE) can be calculated by summing the energies of all the *d*-electrons. All the possible orbital occupation patterns and crystal field stabilisation energies for an octahedral geometry are listed in Table 1.4.

n	High spin configuration	High spin CFSE	Low spin configuration	Low spin CFSE
1	t_{2g}^1	$-2/5\ \Delta_O$		
2	t_{2g}^2	$-4/5\ \Delta_O$		
3	t_{2g}^3	$-6/5\ \Delta_O$		
4	$t_{2g}^3e_g^1$	$-3/5\ \Delta_O$	t_{2g}^4	$-8/5\ \Delta_O$ + 1 pair of e^-
5	$t_{2g}^3e_g^2$	0	t_{2g}^5	$-2\ \Delta_O$ + 2 pairs of e^-
6	$t_{2g}^4e_g^2$	$-2/5\ \Delta_O$ + 1 pair e^-	t_{2g}^6	$-12/5\ \Delta_O$ + 3 pairs of e^-
7	$t_{2g}^5e_g^2$	$-4/5\ \Delta_O$ + 2 pairs e^-	$t_{2g}^6e_g^1$	$-9/5\ \Delta_O$ + 3 pairs of e^-
8	$t_{2g}^6e_g^2$	$-6/5\ \Delta_O$ + 3 pairs e^-		
9	$t_{2g}^7e_g^2$	$-3/5\ \Delta_O$ + 4 pairs e^-		
10	$t_{2g}^8e_g^2$	0		

Table 1.4: Occupation of orbitals in the different configurations for increasing numbers of *d*-electrons.

Generally, in local models such as crystal field theory, band gaps are treated as *charge transfer* excitations between atoms. This description is particularly accurate when non-metallic oxides are being dealt with, especially magnetic insulators such as NiO. Metal and oxygen ions induce long-range coulombic interactions that can be summed up in a lattice-wide potential, the *Madelung potential*. This potential, calculated by considering the ions as point charges, stabilises electron states and destabilises cation sites. As a result, the oxygen *2p* levels will form the valence band; conversely, destabilised metal *nd* levels will be at higher energies and form the conduction band.

The Madelung potential alone is an overestimation of the band gap of a TMO, as other factors must be taken into consideration; one of these, arguably the most important, is the polarisation energy of moving charges in the lattice. This tends to decrease the energy of empty states (the metal *nd* ones) and raise that of filled states (the oxygen *2p*). Finally, when the ionic levels overlap in a solid, their broadening results in the formation of bands: the difference between the top of the oxygen *2p* band (occupied) and the bottom of the metal *nd* band (unoccupied) is therefore an estimate of the gap for ionic models. This estimate is true for d^0 TMOs (e.g. V_2O_5, MoO_3, and WO_3), while the presence of *d*-electrons complicates things because of correlation effects.

1.2.3.2 Ligand field theory

Purely ionic approaches such as crystal field theory have their limitations; as the metal-oxygen bonds in TMOs show some covalent contributions beside the ionic nature, some degree of orbital overlapping is present and can be modelled using a molecular orbitals approach, namely the *linear combination of atomic orbitals* (LCAO) approximation. The consideration made above about the effect of the coordination geometry on *d*-orbitals still holds true. Combining crystal field theory with the LCAO approach produces a model called *ligand field theory*.

The formation of molecular orbitals and their subsequent broadening into energy bands is shown in Figure 1.11. The final number of molecular orbitals must be equal to the total number of atomic orbitals (metal plus oxygen) that were present at the beginning; in the situation illustrated here, an oxide of the type MO_2 (e.g. TiO_2) was used as an example. For clarity, only *nd* orbitals from the metal atom and *2p* orbitals from the oxygen atom are shown; of course, the *(n+1)s* and *(n+1)p* orbitals of the metal also participate in the formation of molecular orbitals, as do the oxygen *2s* electrons. It can be seen that, depending on the orientation of the oxygen *2p* orbitals with respect to the t_{2g} orbitals of the metal (dictated by symmetry considerations), either non-bonding orbitals or molecular orbitals can be obtained. When molecular orbitals are formed, because they are perpendicular to the M-O bonds, they are π-type orbitals (bonding and antibonding). On the contrary, e_g orbitals of the metal will combine with *2p* orbitals oriented along the M-O bond; therefore, there is a larger overlap and the resulting molecular orbitals are σ-type (bonding and antibonding). This means that e_g orbitals are more perturbed and show a stronger antibonding character than t_{2g} orbitals. As the overlap integrals between oxygen *2p* and metal *nd* orbitals are quite small (because of the mainly ionic character of the bond), bonding orbitals are mostly *2p* in nature, while antibonding ones are mostly derived from the metal's *nd*. *d*-orbitals are smaller (more contracted) than both *s*- and *p*-orbitals, therefore their overlapping is less efficient. This, together with the stronger

antibonding character of e_g orbitals with respect to t_{2g}, explains why a gap is opened between π^* and σ^* bands but not between π and σ (see Figure 1.11).

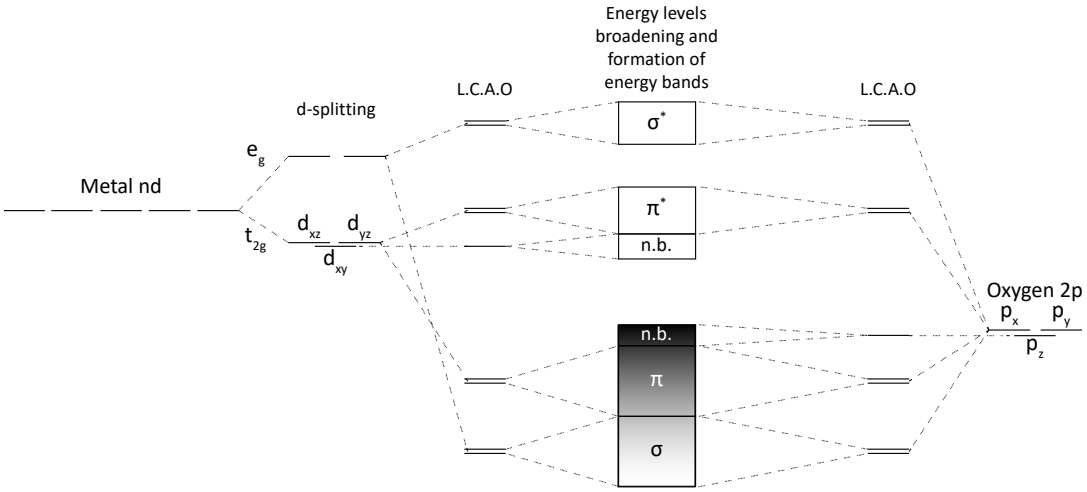

Figure 1.11: Linear combination of *d* orbitals from the metal and *p* orbitals from the oxygen, resulting in the formation of bonding and antibonding molecular orbitals that are broadened into bands (case of a MO_2-type oxide). N.b. indicates non-bonding orbitals. Adapted from [81].

For simplicity, these bands formed from antibonding molecular orbitals, that are similar in nature to the *d*-orbitals of the metal, are termed *d*-bands.

d-bands Occupancy and Electronic Properties

The occupancy of *d*-bands determines the electronic behaviour of different TMOs[78], which can range from insulating to conducting. The possible situations are illustrated in Figure 1.12.

d^0 oxides like MoO_3 do not have any electrons available to populate the *d*-bands, and are therefore insulators: their valence band is of *2p* nature from the oxygen orbitals and the *d*-band acts as the conduction band. However, the formation of oxygen vacancies is favoured and very common, and these defects act as electron donors therefore moving the Fermi level away from the mid-gap position towards the conduction band. Hence, they are considered n-type materials. When a large number of oxygen vacancies are present, the density of defect states within the gap is very high and the TMOs act as semiconductors, because electrons from the defect states can easily hop into the conduction band. It is worth noting that these semiconducting oxides, for example substoichiometric MoO_{3-x} or WO_{3-x}, maintain their transparency in the visible range.

When electrons are available to fill the *d*-bands, the situation is complicated and the degree of occupancy plays a significant role. For oxides like MoO_2 and WO_2, the number of available electrons is enough to fill part of the t_{2g} band. Because the Fermi level is within a band and filled and empty states are not separated by an energy gap, these oxides behave as metallic conductors.

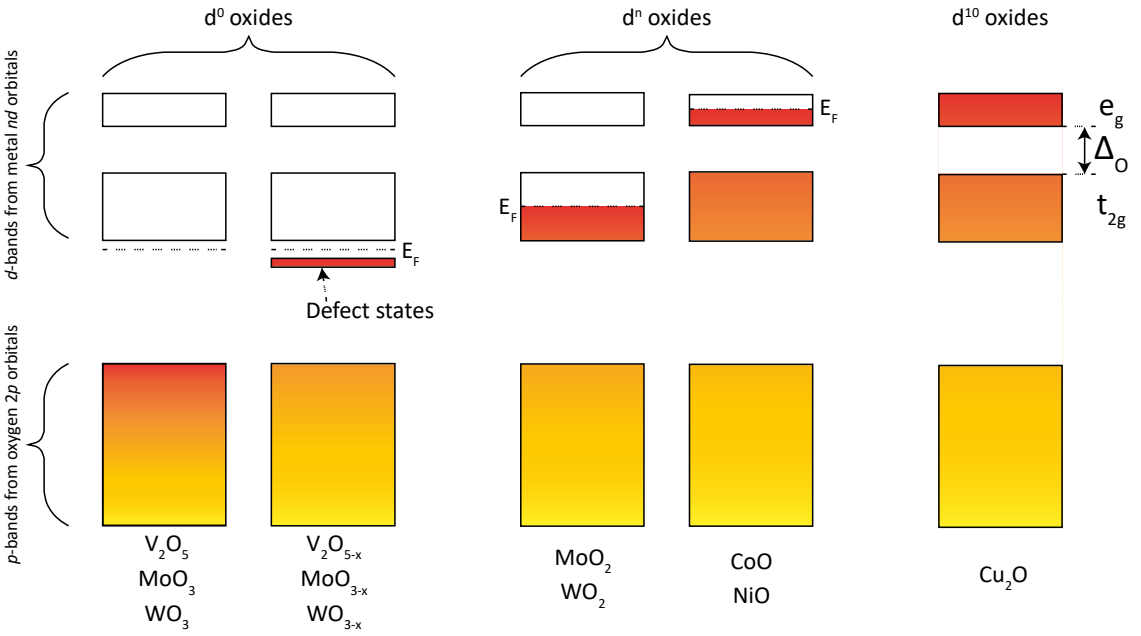

Figure 1.12: *d*-band occupancy in different TMOs. Bands formed by non-bonding orbitals were incorporated into *p*- and *d*-bands for simplification. The *d*-splitting is also shown. Adapted from [78,79].

When there are enough electrons to completely fill the t_{2g} band and partly fill the e_g band, the electronic behaviour of the material is different, as the e_g band is very narrow and electron localisation in it is strong. The very weak delocalisation of e_g states is due to Coulombic repulsion between electrons, which effectively confines them to the metal sites and affects their ability to move across the material[82,83], making these materials insulators. Two different situations can arise from the strong localisation of e_g electrons, depending on the nature of the energy gap formed by the electron correlation effects.

In the first scenario, the Mott-Hubbard model, electrons can hop from one metal site to an adjacent site[84], as shown in Equation 1.15:

$$M^{2+} + M^{2+} \rightarrow M^{3+} + M^{+}$$

Equation 1.15

The Mott-Hubbard term *U* derives from the Coulombic repulsion generated by the presence of the extra electron in M^{+}. The expected electrical conductivity of such d^n oxides would occur through hopping of electrons across metal sites, but the Mott-Hubbard term works against that by opening a gap within the e_g band[85]. Therefore, these materials act as insulators (*Mott-Hubbard insulators*).

The second situation mentioned above occurs when the lowest energy transition is not a *d-d* transition but rather a charge transfer between the oxygen and the metal. This happens when electron correlation effects are so strong that the Mott-Hubbard term becomes very large; when it becomes larger than the energy needed to excite an electron from a *2p* oxygen state to an empty metal *d*-state, the material is called a *charge-transfer insulator*[86]. One of the main

difference between the two situations is that in the Mott-Hubbard model electrons are transferred between different unit cells of the lattice, while in charge-transfer insulators their movement is restricted within the same unit cell.

To conclude, the last class of oxides comprises those with a full *d*-band. These are generally semiconducting materials, where the e_g band is the valence band and the empty band above it (formed by metal *s*-orbitals) is the conduction band. The ease of formation of metal vacancies makes them p-type semiconductors[87].

1.3 SELECTIVE CHARGE TRANSPORT INTERLAYERS

The range of properties expressed by TMOs makes them an ideal candidate for incorporation in organic optoelectronic devices. As mentioned above, their transparency is a desired feature in interlayer materials, which must not affect the interactions between light and the active layer. However, it is the work function that determines the suitability of TMOs as charge selective layers to the greatest extent. Early work by Fahlman *et al*[88,89] found a connection between the Fermi level of interlayers and the energy level alignment with organic materials. After that, a comprehensive study of a wide variety of TMOs was carried out by Greiner *et al*[14,68,90–96]: their extensive work provided the theoretical background and justification for this work. This section summarises their findings, prioritising those parts that were most important for this research.

1.3.1 Importance of work function

The energy level alignment (ELA) behaviour at the interface between a TMO and an organic semiconductor is governed by the oxide work function only, as long as there is no chemical reaction between the interlayer and the organic and the oxide thickness is large enough so that the work function is not affected[u] and tunnelling effects are absent. The advantage of using TMOs arises from the fact that their work function values are spread over a wide range, and can therefore form favourable interfaces with a variety of organic semiconductors. Their work function can also be tuned by inserting defects and changing their stoichiometry through changes in processing conditions[94,95], therefore making them suitable for the fabrication of bespoke interlayers that can adapt to many different active layers.

Depending on the position of the work function of the oxide, the interlayer can either pin the HOMO or the LUMO level of the organic material. Examples of the two different scenarios are pictured in Figure 1.13a. The first situation (on the left), where an oxide with a deep work function can pin the HOMO level of an organic molecule, is important for interfaces at the anode

[u] For very thin films, the work function is lowered compared to bulk films.

of a device. In cathodic interfaces (on the right), an oxide with a shallow work function can pin the LUMO level of an organic molecule like C_{60}.

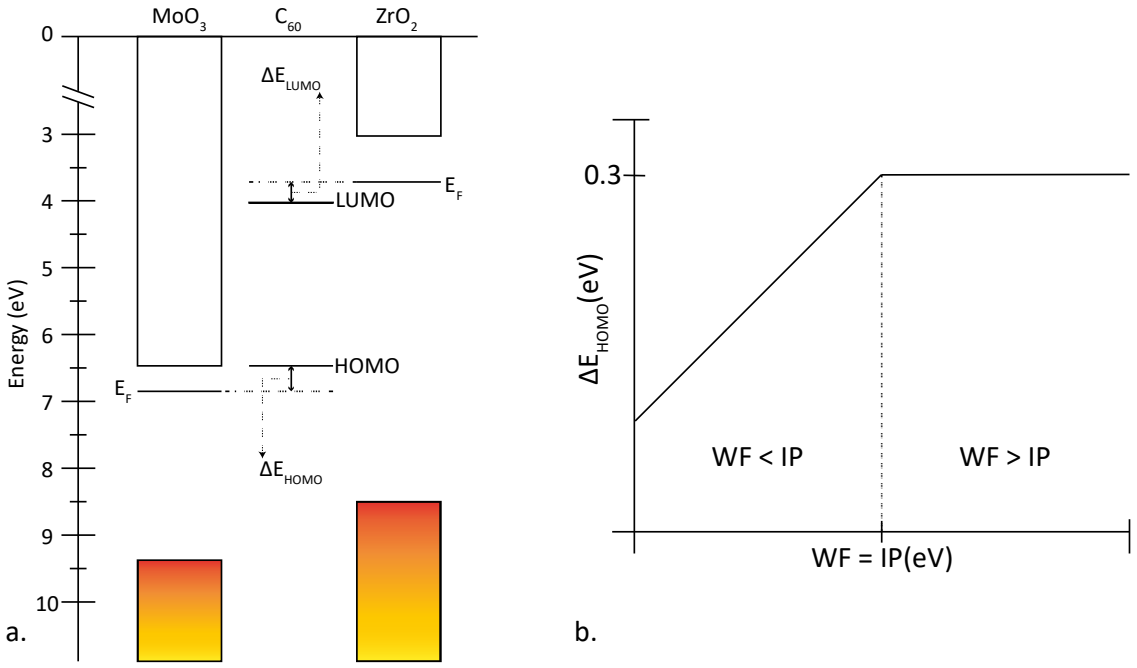

Figure 1.13: a. Schematics highlighting ELA between a high work function oxide (MoO_3) and the HOMO of C_{60} or between a low work function one (ZrO_2) and the LUMO of C_{60}. Adapted from [68]. b. Plot of HOMO offset ΔE_{HOMO} against the difference between the work function of the oxide WF and the HOMO level of the organic material IP[v].

1.3.2 Anode interlayers

The mechanism through which ELA takes place will be discussed for alignment with the HOMO level of organic materials (the process happening in anode interlayers). The same considerations hold true when the oxide has a low work function that allows alignment with the LUMO level of the active layer[68,79,97], which is the case when dealing with cathode interlayers.

Pinning of the organic's HOMO level

In the work of Greiner, it was observed that the formation of an anodic energy offset at the oxide-organic interface showed two separate behaviours depending on the magnitude of the work function of the oxide. When this is smaller than the HOMO of the organic, the energy offset depends on the difference between the two. Choosing oxides with work function values approaching the HOMO level of the organic material results in a decrease in the offset, until it reaches a minimum value of 0.3 eV when the two are equal. Interestingly, further increases in the oxide work function do not produce any more changes in the offset value. This trend is summarised in Figure 1.13b.

The behaviour can be understood by treating the organic material as an adsorbate molecule on an oxide substrate. When a molecule is adsorbed it can become positively charged by donating

[v] IP is the ionisation potential, equivalent in absolute value to the energy of the HOMO level.

an electron to the substrate: this happens through electron transfer between the HOMO level of the molecule and the Fermi level of the oxide. The energy of formation of the charged molecule therefore depends on the Fermi level of the oxide. If it falls at lower energies than the HOMO level, it becomes favourable for an electron to jump onto it because it would find itself at a more negative energy (thus in a more stable state). Contrarily, when the Fermi level is closer to the vacuum level than the HOMO of the organic, the adsorbed molecule is found in a neutral state. The two different scenarios mirror the plot showed in Figure 1.13b: the situation where the adsorbate is found in a charged state correspond to the right side of the plot (where the work function of the oxide is equal to or greater than the HOMO level of the adsorbate), while the neutral state is observed when the energetics are those of the left side of the plot. In the latter case, the HOMO offset depends linearly on the contact potential difference (CPD) between the oxide and the adsorbates[w]; as the CPD varies with the work function of the oxide, so does ΔE_{HOMO}.

Once the formation of charged species becomes favourable, their positive charge can balance the negative electric field produced by the CPD. With the work function becoming larger than the HOMO level of the adsorbate (right side in Figure 1.13b) more molecules enter a charged state; the system reaches steady-state where further increases in the field produced by the CPD are countered by an increase in the positive field produced by the charged adsorbate molecules. The HOMO level of the organic adsorbate is now *pinned* to the Fermi level of the oxide. The effect on the band structure at the interface is shown in Figure 1.14 for two different oxides: electron transfer occurs from the HOMO of the organic to the Fermi level of the oxide, and the CPD (not shown for clarity) is counterbalanced by the positive field produced by the charged adsorbates. The HOMO level gets pinned to the Fermi level and the band bending produces the HOMO offset which, as the work functions in both cases are larger than the HOMO level, has the minimum value of 0.3 eV.

Role of Energy Bands

The energy bands of the oxide do not participate in the energy level alignment process, which is only regulated by the work function value and its position relative to the HOMO level of the organic material. However, they deliver the needed pathways for charge extraction/injection in devices; in anode interlayers, the carriers to be moved are holes. Depending on the semiconducting nature of the oxide considered, two processes can take place; both are shown in Figure 1.14:

[w] See the Kelvin Probe section in the Materials & Methods for more details about the band structure at interfaces between different materials.

- n-type oxides such as MoO_3 can extract (inject) holes from (into) the organic material via electron transfer between the conduction band of the oxide and the HOMO of the organic (top diagram in Figure 1.14);
- p-type oxides such as NiO can extract (inject) holes from (into) the organic material via hole transfer between the HOMO of the organic into the valence band of the oxide (bottom diagram in Figure 1.14).

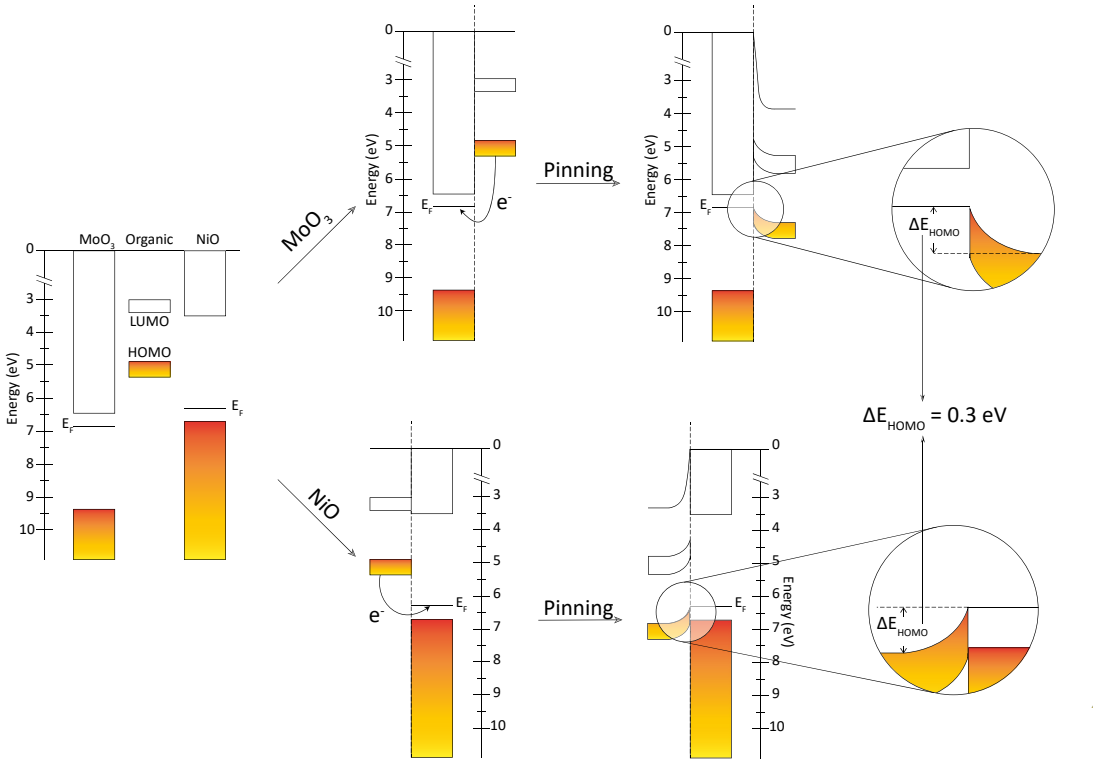

Figure 1.14: Schematics of the mechanism behind the HOMO level pinning of organics adsorbed on oxide substrates. Two different oxides with deep work function, one n-type (MoO_3) and one p-type (NiO). Electron transfer from the organic HOMO level to the Fermi level of the oxide is highlighted.

While it may have seemed counterintuitive to use n-type materials as anode interlayer, the top diagram in Figure 1.14 helps understand the charge transfer mechanism. After HOMO pinning to the Fermi level, empty states in the conduction band find themselves close to occupied states in the HOMO levels of the organic. Therefore, a hole can be extracted from the organic into the oxide (charge extraction in OPV devices) by means of an electron moving in the opposite direction. On the contrary, if the anode is kept at a positive bias (like an OLED device) electron transfer happens from the HOMO of the organic into the empty states of the conduction band of the oxide: this process is the equivalent of a hole being injected into the organic.

1.4 SOLUTION PROCESSING

Organic photovoltaic devices and organic LEDs can be fabricated in two different architectures, identified by the electrode exposed to atmosphere. If the exposed electrode is the cathode, the device is in standard architecture (OLEDs devices in this architecture are sometimes called top-cathode). An example of this architecture is shown in Figure 1.15. If the electrodes are inverted, and the cathode is the transparent electrode, the device is said to be in inverted architecture (sometimes top-anode for OLEDs). As the state-of-the-art transparent electrode is ITO, the nature of the hole transport layer will determine the architecture: for instance, when PEDOT:PSS is used (a hole transport layer) the device will be standard architecture; on the contrary, if ZnO is deposited on top of the ITO (an electron transport layer), the architecture will be inverted.

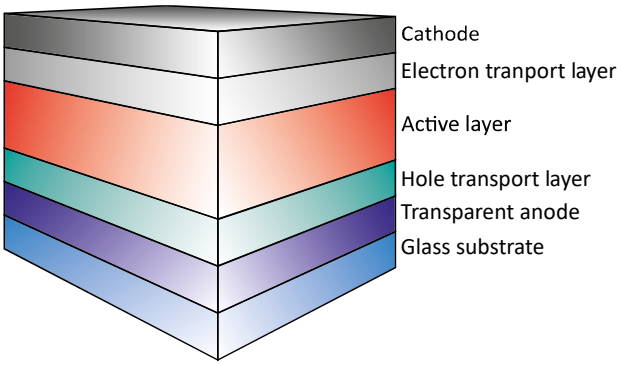

Figure 1.15: Structure of a standard architecture (top-cathode) optoelectronic device.

The anode interlayer of choice before the introduction of TMOs was PEDOT:PSS, which has high conductivity and is selective for hole transport; even nowadays, PEDOT:PSS is widely used despite the growing adoption of TMOs-based hole transport layers[30,35,41,62,63,98] because of its transparency and its ability to form an Ohmic contact with ITO[99,100]. Nevertheless, PEDOT:PSS has a major problem in its acidic nature, which is very detrimental to the ITO electrode and therefore affects the devices' lifetime and stability[101,102]. When the suitability of ZnO and TiO_2 as cathode interlayer was demonstrated[51,67], the first devices with in inverted architecture were fabricated, thus preventing damages to the ITO by the PEDOT:PSS layer, which was repositioned above the active layer. Even in this position, the acidic and aqueous nature of the PEDOT:PSS and its precursor solution resulted in stability and lifetime issues, suggesting the need to remove it altogether[101]. The inverted architecture has however an intrinsic advantage, in which high work function metals such as Au can be used as the air-exposed anode, enhancing the environmental stability of the devices.

As shown before, several TMOs can be employed as anode interlayers because they allow for efficient energy level alignment with the HOMO of various polymers, and they can be deposited via thermal evaporation together with the anode. Yet, thermal evaporation is not compatible with large scale deposition, and furthermore it introduces a processing step requiring high-vacuum which adds to costs and time requirements. Ideally, all the layers should be deposited

via solution routes, to unlock the possibility of inkjet printing the whole device. Hence the need to develop novel routes to deposit TMOs from solution.

Inverted architecture devices have strict requirements on the processing route of the overlying anode interlayer material. The organic materials in the active layer are very sensitive to high temperatures, thus solution deposition of hole transport TMOs cannot involve high temperature post-deposition treatment. Also, the active layer is usually very sensitive to harsh chemical environments, restricting the precursor solution of the TMOs to mild, non-reacting chemistries. Usually, alcoholic solvents such as isopropanol or ethanol can fulfil the last requirement, giving at the same time good wetting on various organic films.

The most investigated solution-based routes in organic electronics are arguably those involving nanoparticle dispersions or sol-gel depositions. Recently, an innovative method based on combustion synthesis was reported: despite being relatively unexplored yet, it has shown some promising preliminary results. All three pathways will be described in the following, with a greater focus on sol-gel methods, which were employed in this work.

1.4.1 Nanoparticles dispersion

Nanoparticles have the advantage of not exposing the active layer to harsh chemical environments. They can be synthesised according to any chemical route required, then separated from the solution and dissolved in mild alcoholic solvents. Most reports found in the literature for nanoparticle films used as anode interlayers deal with MoO_3[103–105] and WO_3[106,107], while a few groups reported nanoparticle films of VO_x, NiO and CuO_x, albeit not used as anode interlayers in devices[108–115]. The use of nanoparticle films as hole transport layer introduces many challenges despite solving the problem of aggressive chemistries. An example is the need for capping agents: to disperse nanoparticles in alcohols, Van der Waals interactions between them must be attenuated, otherwise the nanoparticles will tend to coalesce. Organic materials such as fatty acid chains can be used, but they will need to be removed from the film or else they could affect charge transport across it. Either high temperature annealing, or UV-O_3 treatment, or oxygen plasma treatment can be used to remove them. However, high temperatures are not compatible with inverted architectures, while the non-thermal treatments are likely to damage the organic active layer. A solution to the capping issue was proposed by the Marks' group: the capping agents are converted into a conducting oxide matrix via a combustion reaction; this matrix ensures good charge transport across the films[116]. As the temperature needed to start the combustion reaction can be made quite low by carefully choosing its chemistry, this approach could prove useful in inverted devices.

A second problem commonly found with nanoparticles is the film quality. The active layer and the electrode must be separated by a continuous, uniform interlayer film, otherwise shunts, pinholes and other electrical losses can decrease a device performance. Nanoparticle films are non-continuous by nature, and additional efforts must be made to ensure a complete coverage. In addition to this, the films are very rough as well as inhomogeneous; therefore, the evaporated anode needs to be very thick to cover the whole device area without leaving exposed areas.

Finally, the health implications of nanoparticle exposure are not clear yet. After fabrication, a device is encapsulated, and the nanoparticle film would be sandwiched between the active layer and the electrode. This should lower the exposure to a minimum, but to safely dispose of devices at the end of their life cycle there is a great need for a full understanding of the nanoparticle toxicity and environmental impact.

1.4.2 Sol-Gel

Sol-gel processing is arguably the most used route to process TMOs from solution. A solution of a TMO precursor is prepared, aged, and then deposited via various methods (for instance, spin or spray coating) on the substrate of choice. The deposited film can be converted into the desired oxide upon hydrolysation of the precursor and heat treatment to remove organic residues. Hydrolysis is the driving process in the formation of the oxide, and happens in solution as well as after deposition. As TMOs are insoluble in water and alcohols, if the precursor is hydrolysed in solution flocculation processes can occur which affect the quality of the deposited film. Therefore, the precursor solution must be carefully prepared, controlling factors such as pH and amount of water present[117]. pH can be taken as an example of the importance of the precursor solution chemistry; its value will in fact determine the ligand that coordinates the metal cation, which can be O^{2-}, OH^-, or H_2O. Most sol-gel routes involve alcoholic solvents, which are usually hygroscopic and contain a small amount of water[x]; upon solvation of the metal cation, M-OH_2 bonds are formed. These bonds are partially covalent in nature, and induce an electron transfer from the water molecule to the metal cation.

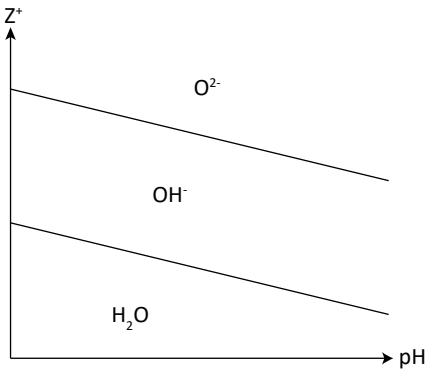

Figure 1.16: Ranges of pH where each ligand coordinates a metal cation of valence Z^+. Adapted from [59].

[x] Dehydrated solvents can be used but in reality, the small quantities of water usually present are beneficial because they can promote hydrolysis in solution and therefore lower the post-deposition temperature needed to convert the precursor in the oxide.

This makes the aqueous ligand more acidic and prone to dissociation according to the following equilibria[118]:

$$M - OH_2 \rightleftharpoons M - OH^- + H^+ \rightleftharpoons M - O^{2-} + 2H^+$$

Equation 1.16

The pH of the solution regulates these equilibria, together with the coordination of the cation (and therefore its charge). The influence of pH and cation charge Z^+ on Equation 1.16 are shown in Figure 1.16: depending on both factors, different ligands will coordinate the metal cation. The point at which the pH favours precipitation of the oxide is termed the *point of zero charge*.

1.4.2.1 Carboxylate precursors

Metal carboxylates, or acetates, are the most commonly used precursors for NiO and CuO_x[119–125]. Thermal decomposition of these compounds to the corresponding oxide occurs at very high temperatures, usually non-compatible with plastic substrates or inverted architecture devices. For instance, nickel acetate can be converted into NiO when heated at 330°C in air[126], according to:

$$Ni(CH_3COO)_2 \rightarrow NiCO_3 + CH_3COCH_3$$
$$NiCO_3 \rightarrow NiO + CO_2$$

Equation 1.17

When considering copper acetate, the decomposition starts at 168°C and finishes at 310°C, resulting in a mixture of metallic Cu and its two oxides, CuO and Cu_2O (Equation 1.18, first step). To obtain single phase CuO (albeit with a small amount of Cu_2O leftover), the temperature must be increased to 510°C (Equation 1.18, second step)[127]:

1st Step:

$$Cu(CH_3COO)_2 \rightarrow CuCH_3COO + CH_3COOH \Rightarrow$$
$$CuCH_3COO \xrightarrow{\dot{H}} CH_3COH + CuO$$
$$\rightarrow Cu + CO_2 + \dot{C}H_3$$
$$\xrightarrow{\dot{H}} Cu + CH_3COOH$$
$$CuO + Cu \rightarrow Cu_2O$$

2nd Step:

$$Cu \xrightarrow{\frac{1}{2}O_2} CuO \quad \text{AND} \quad Cu_2O \xrightarrow{\frac{1}{2}O_2} 2CuO$$

Equation 1.18

The precursor can be decomposed in solution, by promoting hydrolysis to some extent for example, and thus a soluble precursor gel can be obtained, which contains either the TMO of

interest or the corresponding hydroxide (the hydroxide can be oxidise after deposition through thermal annealing). Solvents used in these scenarios are alcohols or mixed polarity solvents such as 2-methoxyethanol, as pure water will induce complete hydrolysis and subsequent precipitation of the oxide[128]. Chelating agents are used to improve the solubility of the metal salt and the stabilisation of the precursor solution: commonly used ligands are (mono)ethanolamine or ethylenediamine[61,121,125,129,130]; their amine group can coordinate the metal cation in solution, avoiding flocculation and precipitation of insoluble products. However, these chelating agents must be removed from the deposited film, requiring a post-deposition annealing step. Their high decomposition temperatures[131] implies that, in order to employ this route with flexible substrates or in inverted devices, a compromise must be found between the need to remove residues and the maximum achievable annealing temperature, and this compromise results in the presence of leftover organic impurities in the TMO film, and those can greatly affect the performance of the interlayer. The Olson's group[112,132,133] investigated this, depositing NiO from a metal-organic ink containing diamine groups to complex the Ni cations and stabilising them in a suspension in alcohol; water was then added to promote hydration and subsequent hydrolysis. However, to remove the chelating agents, temperatures as high as 300°C were required, which are non-compatible with inverted architectures.

1.4.2.2 Hydrogen bronze route

To deposit MoO_{3-x} and V_2O_{5-x} films, a very simple route was developed to exploit the formation of a hydrogen bronze (H_yMO_x) in an alcoholic solution. The process works with the precursor being a powder of either the metal[49,134] or the oxide[135,136]: the powder is dispersed in an alcohol (theoretically every alcoholic solvent will work) and then H_2O_2 is added. When the precursor is the oxide, the solvent favours reduction and provides hydrogen for intercalation, while H_2O_2 promotes dissolution and solubility of the bronze product. When a metallic precursor is used, H_2O_2 induces its oxidation, which is moderated by the reducing action of the alcohol. The reducing power of the alcohol produces substoichiometric oxides by changing the valence of some of the cations (e.g. reducing Mo^{6+} to Mo^{5+} and V^{5+} to V^{4+}): substoichiometry will result in oxygen vacancies making the resulting oxide a n-type semiconductor. Films of good quality were deposited using both the metal and the oxide as precursors and only required a mild temperature post-deposition treatment, with improvements in performance over PEDOT:PSS, particularly in J_{sc} and FF[134,135].

A similar process can be used to deposit WO_{3-x} films from a metallic precursor[137,138]: the metal powder is solvated in H_2O_2, then an alcohol is added. It is worth noting that the first step of the process is highly exothermic and extra care must be taken when using this procedure.

1.4.2.3 Alkoxide precursors

Routes involving alkoxide precursors are very popular because of the ease in preparation and the simple chemistry involved. The alkoxide can be dissolved in either the parent alcohol or a different one, and films deposited from the precursor solution are readily converted in the oxide of interest without the need for high temperature treatment. Instead, the film is usually already composed of the oxide of choice right after deposition, because of hydrolysis promoted by the small amount of water present in the solution. Three reactions can take place[128,139]:

$$M(OR)_x + H_2O \rightarrow M(OR)_{x-1}(OH) + ROH \quad \text{(Hydrolysis)}$$

Equation 1.19

$$2M(OR)_{x-1}(OH) \rightarrow M_2O(OR)_{2x-2} + H_2O \quad \text{(Condensation via water elimination)}$$

Equation 1.20

$$2M(OR)_{x-1}(OH) \rightarrow M_2O(OR)_{2x-3} + ROH \quad \text{(Condensation via alcohol elimination)}$$

Equation 1.21

As for routes involving carboxylates, the amount of water must be carefully controlled to avoid flocculation. Also, the polarity of the M-OR bond is very important, as more polar bonds are more likely to undergo hydrolysis[128].

V_2O_{5-x} was synthesised from a vanadium (V) oxytriisopropoxide precursor, by dissolving it in a water-isopropanol mixture[140]; a number of additives were used to stabilise the reaction and avoid precipitation. The same precursor was used, solvated in isopropanol, to deposit V_2O_{5-x} films without the need for additives or high temperature post-deposition treatments[125,141,142]; in another report, the beneficial effects of a post-deposition oxygen plasma treatment were investigated[143].

WO_{3-x} films were deposited from alkoxide routes involving a tungsten ethoxide precursor (with tungsten in either the V or the VI oxidation state). The simplest procedure involves dissolution in ethanol followed by spin-coating; the conversion to the oxide is obtained through hydrolysis at room temperature[144]. In this work, the authors fabricated inverted architecture devices, but an organic interlayer was introduced between the active layer and the WO_{3-x} layer: this makes it difficult to isolate the performance benefits introduced by the TMO film. A similar recipe involving tungsten (V) ethoxide involves the use of a small amount of acetic acid (0.1 $\%_{vol}$) as a stabiliser[145]. The authors reported good quality films deposited without the need for post-deposition annealing; they investigated the effect of both ethanol and isopropanol solvents, claiming that ethanol resulted in unstable solutions with less than four days of shelf life.

1.4.3 Combustion synthesis

In recent years, a novel deposition method has been investigated by Marks *et al.*[116,146] to fabricate good quality oxide films to be used in transistor devices. The authors synthesised ZnO, ZTO[y], IZO[z], and ITO using a process called *solution combustion synthesis (SCS)*. This process was first discovered accidentally, in a reaction between $AL(NO_3)_2$ and urea[147], and has since been used to fabricate a number of binary and ternary oxides[148]. The chemistry is similar to that involved in propellants: a metal precursor, usually a nitrate salt, is the *oxidiser*, which reacts with an amine-containing organic compound, the *fuel*. The process yields metal oxide powder (film if the solution was cast on a substrate) and gaseous products (CO_2, H_2O, and N_2).

The combustion reaction is a redox reaction in nature, and it is highly exothermic; once it has started, there is enough self-generated energy to fully convert the precursors in the oxide of interest, without the need for external sources of energy (that is, post-deposition annealing steps). To start the reaction, the system must be brought to the ignition temperature, which depends on the chemistry of the solution; once ignited, the reaction will evolve even if the system is not kept at ignition. This is a great improvement over methods requiring high temperatures to oxidise the organometallic precursors. Delayed ignition is also possible: the reaction can start is the precursor is kept for a longer time at a temperature lower than that needed for ignition.

Several fuels have been reported, most of which are compounds containing nitrogen in amine groups (a source of nitrogen must be included as an additive if the fuel does not contain any). Urea ($CO(NH_2)_2$) was the first fuel reported[147]; other explored compounds are hydrazine-based materials, for instance oxalic acid dihydrazide ($C_2H_6N_4O_2$) which has a low temperature of ignition. Glycine ($C_2H_5NO_2$) was used to deposit NiO films used in organic devices with good results[149]. A common fuel that does not contain nitrogen is acetylacetone ($C_5H_8O_2$), which is used in combination with ammonium nitrate or ammonia as a source of nitrogen[116,146,150]. Another compound used together with nitrogen-containing additives is citric acid[151–153], in a reaction similar to the Pechini method[154].

An example of a simple combustion reaction that involves oxalic acid dihydrazide and results in the formation of a monoxide was proposed by Patil[155]:

$$M(NO_3)_2(l) + C_2H_6N_4O_2(l) \rightarrow MO(s) + 2CO_2(g) + 3N_2(g) + 3H_2O(g)$$

Equation 1.22

[y] Zin-tin oxide
[z] Indium-zinc oxide

Any combustion reaction will ignite if heated at high enough temperatures, regardless of the fuel. However, the ignition temperature can be lowered by an appropriate choice of fuel and fuel/oxidiser molar ratio, making this approach suitable for low temperature solution processing of TMOs.

The optimal oxidiser/fuel molar ratio is the ratio which will result in the complete conversion of the nitrate precursor; it can be calculated, following propellant chemistry, by knowing the valence of the oxidiser and the valence of the fuel[156]:

- Valence of oxidising elements is negative;
- Valence of reducing elements is positive;
- Valence of nitrogen is always zero.

According to this approach, the valences of the reactants in Equation 1.22 are:

- $M(NO_3)_2$: M = +2, N = 0, 6O = -12;
- $C_2H_6N_4O_2$: 2C = +8, 6H = +6, 4N = 0, 2O = -4.

It follows that the molar ratio in Equation 1.22 is 1 (oxidising valence of nitrate: -10; reducing valence of fuel: +10). If the fuel in Equation 1.22 was urea, the molar ratio would be 3/5.

SCS is relatively new, and apart from the work from the Marks' group a few other publications have investigated this approach. Two instances of SCS-deposited TMOs used for anode interlayers investigated MoO_{3-x}[157] and NiO[149], using acetylacetone or glycine as fuels, respectively. The precursors used were polyoxomolybdate ($(NH_4)_6Mo_7O_{24}\cdot 4H_2O$) and nickel nitrate ($Ni(NO_3)_2$), while in both cases standard architecture devices were fabricated. MoO_{3-x} was synthesised at 110°C, NiO at 175°C; the performances of both were similar to those obtained with PEDOT:PSS, a good sign of the quality of the deposited films.

2 MATERIALS AND METHODS

In this chapter, both the details of the synthesis and deposition of the films and the characterisation techniques employed will be discussed. The films characterisation can be divided in 3 primary areas: morphological, compositional, and optoelectronic. In addition, device performance characteristics are reported. Devices were realised employing films deposited with all the different parameters (spin speed, solvent, post-deposition treatment), to identify the optimal set of conditions resulting in the best working devices. In some circumstances, the analysis was not focused on every variable (reported in the text as appropriate), because changing certain parameters does not affect one or more of the properties of the films. Therefore, to avoid multiple results that would effectively be duplicates, each set of samples for characterisation was carefully thought out to minimise analysis time and amount of resulting data.

The different techniques used in this work will be briefly explained. The focus will be on the information that can be extracted from the data and also on the limitations and challenges that the technique poses for the prepared material.

2.1 SYNTHESIS

This section will present the routes employed to deposit the anode interlayer films. Furthermore, the device fabrication process will be described at each stage, from substrate cleaning to thermal evaporation of the cathode.

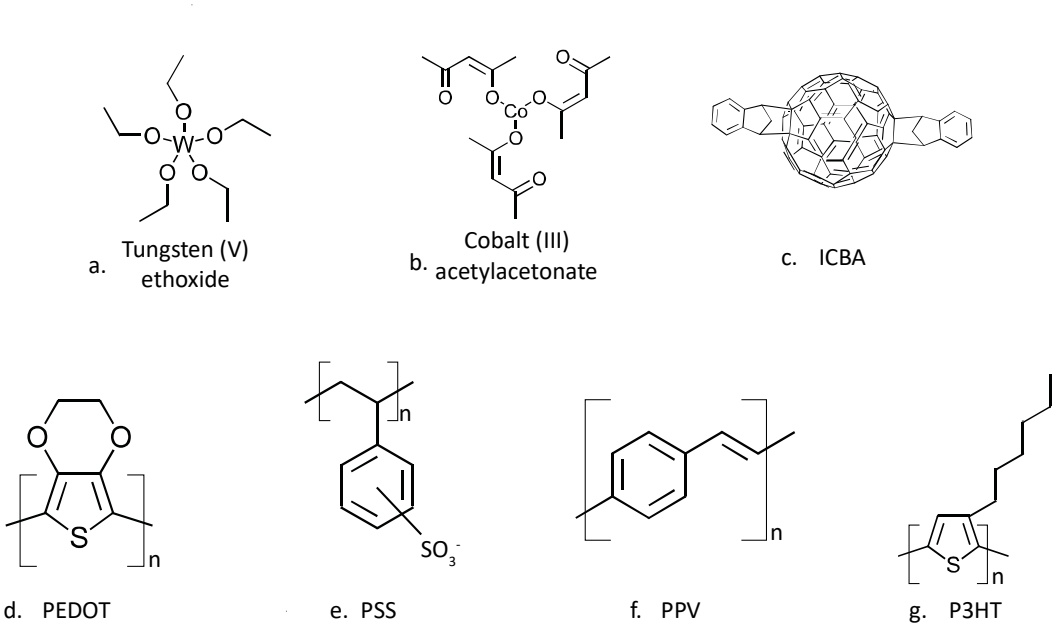

Figure 2.1: Chemical structures of the precursors and active layer materials used in this work.

The chemical structures of the materials used are summarised in Figure 2.1. The first three (a, b, c) are precursors for the TMOs, whereas the others are the organic active layer materials. The precursor for both MoO_{3-x} and V_2O_{5-x} was a powder of the respective metal.

2.1.1 MoO_{3-x} and V_2O_{5-x}

The route used is a variation of the well-known **hydrogen bronze route**[64,119,134,135]. More specifically, 10 ml of alcoholic (methanol, ethanol, or isopropanol) dispersion of metallic molybdenum or vanadium powder (Alfa Aesar, 0.1 M) was prepared. The solution was then sonicated in order to disperse the insoluble powder in the alcohol. After 30 minutes of sonication, 0.5 moles of H_2O_2 were added (in the form of a 30 %w/w solution in water). The solution was then stirred at room temperature for 24 hours. After aging, the appearance changed - from a grey dispersion to a blue solution (molybdenum) or a brown one (vanadium); at this point, the solution was filtered using a 0.45 µm PTFE filter.

Spin speed (rpm)	MoO_{3-x} film thickness (nm, +/- 2)	V_2O_{5-x} film thickness (nm, +/- 2)	WO_{3-x} film thickness (nm, +/- 2)
2000	16	12	13
5000	11	7	9
8000	6	4	6

Table 2.1: The thicknesses resulting from different spin speeds for the two hydrogen bronze solutions, measured by profilometry.

The films were subsequently deposited by spin-coating. The thickness was controlled by altering the spin speed, with the spin time fixed at 40 seconds; the measured thicknesses are shown in Table 2.1. The solution was dispensed dynamically: this guarantees a better uniformity and removes the risk of solvent evaporation before the start of the spinning[158]. After spinning, the films were subject to different post-deposition treatments. Films were either annealed (at 75 °C or 150 °C) or underwent a vacuum-assisted solvent evaporation. All three treatments were performed for 10 minutes. Solution preparation, deposition and post-deposition treatments were carried out in an N_2-filled glovebox.

Solvent	Methanol
	Ethanol
	Isopropanol
Post-deposition treatment (10 mins)	Vacuum-assisted solvent evaporation
	Annealing at 75 °C
	Annealing at 150 °C

Table 2.2: The solvents and post-deposition treatments used to synthesise MoO_{3-x}, V_2O_{5-x} and WO_{3-x} films.

2.1.2 WO_{3-x}

This route was derived from a previously published procedure[145] involving tungsten (V) ethoxide as the precursor (Alfa Aesar, structure in Figure 2.1a). A 0.05 M solution in alcohol (methanol,

ethanol, or isopropanol) was prepared; acetic acid was added at a concentration of 0.02 M. The solution was then stirred overnight for a minimum of 18 hours. After aging, the solution was filtered using a 0.45 µm PTFE filter. Spinning and post-deposition processing were carried out in the same way already detailed for MoO_{3-x} and V_2O_{5-x} (see Table 2.1 for resulting thicknesses and Table 2.2 for the parameters that were changed).

2.1.3 PEDOT:PSS-MoO_{3-x} hybrid

The route described in Sec. 2.1.1 was again used to prepare the MoO_{3-x} solution. PEDOT:PSS in aqueous solution (Heraeus Clevios™ AI 4083 from Ossila Ltd[159], see Figure 2.1d, Figure 2.1e) was used as purchased, after filtering with a 0.45 µm PTFE filter. The PEDOT:PSS solution and the MoO_{3-x} solution were mixed in different ratios (see Table 2.3) and spun at 5000 rpm for 40 s. After deposition, the films were annealed at 150 °C for 10 minutes. The decrease in thickness reflected the dilution caused by the addition of the alcoholic solution. However, for the first 2 samples (P2I1 and P1I1) the change in thickness is negligible, while it will be shown that the lower thickness observed in P1I2 was beneficial for device performances.

Volume Ratio (PEDOT:PSS to MoO_{3-x})	Sample Reference	Thickness (nm, +/- 2)
Pure PEDOT:PSS	P1I0	50
2:1	P2I1	49
1:1	P1I1	47
1:2	P1I2	35

Table 2.3: The volume ratios for the different PEDOT:PSS-MoO_{3-x} hybrids are shown together with the resulting thicknesses and the reference assigned to each sample.

2.1.4 CoO_x

Cobalt(III) acetylacetonate (Sigma Aldrich, Figure 2.1b) was dissolved into several organic solvents (chlorobenzene, toluene, p-xylene) to form 0.2 M solutions. The solutions were stirred overnight (minimum of 18 hours) then filtered after aging using a 0.45 µm PTFE filter. Spinning (40 seconds) was carried out dynamically for three spin speeds and two different post-deposition annealing temperatures were explored (see Table 2.4 for details). Both deposition and post-deposition treatments were carried out in air, under a fume hood.

Spin Speed (rpm)		**2000**	**4000**	**6000**
		Thickness (nm, +/- 2)		
Solvent	Chlorobenzene	12	8	5
	Toluene			
	p-Xylene			
Post-deposition treatment (10 mins)	75°C			
	150°C			

Table 2.4: Details of the different parameters used in CoO_x thin films deposition.

2.1.5 hyPV devices

The active layer for photovoltaic devices was the widely studied P3HT:ICBA bulk heterojunction. A solution of P3HT (obtained from the group of Prof. John De Mello, MW=62 kDa[160], see Figure 2.1g) and ICBA (Ossila Ltd, see Figure 2.1c) in chlorobenzene was prepared, with the two materials mixed in a 1:0.6 weight ratio and a total concentration of 25 mg/ml. The solution was then stirred in dark under a nitrogen atmosphere overnight at 60 °C. After aging, the solution was spin-coated on the substrates (dynamic dispense) at 2000 rpm for 40 seconds, resulting in films 100 nm thick. The samples were then transferred in a thermal evaporator. Evaporation was carried out at a pressure of $1*10^{-6}$ mbar. 20 nm of Ca were deposited first, at a rate of 0.5 $Å s^{-1}$, followed by 100 nm of Ag deposited at a rate of 1.5 $Å s^{-1}$. The samples were annealed at 150 °C for 10 minutes and then stored in the dark under nitrogen until testing. The final device structure is shown in Figure 2.2a: the six pixels are each a single device. The device area is determined by the overlap between the ITO strip and the cathode finger (0.045 cm^2).

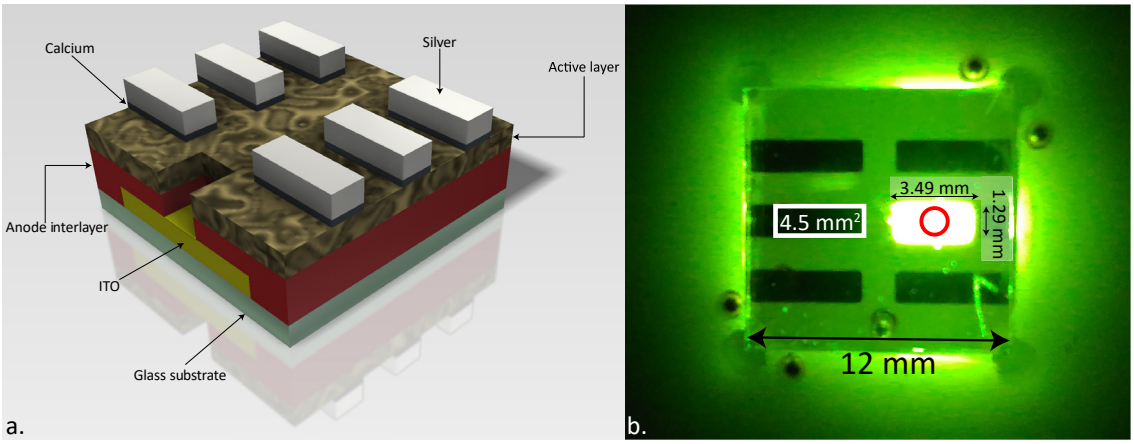

Figure 2.2: a. Diagram representing a standard architecture hyPV device. The thicknesses are not to scale. The pattern of the active layer simulates the bulk heterojunction intermixing. b. Photograph of an operational hyLED with a PPV active layer. The 6 pixels (with dimensions shown) are clearly visible even though only one is lit up. The red spot in the middle of the lit pixel indicates the spot size of the luminance meter.

2.1.6 hyLED devices

The active layer of light-emitting diodes was a green emitter obtained from Merck, a derivative of PPV (see Figure 2.1f). The polymer was dissolved in p-xylene at a concentration of 10 mg/ml and then spin-coated (dynamic dispense) at 1500 rpm for 40 s, resulting in a thickness of 60 nm. The cathode deposition process was the same one already detailed for hyPVs. After the thermal evaporation of the cathode bilayer, the samples were annealed at 60 °C for 10 minutes and then stored in the dark under nitrogen until testing. The structure is similar to that of the hyPV devices (Figure 2.2a). An operational device is shown in Figure 2.2b: the six pixels are tested one

at the time, effectively resulting in six different devices on a single substrate (again with an area of 0.045 cm^2 each).

2.2 Compositional Characterisation

X-ray photoemission spectroscopy (XPS) was used to analyse the composition of the TMO films.

2.2.1 X-ray photoemission spectroscopy

X-ray photoemission spectroscopy is a technique that enables the user to study both the composition and the electronic structure of the material of interest. It is based on the photoelectric effect: a photon of known energy $h\upsilon$ impinges on the sample, exciting an electron out of its energy level. The electron (photoelectron) has a certain amount of kinetic energy E_{kin} (that can be measured), therefore the binding energy E_b of the level can be calculated if the work function of the material ϕ is known (Equation 2.1). For XPS analysis, the sample is in electrical contact with the instrument; the work function of the machine is the zero of the binding energy scale.

$$h\upsilon = E_b + E_{kin} + \phi$$

Equation 2.1

The primary photon energy is in the order of 1400 eV, located in the X-ray region. This is high enough to excite electrons from the inner (core) levels of a material. Even though X-rays can penetrate far into the sample (even microns in depth) the XPS signal only comes from the topmost layers of the material. This is because scattering processes reduce the mean free path of electrons, therefore only electrons from the surface have a high probability of leaving the material before undergoing energy losses. This limits the probing depth of the technique to the first 10 nm of the sample, making it a highly surface sensitive analysis. It is thus fundamental to carry out measurements on clean samples and under ultra-high vacuum which reduces the rate of formation of an adsorbate layer.

XPS analysis is based on excitation of electrons away from a sample; it is therefore important that the sample is conducting, so that removed electrons can be replaced and charging effects avoided. For semiconducting and insulating samples, some measures must be taken: usually the use of conducting substrates and a flood gun are sufficient. A flood gun works by flooding the samples with low-energy electrons that replace those removed by the photoemission process. Moreover, signal from a non-conducting sample can be corrected using the position of a reference peak, most often the carbon 1s signal which is taken to be 284.8 eV (depending on the spectrometer used, can be sometimes positioned as 284.6 or 285.0 eV).

An XPS spectrum is constructed by analysing the distribution of photoelectrons with E_{kin}. All occupied orbitals will produce a peak. Other peaks arise from multi-electron processes like the

Auger effect. A **survey spectrum** is a wide scan over all binding energies (from the Fermi energy, which is the 0 of the scale, to the energy of the incoming X-ray photon, which is the maximum of the scale). Core levels of different elements give a signal at different energies; a survey spectrum can therefore be compared with standards in the literature for elemental identification.

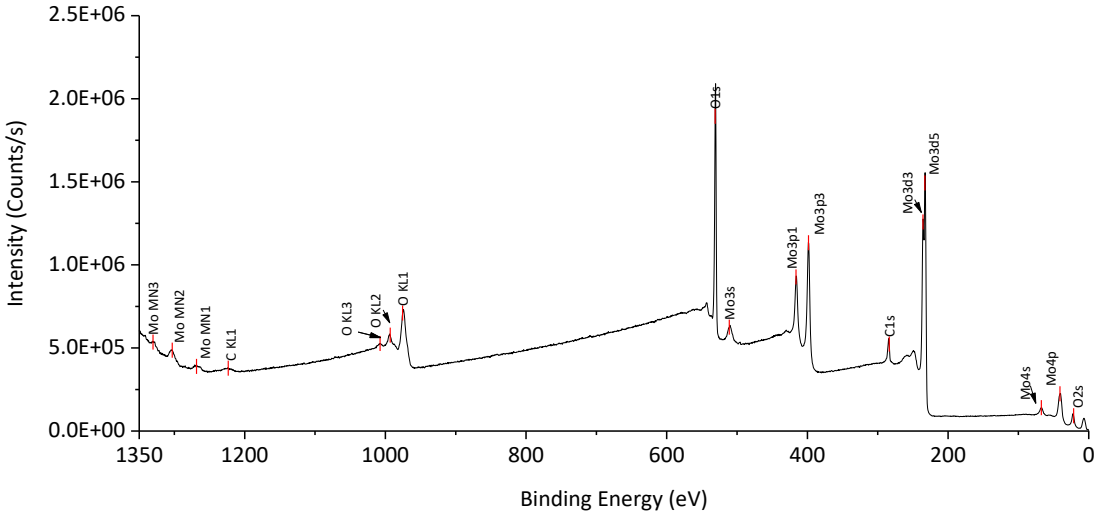

Figure 2.3: A XPS survey spectrum of a MoO_{3-x} sample. Both core level peaks (identified by orbitals notation) and Auger peaks (identified by spectroscopic notation) are present. Low and high spin states are labelled with numbers after the orbital letter (1 for spin-$^1/_2$, 3 for spin-$^3/_2$, 5 for spin-$^5/_2$).

An example of a survey spectrum is shown in Figure 2.3; the spectrum was measured from a MoO_{3-x} sample deposited as described in the Materials section. It is clear that different core levels result in peaks of different intensities and position. For molybdenum, the 3d peak is the most intense, whereas for oxygen it is the 1s. It is worthwhile noting that s-orbitals, having spherical symmetry, will produce a single peak. On the other hand, *p*-, *d*-, and *f*-orbitals will all present doublets due to spin orbit splitting; the ratio between the low spin peak and the high spin peak is fixed for every orbital (see Table 2.5). In the spectrum presented, at high binding energies there is a series of small peaks. These are Auger electrons, that produce a very low signal compared with photoelectrons. These peaks are not usually analysed; however, they can provide useful information if there are overlapping core level peaks from different elements which make identification difficult.

Orbital	Low spin state	High spin state	Peak area ratio
p	$^1/_2$	$^3/_2$	1:2
d	$^3/_2$	$^5/_2$	2:3
f	$^5/_2$	$^7/_2$	3:4

Table 2.5: The low and high spin states for the different orbitals. The last column states the ratio between the peak areas, this ratio being constant notwithstanding the element.

From a survey spectrum, an insight on the elements present in the sample can be obtained. It is worth bearing in mind that hydrogen and helium cannot be detected in XPS; this affects the capability of the technique to produce quantitative results. Helium is seldom found in materials,

but hydrogen is a fundamental element in organic materials and frequently present in many other samples. The restriction on detection means that any quantitative analysis can only result in relative composition: peak areas of different elements can be compared and the ratio between them gives information about their relative quantities within the sample.

Once the elements present in the sample are known, core level spectra can be collected with a high-resolution scan, which is taken with a smaller energy step and a lower pass energy than the survey spectrum. To increase the signal-to-noise ratio, multiple spectra are recorded and then averaged. As core level energies are influenced by the oxidation state and the chemical bonding environment, analysis of the resulting peaks can provide information about the chemical state of the element and therefore the material.

For example, in Figure 2.4, data from different samples containing molybdenum are shown. In Figure 2.4a, metallic Mo and MoO_3 signals are compared: it is evident the shift to higher binding energy of the oxide doublet with respect to the metallic sample. Higher oxidation states are always shifted towards higher binding energy[161]. In Figure 2.4b the Mo3d signal from the oxide sample is analysed in more detail; peak fitting and deconvolution show clearly that there are two separate signals, one for Mo^{6+} and one attributed to Mo^{5+}: again, higher oxidation state has higher binding energy. The fitting therefore demonstrate that the film is substoichiometric. Oxygen vacancies are common in TMOs and are one of the causes of their semiconducting behaviour.

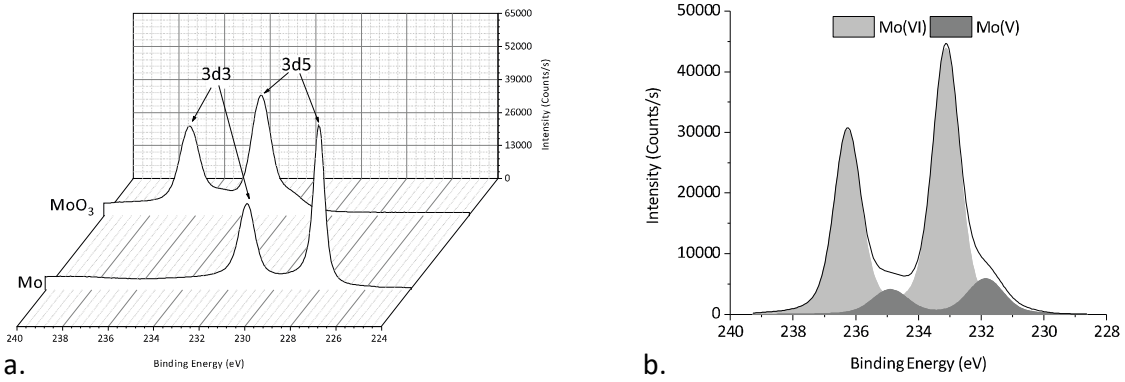

Figure 2.4: XPS data from Mo3d core level. a. Data from both metallic Mo and MoO_3, to highlight the binding energy shift that the chemical state produces. b. Data from the MoO_3 sample is analysed in more details. Peak fitting and deconvolution shows that there are two oxidation states present: Mo^{6+} and Mo^{5+}. The sample is therefore slightly substoichiometric.

2.3 Morphological Characterisation

Atomic force microscopy (AFM) was used to image the surface of the films and to analyse parameters such as roughness and height distributions, in order to understand the influence of

the surface structure on the performances of devices. Surface profilometry was instead used to measure the thickness of the deposited films, both oxides and polymers.

2.3.1 Atomic force microscopy

AFM is a powerful technique for imaging any kind of surface (hard, soft, insulating, conducting, etc.). It can be carried out in air, as long as the environment is clean (to avoid dust or other impurities from settling on the sample) and the instrument is insulated from vibrations. AFM instruments measure the force between the sample surface and the atomically sharp tip of a *cantilever* and use it to draw an image of the topological features of the surface. AFM is relatively cheap and simple to carry out. It does not require any specific treatments on the sample, which is a huge advantage compared for instance to electron microscopy that would require conducting coatings on insulating samples. The resolution can be brought down to 0.1 nm[162], that is the same as transmission electron microscopy (TEM). The image is recorded by measuring the vertical movement of the cantilever which is caused by topological features on the sample interacting with the tip. Feedback electronics are used to measure changes in the tip-sample interactions and to correct the parameters in order to maintain a constant force between the two, or a constant height of the tip on the sample. The most commonly used system to record the movement of the cantilever uses beam deflection sensors. For this system, the back side of the cantilever is coated with a high-reflectivity material; a laser is shone on it and it is reflected on a 4-quadrant photodiode, whose signal is analysed and used to produce the surface images. The tip of the cantilever is very important. It is the part in contact with the sample and the images produced by the instrument are a convolution of the tip geometry and the sample surface. It is therefore paramount to use good quality, micro-machined tips (commonly made of Si) that are as sharp as possible. Even though in theory a tip should not wear out and could be used indefinitely, this is seldom the case in real-life scenarios. Lateral forces as well as the interactions with the samples will produce indentations and blunting on the tip, effectively making their useful working life much shorter than expected[162].

There are various forces that regulate the interaction between the tip and the sample surface, and all will contribute to the final image of the surface:

a) Short-range forces: they can be both attractive and repulsive. An example of this can be the overlap of electronic wave functions. These forces have a decay length which is of the same order of magnitude of atomic scales, and thus can be used to obtain atomic resolution images;

b) Van der Waals forces: they are also called *dispersion forces* and are always present. Their range is very limited, with long-range attraction almost exclusively ascribed to London dispersion forces;

c) Electrostatic forces: they act between localised charges, can be modelled using Coulomb's law. Their exact formulation depends on the geometry of both the tip and the substrate;

d) Capillary forces: these are important when measurements are carried out in air. A water droplet can form at the contact point between the cantilever and the surface, and thus their interaction will be influenced by capillary forces. These depend on surface tension of the droplet, the radius of the tip, its distance from the surface.

All these forces will collectively produce a force on the tip. This interaction depends on the distance between the tip and the surface. When the two are far away, forces are zero and there is no interaction. The tip is then approached until attractive forces come into play and 'snap' it into contact with the surface. Now the tip is pushing onto the sample and is subject to an opposite reaction from the surface: further approach will result in an increasing repulsive force. There are several ways (modes) AFM images can be collected; also, there are many different forces than can be used for imaging and even for surface manipulation. Table 2.6 lists the different variations of the AFM technique; the ones used in this work are tapping mode AFM (a form of intermittent contact mode) and Kelvin Probe Force Microscopy (which uses the same principles as the Kelvin Probe technique).

Topographic modes	Contact mode
	Non-contact mode
	Intermittent contact mode
Specific forces	Chemical force
	Lateral force
	Electric force
	Magnetic force
	Kelvin Probe force
Sample manipulation	Nano-indentation
	Nano-oxidation lithography
	Dip-pen nanolithography
Others	Force spectroscopy
	Scanning thermal microscopy

Table 2.6: Different modes of operation, force that can be analysed and other features available in AFM technology. The two variations used in this work are highlighted in bold. Adapted from [162].

The simplest way a measurement can be carried out is in contact mode, where the tip is always in contact with the surface and is dragged across it; the measurement is carried out in the repulsive regime. In contact mode, the cantilever is subject to lateral forces as well as vertical ones, so torsional motion becomes important and can even be used for lateral (friction) forces measurements and manipulation of surface features. Although it can produce very high-resolution images (higher than non-contact modes), contact mode present several limitations: for instance, if soft samples are to be imaged,

strong tip-surface interactions can be counterproductive; also, capillary forces will affect the measurement if it is carried out in air. However, it is the preferred mode for imaging in liquids and high speed AFM set-ups[162].

As opposed to contact-mode, non-contact and intermittent contact modes have an obvious advantage: the cantilever can be made to oscillate. This will produce a modulated signal which can be used to improve the signal-to-noise ratio. The oscillation of the cantilever (its frequency and amplitude) will change because of sample-tip interactions: approaching the tip to the surface will reduce both frequency and amplitude of the oscillatory movement. Using a feedback loop, the probe is maintained at a constant distance from the sample. Intermittent contact mode, or tapping mode, is the configuration of choice in this work. Lateral forces are eliminated and capillary forces are strongly reduced. Tapping mode produces topography images (Figure 2.5) but also *phase images*, collected by measuring the phase shift. The phase depends on tip-surface forces, therefore phase imaging can be used to distinguish between different materials in the scanned area[162].

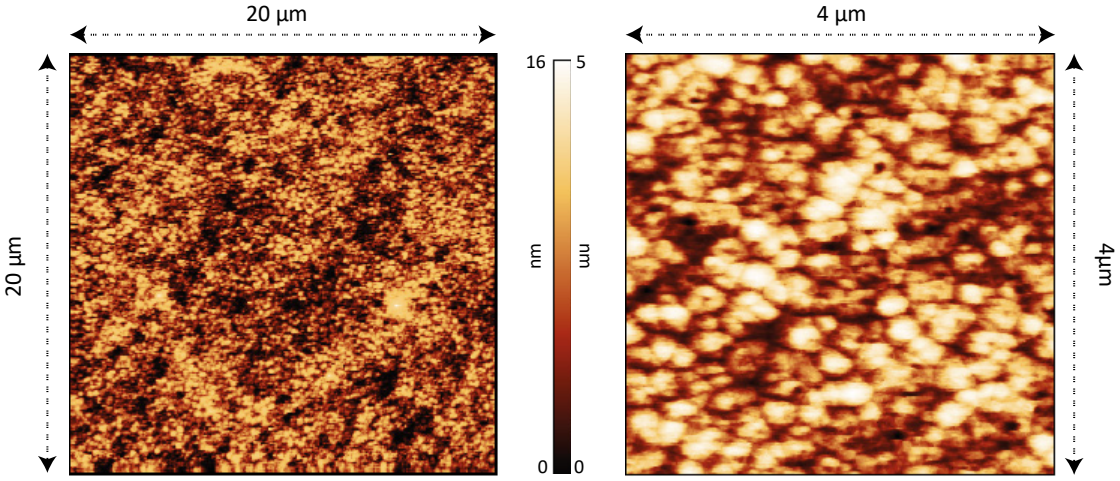

Figure 2.5: Typical AFM images of a WO_{3-x} sample. On the left, a wide area scan is shown. The colour bar indicates that the features heights are distributed over a 16 nm range. Multiple features are visible and further investigated in the image on the right, which zooms in on a smaller area of the sample. The height colour bar now suggests a 5 nm height scale. The features observed in the left image are now enlarged and can be identified as grains of WO_{3-x}.

In Figure 2.5, a WO_{3-x} sample surface is shown. On the left, a wide area is scanned (400 μm^2) and the microstructure of the film can be observed. The colour bar on the side provides information on the height of the features on the surfaces. On the right, an image of the same sample was taken using a much smaller area (16 μm^2). Now the features observed on the left are more clear and can be identified to be nanograins of WO_{3-x}. This is an example of the usefulness of AFM analysis. This sample was previously analysed using X-ray diffraction, but no reflection peaks could be detected: this suggested that the sample was either amorphous or

nanocrystalline. AFM analysis was crucial in the process of correctly identifying the morphology of the film.

2.3.2 Surface Profilometry

The thickness of the various films was measured using surface profilometry. The technique is broadly based on the same concept as AFM: a stylus tip in put in contact with the sample and dragged across it, while the contact is maintained by applying a force to the tip. The vertical displacement is measured and plotted against the x or y direction. To measure the thickness of a film, the substrate is exposed in some areas, and the analysis is carried out to measure the vertical displacement at the edge of the exposed area; this is the thickness of the film. The substrate can be exposed by mechanical scratching (in soft samples, e.g. polymers) or by acid etching (in hard samples, e.g. some oxides). When neither of the abovementioned methods work, a slice of tape can be used to mask an area of the substrate during spin-coating. After deposition, the tape is removed and the thickness measured as detailed above.

2.4 Optoelectronic Characterisation

UV-Vis spectroscopy was employed to assess the transparency of the samples in the range of interest for optoelectronic devices. Kelvin probe measurements presented many challenges and the results cannot always be deemed reliable. These challenges will be described and the reasons to disregard some results will be explained in detail.

2.4.1 UV-Vis spectroscopy

UV-Vis spectroscopy is used to measure the optical absorption of materials over the UV and visible range of the light spectrum, with some instruments extending into the near infrared range (UV-Vis-NIR spectroscopy, see Table 2.7). White light from the sources listed in Table 2.7 is passed through a monochromator and shone on a sample. The monochromator scans over the different wavelengths and a transmission spectrum (T) is recorded. An integrating sphere is used to collect a reflection spectrum (R), which is then combined with the transmission to obtain absorbance (A) and absorption coefficient (α) of the material[163,164] (Equation 2.2, for a thin film of thickness *d*):

Region	Range (nm)	Light source
Near infrared	700-1400	Tungsten bulb
Visible	400-700	Tungsten bulb
Ultraviolet	200-700	Xenon lamp

Table 2.7: Different spectral regions and sources used in UV-Vis-NIR instruments.

$$\alpha = \frac{-\ln \frac{T}{1-R}}{d}$$

Equation 2.2

UV-Vis spectroscopy can be performed on solutions of the material of interest or on thin films. In Equation 2.2 the term *d* refers to the thickness of the film or to the length of the container in which the solution is housed (called *cuvette*). Whether performing the analysis on solution or film, there is a requirement of transparency on the cuvette or the substrate of the film. Fused silica is the material of choice due to its high transparency in the range 200-1400 nm[165]. Glass also has quite high transparency in visible and near infrared, but it absorbs strongly at wavelengths shorter than 350 nm; it is therefore not recommended for materials that have a large band gap (like most TMOs). A comparison between fused silica and glass is shown in Figure 2.6a: the spectrum is recorded between 220 and 1400 nm (the same interval used in this work) and it is clear that fused silica has higher transparency overall, and especially in the UV range below 350 nm. To provide an example of the information obtainable from UV-Vis-NIR spectroscopy, a V_2O_{5-x} film, 12 nm thick, was analysed with the spectrometer used in this work. Transmission and reflection data were recorded and used to calculate the absorption coefficient with Equation 2.2. The result is plotted in Figure 2.6b, with the bottom axis showing wavelength and the top axis the corresponding photon energy in eV. It can be seen how the material only really absorbs below 400 nm, therefore the use of a glass substrate would affect any measurement of T and R. From the absorption coefficient, the optical band gap (E_g) of the material can be calculated (Figure 2.6c). This can be done following the pivotal work of Tauc[166,167]; using Equation 2.3, a plot of $(\alpha h\nu)^{1/r}$ vs hν was drawn and the optical band gap was calculated to be 2.8 eV by extrapolating to zero.

$$\alpha = B\frac{\left(h\nu - E_g\right)^r}{h\nu} \Longrightarrow (\alpha h\nu)^{1/r} = A(h\nu - E_g)$$

Equation 2.3

The exponent in Equation 2.3 is $^3/_2$ for direct allowed transitions or 2 for indirect allowed transitions (the latter will be used throughout this work)[168].

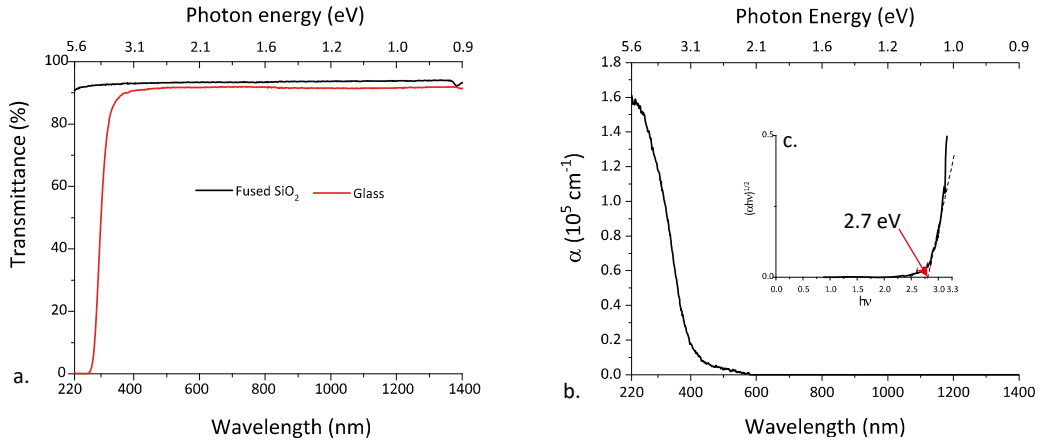

Figure 2.6: a. Fused silica and glass transmission spectra. b. Absorption coefficient of a V_2O_{5-x} thin film, calculated using *Equation 2.2*. c. The optical band gap is calculated following Tauc's work (*Equation 2.3*).

2.4.2 Kelvin probe

Kelvin Probe is a surface technique that measures the Fermi level E_F of a sample. The Fermi level is defined by IUPAC as "The chemical potential of electrons in a solid (metals, semiconductors and insulators)."[69] Following this definition, in solid state physics E_F is often described as the state having a 50% probability of being occupied by an electron at any temperature. A mathematical expression is given by Livingston[169]:

$$F(E) = \frac{1}{1 + e^{\frac{(E-\mu)}{k_B T}}}$$

$$\Longrightarrow F(E_F) = \frac{1}{2}$$

Equation 2.4[aa]

Using the Fermi level, the work function ϕ of a material can be defined in terms of E_F and the electrostatic potential of an electron in vacuum E_{vac}[170]:

$$\phi = E_{vac} - E_F$$

Equation 2.5

What Equation 2.5 means is that the work function is a thermodynamic quantity, specifically the work required to remove the outermost electron from the material. The electrostatic term can be taken as the zero of the energy scale, resulting in:

$$\phi = -E_F$$

Equation 2.6

To measure the work function with Kelvin Probe, a stainless-steel tip is put in electrical contact with the sample and is then approached down to 0.5 – 2.0 mm from the surface. When the tip and the sample are in (electrical) contact, the result is the same as when a junction between the two is formed (Figure 2.7). Charges move from the material with the smaller work function to the other, until the Fermi level is constant across the junction. The Fermi level shift produces a potential difference between the two materials called *contact potential difference* or V_{CPD}. The tip is oscillated over the sample and a bias V_b is applied to it. The instrument scans over a range of V_b and the voltage change is recorded during the oscillation. When the voltage change is zero, V_b equals $-V_{CPD}$, yielding a measurement of the contact potential difference.

In Figure 2.7 the two types of junction are shown: the metal on the left represents the tip (M_1). Figure 2.7a show the formation of a junction between two conducting (metallic) materials (the tip M_1 and the sample S_1). Figure 2.7b presents the situation of a semiconducting sample (S_2) in

[aa] F(E) is the Fermi distribution, with μ indicating the Fermi energy, T the temperature and k_B the Boltzmann constant. Note that the chemical potential μ is used instead of the Fermi energy to avoid confusion between the latter and the Fermi level (they are both indicated with E_F). Although this substitution is usually only considered valid at T=0[233], it is used here for sake of clarity.

contact with the conducting material of the tip. The presence of a band gap in the semiconductor makes things more complicated to model, as band bending and pinning must be considered; however, a contact potential difference is still established, equal to the difference in Fermi level, and allows for analysis on semiconducting samples. The continuous measurement under applied bias removes or adds charges to the sample, and for non-conducting materials there is the possibility of charging of the surface, which will affect the measurement.

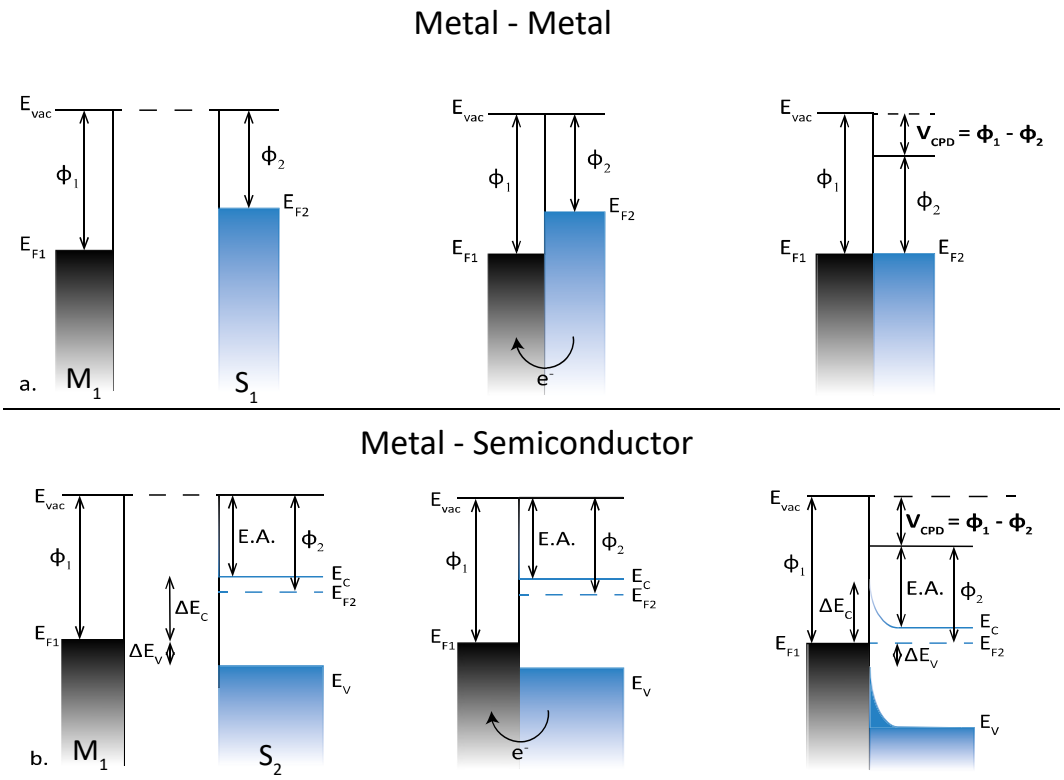

Figure 2.7: a. Energy level alignment at a metal-metal junction. b. Energy level alignment at a metal-semiconductor junction. The quantities shown are: Fermi level E_F, electron affinity E.A., valence and conduction band edge E_V and E_C.

Therefore, semiconducting samples are better measured when deposited on conducting substrates: this allows extra charges to be removed and avoids charging. There are, however, other problems with semiconducting samples. One is the formation of a surface dipole that induces band bending at the surface of the sample, similar to that induced by the formation of a junction (Figure 2.8a). Things are complicated further by adsorbates (Figure 2.8b): the electrostatic potential is shifted and the electron affinity is changed by the formation of a dipole ΔV_{dip}. This influences the work function of the sample:

$$E.A. = E.A.' + \Delta V_{dip} \Rightarrow \phi' = \phi - \Delta V_{dip} - \Delta V_s$$

Equation 2.7[bb]

[bb] $\Delta V_s = V_s - V'_s$

Yet, the biggest issue when measuring semiconductors with a Kelvin probe is the influence of air, particularly oxygen, as TMOs get their semiconducting nature from defects. TMOs such as MoO_{3-x}, V_2O_{5-x} and WO_{3-x} have oxygen vacancies that are responsible for their n-type behaviour, and a very deep work function (~7 eV)[14,50,98,141].

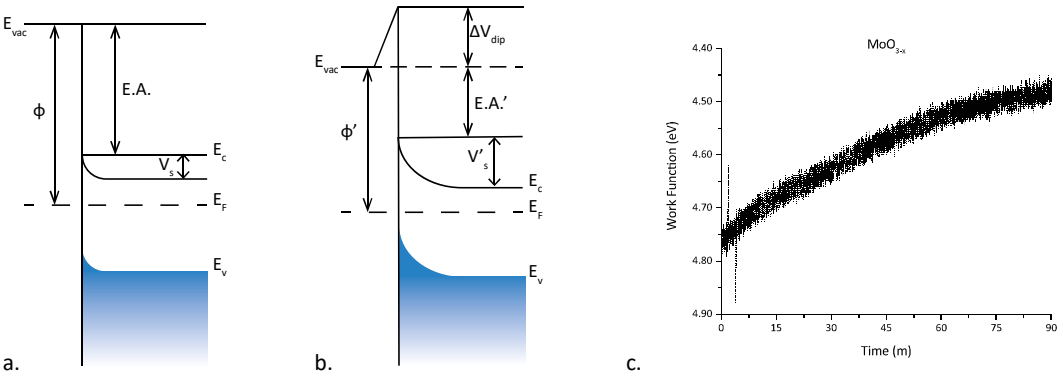

Figure 2.8: a. Semiconductor surface showing band bending V_s, a situation similar to that depicted in Figure 2.7b. b. The situation is complicated by the presence of an adsorbate: band bending is increased, the electron affinity is changed by the formation of a dipole (ΔV_{dip}) and the electrostatic potential is shifted. c. The work function change of a MoO_{3-x} film as it is measured in air. a. and b. adapted from [171].

For these TMOs, air exposure has a dramatic effect on the work function, lowering it by as much as ~2eV[172,173]. In Figure 2.8c a Kelvin probe measurement of a MoO_{3-x} thin film is shown. The sample was prepared in a N_2-filled glovebox and was then measured in air. Air exposure in the time it took to transfer the sample from the glovebox to the instrument and to start the analysis accounts for the biggest change in work function. However, the measurement still showed a considerable loss in work function over time. WO_{3-x} and V_2O_{5-x} showed a similar behaviour, therefore the technique is of no use for this kind of TMOs.

2.5 Device Characterisation

In this work, both photovoltaic devices and light emitting devices were fabricated. These were characterised mainly by measuring the current density-voltage J-V (for hyPV) and current density-voltage-luminance J-V-L (for hyLEDs) curves and by calculating efficiency parameters from those curves. Further studies were carried out mainly on hyPV devices, since the P3HT:ICBA system is well known and understood and therefore the behaviour of our films could be easily decoupled from any influence caused by other layers. In particular, hole injection was measured by fabricating *single carrier* (hole-only) devices. *External quantum efficiency* measurements were also carried out to better understand the observed increase in efficiency for hyPV devices. Injection from the ITO anode into the films was investigated by fabricating 'sandwich' devices and measuring their J-V characteristics.

2.5.1 Photovoltaic devices

Solar cells can be modelled with an equivalent circuit (Figure 2.9a). Although the circuit is commonly drawn with values of current, from here on we will consider current densities only.

In dark conditions a photovoltaic device is simply a (ideal) diode, with the J-V relationship expressed by:

$$J_{dark}(V) = J_0 * (e^{\frac{eV}{kT}} - 1)$$

Equation 2.8[cc]

When light is shone on the device, it induces a *photocurrent* J_{light}:

$$J(V) = J_{light} - J_{dark} = J_{sc} - J_0 * (e^{\frac{eV}{kT}} - 1)$$

Equation 2.9

J_{sc} is the maximum current that can be extracted from a device and it is measured when no load is connected; it is therefore called *short-circuit current*.

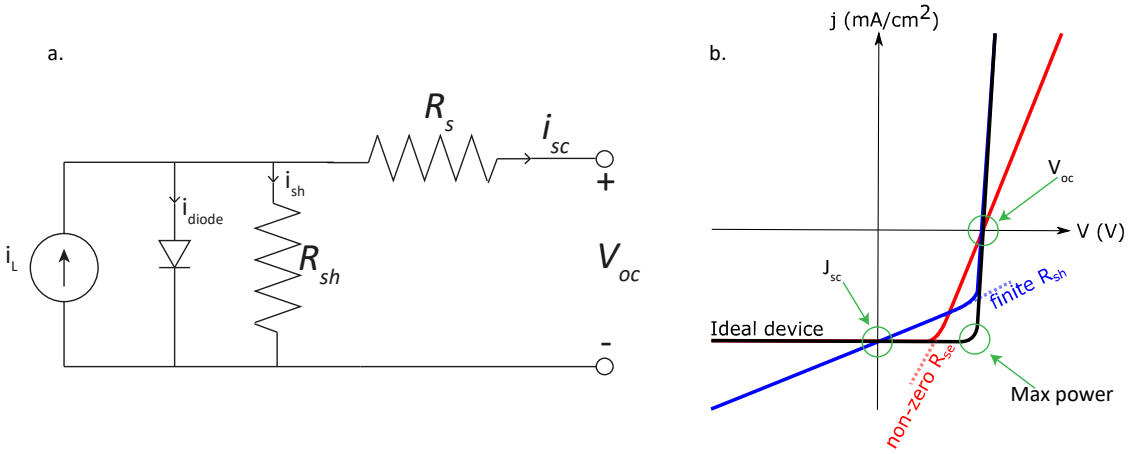

Figure 2.9: a. Equivalent electric circuit of a solar cell. b. J-V curves for an Ideal (black line), a high-R_{sh} (blue line), and a high-R_s (red line) photovoltaic device.

Another important quantity is measured in open circuit conditions (J=0) and it is called *open-circuit voltage* V_{oc}:

$$V_{oc} = \frac{kT}{e} * \ln(\frac{J_{sc}}{J_0} + 1)$$

Equation 2.10

In organic photovoltaic devices the V_{oc} is given by the difference between the HOMO level of the donor and the LUMO level of the acceptor, minus the exciton binding energy[35,174]. However, this only holds true if the energy level alignment at the contacts is favourable and there are no other losses in the device.

[cc] J_0: saturation current

The most important property of a solar cell is the *power conversion efficiency* PCE. It is defined as the ratio between the output power density (electrical) and the solar power density provided by the solar simulator:

$$PCE = \frac{P_{out}}{P_{in}}$$

Equation 2.11

2.5.1.1 Losses

The maximum power that can be extracted from a solar cell can be measured by plotting J*V against V; the values of J and V at the maximum power point (J_m and V_m) can be combined with J_{sc} and V_{oc} to calculate the *Fill Factor* FF:

$$FF = \frac{J_m * V_m}{J_{sc} * V_{oc}}$$

Equation 2.12

The fill factor is very useful in identifying the cause of eventual losses in a device. It is an indication of the "squareness" of the J-V plot (the black line in b represents an ideal cell with a FF of 1, or 100%). Its shape can be changed by the losses identified in Figure 2.9a: power losses throughout the device are due to high resistivity of the different materials in the device: these contributions can be summed up and expressed as the *series resistance* R_s, a resistance in series with the current source in the equivalent circuit. Parasitic losses can be present as well, and are usually ascribed to short circuits produced by pinholes in the active layer that can bring the cathode and the anode in contact. Also, charge recombination at the interface can act as a parasitic loss[37]. All these will result in a parasitic current in parallel with the current source in the equivalent circuit, and they can be summed up in a single parameter called the *shunt resistance* R_{sh}. In the ideal case, R_s should be 0 and R_{sh} should be infinite, but in reality, losses are always present. Both resistances can be analysed using the J-V curve of the device under illumination. A finite R_{sh} (blue line in Figure 2.9b) will introduce a dependence of the photocurrent on the voltage applied and therefore a slope on the horizontal part of the curve. In the limit of a very low R_{sh} the losses will affect the V_{oc}. A high R_s will instead affect the vertical portion of the curve, and in the limit of a very high series resistance the J_{sc} will be affected. Both R_{sh} and R_s can be evaluated by the slopes *m* at J_{sc} and V_{oc}, respectively. It is worth noting that the series resistance measured in this way is actually higher than the real one[175].

$$R_{sh}(k\Omega) = \frac{1}{m_{J_{sc}}} * \frac{1}{0.045}$$

$$R_s(k\Omega) = \frac{1}{m_{V_{oc}}} * \frac{1}{0.045}$$

Equation 2.13

Note that, as we are using current density, the values must be divided by the device area, which in this work is 0.045 cm^2.

2.5.1.2 External quantum efficiency

The spectral response of a cell is important. Knowing how the cell efficiency changes when absorbing photons of different wavelength can be important to understand the photophysical dynamics inside it; it can also be compared to the absorption spectra of the active layer materials. A simple way of measuring it is to illuminate the device with monochromatic light and obtain J_{sc}. By dividing this by the intensity of the incident light one can calculate the *spectral responsivity*:

$$S(\lambda) = \frac{J_{sc}(\lambda)}{I(\lambda)}$$

Equation 2.14

From S(λ), the *incident photon-to-current conversion efficiency* (IPCE) can be calculated. This is more commonly referred to as *external quantum efficiency* EQE. It is expressed as the ratio between the number of electrons extracted from the cell (J_{sc}/e) and the number of incident photons (I(λ)/hν):

$$EQE = \frac{J_{sc}(\lambda)}{I(\lambda)} * \frac{h\nu}{e}$$

Equation 2.15

2.5.1.3 Single carrier devices

Single carrier devices are fabricated by depositing the active layer between two electrodes which both have a high barrier to the injection of one type of carrier. In this way, there is the certainty that the only current passing through this kind of device is carried by the other type of carrier. For instance, by using ITO and Au as electrodes, a hole-only device is fabricated. Conversely, an electron only device can be realised with Ca at both electrodes. In this work hole-only devices were employed to understand the injection behaviour of the different anode interlayers with respect to that of PEDOT:PSS. Therefore, devices were realised in the same way as hyPVs already described but the Ca/Ag cathode bilayer was replaced with Au. J-V data was recorded in the dark and the forward current densities of the different devices were compared. Only holes were injected into the devices, therefore a higher current density implied a better hole injection from the ITO/HIL side of the device.

2.5.2 Light emitting diodes

As for photovoltaic devices, the J-V curves of the fabricated hyLEDs were measured, with the data expected to follow Equation 2.8. The characterisation of the light emission and its

efficiency is fundamental in hyLED studies. The first parameter to consider is the luminance L, the ratio between the luminous intensity of the device and its surface area, it is expressed in cd/m^2. The luminance is also referred to as the *brightness*; usually, the reference for display applications is 100 cd/m^2 and for lighting purposes is 1000 cd/m^2. The light turn-on voltage V_{on} in this work is taken as the voltage at which L exceeds 1 cd/m^2.

The luminance can be related to the electrical behaviour of the device and two efficiency parameters can be calculated. The *luminous intensity* (in candelas) divided by the current (in A) is termed *current efficiency*:

$$\boldsymbol{CE} = \frac{L[\frac{cd}{m^2}] * 10^{-4} * 0.045}{J[\frac{mA}{cm^2}] * 10^{-3} * 0.045} = \frac{L * 10^{-4}[\frac{cd}{cm^2}]}{J * 10^{-3}[\frac{A}{cm^2}]} = \boldsymbol{\frac{L}{J} * 0.1[\frac{cd}{A}]}$$

Equation 2.16[dd]

The luminous intensity depends on how focused the beam is, that is on the solid angle of the beam. The total intensity of light that a source emits is called *luminous flux* L_f (in lumen). This can be divided by the electrical power P (in W), resulting in the *power efficiency*:

$$\boldsymbol{PE} = \frac{L_f[lm]}{P[W]} = \frac{L\left[\frac{cd}{m^2}\right] * 10^{-4} * 0.045 * \pi[sr]}{J\left[\frac{mA}{cm^2}\right] * 10^{-3} * 0.045 * V[V]} = \boldsymbol{\frac{\pi[sr]}{V[V]} CE[\frac{cd}{A}]}$$

Equation 2.17[ee]

For the purposes of this work the current efficiency CE was considered the main parameter. For the other metrics, their value at the maximum CE was taken (Table 2.8).

Parameter	Max CE	V at max CE	PE at max CE	L at max CE	J at max CE
Units	cd*A^{-1}	V	lm*W^{-1}	cd/m^2	mA*cm^{-2}

Table 2.8: The performance metrics considered for hyLED devices and their units.

2.5.3 Injection from the anode

A good electrical contact between the ITO and the anode interlayer is required to minimise losses in devices. Barriers to charge injection could cause accumulation of charges which will reduce the ability of the interlayer to inject/extract carriers. So-called sandwich devices were fabricated to understand the nature of the electrical contact at this interface. The different anode interlayers and a PEDOT:PSS reference were casted on ITO and a metal electrode was evaporated on top (Ag or Au). J-V data was then recorded and compared to highlight possible differences in the injection mechanism.

[dd] Both luminance and current density depend on the area of the device (0.045 cm^2). Therefore, the luminous intensity is L*0.045 and the current is J*0.045, with factors to ensure the area units are the same.

[ee] The luminous flux is derived by the luminous intensity by multiplying it for the solid angle (in steradiants).

3 MOLYBDENUM AND VANADIUM OXIDES

In this chapter, the results from MoO_{3-x} and V_2O_{5-x} thin film synthesis will be presented and discussed. The chapter is divided in two main parts, each structured in a similar way, as common structure allows for comparison between the two materials:

a. Preliminary characterisation to assess the films' suitability as anode interlayers;
b. Analysis of the performance metrics of devices to determine the best combinations of synthesis and post-deposition treatment;
c. Further analysis on selected set of parameters to understand what factors were having the biggest impact on device performances.

Interestingly, there was not one common behaviour for both oxides in both device types. For instance, V_2O_{5-x} did not outperform PEDOT:PSS in hyLEDs, whereas a few MoO_{3-x} films did. On the other hand, in hyPV devices both oxides had a few solvent – post-deposition treatment combinations that performed better that the PEDOT:PSS reference. The best performing set of parameters for MoO_{3-x} in hyPV devices was different than that in hyLEDs. Similarly, the best performances in solar cells employing V_2O_{5-x} were obtained with films processed differently than the champion set of parameters identified for MoO_{3-x}. This diversity could prove very useful in a "bespoke" approach to device fabrication, where the interlayer deposition can be tailored around special requirements on solvents and temperatures for both the substrate and the active layer.

3.1 MoO_{3-x}

The first TMO that will be considered is MoO_{3-x}, arguably the most widely used as HTL. The recipe used here is a variation from the well-known *hydrogen bronze* route[64,134,135]. This exploits a combination of hydrogen peroxide and an alcohol to solvate and oxidise a Mo precursor (role of H_2O_2) and then inducing substoichiometry by partial reduction (role of the alcohol). All the variations of this route so far have relied on the removal of the solvent system (alcohol + H_2O_2) after the synthesis of MoO_{3-x} was complete. This involves solvent evaporation in a vacuum oven, with the resulting MoO_{3-x} powder then re-dissolved in ethanol for deposition. This process is cumbersome and involves two unnecessary steps, the evaporation and the consequent dissolution. Besides, it was observed that the evaporation step is critical: if it is performed too quickly or if the temperature increases too fast the resulting powder is insoluble in alcohol (previous work found it to be nearly stoichiometric MoO_3). Therefore, the critical steps were removed altogether and instead films were deposited straight from the alcohol/H_2O_2 mixture.

The argument here is that the presence of H_2O_2 does not damage the active layer, because of the very small amount present (as shown in devices).

3.1.1 TMO film preliminary characterisation

XPS analysis and UV-Vis spectroscopy were carried out on the deposited MoO_{3-x} films to study their composition and assess their optical transparency. Details of films deposition, as well as resulting thicknesses, are described in the Materials & Methods chapter.

3.1.1.1 XPS

XPS analysis was performed on films deposited from different solvents to understand whether a choice of solvent can influence the stoichiometry. The initial analysis was carried out on films subject to a post-deposition thermal treatment at 150 °C; thus, eventual effects of residual solvents on the analysis were removed and the role of the alcoholic solvent on the sol-gel synthesis could be isolated. The Mo core levels are shown in Figure 3.1 for films deposited from the three different solvents. There were subtle differences on the overall peak shapes, and peak fitting was carried out to understand whether the stoichiometry was different. In all the samples two different doublets were observed, assigned to Mo(VI) and Mo(V). While Mo(VI) is the characteristic oxidation state of MoO_3, Mo(V) is more exotic. It has however been reported for materials called molybdenum blues[176,177]: these are prepared with procedures that have much in common with the synthesis route developed here, therefore justifying the attribution of the unknown peak. It has also been observed in partially reduced MoO_3 used in catalysis[178].

The data in Figure 3.1 suggests that methanol and isopropanol produce very similar films. Ethanol, however, presented a much smaller contribution from Mo(V) with respect to Mo(VI) than the other two. This could be ascribed to a less effective reducing power of the alcohol on MoO_3. However, the stoichiometry must be estimated before any speculation is made.

Assigning a stoichiometry to the films proved challenging. The presence of ITO underneath the TMO films could result in an overestimation of the oxygen quantity in the sample. This was already reported and discussed by Jasieniak[43]: in that work, the problem was avoided by estimating the stoichiometry from the ratios between the different Mo oxidation states, and an experiment was devised to prove that the method was valid by depositing the films on Au substrates, estimating the Mo:O ratio and then comparing these results with those obtained from the Mo(VI):Mo(V) ratio[43]. We therefore used the ratio between the oxidation states to estimate the stoichiometry, and the result was that the films all showed a similar formula $MoO_{2.7}$. This is simply an estimate, but it is consistent with other reports of MoO_{3-x} films prepared with a similar route and showing a similar distribution of oxidation states[135,179].

The O core level spectra are also shown in Figure 3.1. The main peak is due to the Mo-O bond and for all the three solvents is located between 530.60 eV and 530.70 eV; the satellite peak observed at higher binding energy is common in TMOs and it is ascribed to defect in the subsurface layers, i.e. hydroxyl groups[180] and oxygen vacancies[71].

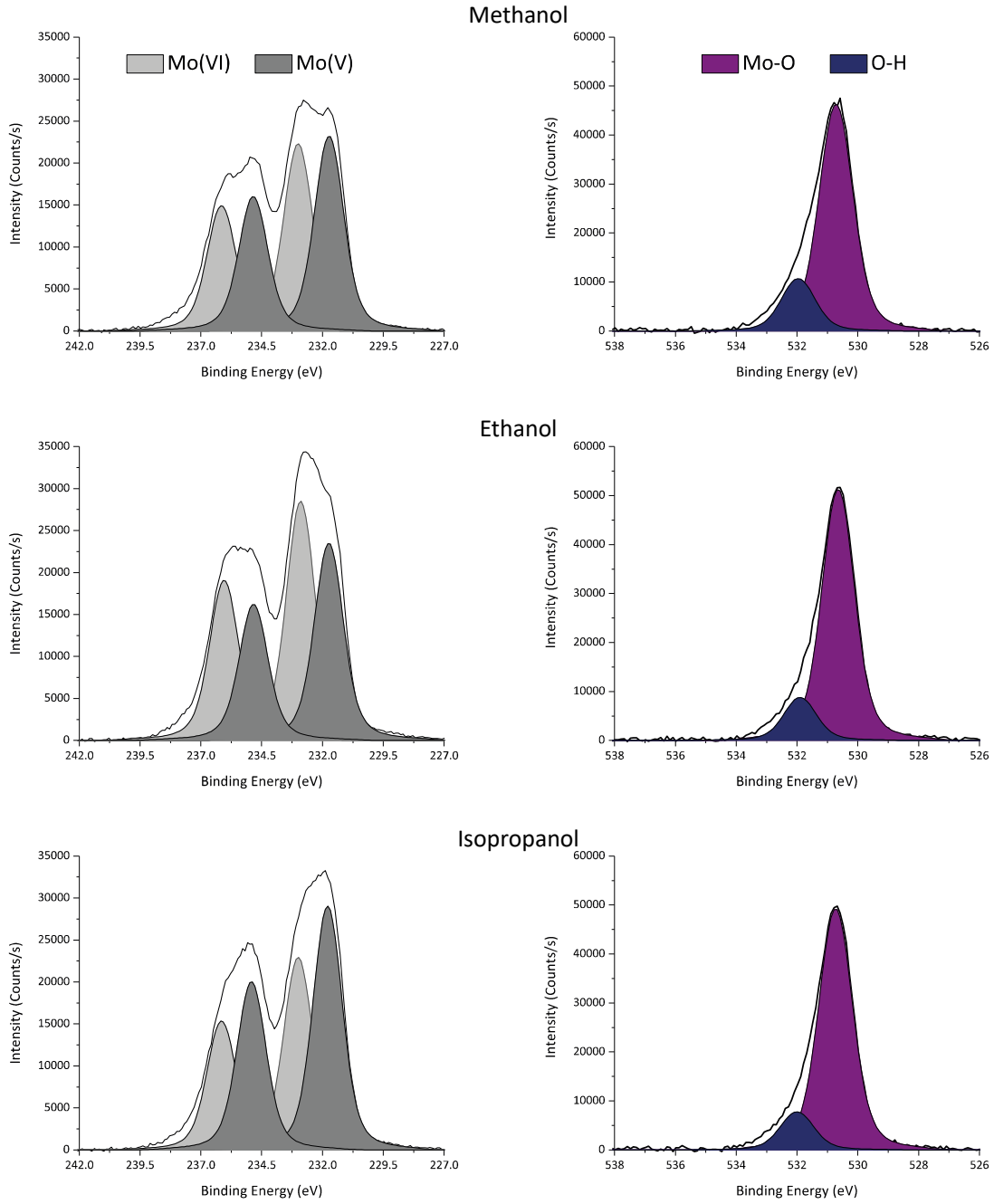

Figure 3.1: XPS spectra and peak fitting of Mo3d (left) and O1s (right) core levels.

The intensity of the main peak is very similar for the three samples; the intensity of the satellite peak is between 22% and 28% of the main one. These similarities in the data are in agreement with the similarities in stoichiometry observed above.

One of the advantages of the hydrogen bronze route is the use of simple precursors such as metallic Mo or MoO_3. This ensures that after deposition there are no organic residues on the films, which could be the case when other routes involving organo-metallic precursors are used. Observation of the carbon core level signal, shown in Figure 3.2a, confirmed very little contamination of the samples. The intensity of the signal is very low and peak fitting cannot be performed to a satisfactory level. However, the most intense peak is ascribed to C-C bonds. This signal is almost always present in XPS, in fact it is used to reference the other peaks (as detailed in the Materials & Methods chapter): therefore, it can be assumed that it is coming from environmental contamination rather than from the film.

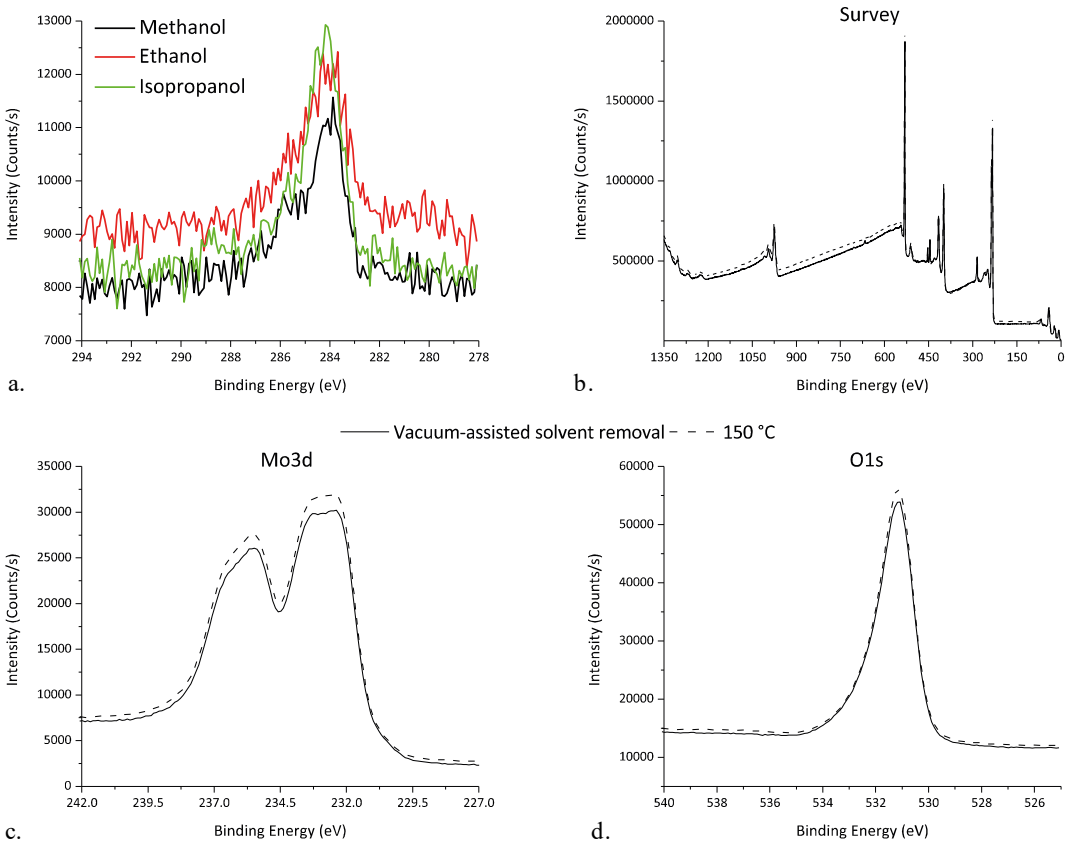

Figure 3.2: a. C1s core level spectra of MoO_{3-x} films deposited from different solvents. b. Survey spectra for MoO_{3-x} deposited from isopropanol and subject to a vacuum-assisted solvent removal step. c. Mo3d spectra for the same films. d. O1s spectra for the same films.

So far, it has been shown that the choice of solvent did not have any major effect on the composition of the MoO_{3-x} films. The effect of post-deposition treatments must also be considered: as stated above, in the hydrogen bronze route the oxide is supposed to form already in solution. To prove this, XPS analysis was performed on films cast from isopropanol and subject to a vacuum-assisted solvent removal step and a thermal treatment at 150 °C. The data is shown in Figure 3.2b-d, specifically the survey spectra, the Mo3d spectra, and the O1s spectra. The samples did not present any observable differences, with both the survey and the

core levels spectra almost completely overlapping. From this it can be inferred that MoO_{3-x} was already synthesised in the solution and the H_2O_2-alcohol solvent removal step observed in previous variations of the hydrogen bronze route was not needed to produce the oxide. Moreover, in terms of composition of the films, the choice of low temperature post-deposition treatments was completely justified.

3.1.1.2 UV-Vis

Having determined the composition of the films, the next step was to assess their transparency. Given that the choices of solvent and post-deposition treatment did not affect the composition, it was assumed that the band gap would not change, either. The optical behaviour was instead studied for the different thicknesses that were later implemented in devices.

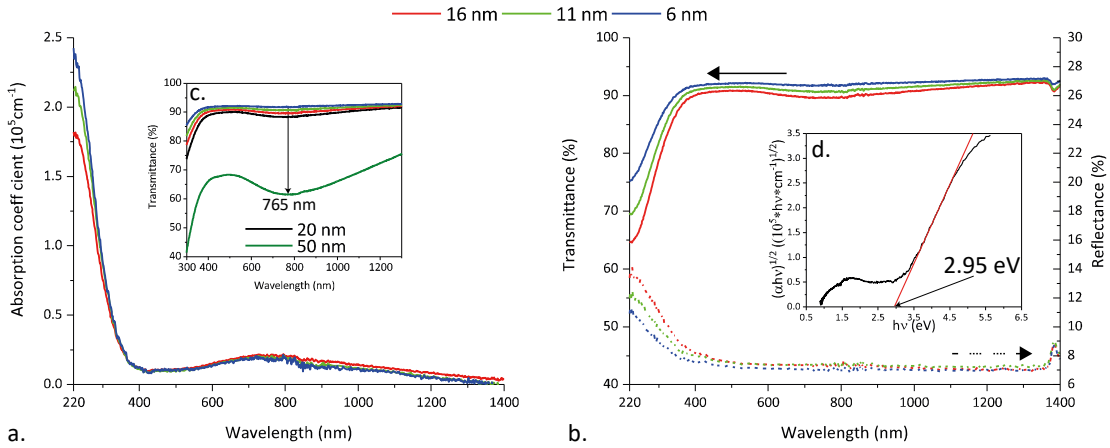

Figure 3.3: a. Absorption coefficient of MoO_{3-x} films of different thicknesses. b. Transmittance and reflectance data for the same films. c. Transmission spectra from films of different thicknesses, highlighting the plasmonic absorption feature. d. Tauc plot of for an 11 nm thick MoO_{3-x} film, with the extrapolated value indicated.

Figure 3.3 shows the data obtained. All films presented similar behaviour in both transmission and reflection: these were used to calculate the absorption coefficient, which should be independent of thickness. Indeed, the different spectra showed excellent agreement. The slight differences observed at low wavelengths can be ascribed to variations in thickness: the values used in the calculations were absolute numbers but the thickness measurements had an experimental error associated with them. The films showed high transparency across the visible range (T>90%), making them suitable for use in standard architecture devices where the HTL must be transparent in order to let light through. Even though the absorption coefficient showed a bowing in the middle of the visible range, centred at 765 nm, in transmission this feature was only evident for the thicker films (16 nm). Yet, thick films were investigated and compared with those already analysed. The data is shown in Figure 3.3c: two extra films were analysed, one 20 nm thick and another one much thicker at 50 nm. It is clear that even for 20 nm

of MoO_{3-x} the broad absorption feature is only inducing a 2.5% decrease in transmission, and to observe a sizeable effect much thicker films must be used (e.g. 50 nm). This feature was observed in the literature for MoO_{3-x} nanoflakes and it was ascribed to plasmonic resonance broadened by the size distribution of the particles in solution[181]. A possible cause of this resonance had been postulated by Fleisch[182] as charge transfer from O to Mo, effectively a reduction from Mo^{6+} to Mo^{5+} (Equation 18).

$$MoO_3 + h\nu \rightarrow Mo^{5+}O^{-}O_2$$

Equation 18

This is consistent with XPS analysis which showed both Mo^{6+} and Mo^{5+}. Nevertheless, as noted above, this absorption is very weak at the thicknesses used in devices in this work, so it is not a source of concern.

The optical band gap was also calculated using the Tauc method. It was found that the values were very close to each other for the different thicknesses, only differing by 0.01 eV. They can be assumed to be equal in the range 2.90-2.95 eV, considering experimental errors and the nature of the Tauc method which involves manually fitting a straight line to the plot, a process likely to induce errors of the same order of the difference between the measured values. The band gap thus obtained for the 11 nm thick film is shown in Figure 3.3d (for an indirect allowed transition, as found in the literature references). The value is consistent with those reported in the literature for MoO_3 and MoO_{3-x}[50,71].

3.1.2 Optoelectronic devices

After having assessed the composition and transparency of the MoO_{3-x} films, devices were fabricated as detailed in the Materials and Methods chapter. First, the optimal thickness was identified and then the various conditions were studied and their performance compared with that of PEDOT:PSS. Only device data was analysed in this section; speculations on the factors improving performances will be made. Further analysis to prove them will be dealt with in a separate section. As detailed in the Materials & Methods chapter, the active layer in hyPV devices was a P3HT:ICBA blend, while in hyLEDs the emitting polymer was a green derivative of PPV.

3.1.2.1 hyPV devices

The optimal thickness for MoO_{3-x} was found to be 11 nm, from devices realised with films deposited using isopropanol as alcoholic solvent and subject to a 150 °C post-deposition thermal treatment (results in Table 3.1, with the optimal choice shaded in grey). This value is in agreement with the literature where values around 10 nm are commonly reported for both sol-gel synthesised and thermally evaporated MoO_3 and MoO_{3-x}[64,105,136,183–185]. It is worth noting that

the 16 nm film only differs significantly from the 11 nm one for the fill factor, which is significantly lower (~9%). This difference can be ascribed to the increased resistance introduced by the thicker film. On the other hand, the 6 nm film has a similar fill factor to the 11 nm one: however, both the V_{oc} and the J_{sc} are lower. This can be ascribed to the presence of pinholes caused by non-uniformity of the MoO_{3-x} film due to the very low thickness.

Thickness	Measured parameter			
	V_{oc} (V, +/- 0.02)	J_{sc} (mA*cm^{-2}, +/- 0.05)	FF (+/- 0.01)	PCE (%, +/ 0.05)
16 nm	0.81	-7.12	0.46	2.62
11 nm	0.79	-7.18	0.55	3.17
6 nm	0.64	-6.42	0.54	2.23

Table 3.1: Parameters of hyPV devices realised with MoO_{3-x} of different thicknesses.

Having determined the optimal thickness for the interlayer, the next step was to analyse the effects of different solvents and post-deposition treatments on the performances of devices. A summary of the results is shown in Table 3.2.

Sample		Measured parameter			
Solvent	Post-deposition treatment	V_{oc} (V, +/- 0.02)	J_{sc} (mA*cm^{-2}, +/- 0.05)	FF (+/- 0.01)	PCE (%, +/- 0.05)
PEDOT:PSS Reference		0.73	-8.16	0.58	3.41
Methanol	V.A.S.R.[ff]	0.80	-8.51	0.57	3.91
	75 °C	0.79	-8.31	0.58	3.83
	150 °C	0.76	-7.90	0.58	3.50
Ethanol	V.A.S.R.	0.79	-7.66	0.49	2.97
	75 °C	0.80	-8.15	0.53	3.47
	150 °C	0.79	-8.19	0.58	3.79
Isopropanol	150 °C	0.72	-7.33	0.55	2.91

Table 3.2: Summary of the main performance metrics for hyPV devices realised with MoO_{3-x} films, compared with a PEDOT:PSS reference.

There were many combinations of parameters that resulted in films with higher performances than PEDOT:PSS. The champion device employed a MoO_{3-x} film deposited from methanol and subject to a vacuum-assisted solvent removal step for 10 minutes: it showed an impressive 15% increase in PCE, a 10% increase in V_{oc} and a 4% increase in J_{sc}. J-V plots for the different sets of parameters are shown in Figure 3.4; the data shown is representative of the values listed in Table 3.2. The improvement in V_{oc} for films deposited from both methanol and ethanol is clearly visible; from the shapes of the curves it can be argued that electrical losses were similar for PEDOT:PSS films and MoO_{3-x}, with the exception of films casted from ethanol and subject to a vacuum-assisted solvent removal step. For films cast from isopropanol only one post-deposition

[ff] Vacuum assisted solvent removal

treatment (150 °C) resulted in viable devices, while both the vacuum-assisted solvent removal step and the 75 °C thermal treatment produced short-circuited devices.

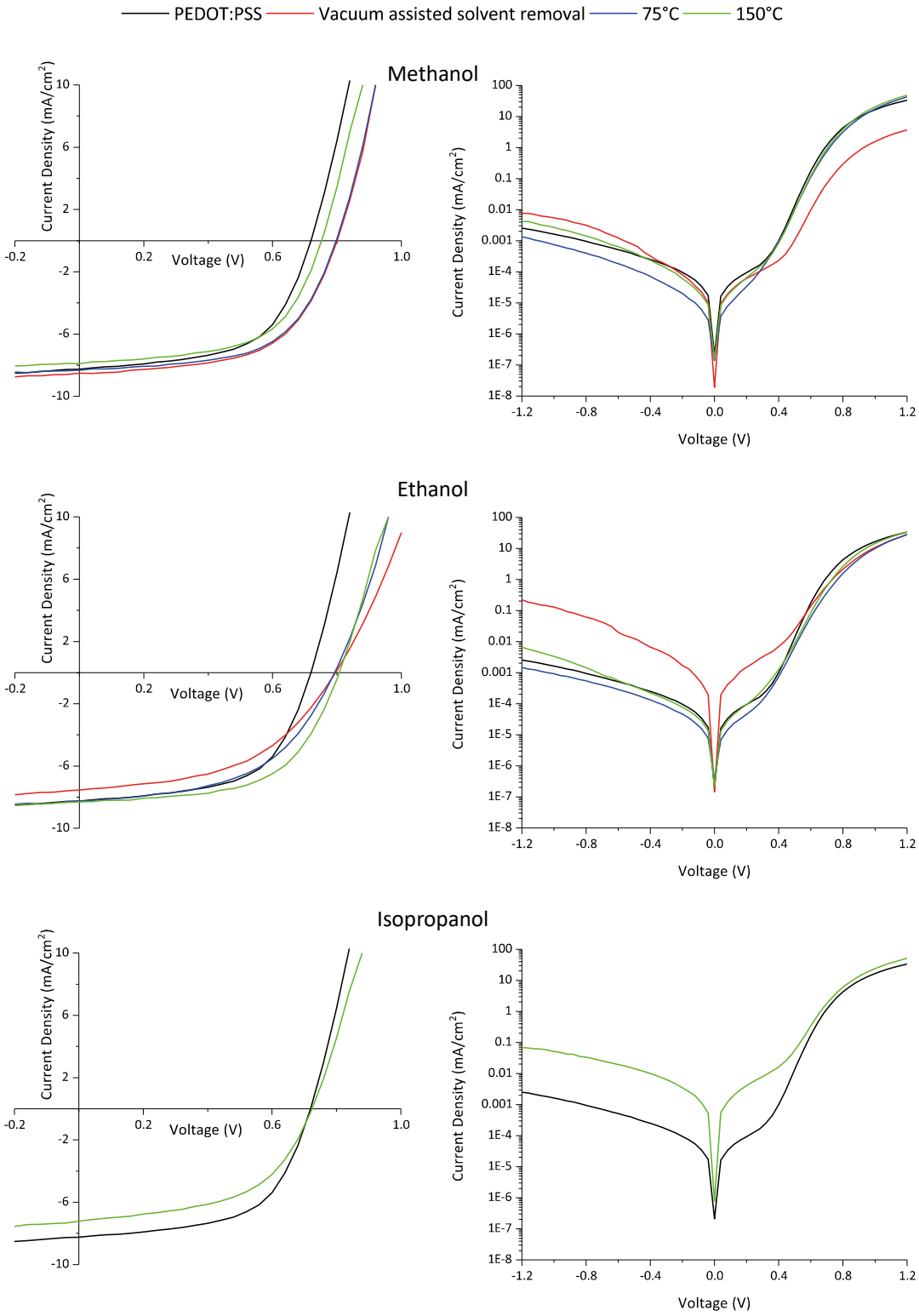

Figure 3.4: Representative J-V curves for the set of parameters listed in Table 3.2, measured under illumination (left) and in dark (right).

To better understand the loss mechanisms associated with the films R_{sh} and R_s were calculated (Table 3.3). The increase in performances observed for several MoO_{3-x} films when compared to PEDOT:PSS was reflected in better electrical metrics for the devices. The shunt resistance of devices incorporating the best performing MoO_{3-x} films was higher than that of reference devices by as much as 37% (MoO_{3-x} cast from methanol and treated at 75 °C). This suggests that the films were uniform and pinhole-free (pinholes would result in localised short-circuited areas which would in return lower R_{sh}); moreover, the charge extraction process is selective and efficient. The high R_{sh} coupled with the excellent V_{oc} (higher than devices incorporating PEDOT:PSS) is also an indication of a favourable energy level alignment of the HTL with the active layer, as expected from the very high work function values commonly reported for MoO_{3-x} films[49,179,186]. The series resistance, on the contrary, is very similar for devices incorporating PEDOT:PSS and devices with the best performing MoO_{3-x} films. The high resistivity of the oxide films was not an issue at the thickness used (as opposed to what observed for 16 nm films before). The values of J_{sc} and R_s for both PEDOT:PSS and MoO_{3-x} based devices prove that MoO_{3-x} films provided good electrical contact with the ITO electrode and the active layer, as good as that of PEDOT:PSS.

Sample		Measured parameter	
Solvent	**Post-deposition treatment**	**R_{sh} (kΩ, +/- 1)**	**R_s (Ω, +/- 10)**
PEDOT:PSS Reference		17	380
Methanol	V.A.S.R.	21	390
	75 °C	23	350
	150 °C	19	350
Ethanol	V.A.S.R.	13	640
	75 °C	19	520
	150 °C	21	380
Isopropanol	150 °C	15	430

Table 3.3: Shunt and series resistances for hyPV devices fabricated with PEDOT:PSS and MoO_{3-x} anode interlayers.

The suitability of MoO_{3-x} films as selective charge transport layers was further confirmed by analysing the J-V plots of the devices measured under dark conditions (Figure 3.4). The devices all showed the characteristic diode behaviour, with the best performing films all showing leakage currents of the same order of magnitude of the reference. In reverse bias the cathode acts as the hole injecting electrode and the ITO as the electron injecting one; therefore, the excellent rectifying behaviour observed is a demonstration that the MoO_{3-x} films acted as good electron blockers as well as hole extractors/injectors. Furthermore, the dark curves in the 0.5-0.8 V region showed similar trends for MoO_{3-x} and PEDOT:PSS, suggesting a similarity in the recombination processes between the two[37,40].

Not all MoO_{3-x} outperformed the PEDOT:PSS reference, instead showing reduced performance. Films deposited from ethanol and subject to a vacuum-assisted solvent removal step and films deposited from isopropanol and subject to a 150 °C thermal treatment did not show

performances as good as the other MoO_{3-x} films, and were not even in par with the PEDOT:PSS reference. The poor behaviour of the former can be ascribed to electrical losses, as highlighted by the low FF and the drop in R_{sh} together with a rise in R_s. Using a higher temperature for the post-deposition treatment of films cast from ethanol improved the results, with the films treated at 75 °C already recovering 4% on the FF to yield a PCE comparable with that of PEDOT:PSS. On the other hand, films cast from isopropanol and treated at 150 °C did not show massive differences in the characteristic resistances: R_{sh} and R_s are similar to those of PEDOT:PSS, only slightly lower (the former) and higher (the latter), but nothing that justified the major difference in performance. Even the fill factor, albeit not as good as the other HTLs, was still acceptable for this kind of devices. The main difference with the other MoO_{3-x} films was the V_{oc}, more similar to that obtained with PEDOT:PSS. A change in work function of this entity is unlikely; instead, a non-favourable morphology is the best candidate. Very rough films could produce local short-circuits by inducing holes in the active layer and subsequent direct contact with the cathode bilayer. Furthermore, films deposited from isopropanol and treated at T<150 °C resulted in short-circuited devices. After deposition of the active layer, its final colour showed a purple hue rather than the red/orange tone typical of P3HT-based blends. These two clues pointed towards the possibility of dissolution of the MoO_{3-x} films by the chlorobenzene used to make up the active layer solution. This would indeed result in the different colour of the blend, with the MoO_{3-x} component providing a blue contribution to the red tonality of the blend, and in the short-circuiting of the device, as the MoO_{3-x} particles in the blend could act as recombination centres.

3.1.2.2 hyLED

The optimal MoO_{3-x} thickness for hyLED was identified at 11 nm (shaded in grey in Table 3.4).

Thickness	Measured parameter				
	Max CE	V at max CE	PE at max CE	L at max CE	J at max CE
	cd/A (+/- 0.02)	V (+/- 0.2)	lm/W (+/- 0.02)	cd/m² (+/- 10)	mA/cm² (+/- 0.05)
16 nm	3.95	5.4	2.32	1053	24.63
11 nm	4.34	5.2	2.74	1310	30.75
7 nm	3.71	5.6	1.76	1234	33.12

Table 3.4: Performance metrics of hyLED devices fabricated with MoO_{3-x} of different thicknesses.

Thicker films resulted in lower efficiencies and luminance, as well as lower current density. As seen for hyPV this was likely caused by the increased resistance of thick films. Thinner films, on the other hand, showed high luminance and higher current, which combined in a resulting efficiency lower than that of 11 nm films. Non-uniform coverage can be identified as the cause of the lower performance, as already observed in hyPV devices.

In Table 3.5 the results from hyLEDs incorporating MoO_{3-x} films are compared with those from a reference device fabricated using PEDOT:PSS. By considering the current efficiency metric, three set of conditions resulted in devices that outperformed the reference: these were the films subject to a 75 °C thermal treatment.

Sample		Measured parameter				
		Max CE	V at max CE	PE at max CE	L at max CE	J at max CE
Solvent	Post-deposition treatment	cd/A (+/- 0.02)	V (+/- 0.2)	lm/W (+/- 0.02)	cd/m² (+/- 10)	mA/cm² (+/- 0.05)
PEDOT:PSS Reference		5.57	6.2	2.80	1210	21.95
Methanol	V.A.S.R.	5.41	5.2	3.28	1299	24.12
	75 °C	6.39	5.8	3.46	1624	25.39
	150 °C	5.34	5.2	3.23	1314	24.56
Ethanol	V.A.S.R.	5.48	5.7	3.04	1160	45.78
	75 °C	6.06	5.7	3.32	1431	23.55
	150 °C	5.03	4.9	3.25	1379	27.50
Isopropanol	V.A.S.R.	3.44	7.2	1.52	1666	48.55
	75 °C	5.80	6.2	2.94	1469	25.35
	150 °C	4.55	5.2	2.75	1340	29.59

Table 3.5: Performance metrics of different MoO_{3-x} films, compared with those of a PEDOT:PSS reference.

Also, for films cast from both ethanol and methanol, the other post-deposition treatments resulted in efficiencies comparable with those of PEDOT:PSS; however, the CE values must be put into perspective. The second column of results in Table 3.5 shows the voltages at which the maximum CE was achieved for all the devices. All MoO_{3-x} films deposited from methanol and ethanol had their peak in CE at lower voltages than the reference PEDOT:PSS devices. This was indeed an improvement with respect to the reference, and a slightly lower current efficiency can easily be tolerated considering the possibility of operating the device at lower driving voltages. In addition, the power efficiencies of these MoO_{3-x} films were similar or higher than those of PEDOT:PSS, despite the lower operating voltages. Again, this is an indication that it was possible to obtain performances similar to PEDOT:PSS with lower power usage. Finally, the current density going through the devices was higher for these MoO_{3-x} films, likely due to better charge injection from the ITO electrode; moreover, the simultaneous increase in luminance suggests that the extra carriers injected were indeed participating in the emission process.

In Figure 3.5, the J-V-L curves for representative hyLED devices are shown. The on/off ratio, which is the ratio between the current density at 5 V and at -5 V, is 10^1-10^2 for all of them, with the PEDOT:PSS performing slightly better (i.e. showing a higher ratio). The reverse current was generally an order of magnitude higher for MoO_{3-x} when compared with PEDOT:PSS.

Nevertheless, all devices showed an excellent rectifying behaviour typical of a diode. The turn-on voltage (defined as the voltage at which the luminance exceeded 1 cd/m^2) was 2.4 V for all devices. This, coupled with the fact that the voltage needed to reach the maximum CE is lower for MoO_{3-x} than for PEDOT:PSS, is an indication of the favourable energy level alignment between MoO_{3-x} and the active layer, confirming what was already postulated based on the trend in V_{oc} observed in photovoltaic devices. As seen for hyPV devices, films cast from isopropanol performed worse than films deposited from the other solvents. While films treated at 75 °C still slightly outperformed the reference, they did so at the same voltage. The other two post-deposition treatments resulted in performances well below those obtained with PEDOT:PSS. A change in work function with respect to the other MoO_{3-x} films can be excluded, both because a substantial change between very similar films is unlikely but mostly because the turn-on voltage did not change. As already conjectured when analysing photovoltaic devices, the reason could be the morphology of the MoO_{3-x} films.

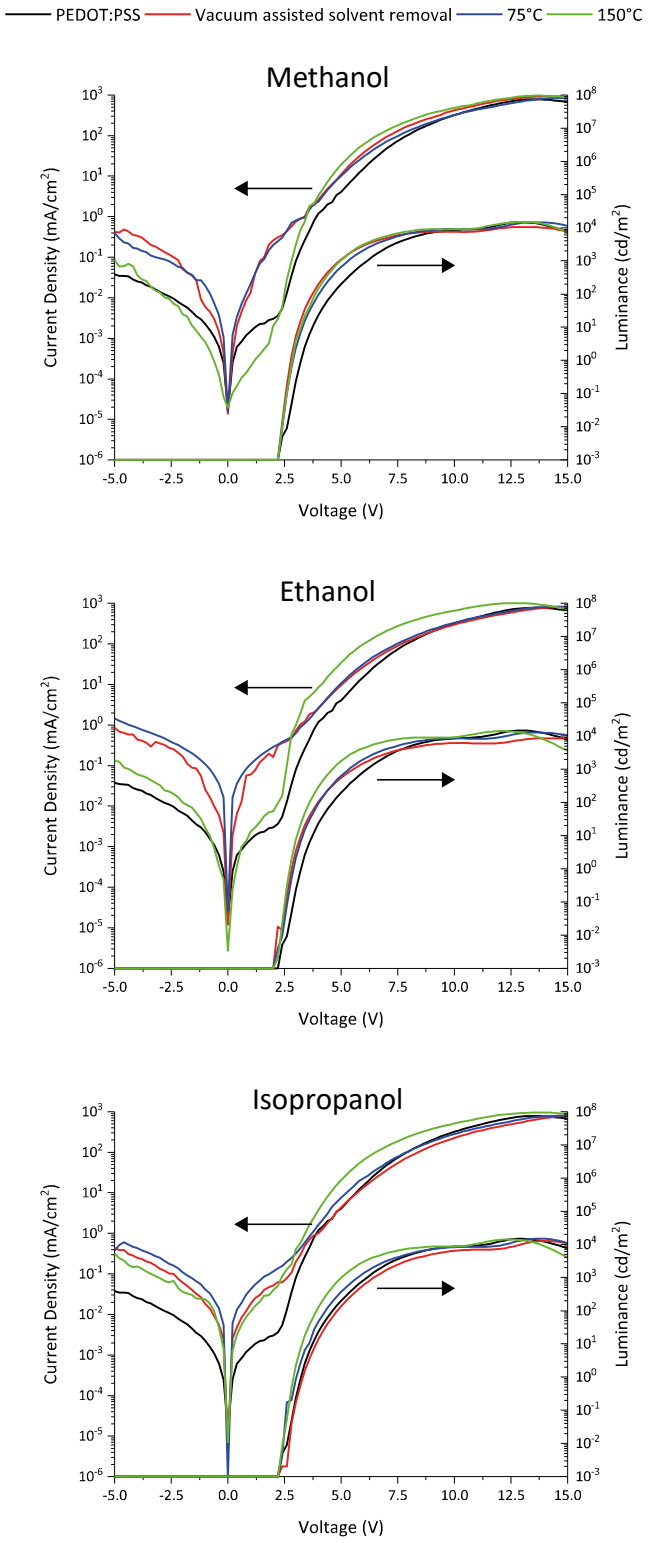

Figure 3.5: Representative J-V-L curves for hyLEDs incorporating MoO_{3-x} films, compared with those of a reference employing PEDOT:PSS.

3.1.3 Further characterisation to explain device performances

A large quantity of information was extracted from the performances of both hyPV and hyLED devices. Nevertheless, more characterisation was carried out in order to fully understand the trends observed in the behaviour of devices.

The most striking anomaly that was observed in hyPV was with MoO_{3-x} films deposited from isopropanol and treated at T<150 °C. It was hypothesised that the chlorobenzene from the active layer was dissolving the HTL resulting in short-circuited devices. To confirm this, samples were prepared in the same way as devices but without the cathode bilayer and XPS analysis was carried out.

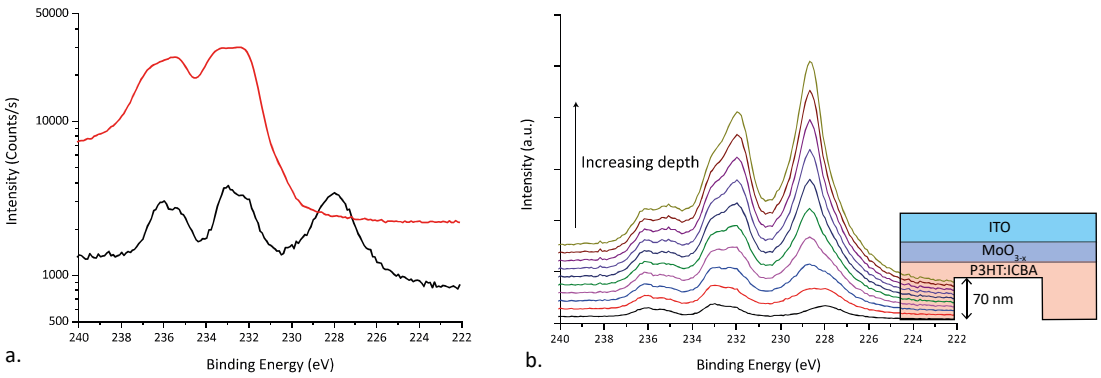

Figure 3.6: a. XPS data for P3HT:ICBA blend (black line) deposited on top of MoO_{3-x}, shown together with the Mo3d signal from a MoO_{3-x} film (red line). b. Depth profile data for the same sample (blend on top of MoO_{3-x}). Each step corresponds to an increase in depth of about 7 nm.

The resulting data is shown in Figure 3.6. In a, the data collected from the sample (black line) is compared with data from typical Mo3d data from films cast from isopropanol (red line). The Mo3d region overlaps with the S2s region, whose signal was clearly visible at 228 eV. While the sulfur signal was expected from P3HT, the Mo3d peaks should not have been there. Their presence suggests that the active layer solution might indeed be dissolving the MoO_{3-x} film underneath. The presence of pinholes which would expose the underlying oxide film is unlikely, as the active layer was 100 nm thick. To obtain further confirmation a depth profile analysis was performed; the sample was etched and data was collected at regular intervals. Each etching interval removed ~7 nm of material; the data obtained is shown in Figure 3.6b. The Mo3d signal was always present, with an increasing contribution at 232 eV. The S2s signal seemed to both increase in intensity and shift towards higher binding energy. This increase and shift can be explained by considering that the etching beam can reduce metal oxides[187–189]. Reduction of MoO_{3-x} produced an increase in signal from Mo^{4+}, which was seen in the growing feature at 232 eV: this is the $^3/_2$ spin state. The high spin state overlapped with the S2s signal, producing its apparent shift towards higher binding energy. The presence of Mo3d signal over the whole

depth of the active layer provided definitive proof that the cause of short-circuiting was the dissolution of MoO_{3-x} by the active layer solution.

Films cast from isopropanol did not yield exciting performances even when they resulted in working devices. Speculations were made that unfavourable morphology was to blame for their poor behaviour. To prove this, AFM analysis was performed on MoO_{3-x} films deposited from different solvents and subject to a 150 °C post-deposition treatment. Data extracted from AFM analysis is shown in Figure 3.7. The RMS roughness, shown in Figure 3.7c, was very high for films deposited from methanol as compared with the other alcohols. This was consistent with the much lower boiling point of methanol: the very quick evaporation of the solvent during spin-coating would result in very rough films as opposed to what would happen with a more gradual evaporation. By looking at the height distribution (in Figure 3.7a) this became even clearer: methanol produced features whose dimensions were spread over a wide range. Also, the line profile (in Figure 3.7b) show much rougher films as compared with both ethanol and isopropanol.

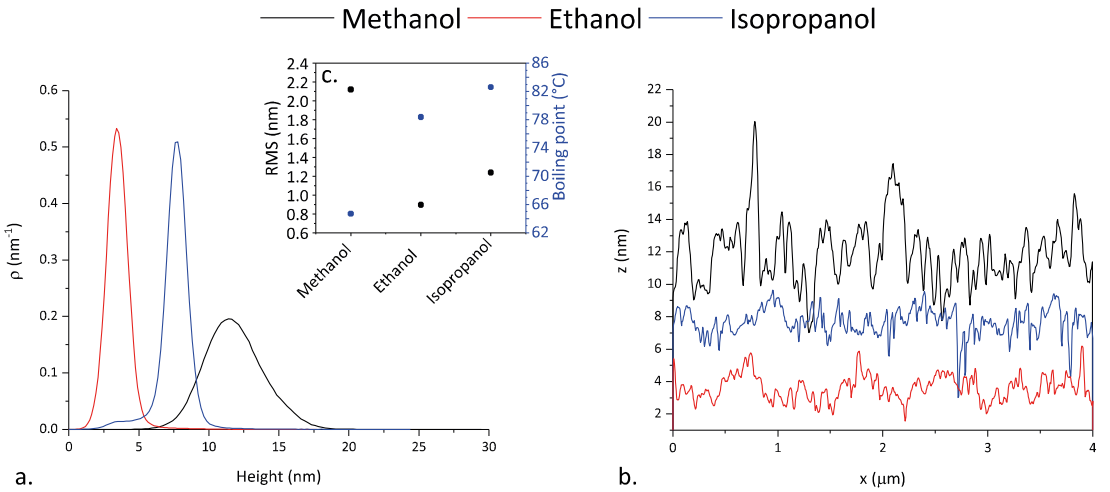

Figure 3.7: AFM data for MoO_{3-x} deposited from different solvents. a. Height distributions. b. Line profiles. c. RMS roughness and boiling points of the solvents.

However, the trend observed in devices seemed to favour the harsher morphology presented by films deposited from methanol. This can be explained by looking at the actual AFM images, shown in Figure 3.8: it is clear that methanol resulted in rougher but also more uniform films, whereas both ethanol and isopropanol yielded films covered with particles. While the situation was not dramatic for films cast from ethanol, as confirmed by the good performances obtained in devices, isopropanol presented a much more serious issue. The particles were numerous even in the small 16 μm^2 area analysed. They almost completely mask the underlying MoO_{3-x} film morphology, hence the apparent low roughness and sharp height distribution seen in Figure 3.7. The performance of devices was clearly affected by the unfavourable morphology:

while rough films can be viable HTLs because they have a greater surface area which increases the number of interfaces available for exciton splitting, scattered particles will act as recombination centres and could possibly cause pinholes in the active layer, thus affecting the whole device.

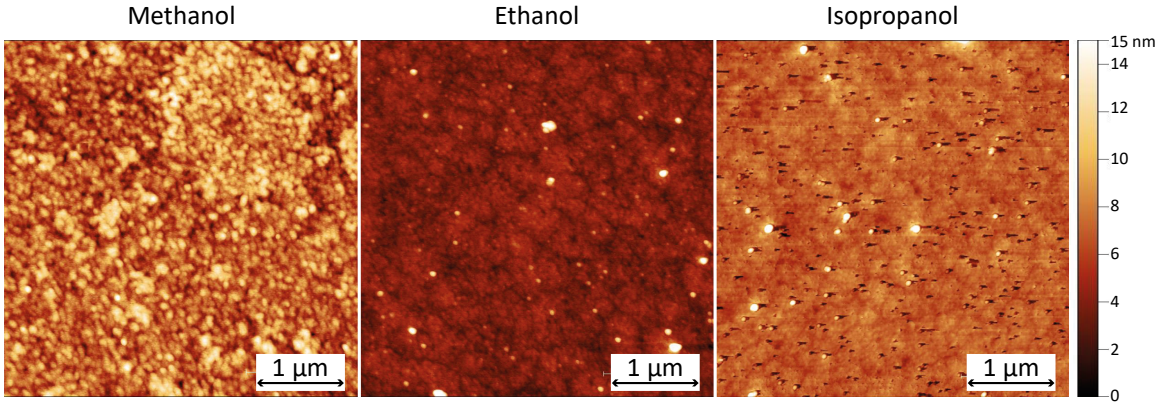

Figure 3.8: AFM images from MoO_{3-x} films cast from different solvents and subject to a 150 °C post-deposition treatment.

Having confirmed the speculations made to justify the poor performances of some of the films, further analysis was done to understand what made other films strikingly outperform PEDOT:PSS. The first analysis that was carried out was Kelvin Probe, to try and correlate the increase in V_{oc} observed with the expected increased work function of MoO_{3-x} with respect to PEDOT:PSS. The Kelvin Probe data is shown in Figure 3.9: the red line is for a film deposited in air and the black line for a film deposited in glovebox. As mention when describing the Kelvin Probe technique, air exposure is detrimental to n-type TMOs work function; the Kelvin Probe data shown here was a confirmation of this. A high work function (>5 eV) was expected, because of the improved V_{oc} with respect to PEDOT:PSS devices and from literature values[49,172,186]. However, MoO_{3-x} films deposited in the glovebox (like the ones employed in devices) showed a work function of ~4.97 eV, which also dropped to ~4.90 eV after only a few minutes of analysis. Moreover, films deposited in air showed an even lower initial work function, at less than 4.90 eV, which dropped to ~4.75 eV in the same time interval. From these results, and considerations on devices' metrics, it was concluded that the work function of MoO_{3-x} films was indeed higher than that of PEDOT:PSS, albeit it was impossible to measure. Even the starting value of ~4.97 eV cannot be deemed reliable, as even though these films were deposited in a glovebox, they were exposed to air for at least 10 minutes before the actual start of the analysis (because of transfer from the glovebox to the instrument, set-up of the analysis, approach of the probe).

To rule out entirely any doubts regarding the unreliability of Kelvin Probe measurements on this kind of oxides, a reference stoichiometric MoO_3 film was deposited via thermal evaporation and then measured in the same conditions (stored in glovebox, air exposure kept to a minimum). The measured work function for this sample was 4.72 eV, which was clearly not the real value: as this film was deposited in vacuum, without any wet chemistry involved and with minimum, if any, substoichiometry, the measurement should have yielded a value close to 7 eV; the much lower result gave the final confirmation that Kelvin Probe measurements on these films should not be trusted.

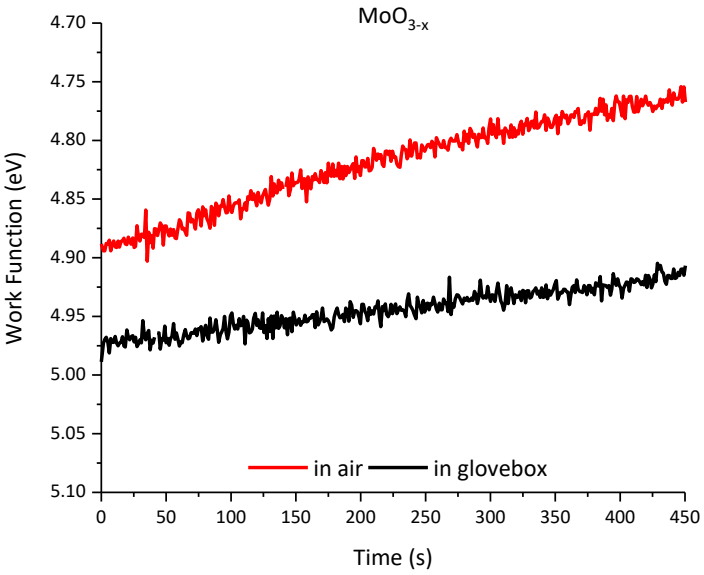

Figure 3.9: Kelvin Probe measurements of MoO_{3-x} films deposited from isopropanol and subject to a 150 °C post-deposition treatment. Different films were deposited in air (red line) or in glovebox (black line) to understand the effect of oxygen and moisture exposure.

Given the null results obtained from Kelvin Probe, a different approach was taken next. The expected high work function and the subsequent enhanced energy level alignment would result in better charge injection from the MoO_{3-x} as opposed to PEDOT:PSS films. Therefore, the injection properties of the champion MoO_{3-x} film (deposited from methanol and subject to a vacuum-annealed solvent removal step) were analysed and compared with those of PEDOT:PSS.

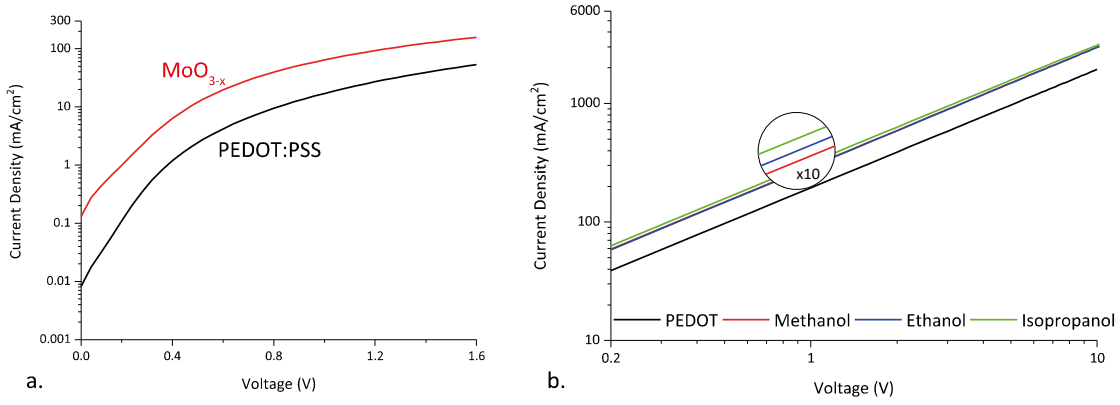

Figure 3.10: a. J-V plots of hole-only hyPV devices incorporating PEDOT:PSS (black line) or MoO_{3-x} (red line) as HTL. The MoO_{3-x} film was the best performing one in hyPV devices. b, "Sandwich" devices (ITO/HTL/Au) fabricated with either MoO_{3-x} films deposited from different solvents or PEDOT:PSS. The MoO_{3-x} films were subject to a 150 °C post-deposition treatment.

To do this, hole-only devices were fabricated and their J-V curves measured. The resulting plots are shown in Figure 3.10a, with the current density in a log scale to highlight differences. It is worth remembering that in these devices the current is carried only by holes, because of the high barrier to electron injection at the Au electrode and because the devices were tested in dark, therefore no photogenerated electron would be present.

The current density of the MoO_{3-x} device was one order of magnitude greater than that of the PEDOT:PSS device at all voltages. This was consistent with the trend observed in hyPV devices, where the increase in V_{oc} was ascribed to a more efficient energy level alignment at the MoO_{3-x}/P3HT:ICBA junction: good electrical contact was ensured by the high work function of MoO_{3-x}, while gap states due to its substoichiometry further helped with hole transport across the interface; this findings were also confirmed in the literature[45,46,190,191]. The excellent hole transport capabilities of the MoO_{3-x} films were also confirmed by fabricating "sandwich" devices (ITO/HTL/Au) to study the injection properties from ITO into the HTL (Figure 3.10b). The current density for MoO_{3-x} devices was 50% higher than that of PEDOT:PSS; the solvent used did not result in any significant difference. This excellent charge injection was again ascribed to enhanced hole transport via gap states in the MoO_{3-x} films. The XPS valence band spectra of MoO_{3-x} films (Figure 3.11) confirmed this hypothesis. The valence band is formed by O2p states, with the presence of occupied Mo4d gap states (see [65]). These gap states, due to the substoichiometry of the films and especially from O vacancies, were the key to the enhanced charge injection properties observed in single carrier, sandwich, and optoelectronic devices.

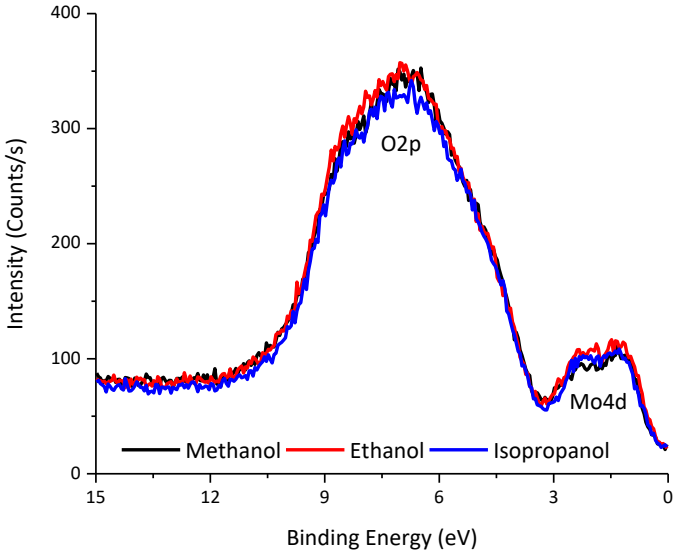

Figure 3.11: Valence band spectra of MoO_{3-x} films deposited from different solvents and subject to a 150 C post-deposition treatment.

To conclude, the EQE spectrum of the champion MoO_{3-x} device was measured and compared with that of the PEDOT:PSS-based reference device (Figure 3.12); also shown are the absorption spectra of a MoO_{3-x} film deposited with the champion set of parameters[gg], of PEDOT:PSS and of the P3HT:ICBA blend. The EQE result presented the same shape of the absorption of the blend,

[gg] Solvent: methanol; post-deposition treatment: vacuum-assisted solvent removal.

as expected. However, the device with MoO_{3-x} HTL showed an increased efficiency on the low wavelength side of the visible range. This cannot be related to light absorption from the MoO_{3-x} and subsequent exciton dissociation at the interface, as the absorption spectrum showed that MoO_{3-x} started absorbing at higher frequencies. This higher EQE at low wavelengths had already been observed in hyPV employing TMOs as anode interlayers, and it was attributed to light intensity distribution changes in the P3HT:ICBA blend induced by the HTL[73] (optical spacer effect): this redistribution was likely caused by a combination of the higher refractive index and the lower thickness of the oxide compared to PEDOT:PSS. Finally, J_{sc} for the devices can be calculated by integrating the EQE spectrum over all wavelengths. The value for MoO_{3-x} was 5% larger than that of PEDOT:PSS: this was in excellent agreement with the increase in J_{sc} measured with the solar simulator setup; the improvement in J_{sc} is split between a contribution between 350 and 450 nm, accounting for a 4% increase, and a contribution between 550 and 630 nm, accounting for the remaining 1% increase.

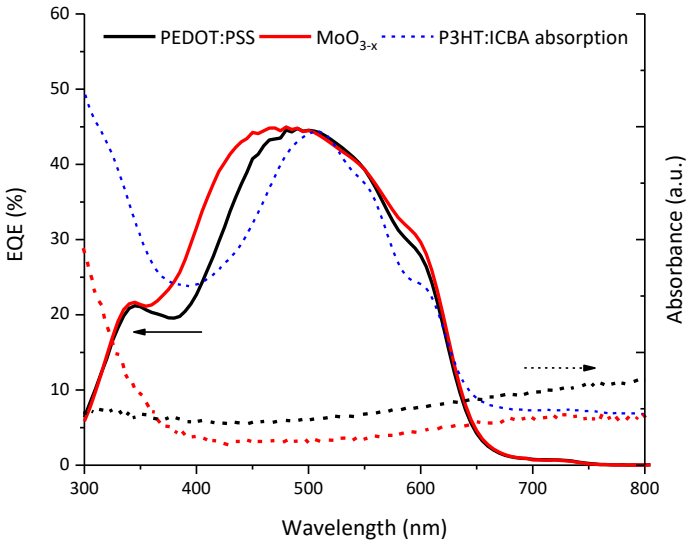

Figure 3.12: EQE spectrum (continuous line) for champion MoO_{3-x} device, compared with the PEDOT:PSS reference. The dashed lines represent the absorption spectra of PEDOT:PSS, MoO_{3-x} and P3HT:ICBA blend.

3.2 V_2O_{5-x}

Much of this section will draw from the MoO_{3-x} part, as both the synthesis route and the characterisation were carried out in the same way and at the same time. The use of V_2O_{5-x} is less widespread than MoO_{3-x} and, to the author's knowledge, mostly hyPV devices have been reported so far. The hydrogen bronze route reported for V_2O_{5-x} again involves the evaporation of the alcohol-H_2O_2 solvent system, followed by redissolution in alcohol (usually ethanol)[134]. It will be demonstrated that, similar to the case of MoO_{3-x}, there is no need for this step as working devices can be fabricated from the original solvent system.

3.2.1 TMO film preliminary characterisation

Composition and transparency of the films were analysed first, to assess the films' suitability for optoelectronic devices.

3.2.1.1 XPS

XPS was once again employed to study the effects of the different solvents on the composition of the films. The V2p signal is very close to the O1s, therefore the 2 must be analysed together. The results are shown in Figure 3.13a-c. Two different V signals were identified via peak fitting, consistent with the oxidation states V(IV) and V(V)[192–194].

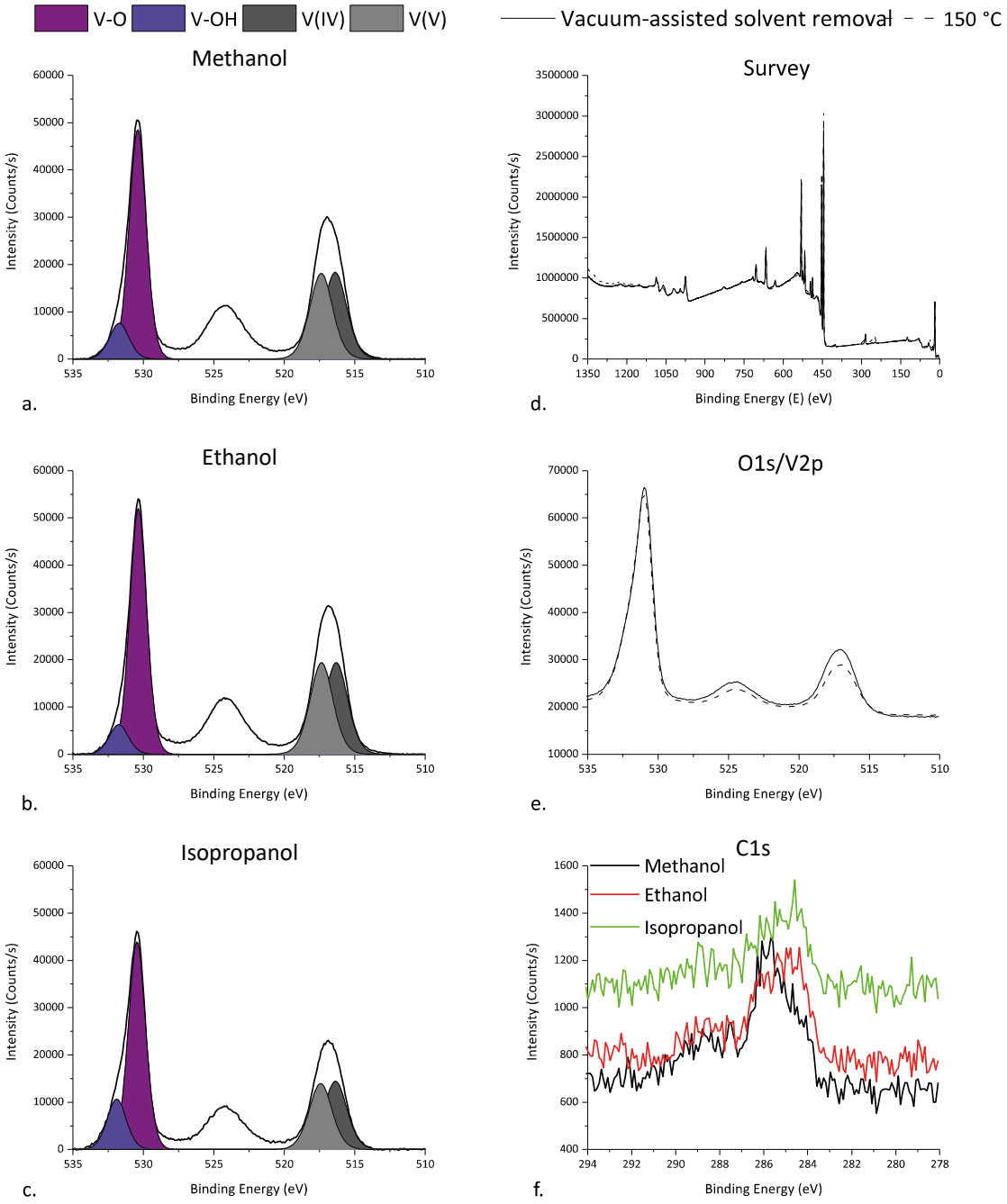

Figure 3.13: a. XPS spectra of V2p/O1s core levels from V_2O_{5-x} films cast from methanol. b. XPS spectra of V2p/O1s core levels from V_2O_{5-x} films cast from ethanol. c. XPS spectra of V2p/O1s core levels from V_2O_{5-x} films cast from isopropanol. All these films were annealed at 150 °C after deposition. d. Survey spectra from V_2O_{5-x} cast from isopropanol and subject to two different post-deposition treatments. e. V2p/O1s signals from the same films. f. XPS carbon signal from the films in a-c.

Only the V2p $^3/_2$ spin state was used in fitting, as the $^1/_2$ state presents some deviations and differences in shape from the former and it would have complicated the procedure[76]. The ratio between the two V peaks was 1:1 for all the samples, suggesting a stoichiometry close to $V_2O_{2.3}$; this was estimated following the same line of reasoning employed for MoO_{3-x}. It is interesting to note that the OH shoulder in the O1s peak is larger for films deposited from isopropanol than for films deposited from methanol or ethanol. This did not result in a change in the V(IV):V(V) ratio, suggesting that the increased signal might come from adsorbed groups on the surface or from the substrate. Analysis of the C1s signal (Figure 3.13f) showed, as for MoO_{3-x} films, that organic contaminants are absent and only adventitious carbon was present on the sample. XPS analysis was also performed on films cast from isopropanol and subject to a vacuum-assisted solvent removal step or to a 150 °C thermal treatment. Survey (Figure 3.13d) and core level (Figure 3.13e) were almost undistinguishable: as for MoO_{3-x}, there was no need for a high-temperature annealing step to obtain the oxide.

3.2.1.2 UV-Vis

The optical characteristics of films of different thicknesses were analysed next. The films were cast from isopropanol and treated at 150 °C after deposition; the thicknesses used were those analysed in devices. The spectra are presented in Figure 3.14 (absorption, transmission and reflection). The thinnest film (4 nm) resulted in noisier than average data, most likely because at that thickness coverage of the substrate may not be uniform. Apart from that, all films showed very high transparency over the whole visible range, with the absorption onset around 400 nm. Unlike the MoO_{3-x} films there was no plasmonic feature in the spectra.

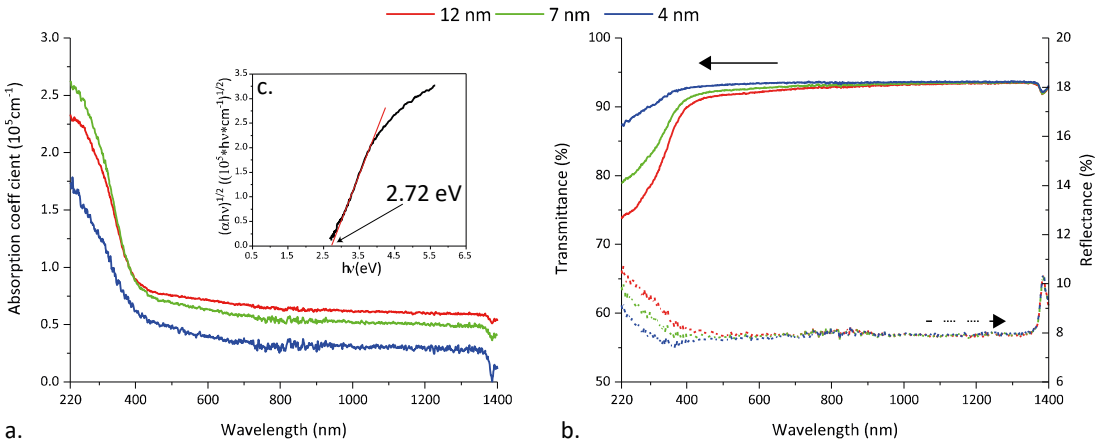

Figure 3.14: a. Absorption coefficient of V_2O_{5-x} films of different thicknesses. b. Transmittance and reflectance data for the same films. c. Tauc plot of for a 7 nm thick V_2O_{5-x} film, with the extrapolated value indicated.

The Tauc method was again employed to evaluate the optical band gap (Figure 3.14c, 7 nm thick film). The measured values were very close, as for MoO_{3-x} samples. The measured value of 2.70-2.72 eV was consistent with what is reported in the literature[70].

3.2.2 Optoelectronic devices

Following the procedure already detailed for MoO_{3-x}, devices were fabricated next and their performance analysed. It is interesting to note that, while hyPV devices showed performance enhancements with respect to PEDOT:PSS similar to those observed in MoO_{3-x}-based devices, hyLEDs did not follow the same trend, instead showing poor behaviour regardless of the processing parameters. Indeed, hyLED devices fabricated with a V_2O_5 HTL are seldom reported in the literature. It is not clear if there are intrinsic problems in using this material, for instance a high number of recombination centres on the surface which, albeit beneficial for photovoltaic devices, would kill light-emitting ones, or simply because MoO_3 has monopolised the field.

3.2.2.1 hyPV devices

The optimal thickness for photovoltaic devices was evaluated first, the resulting data shown in Table 3.6. The thickest, 12 nm film, albeit presenting V_{oc} and J_{sc} very similar to the other two, had a much lower FF than the 7 nm film. The thinnest, 4 nm film showed the same problem, even though its PCE was very close to the 7 nm film. Therefore, 7 nm was chosen as the optimal thickness for hyPV devices. As for MoO_{3-x}-based devices, the chosen value reflected those commonly reported in the literature[98,195].

Thickness	Measured parameter			
	V_{oc} (V, +/- 0.02)	J_{sc} (mA*cm^{-2}, +/- 0.05)	FF (+/- 0.01)	PCE (%, +/- 0.05)
12 nm	0.69	-8.17	0.48	2.70
7 nm	0.70	-8.42	0.55	3.01
4 nm	0.69	-8.46	0.49	2.96

Table 3.6: Parameters of hyPV devices realised with V_2O_{5-x} of different thicknesses.

Next, the effects of the post-deposition treatments of the HTL performance were analysed and compared with the performance of a reference device incorporating PEDOT:PSS.

Sample		Measured parameter			
Solvent	Post-deposition treatment	V_{oc} (V, +/- 0.02)	J_{sc} (mA*cm^{-2}, +/- 0.05)	FF (+/- 0.01)	PCE (%, +/- 0.05)
PEDOT:PSS Reference		0.73	-8.16	0.58	3.41
Methanol	V.A.S.R.	0.78	-6.50	0.38	1.93
	75 °C	0.76	-5.18	0.45	1.76
	150 °C	0.78	-8.59	0.52	3.51
Ethanol	V.A.S.R.	0.81	-8.78	0.52	3.74
	75 °C	0.80	-8.52	0.48	3.30
	150 °C	0.78	-8.80	0.53	3.64
Isopropanol	V.A.S.R.	0.83	-7.86	0.55	3.56
	75 °C	0.76	-7.44	0.60	3.37
	150 °C	0.77	-8.14	0.54	3.32

Table 3.7: Summary of the main performance metrics for hyPV devices realised with V_2O_{5-x} films, compared with a PEDOT:PSS reference.

Notably, all sets of parameters resulted in viable devices. Nevertheless, films deposited from methanol only showed performances comparable with the reference when subject to a 150 °C post-deposition treatment.

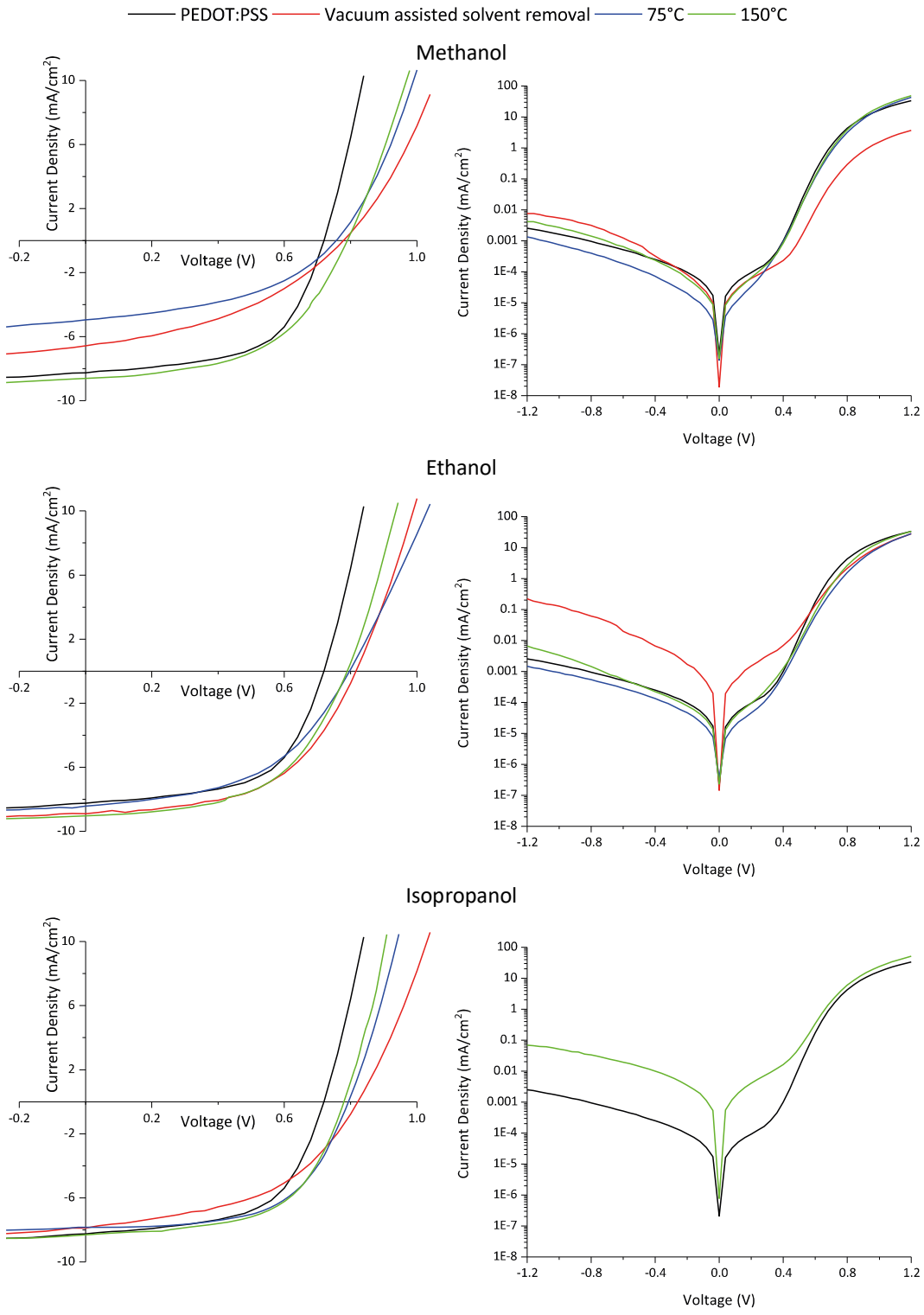

Figure 3.15: Representative J-V curves for the set of parameters listed in Table 3.7, measured under illumination (left) and in dark (right).

For films deposited from methanol and treated at T<150 °C, when the active layer was deposited on the HTL, a change in colour was observed, much like the one seen with MoO_{3-x} films cast from isopropanol and subject to treatments at T<150 °C. This, coupled with the very low FF, pointed to the same explanation already given for MoO_{3-x}: the active layer solution dissolved the HTL, although to a lesser extent as devices were not short-circuited completely.

Sample		Measured parameter	
Solvent	**Post-deposition treatment**	**R_{sh} (kΩ, +/- 1)**	**R_s (Ω, +/- 10)**
PEDOT:PSS Reference		17	380
Methanol	V.A.S.R.	7	1150
	75 °C	12	980
	150 °C	17	500
Ethanol	V.A.S.R.	20	520
	75 °C	15	640
	150 °C	18	440
Isopropanol	V.A.S.R.	16	460
	75 °C	16	420
	150 °C	16	370

Table 3.8: Shunt and series resistances of hyPV devices fabricated with V_2O_{5-x} and PEDOT:PSS HTL.

Fill factor, however, was lower than PEDOT:PSS for all but one of them; even if the values were still acceptable (the J-V plots did not show dramatic changes compared to PEDOT:PSS), this may be an indication of increased electrical losses. The characteristic resistances were calculated and their values are shown in Table 3.8. The underperforming films deposited from methanol showed simultaneous decrease in R_{sh} and increase in R_s: the low R_{sh} was not paired with a drop in V_{oc}, suggesting that bad energy level alignment was not the cause of the high losses. The problems were thus definitively ascribed to the dissolution of the HTL by the active layer solution. The R_{sh} calculated for the other V_2O_{5-x} films were on par with those of the PEDOT:PSS reference; however, they did not outperform it as much as MoO_{3-x} films, although the V_{oc} values were much higher than that obtained from PEDOT:PSS. This corroborated the hypothesis made above about the lower FF shown by V_2O_{5-x} devices being caused by increased electrical losses. A low R_{sh} coupled with a low V_{oc} would indicate inefficient energy level alignment, but this was not the case. Moreover, the high R_s did not result in depleted J_{sc}, which was indeed very high (as much as 8% higher than the reference). Thus, charge injection was not an issue, but other loss processes were involved. This was in agreement with the very poor results from hyLED devices in pointing towards charge recombination centres present at the interface between the HTL and the active layer. The dark J-V plots (Figure 3.15) showed an excellent rectifying behaviour, very close or even better than PEDOT:PSS. This proved that V_2O_{5-x} films acted as selective charge injecting layer by blocking electrons and allowing holes to pass through. Incidentally this confirmed that the energy level alignment was favourable when using V_2O_{5-x} films and therefore it was not the cause of the low

FF. As seen in MoO_{3-x}, the similar slope between V_2O_{5-x} and PEDOT:PSS devices in the range 0.5-0.8 V demonstrated that the recombination behaviour is similar for the two.

3.2.2.2 hyLED devices

The optimal thickness of V_2O_{5-x} for hyLED devices was identified at 12 nm (Table 3.10), using films deposited from isopropanol and subject to a 150 °C post-deposition treatment.

Thickness	Measured parameter				
	Max CE	V at max CE	PE at max CE	L at max CE	J at max CE
	cd/A (+/- 0.02)	V (+/- 0.2)	lm/W (+/- 0.02)	cd/m² (+/- 10)	mA/cm² (+/- 0.05)
12 nm	2.71	4.89	1.73	56.88	1.91
7 nm	1.66	4.80	1.17	38.72	3.43
4 nm	1.37	4.41	0.98	3.99	0.31

Table 3.9: Performance metrics of hyLED devices fabricated with V_2O_{5-x} films of different thickness.

The thickness study already hinted at the possibility that V_2O_{5-x} might not result in high performing hyLED devices. Films from different sets of parameters were fabricated next and their performance compared with those of reference devices incorporating PEDOT:PSS; the results are shown in Table 3.10.

Sample		Measured parameter				
		Max CE	V at max	PE at max	L at max CE	J at max CE
Solvent	Post-deposition treatment	cd/A (+/- 0.02)	V (+/- 0.2)	lm/W (+/- 0.02)	cd/m² (+/- 10)	mA/cm² (+/- 0.05)
PEDOT:PSS Reference		5.57	6.2	2.80	1210	21.95
Methanol	V.A.S.R.	0.03	15.8	0.01	40	119.36
	75 °C	0.03	15.4	0.01	25	114.56
	150 °C	3.01	5.2	1.80	110	3.77
Ethanol	V.A.S.R.	2.01	6.3	1.01	90	4.65
	75 °C	2.41	6.0	1.26	110	4.77
	150 °C	2.15	5.6	1.20	70	3.07
Isopropanol	V.A.S.R.	1.85	6.0	0.96	50	2.86
	75 °C	0.58	8.5	0.22	70	12.30
	150 °C	2.03	7.4	0.85	260	13.08

Table 3.10: Performance metrics of hyLED devices incorporating V_2O_{5-x} films as HTL, compared with a PEDOT:PSS reference.

Interestingly, V_2O_{5-x} films that underperformed in hyPV devices did not deliver in hyLEDs either. Films deposited from methanol and treated at T<150 °C only lit up at V>7 V and with a very low luminance. This resulted in barely detectable efficiencies. Films deposited under different sets of parameters, while not failing so spectacularly, were not on par with the PEDOT:PSS reference. The maximum current efficiencies were low for all of them, with only one set of conditions barely exceeding 3 cd/A. This must be read in conjunction with the other performance metrics: the decrease in the voltage needed to achieve the maximum CE observed with MoO_{3-x} here was

absent; moreover, the luminance values at the same point were much lower than those obtained with PEDOT:PSS, so much so that these devices would not be useful in any display/lighting application.

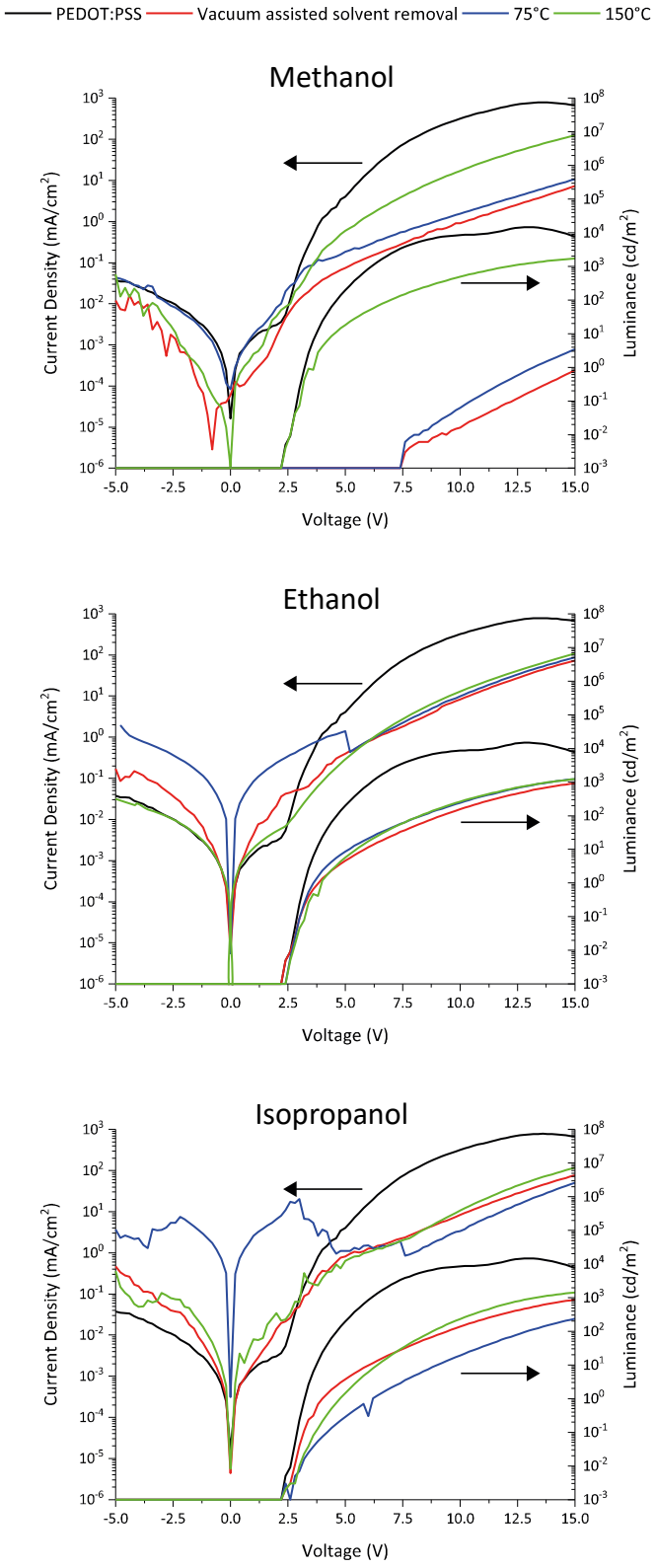

Figure 3.16: Representative J-V-L plots for hyLED devices incorporating V_2O_{5-x} films as HTL, compared with a PEDOT:PSS reference.

The poor behaviour of V_2O_{5-x} devices becomes even more evident when the J-V-L plots (shown in Figure 3.16) are analysed. The luminance curves were much lower than the reference, failing to get within one order of magnitude from it at voltages between 5 and 10 V. The J-V curves presented similar reverse behaviour in most cases: this, together with the fact that the turn-on voltage was the same for all the (viable) devices, offered further proof that the energy level alignment between the HTL and the active layer was very good. On the other hand, the J-V plots were very noisy, much noisier than the reference and also of the curves for MoO_{3-x} devices. The cause of this noise can be identified as trap states at the V_2O_{5-x} surface, a hypothesis supported by the considerations already made in the hyPV section about recombination centres being present and affecting performances.

3.2.3 Further characterisation to explain device performances

As before, further characterisation was carried out to understand the

behaviour of V_2O_{5-x} films in devices. Work function measurements were tried first, but as seen for MoO_{3-x} films Kelvin Probe is not suitable for these materials in air. Data from a film deposited in air (red line) and in glovebox (black line) are shown in Figure 3.17. There was a clear decreasing trend in work function that suggests air exposure is affecting the films' surface potential.

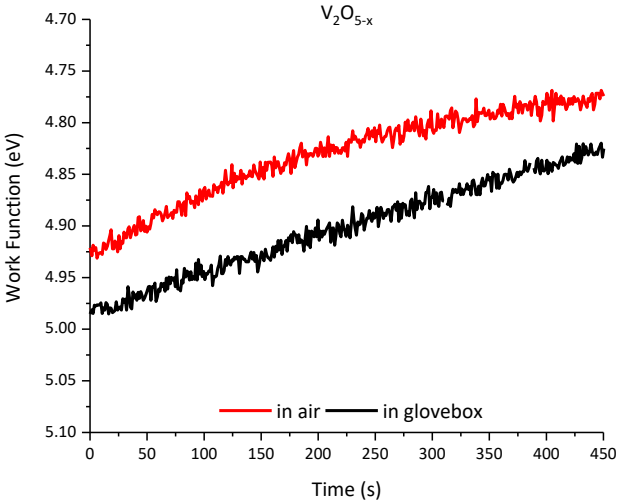

Figure 3.17: Kelvin Probe measurements of V_2O_{5-x} films deposited in air and in glovebox.

Charge injection was therefore analysed next to probe the energy level alignment at the interface and understand if charge transport was improved with respect to PEDOT:PSS. The data is shown in Figure 3.18: hole-only devices fabricated with PEDOT:PSS and the best-performing V_2O_{5-x}[hh] layer in hyPV are shown in a, while sandwich devices fabricated with V_2O_{5-x} films deposited from different solvents are shown in b. Injection from the ITO electrode to the HTL was better when using V_2O_{5-x} rather than PEDOT:PSS, similar to what already observed with MoO_{3-x}. Hole-only devices showed the same trend at low voltages, confirming what already observed in hyPV devices with V_{oc} and J_{sc}; however, as the voltage gets higher, the difference in the two HTL is reduce to the point where the current density is the same for both.

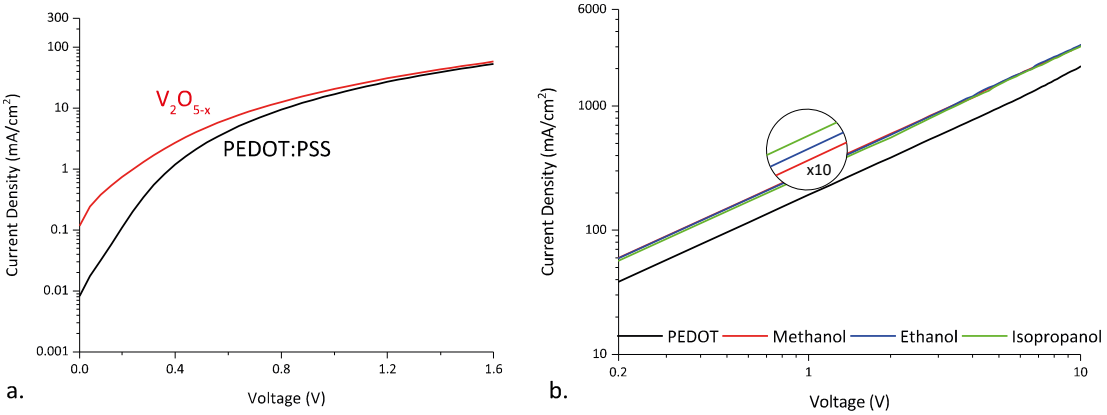

Figure 3.18: a. J-V plots of hole-only hyPV devices incorporating PEDOT:PSS (black line) or V_2O_{5-x} (red line) as HTL. The V_2O_{5-x} film was the best performing one in hyPV devices. b. "Sandwich" devices (ITO/HTL/Au) fabricated with either V_2O_{5-x} films deposited from different solvents or PEDOT:PSS. The V_2O_{5-x} films were subject to a 150 °C post-deposition treatment.

[hh] Solvent: ethanol. Post-deposition treatment: vacuum-assisted solvent removal.

This was not observed with MoO_{3-x} films which maintained their improvement over PEDOT:PSS at all voltages. This depleted injection at higher voltages would affect hyLEDs more than hyPV, as the former are driven at higher voltages than the latter. Indeed, the J-V plots shown in Figure 3.16 seem to confirm this: for $V<V_{turn-on}$, the current density through the device was similar for V_2O_{5-x} and PEDOT:PSS; for $V>V_{turn-on}$, PEDOT:PSS-based devices showed a much higher current density than V_2O_{5-x}. The same was also through for hyPV devices measured under dark (see Figure 3.15). Surface recombination processes can be important at high voltages in these kind of devices[196]; the decreased hole injection will shift the recombination zone towards the anode[44,197], thus increasing the possibility of recombination at the interface rather than radiative recombination in the active layer.

The valence band spectra of films deposited from different samples was measured with XPS (Figure 3.19a). The valence band edge was composed of oxygen *2p* orbitals; as with MoO_{3-x}, substoichiometry resulted in partially filled vanadium *3d* orbitals which gave rise to intraband defect states. This explains the enhanced charge transport at low voltages observed in single carrier and optoelectronic devices. These states did not extend as far as the Fermi level (unlike intraband states in MoO_{3-x} films, see Figure 3.11) and this could be the reason for the different behaviour at high voltages. To conclude, EQE spectra of PEDOT:PSS and the champion V_2O_{5-x} device were compared (Figure 3.19b). The photogenerated current in V_2O_{5-x} devices was higher than that of PEDOT:PSS at lower wavelength; this was already explained above as an "optical spacer" effect. The integral of the EQE over all wavelengths was 6% higher for V_2O_{5-x} than PEDOT:PSS, a result in excellent agreement with the 7% measured with the solar simulator.

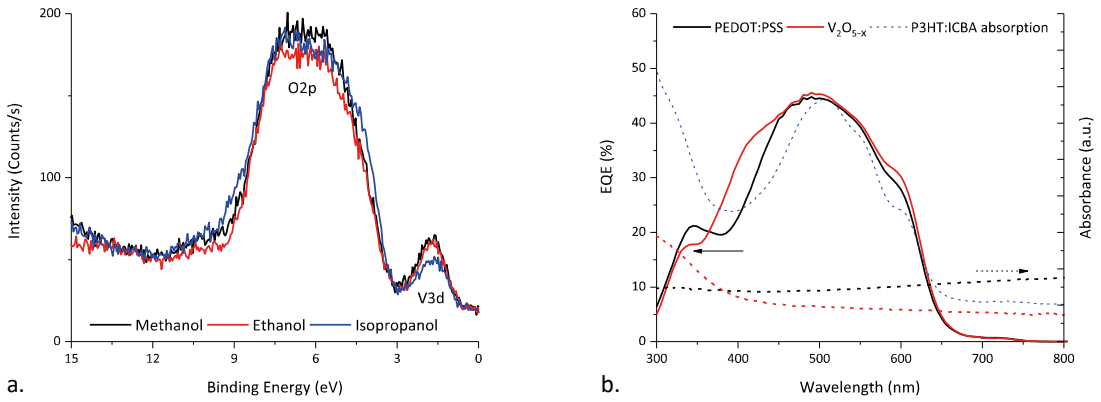

Figure 3.19: a. Valence band spectra of V_2O_{5-x} films deposited from different solvents and subject to a 150 °C post-deposition treatment. b. EQE spectrum (continuous line) for the champion V_2O_{5-x} device, compared with the PEDOT:PSS reference. The dashed lines represent the absorption spectra of PEDOT:PSS, V_2O_{5-x} and P3HT:ICBA blend.

The improvement was split between the two contributions, one in the range 350-450 nm and the other in the range 550-620 nm, which accounted for an increase of 2.5% each of the J_{sc} obtained with PEDOT:PSS. The remaining 1% was obtained from the slight increase over the

range 450-550 nm which, albeit very small, was distributed over the absorption of the P3HT:ICBA blend. The higher EQE measured with PEDOT:PSS in the interval 300-350 nm only accounted for 0.1% of the total J_{sc}, being away from the absorption spectral range.

3.3 CONCLUSIONS

A simplification of the widely-used metal bronze route was employed to synthesise MoO_{3-x} and V_2O_{5-x}. The effect of solvent and post-deposition treatment on the composition of the films and their performance as HTL was analysed. Substoichiometric, transparent films were deposited and both hyPV and hyLED devices were fabricated and their performances compared with those of reference PEDOT:PSS-based devices.

In hyPV devices, almost every set of conditions resulted in working devices, with efficiencies comparable to those of the PEDOT:PSS standard and, in a few cases, superior. The most striking enhancement was observed in V_{oc}, a tell-tale sign of an improved energy level alignment at the interface. This improvement resulted in higher hole current density flowing through the devices, helped by defect states within the band gap. Interestingly, the effect of solvo-thermal processing on devices was different for the two oxides, even though there was no observable effect on composition and charge injection. Champion devices were realised with methanol as a solvent for MoO_{3-x} and ethanol for V_2O_{5-x}, with both films subject to a vacuum-assisted solvent removal step.

For MoO_{3-x}, all of the above also held true for hyLED devices. The higher number of holes injected as opposed to PEDOT:PSS resulted in higher luminance and efficiency; moreover, the increase in these parameters went on par with a decrease in the voltage needed to achieve them. For V_2O_{5-x} light emitting diodes, on the other hand, no improvement was observed. Instead, a decrease in the hole current was recorded at voltages higher than $V_{turn-on}$. As a result, the recombination zone was pushed closer to the anode interlayer, where the defect states acted as recombination centres effectively impeding the light-emitting process.

4 PEDOT:PSS/MoOx BLEND

TMO interlayers can provide organic optoelectronic devices with improved stability and lifetime[35,106,121,144,198]. It was also shown in the previous chapter that enhanced performances can be obtained as compared to the widely implemented PEDOT:PSS. Low thicknesses may however prove detrimental when dealing with very rough substrates, and brittleness may be an issue in flexible devices. A PEDOT:PSS interlayer, on the other hand, is usually deposited with greater thicknesses (usually 40-50 nm), is polymeric, and can be easily incorporated on flexible substrates[199–202]. The well-known problems of PEDOT:PSS have been detailed before, with its acidic and hygroscopic nature being the greatest challenge to device stability[75,144,145]. It has been shown that the lifetime of devices incorporating PEDOT:PSS can be increased if this is substituted by a PEDOT:PSS/MoO_3 hybrid material[203,204]. A few papers have been published on this hybrid, with MoO_3 or MoO_x synthesised following different routes[203–205]. The modified hydrogen bronze route presented in the previous chapter is very suitable for use in this approach. It was demonstrated that MoO_{3-x} particles can be included as a well-dispersed component within a PEDOT:PSS matrix. Three volume ratios were explored, with the label used for them given in brackets:

a) 2 parts of PEDOT:PSS solution/1 part of MoO_{3-x} in volume (P2I1);
b) 1 part of PEDOT:PSS solution/1 part of MoO_{3-x} in volume (P1I1);
c) 1 part of PEDOT:PSS solution/2 parts of MoO_{3-x} in volume (P1I2).

All were compared to standard PEDOT:PSS films. The spin speed was kept the same for PEDOT:PSS and the three different blends: this resulted in similar thickness for all of them (35-50 nm). Their morphology, optical and electronic properties were analysed; XPS was also carried out to gather information about composition. The hybrid films were then incorporated into both photovoltaic devices and light-emitting diodes and their performances compared to those of standard PEDOT:PSS. As done before on TMO films the injection properties at the ITO/HTL/Active Layer junctions were analysed to explain the performance enhancements observed.

The incorporation of MoO_{3-x} in PEDOT:PSS had the greatest impact on the optical behaviour of the HTL, increasing the refractive index of the hybrid with respect to PEDOT:PSS. Resistivity measurements were inconclusive but an indication of the electrical behaviour of the hybrid can be inferred by the devices' characteristics.

4.1 CHARACTERISATION

Following the *modus operandi* from the previous chapter, preliminary characterisation is carried out first to understand some of the features of the hybrid films. The MoO_{3-x} solution was prepared as detailed in previous chapter, using isopropanol as a solvent (hence the 'I' in the labels). After aging and filtering, it was mixed with the filtered PEDOT:PSS solutions in the three different volume ratios indicated above.

XPS analysis was performed first, to determine the composition of the hybrid and whether MoO_{3-x} was bonding to either PEDOT or PSS, or if the materials were simply blended together. The resulting data is shown in Figure 4.1: carbon, oxygen, molybdenum, and sulfur signals are plotted for standard PEDOT:PSS, the three different blends, and a reference MoO_{3-x} film deposited from isopropanol. The S2p signal (Figure 4.1d) was used as the S2s signal (commonly used for sulfur) overlaps with Mo3d (clearly seen in Figure 4.1c).

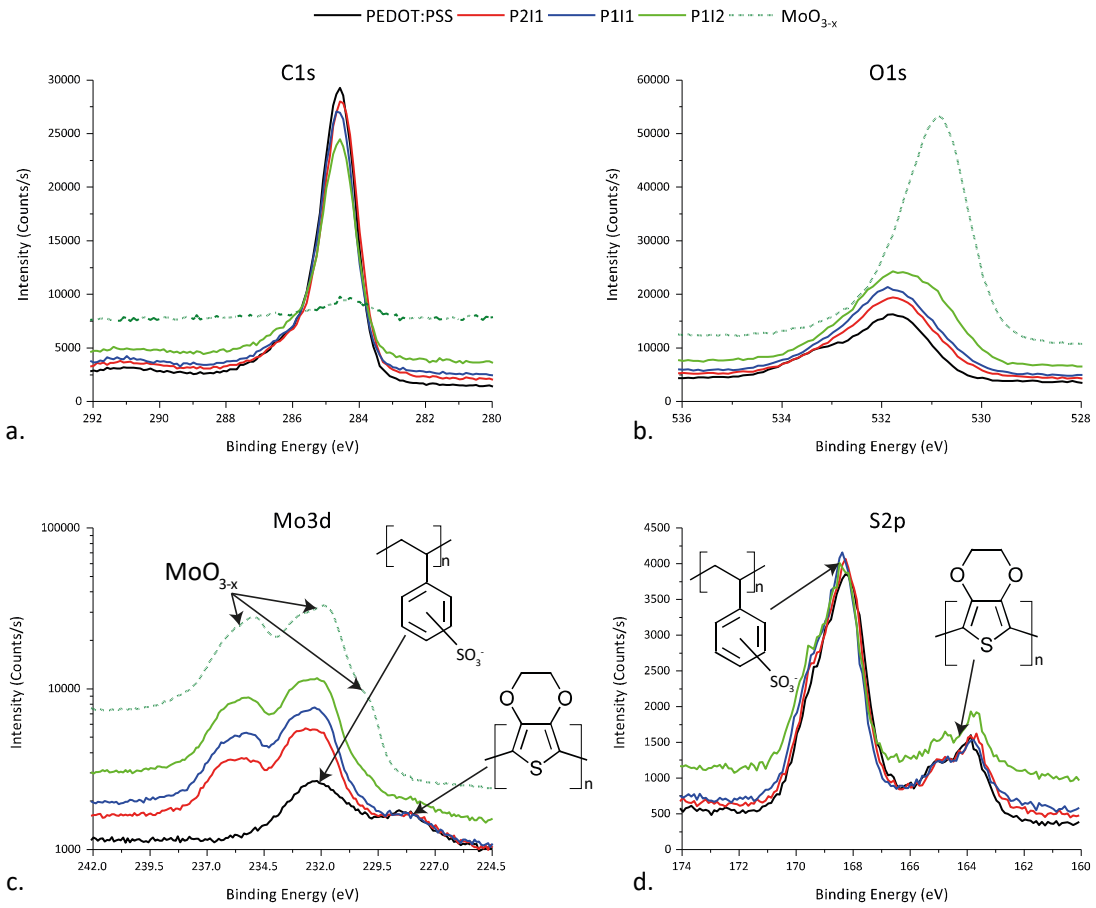

Figure 4.1: XPS data for different PEDOT:PSS/MoO_{3-x} hybrids, standard PEDOT:PSS and MoO_{3-x}.

All the hybrids showed the same shape in C1s signal as PEDOT:PSS (Figure 4.1a), a good indication that the incorporation of MoO_{3-x} is not detrimental to the organic components. In the O1s signal (Figure 4.1b) subtle shifts are observed, with the first two hybrids showing data similar to that of PEDOT:PSS and the third one (P1I2) shifting towards lower binding energy

owing to the increased quantity of MoO_{3-x}. As noted above, Mo3d and S2s signals appeared in the same section of the spectra. The position of the Mo3d signal from the hybrids did not shift with respect to the reference MoO_{3-x} (observed by looking at the $^1/_2$ spin component, not affected by the S2s overlap). The PEDOT:PSS signal clearly showed two different components: these are assigned to the S atom in PEDOT (at higher binding energy) and to the one in PSS (at lower binding energy)[206–208]. This was more evident when analysing the S2p signal where two distinct peaks were identified. Both have high-energy shoulders caused by the unresolved $^1/_2$ spin component of the *p*-doublet. Signals from all the films had the same shape and peak positions, confirming that the incorporation of MoO_{3-x} is not detrimental to PEDOT:PSS. The absence of chemical shifts in both C1s and S2p spectra proved that the oxide particles are not bonded to either PEDOT or PSS, but are simply blended within the organic matrix.

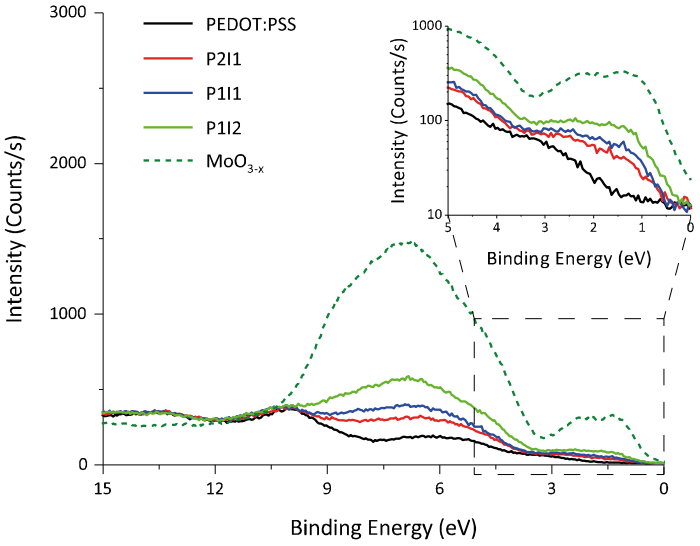

Figure 4.2: Valence band spectra for PEDOT:PSS, the three hybrids, and MoO_{3-x} films. In the inset, the data between 0 and 5 eV is shown on a log scale for the y axis to highlight the gap states.

The valence band of the films was mapped with XPS, too. The spectra are presented in Figure 4.2; in the inset, the 0-5 eV region is shown, with a log scale for the y-axis. The data for PEDOT:PSS and MoO_{3-x} is markedly different, with the hybrid films expressing features of both components. The most interesting information contained in this data is the presence of defect states in the band gap of the material: as seen in the inset, the valence band of PEDOT:PSS tails to zero ~1.5 eV before the Fermi level, while the hybrid films showed defect states compatible with occupied Mo4d orbitals. As seen in the previous chapter, these states may prove beneficial for charge extraction/injection when the films are incorporated in optoelectronic devices.

XPS data was also used to estimate the weight ratio between MoO_{3-x} and PEDOT:PSS in the blends. The mass ratio between PEDOT and PSS, according to the manufacturer, is 1:6[159]. The mass of either PEDOT or PSS can be expressed as the product of the molecular weight of the monomer (MW_{EDOT}[ii] or MW_{SS}[jj]) and the number of monomers present (at_{EDOT} or at_{SS}). The

[ii] 140 g/mol
[jj] 183 g/mol

number of monomers is equal to the number of sulfur atoms, as there is one in every monomeric unit of either PEDOT or PSS. Therefore:

$$\frac{at_{EDOT} * MW_{EDOT}}{at_{SS} * MW_{SS}} = \frac{1}{6} \Rightarrow at_{EDOT} = 0.22 * at_{SS}$$

Equation 19

Moreover, the atomic ratio (at%) between Mo (at_{Mo}) and S (at_{EDOT}+at_{SS}) can be calculated from XPS data:

$$at_{Mo} = at\% * (at_{PEDOT} + at_{PSS})$$

Equation 20

From these quantities, the weight ratio (wt%) between MoO_{3-x} and PEDOT:PSS can be evaluated. The mass of PEDOT and PSS can be expressed in terms of their atomic quantities as seen before; the mass of MoO_{3-x} can be written in the same way[kk].

The weight ratio can be therefore calculated using the atomic ratios obtained from XPS for the different hybrids:

$$\begin{aligned} \boldsymbol{wt}\% &= \frac{\boldsymbol{g_{Mo}}}{\boldsymbol{g_{PEDOT} + g_{PSS}}} = \\ &= \frac{at_{Mo} * MW_{Mo}}{at_{PEDOT} * MW_{EDOT} + at_{PSS} * MW_{SS}} = \\ &= \frac{at\% * MW_{Mo} * (at_{PEDOT} + at_{PSS})}{0.22 * at_{PSS} * MW_{EDOT} + at_{PSS} * MW_{SS}} = \\ &= \frac{at\% * 143.5 * 1.22 * at_{PSS}}{30.8 * at_{PSS} + 183 * at_{PSS}} = \\ &= \boldsymbol{0.82 * at}\% \end{aligned}$$

Equation 21

The results are shown in Table 4.1. It can be seen how the three hybrids covered a wide range of weight ratios, with the MoO_{3-x} component going from 20% to 80% of the total mass (0.2 to 0.8 wt%).

Sample (thickness)	vol% (MoO_{3-x}/PEDOT:PSS)	at% (Mo/S)	wt% (MoO_{3-x}/PEDOT:PSS)
P2I1 (50 nm)	0.33	0.21	0.2
P1I1 (49 nm)	0.50	0.43	0.4
P1I2 (35 nm)	0.67	0.91	0.8

Table 4.1: Volume, atomic, and weight ratios of the different hybrids.

Next, the optical behaviour of the films was analysed: the data is shown in Figure 4.3. The hybrid films showed contributions from both PEDOT:PSS and MoO_{3-x}. The absorption peak occurred at similar wavelengths for all of them, but with increasing amount of MoO_{3-x} a shoulder appeared

[kk] $g_{MoOx} = at_{MoOx} * MW_{MoOx}$, MW_{MoOx} = 143.5 g/mol

around 300 nm. The same behaviour was observed in the transmission spectra. The absorption onset of the MoO_{3-x} film was located at lower wavelengths than PEDOT:PSS, so an intermediate behaviour was suggested. The small feature observed just before the onset of absorption in PEDOT:PSS was not immediately visible in the hybrid films; it was most likely screened by the absorption of the MoO_{3-x} component of the films.

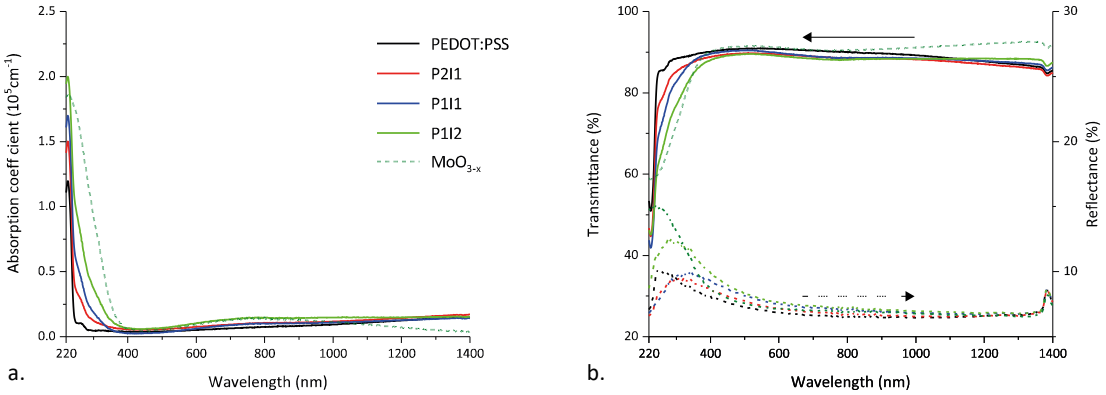

Figure 4.3: a. Absorption coefficient of PEDOT:PSS, MoO_{3-x}, and the three hybrids. b. Transmittance and reflectance data for the same films.

Compared to PEDOT:PSS, the hybrids also showed the plasmonic absorption feature observed in MoO_{3-x} films (see also the previous chapter). However, from Figure 4.3b it was clear that the resulting drop in transmission was very small and unlikely to affect the devices' performance. Despite the presence of MoO_{3-x} in the hybrids, scattering was low and very similar to that of PEDOT:PSS, as seen in the diffuse reflectance spectra (Figure 4.4a). This is excellent as scattered light may lead to optical losses in optoelectronic devices, so it is important to keep it to a minimum.

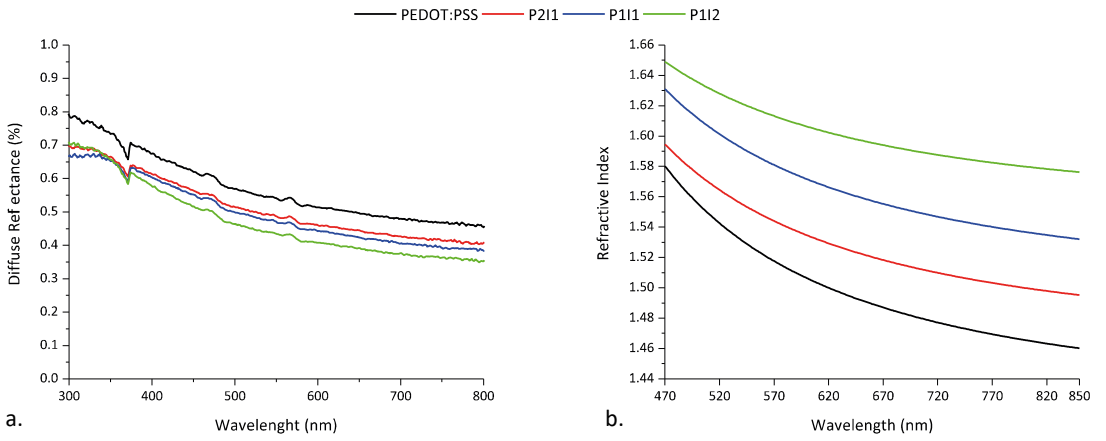

Figure 4.4: a. Diffuse reflectance from PEDOT:PSS and the three hybrid films. b. The refractive index for all four was calculated using the transfer matrix method on Fabry-Perot oscillations from the films.[II]

[II] Thanks to Luca Occhi for help with the refractive index measurements, see Appendix for details.

As the refractive index of inorganic materials is much higher than organic species, the incorporation of MoO_{3-x} (n=3 at 550 nm[209]) should be responsible for variations in the refractive index of the hybrid compared to standard PEDOT:PSS. The transfer matrix method was applied on Fabry-Perot oscillations observed in PEDOT:PSS and the hybrid films to calculate their refractive index. As expected, the refractive index increased with increasing amount of MoO_{3-x} in the film. This could have implications in the optical behaviour of the interlayers in devices and be beneficial for their performances.

Kelvin Probe measurements were performed to understand whether MoO_{3-x} influenced the work function of the hybrid films. Unlike the TMO films seen in the previous chapter, measurements on PEDOT:PSS yielded reliable data; the work function value obtained was 5.1 eV, consistent with what is reported by the manufacturer[159,201]. The value was the same for the first hybrid film P2I1, while the last two showed a slight increase to 5.2 eV.

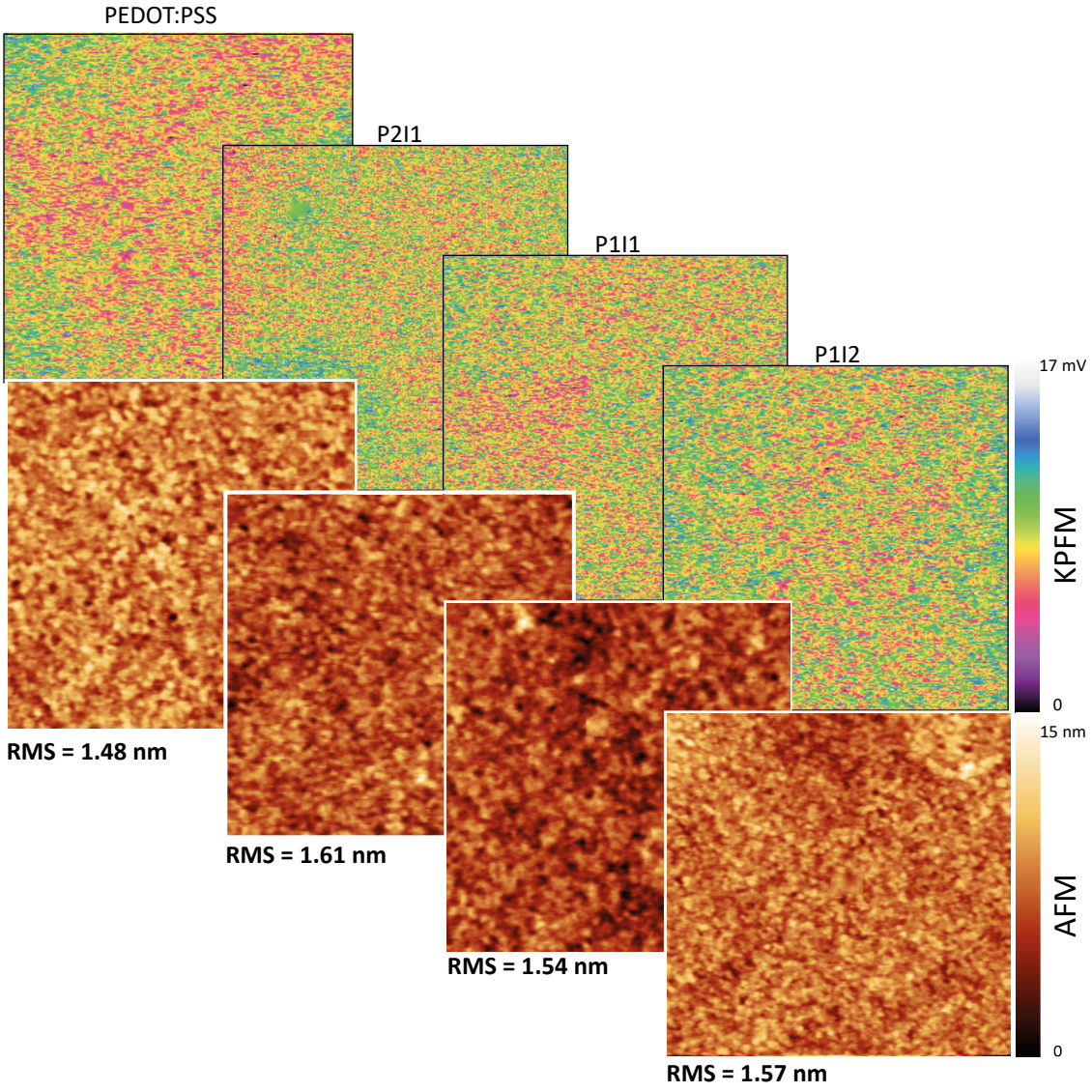

Figure 4.5: KPFM and AFM images of PEDOT:PSS and the three hybrids. All images are 5 μm^2 in size.

The presence of the oxide therefore had no effect on the surface potential of the hybrid films, a possible indication of the excellent dispersion of the particles within the organic matrix.

The surface potential did not change on a microscopic scale either. Kelvin Probe Force Microscopy (KPFM) images of PEDOT:PSS and the three hybrids were taken (Figure 4.5). All images were 5 μm^2 in size; the colour bar represented the potential range, and it was clear that the work function of the films was very similar for the three hybrids and PEDOT:PSS. Moreover, the very small range of values was an indication that the surface potential of the films was uniform and there were no traps or regions with markedly different electronic behaviour. Also, normal tapping mode AFM images were recorded (shown in Figure 4.5); all images show an area of 5 μm^2. The topology of the hybrids was very similar to that of standard PEDOT:PSS; there were not any features disrupting the surface morphology of the films, unlike those observed in the work of Chen *et al.*[205]. The RMS roughness increased only slightly with the incorporation of MoO_{3-x} for all the hybrids. The minor increase in roughness may not be due to the oxide, but to the presence in the solvent mixture of isopropanol: its lower boiling point with respect to water may be the cause. Water and isopropanol form an azeotrope mixture at 91 vol% in alcohol, therefore in the three precursor solutions solvent evaporation may take place in two phases. For P1I1 and P1I2 the precursor solutions are however closer to the azeotrope and that might explain their slightly lower RMS roughness. The height range of all images was 0-15 nm, and there were no particles sticking out of the surface or pinholes induced by the oxide presence. Albeit true that a rougher morphology might increase the interfacial area between the HTL and the active layer, thus improving charge collection efficiency[205], it was observed in the previous chapter that the presence of particles on the surface may be detrimental to the V_{oc} of hyPV devices and their efficiencies. It was observed that particles may produce pinholes that resulted in local shunts; these electrical losses lowered the V_{oc} and the R_{sh}, thus decreasing the efficiency of the photovoltaic devices.

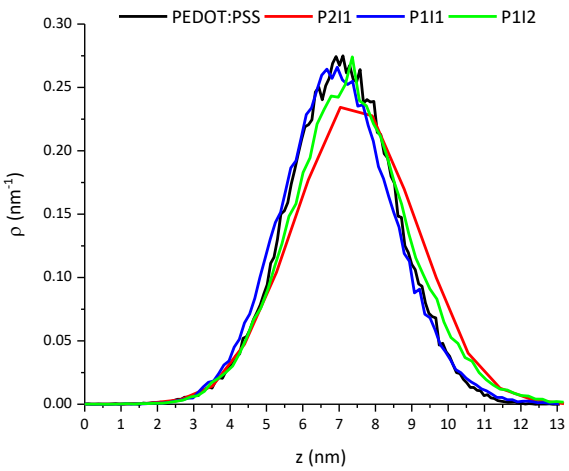

Figure 4.6: Height distribution of PEDOT:PSS and the three hybrid films, extracted from the images in Figure 4.5.

The very similar morphology of the hybrids to PEDOT:PSS was confirmed by extracting the height distribution from the images in Figure 4.5. The results are shown in Figure 4.6; all the films

presented very similar plots both in terms of position (that is, the most common height) and in terms of lineshape (the size distribution of the features).

TEM images of the P1I1 hybrid films were taken to corroborate AFM analysis (Figure 4.7a). As expected, the sample did not show any prominent feature. Different magnifications were used, and none of the image showed any clear contrast, which would have indicated areas where denser MoO_{3-x} agglomerates had formed. In addition to this, EDX analysis was performed, to study the distribution of MoO_{3-x} within the PEDOT:PSS matrix. Carbon, sulfur, and molybdenum signals from the P1I1 hybrid are shown in Figure 4.7b. It is clear from the dataset that molybdenum was evenly spread across the sample. Comparison with carbon and sulfur signals taken from the same region showed the absence of areas containing only MoO_{3-x}, but rather confirmed that the oxide was evenly distributed in the hybrid and no coalescence of MoO_{3-x} particles had occurred.

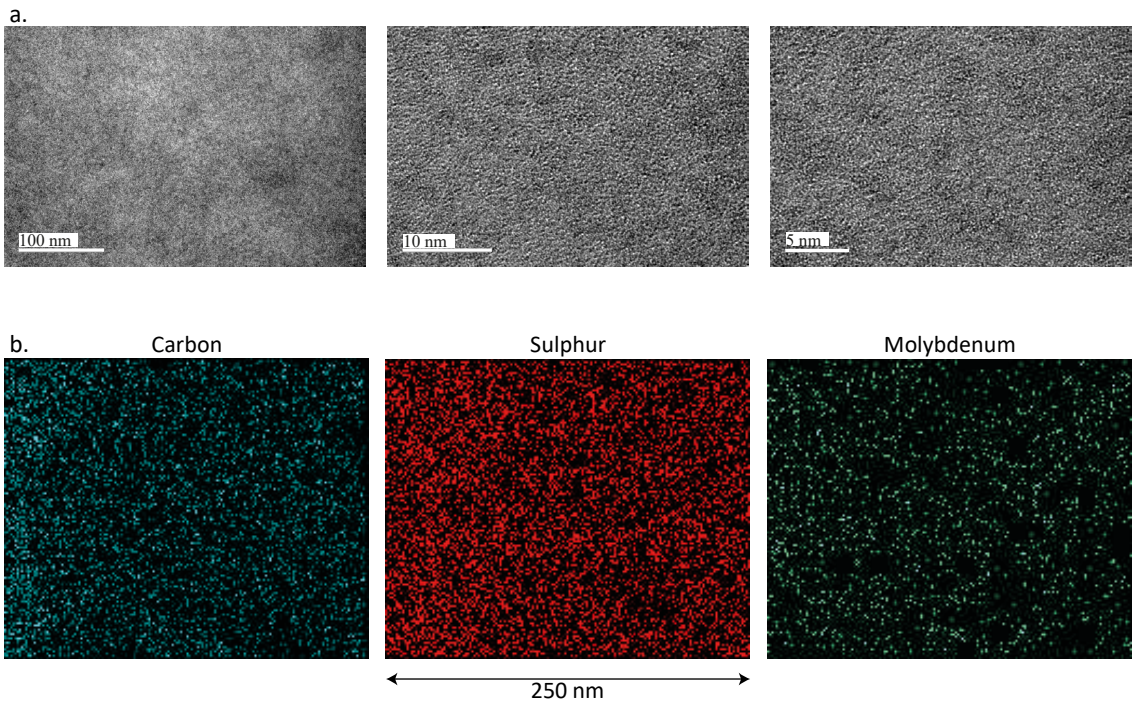

Figure 4.7: a. TEM images of a P1I1 hybrid film, taken at different magnifications. b. EDX signal for carbon, sulfur, and molybdenum from the PI1I film[mm].

So far, it has been shown that incorporation of MoO_{3-x} into PEDOT:PSS can be easily achieved; the resulting hybrid films had morphologies very close to that of standard PEDOT:PSS. MoO_{3-x} particles were well-dispersed within the organic matrix and the surface potential was not affected by the oxide presence, remaining stable at 5.1-5.2 eV. The greatest impact that MoO_{3-x} had was on the refractive index of the material, which shifted from 1.53 for PEDOT:PSS to 1.62 for P1I2 (both at 550 nm). The main findings of this section are summarised in Table 4.2.

[mm] Thanks to Dr Claire Burgess for both TEM and EDX images.

Sample	Wt% Mo (+/- 0.05)	Thickness (nm, +/- 3)	Work Function (eV, +/- 0.1)	RMS Roughness (nm, +/- 0.05)	Refractive Index @ 550 nm (+/- 0.02)	Contact Angle (°, +/- 30')
PEDOT:PSS	0.00	50	5.1	1.48	1.53	19°0'
P2I1	0.20	50	5.1	1.61	1.55	16°0'
P1I1	0.40	49	5.2	1.54	1.59	16°0'
P1I2	0.80	35	5.2	1.57	1.62	13°0'

Table 4.2: Summary of main findings for hybrid films compared with standard PEDOT:PSS.

Before fabricating devices, the contact angle of P3HT:ICBA solution on PEDOT:PSS and hybrids films was measured (results in Table 4.2). As expected from the many similarities between the films, the hybrids did not change compared with standard PEDOT:PSS. The contact angles were lower for the hybrid, by as much as 6° for P1I2. This was consistent with the higher roughness shown by the hybrid films as opposed to PEDOT:PSS, as increased roughness may improve the wetting[210–212].

4.2 HYPV AND HYLED DEVICES

Both types of devices were fabricated incorporating the three hybrids analysed above as HTL. Their performances were compared to those of devices employing standard PEDOT:PSS as anode interlayer.

hyPV devices, with a P3HT:ICBA active layer blend, were analysed first; their performance metrics are shown in Table 4.3. The introduction of MoO_{3-x} in PEDOT:PSS resulted in immediate efficiencies enhancements, even for the hybrid containing the least amount of oxide. The short circuit current remained fairly constant across all compositions, as did the fill factor: both were indications that the hybrid did not introduce new electrical losses compared to PEDOT:PSS. The V_{oc} showed a marked increase that was the major factor in the efficiency improvement.

Sample	Measured parameter			
	V_{oc} (V, +/- 0.02)	**J_{sc} (mA*cm^{-2}, +/- 0.05)**	**FF (+/- 0.01)**	**PCE (%, +/- 0.05)**
PEDOT:PSS	0.73	-8.16	0.58	3.41
P2I1	0.78	-8.12	0.58	3.65
P1I1	0.81	-8.04	0.56	3.59
P1I2	0.82	-8.27	0.56	3.74

Table 4.3: Performance metrics of hyPV devices incorporating the hybrids as HTL, compared with standard PEDOT:PSS.

Representative J-V data for the different devices is shown in Figure 4.8, both under light and dark. From the data measured under illumination the V_{oc} increase is evident, and the shape of the plots did not show any sign of electrical losses. The minor change in work function observed for the last two hybrids may be responsible for the slightly higher V_{oc} of these with respect to

P2I1. The reverse current under dark conditions was one order of magnitude lower for the hybrids than PEDOT:PSS. This could be an indication of the improved blocking behaviour of the hybrid with respect to standard PEDOT:PSS. The standard itself is a good electron blocking layer; the enhancement could be ascribed to the presence of oxide particles: the few electrons able to overcome the extraction barrier at the HTL/active layer interface may be trapped by MoO_{3-x} in the hybrid because of its deep conduction band.

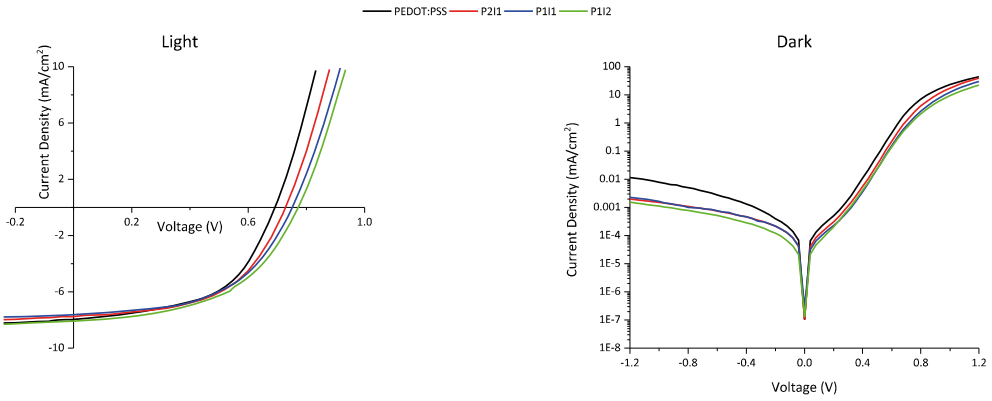

Figure 4.8: Representative J-V plots under light (left panel) and dark (right panel) of the devices in *Table 4.3*

To gain a better understanding of the electrical performances of the devices, shunt and series resistance were extracted from the J-V data (Table 4.4). As expected from the trend in V_{oc} and under reverse bias, R_{sh} is higher for the hybrids than for PEDOT:PSS. This is an indication that coverage of the ITO by the hybrids is indeed complete and no pinholes were present in either the HTL or the active layer. As observed above, the presence of MoO_{3-x} could trap electrons moving through the hybrid more effectively than standard PEDOT:PSS, therefore reducing shunts and increasing V_{oc} and $R_{sh.}$ R_s was higher than PEDOT:PSS, especially for the last two hybrids; this was consistent with the minor drop in FF observed for these two HTL, but it was not accompanied by a corresponding decrease in J_{sc}. The increased resistance was likely caused by the presence of the high resistive MoO_{3-x} particles, which could locally disrupt the conductivity of the PEDOT:PSS network. The absence of any effect in J_{sc} is welcomed, because it means that the charge injection/extraction process is not affected by the higher R_s; moreover, the drop in fill factor is only minor and both hybrids still showed higher efficiencies than standard PEDOT:PSS. There was also a silver lining to this: the last hybrid, because of the highest level of dilution, was thinner than the other two and PEDOT:PSS;

Sample	Measured parameter	
	R_{sh} (kΩ, +/- 1)	R_s (Ω, +/- 10)
PEDOT:PSS	17	380
P2I1	23	440
P1I1	23	490
P1I2	23	490

Table 4.4: Shunt and series resistance of the hyPV devices from Table 4.3.

however, the use of a lower thickness was justified as it compensated for the increase in resistivity.

EQE spectra for devices incorporating the different HTL are shown in Figure 4.9. Both P2I1 and P1I1 showed a behaviour that closely matched that of PEDOT:PSS. Integrating the curves resulted in very similar values, consistent with what observed in Table 4.3. The difference in refractive index was the likely cause of the small deviations observed in the low wavelength portion of the spectra (<400 nm). P1I2, on the other hand, presented a variation on the trend. The behaviour at wavelengths <400 nm was closer to PEDOT:PSS than the other two hybrids, but the main absorption feature in the visible range was wider than with the other films. This can be ascribed to a combination of the increase in refractive index and the decrease in thickness (P1I2 had the highest refractive index and it was thinner than the other two hybrids and PEDOT:PSS)[73]. This suggested that future developments could include a study of how the devices' performances can be optimised by tuning the thickness of the PEDOT:PSS/MoO_{3-x} blends, especially P1I2.

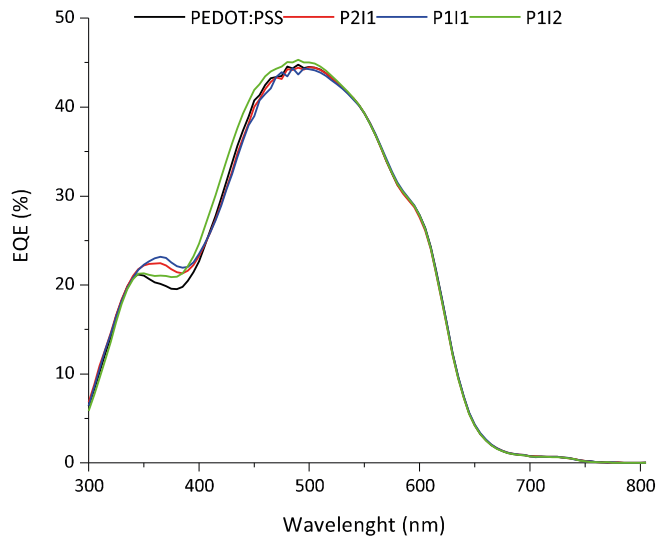

Figure 4.9: Representative EQE data for the devices in Table 4.3.

The charge injection properties at the ITO/hybrid/Active Layer junction were studied next and compared with standard PEDOT:PSS. In Figure 4.10a, single carrier (hole-only) devices were fabricated with a top Au contact instead of the Ca/Ag cathode.

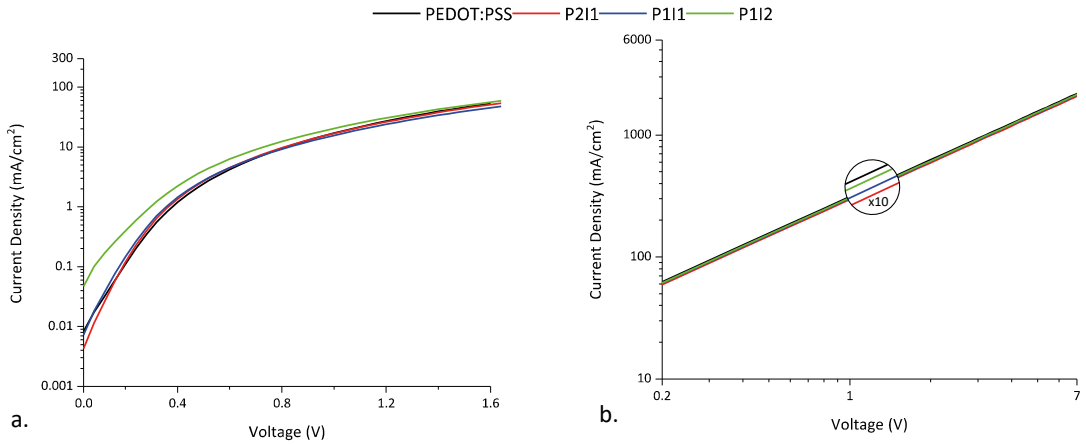

Figure 4.10: a. Results from hole-only devices incorporating either PEDOT:PSS or one of the hybrids. c. Sandwich devices with the structure ITO/HTL/Au, where HTL is either PEDOT:PSS or one of the three hybrids.

The results were again on par with what already observed: P2I1 and P1I1 produced curves very much similar to PEDOT:PSS, while the use of P1I2 resulted in an increased hole injection at low bias. However, for V>1 V, all films lead to very similar current density values; this depletion of hole current at high biases in P1I2 could be a consequence of its higher resistivity and of the higher number of MoO_{3-x} particles, which may act as traps. Also, it was shown that MoO_{3-x} introduced intragap electron states in the hybrid films (Figure 4.2). The highest amount of these states would be present in P1I2, and the electrons occupying them could be recombining with the injected holes effectively depleting the hole current through the device. Charge carrier injection from the ITO into the HTL, shown in Figure 4.10b, was exactly the same for all hybrids and PEDOT:PSS. The higher resistivity of P1I2, theorised from the electrical data extracted from hyPV devices, was compensated for by the lower thickness, with the result that there was no increased barrier to injection from the ITO because of charging of the film.

The improvements in performance brought by the hybrids with respect to PEDOT:PSS should be observed in light-emitting devices as well as solar cells. Therefore, hyLEDs incorporating PEDOT:PSS and the three hybrids as HTL were fabricated; their performances are presented in Table 4.5. There was a clear improvement in performance when using any of the hybrid as anode interlayer. All three had higher maximum current efficiency values than standard PEDOT:PSS. The effect of the excellent charge transfer across the interface could be seen when analysing the voltages needed to achieve the maximum CE. The efficiency of all three hybrids peaked at lower driving bias than that of PEDOT:PSS; the improvement was therefore two-fold: higher efficiency at lower voltages. Power efficiency values were higher for the hybrids, too. The luminance at the maximum CE, albeit slightly lower, was still higher than the 1000 cd/m^2 mark, commonly taken as the reference for lighting purposes; it was also well above the 100 cd/m^2 needed for display applications.

Sample	Max CE	V at max CE	PE at max CE	L at max CE	J at max CE
	cd/A (+/ 0.02)	V (+/- 0.2)	lm/W (+/- 0.02)	cd/m^2 (+/- 10)	mA/cm^2 (+/- 0.05)
PEDOT:PSS	5.57	6.2	2.80	1210	21.95
P2I1	5.89	5.6	3.30	1287	20.37
P1I1	6.13	5.6	3.41	1119	18.48
P1I2	6.03	5.5	3.45	1112	18.67

Table 4.5: Performance metrics of hyLED devices fabricated with standard PEDOT:PSS and the three PEDOT:PSS/MoO_{3-x} hybrids.

The lower luminance may be ascribed to the lower number of carriers available in the device, as seen from the decrease in current density. This decrease can however be explained by considering that the values for the hybrids were taken at lower voltages, and it is therefore not a reason for concern. Moreover, the overall performance of the hyLEDs were greatly improved

when the hybrid films were used (especially P1I1 and P1I2), so lower injected current was not an issue. Nevertheless, an interesting point can be highlighted: albeit being taken at the same voltage, P2I1 showed a higher current than the other two hybrids. This was in agreement with the series resistance, fill factor, and J_{sc} data from hyPV devices, which suggested a higher resistivity of the hybrids as compared to standard PEDOT:PSS; as seen before, the blend with the least amount of MoO_{3-x} was also the one closer to PEDOT:PSS concerning the electrical properties. The J-V-L plots for the hyLED devices are shown in Figure 4.11. PEDOT:PSS and all the hybrids showed excellent rectifying behaviour, with on/off ratios on the order of 10^2 for all of them. The turn-on voltage remained the same (2.4 V) for all the films, an indication that the energy level alignment between the HTL and the emitting materials was not affected by the presence of MoO_{3-x}; this confirmed what already observed for the V_{oc} in hyPV devices. The current densities were comparable for the hybrids and PEDOT:PSS, thus confirming the excellent electrical behaviour of the HTL and the considerations made before.

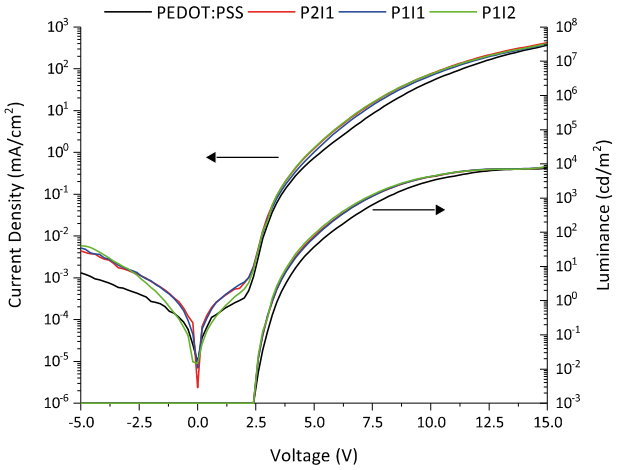

Figure 4.11: Representative J V L plots of the hyLED devices shown in Table 1.5.

Current and power efficiencies against luminance for the best performing hyLEDs are shown in Figure 4.12. The devices' behaviour clearly followed the trends observed in Table 4.5, with PEDOT:PSS and P2I1 showing similar performance between them, and P1I1 coming out as the best HTL.

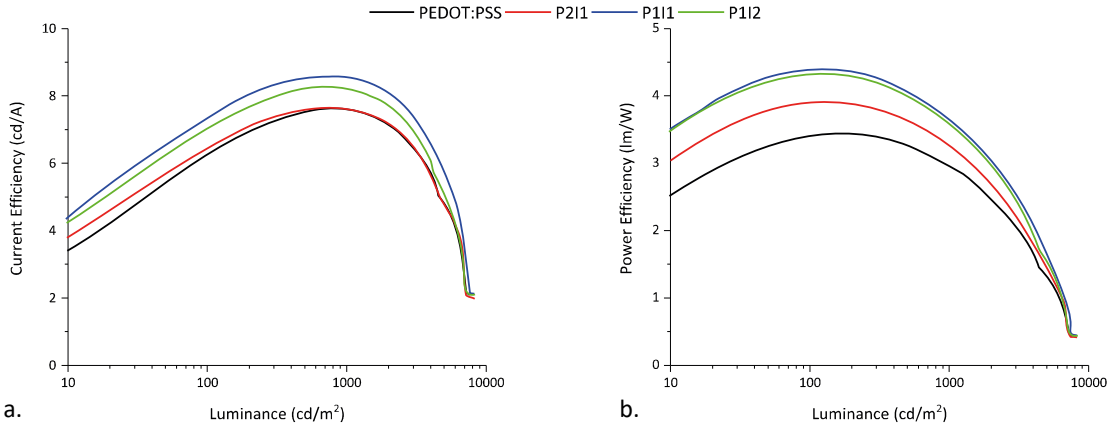

Figure 4.12: a. Current efficiencies (vs luminance) for the best performing devices incorporating PEDOT:PSS or the hybrids as HTL. b. Power efficiencies (vs luminance) for the same devices.

The efficiency roll-off expected at high luminance values[213] was observed for all films, but the presence of MoO_{3-x} in the hybrids did not seem to have a detrimental effect. All devices started to fail at high luminance, as a consequence of the very high driving voltages. Following the works of Baldo[214] and Murawski[215], the critical luminance L_{crit} was defined as the luminance value at which the CE drop to half of its maximum value. When L_{crit} was extracted from the data in Figure 4.12, it was found that the values for the hybrid were slightly higher than for PEDOT:PSS. P2I1 and P1I1 showed the highest increase (6500 cd/m^2 for the hybrids versus 6200 cd/m^2 for standard PEDOT:PSS); P1I2 was somewhat closer to PEDOT:PSS at 6300 cd/m^2. These improvements, albeit very small, were further proof of the excellent HTL characteristics of the PEDOT:PSS/MoO_{3-x} hybrids, which outperformed PEDOT:PSS in almost all the different device metrics.

4.3 DIFFERENT SOLVENTS

As a proof of concept, blends fabricating using different solvents for MoO_{3-x} were also incorporated in devices. MoO_{3-x} precursor solutions were prepared using either methanol or ethanol. They were then mixed with the PEDOT:PSS precursor solution in the same volume ratios as the ones used with isopropanol. They were labelled P2M1, P1M1, and P1M2 when methanol was used and P2E1, P1E1, and P1E2 when ethanol was used instead. The thicknesses were kept the same as those of the corresponding films using isopropanol. Parameters extracted from hyPV devices are shown in Table 4.6, while the J-V data, measured in both light and dark condition, are shown in Figure 4.13.

Sample	Measured parameter					
	V_{oc} (V, +/- 0.02)	**J_{sc} (mA*cm^{-2}, +/- 0.05)**	**FF (+/- 0.01)**	**PCE (%, +/- 0.05)**	**R_{sh} (kΩ, +/- 1)**	**R_s (Ω, +/- 10)**
PEDOT:PSS	0.73	-8.16	0.58	3.41	17	380
P2M1	0.76	-8.42	0.56	3.53	17	460
P1M1	0.76	-8.50	0.56	3.59	18	520
P1M2	0.79	-8.53	0.56	3.66	18	590
P2E1	0.78	-8.04	0.57	3.48	19	500
P1E1	0.81	-8.14	0.56	3.63	21	490
P1E2	0.81	-8.30	0.55	3.68	19	470

Table 4.6: Performance metrics of hyPV devices incorporating hybrids fabricated using methanol or ethanol as MoO_{3-x} solvent.

The trends observed when using isopropanol were replicated with the different solvents. The use of methanol resulted in slightly lower V_{oc} values, accompanied by corresponding lower values of R_{sh}. J_{sc} were instead higher when methanol was used; simultaneously, R_s were higher, too. Hence, a decrease in resistivity of the hybrids can be excluded. Instead, it could be ascribed

to a change in refractive index, which could lead to redistribution of the light intensity within the active layer and therefore to an enhanced photogeneration of current.

Concerning ethanol, the results were closer to those obtained when using isopropanol; the major difference was in the R_s trend, which decreased when the MoO_{3-x} amount increased. However, the change was so small that it could be ascribed to local variations in thickness.

The J-V curves were in good agreement with the performance metrics in Table 4.6. The blocking behaviour, which could be estimated by the current density at reverse biases, was excellent: when ethanol was used, the difference between the hybrid and PEDOT:PSS was almost an order of magnitude. The only outliar curve was the J-V under light for P1M2, which showed the detrimental effect of the higher R_s at voltages greater than V_{oc}.

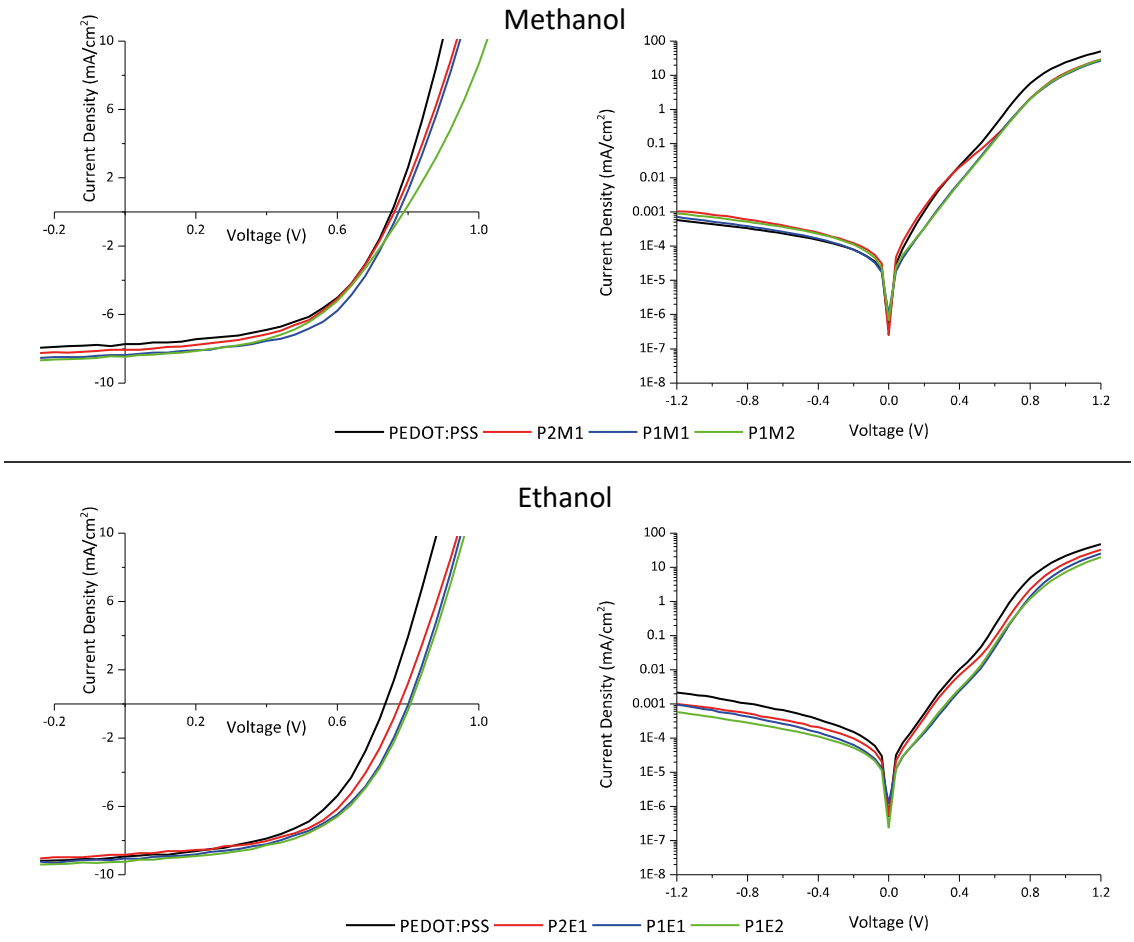

Figure 4.13: Representative J-V data measured under light (left) and dark (right) for the hyPV devices in Table 4.6.

Results from hyLED devices are shown in Table 4.7, with representative J-V-L curves shown in Figure 4.14. The current efficiency values were lower than those obtained when using isopropanol; only P2M1 and P2E1 had CE values very similar to P2I1. Nevertheless, all devices incorporating hybrids outperformed the reference with standard PEDOT:PSS, showing higher current efficiencies which peaked at lower voltages; power efficiencies were also higher.

Luminance values were on the same order of magnitude, as were the current densities: the slightly lower values can be justified as they were recorded at lower voltages.

Sample	Max CE	V at max CE	PE at max CE	L at max CE	J at max CE
	cd/A (+/ 0.02)	V (+/- 0.2)	lm/W (+/- 0.02)	cd/m^2 (+/- 10)	mA/cm^2 (+/- 0.05)
PEDOT:PSS	5.57	6.2	2.80	1210	21.95
P2M1	5.87	5.7	3.20	1200	20.66
P1M1	5.83	5.6	3.22	1190	20.73
P1M2	5.66	5.6	3.19	1170	20.91
P2E1	5.88	5.6	3.27	1150	19.86
P1E1	5.71	5.6	3.17	1110	18.32
P1E2	5.78	5.6	3.26	1050	18.32

Table 4.7: Performance metrics of hyLED devices incorporating hybrids fabricated using methanol or ethanol as MoO_{3-x} solvent.

All J-V-L curves showed the characteristic rectifying behaviour of a diode, with on/off ratios on the order of 10^1-10^2. Energy level alignment at the interface was excellent, similar with isopropanol, as determined by unchanged turn-on voltages when compared with PEDOT:PSS.

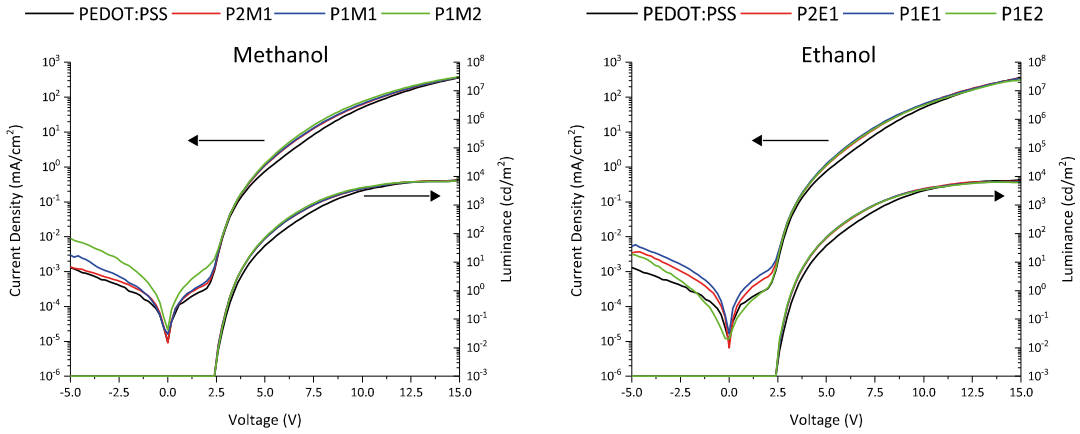

Figure 4.14: Representative J-V-L data for the hyLED devices in Table 4.7.

4.4 Conclusions

It was shown how PEDOT:PSS can be modified with sol-gel synthesised MoO_{3-x}. The modification process is straightforward and carried out by mixing precursor solutions of the two materials in different volume ratios. It was detailed how the weight ratios of MoO_{3-x} and PEDOT:PSS can be calculated using XPS measurements. These same measurements showed how the two materials were not bonded together but simply blended in the hybrid films. The simultaneous presence of both PEDOT:PSS and MoO_{3-x} resulted in some interesting features:

a) The formation of intragap electronic states, similar to those present in MoO_{3-x} films;

b) The increase in refractive index of the hybrids when compared to standard PEDOT:PSS, again caused by the presence of the oxide;

c) The enhancement in wetting of the active layer solutions, likely induced by the higher roughness of the hybrid films with respect to PEDOT:PSS.

In addition to this, it was observed that MoO_{3-x} was well-dispersed in the organic matrix and did not coalesce in large particles. As a result, the work function of the hybrids did not deviate from the reported one for PEDOT:PSS, and the surface of the films did not show protruding features, unlike similar hybrids detailed in the literature[205].

Optoelectronic devices incorporating these hybrids as HTL were fabricated and their performances compared with standard PEDOT:PSS. It was found that for both hyPV and hyLED devices the use of the hybrids resulted in striking performance enhancements. The energy level alignment at the HTL/Active Layer interface was excellent, with hyPV devices showing increased V_{oc} values and hyLED devices showing higher CE values at lower biases when the hybrids were used. MoO_{3-x} likely had a detrimental effect on the hybrid conductivity, as evinced from the electrical behaviour of hyPV devices. However, the decrease was minor; furthermore, in the film with the highest amount of MoO_{3-x}, the higher resistivity was compensated for by the slightly lower thickness, which proved to be beneficial in terms of R_s and J_{sc}. It was noted that the high refractive index of this hybrid, coupled with the decreased thickness, produced an optical spacer effect which widened the photoactive window in the EQE spectrum. It was suggested that a thickness variation study could be carried out to tune the performance of P1I2 by finding the optimal thickness to maximise this optical spacing. Because of the high resistivity of P1I2, this tuning would undoubtedly need to deal with thinner films rather than thicker ones. Finally, the effect of different solvents for MoO_{3-x} on the performance of the hybrids as HTL was analysed. To do this, precursor solutions for the oxide were prepared with either methanol or ethanol instead of isopropanol. They were mixed with PEDOT:PSS in the same ratios as the isopropanol-based one. Both hyPV and hyLED devices were fabricated. The performance enhancements already observed for the isopropanol series were replicated, albeit efficiency values, while still outperforming standard PEDOT:PSS, were slightly lower than the isopropanol-based recipe. While most of the differences in trends can be ascribed to local variations in thickness, an interesting point can be made when methanol is used: the simultaneous increase in R_s and J_{sc} cannot be due to changes in resistivity of the films. Instead, it was suggested that modifications of the refractive index could be the cause. Future work should focus on complete characterisation of the hybrids fabricated from different solvent, to understand whether further tuning of the properties of the films can be achieved.

5 TUNGSTEN AND COBALT OXIDES

In the previous two chapters the synthesis routes presented did not involve any organic precursors or additives. This was done to minimise the presence of organic residue in the oxide films. Indeed, the strive for low temperature post-deposition treatments seems non-compatible with the use of organic precursors which often require elevated temperatures to be removed. However, the hydrogen bronze route has some limitations and not all TMOs can be synthesised in that way. Tungsten (VI) oxide production, for instance, requires metallic tungsten to be mixed directly with H_2O_2 to react before the mixture can be dissolved in alcohol; however, this reaction is highly exothermic[137] and precautions must be taken during the preparation, thus adding to the complexity of the process. Moreover, to the author's knowledge, the use of the hydrogen bronze method has not been reported for any TMOs other than MoO_{3-x}, V_2O_{5-x}, and WO_{3-x}. Therefore, there is a need for different processing routes to add to the library of oxide materials that can be employed as HTL in hybrid organic:inorganic optoelectronic devices. MoO_{3-x} and V_2O_{5-x} are, together with NiO, arguably the most studied TMO anode interlayers. However, n-type WO_{3-x} and p-type CuO_x and CoO_x could also be employed in devices, with a few examples present in the literature for WO_{3-x} and CuO_x[73,121,216–221].

WO_{3-x} has been reported in the literature as a promising candidate to substitute PEDOT:PSS; a variety of routes including solution processing[220,222] and thermal evaporation[34,74] have been described; thus the possibility of comparison with results from other groups was key in the decision to study its sol-gel processing. On the contrary, no evidence was found for the use of CoO_x as HTL, even though its suitability was hypothesised in some theoretical studies[14,79]. Hence, after having refined the synthesis processes of a few known materials (MoO_{3-x}, V_2O_{5-x}, WO_{3-x}), it was decided to try and produce something different.

Two different sol-gel routes were explored. Alkoxide hydrolysis in alcohols was employed to deposit WO_{3-x}, as reports on similar methods highlighted the fact that low temperature post-deposition treatments were enough to obtain good-quality oxide films[145,220]. A completely different approach was taken for CoO_x; alcoholic solvents were exchanged for organic solvents such as chlorobenzene, toluene, and p-xylene, and no additives were used.

5.1 WO_{3-x}

WO_{3-x} films were deposited from a sol-gel recipe involving dissolution of tungsten (V) ethoxide in alcohol and stabilisation of the solution using acetic acid. The organic precursor is obtained as a dispersion in ethanol. It was easily dissolved in alcohol via overnight stirring; however, without the addition of acetic acid the solution was not stable, forming a white precipitate after

24h of mixing, even if kept stirring. XPS analysis was performed to study the composition of the films. The W4f signal was analysed initially (Figure 5.1). The majority of tungsten was in the 6+ oxidation state, an indication that hydrolysis of the precursor had occurred and the film was composed of tungsten oxide. Oxygen vacancies resulted in a small presence of W(V). The stoichiometry, calculated from the relative ratio between the two oxidation states, was $WO_{2.9}$ for all solvents.

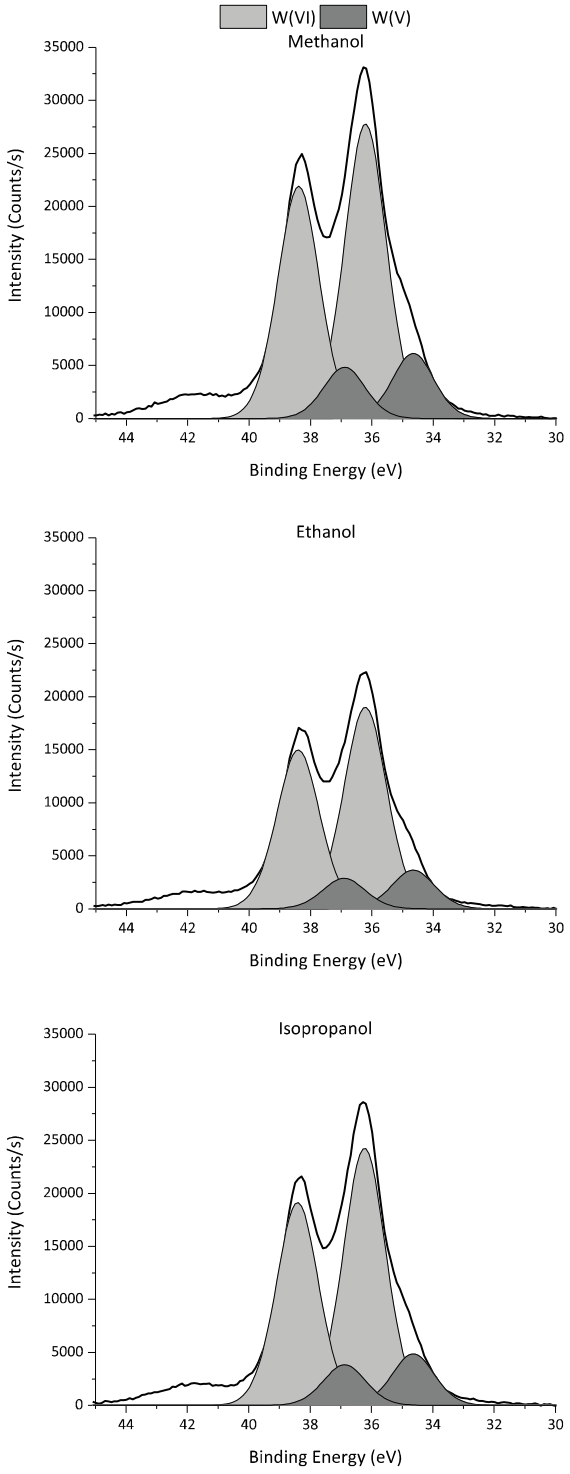

Figure 5.1: XPS data of the W4f signal for WO3 x deposited from different solvents and subject to a 150 °C post-deposition treatment.

The precursor dispersion was used to deposit a film which was also analysed (results in the Appendix). Interestingly, films deposited from the non-treated tungsten (V) ethoxide dispersion showed the same oxide composition and stoichiometry ($WO_{2.9}$). However, direct spin-coating from the precursor dispersion resulted in patchy, non-continuous films with the presence of very large residual white particles, visible by eye. Therefore, solvation in alcoholic solvent, while not fundamental in the conversion process from ethoxide to oxide, was still a key step needed to obtain a clear solution (rather than a dispersion) with all the advantages that that brings in terms of processability. Next, the C1s and O1s signals were analysed, with the results shown in Figure 5.2. The oxygen signal was mainly composed of the metal-oxide peak, with two shoulders on the high-energy side of the spectra. The higher shoulder peak can be assigned to

OH groups on the surface and to the substoichiometry of the films. The second shoulder was more difficult to identify, but ultimately it was assigned to OH groups resulting from ethoxide residues[223].

The carbon signal was very noisy, an indication of the low quantity of organic residue in the film. Apart from the aliphatic C-C bond, it showed two more signals. The one peaking at ~286.5 eV can be assigned to C-O single bonds. The other one, at higher binding energy, was much weaker; it was assigned to the carbon-oxygen single bonds in O-C-O, which can be formed by photo-oxidation of ethanol and ethoxide[224,225].

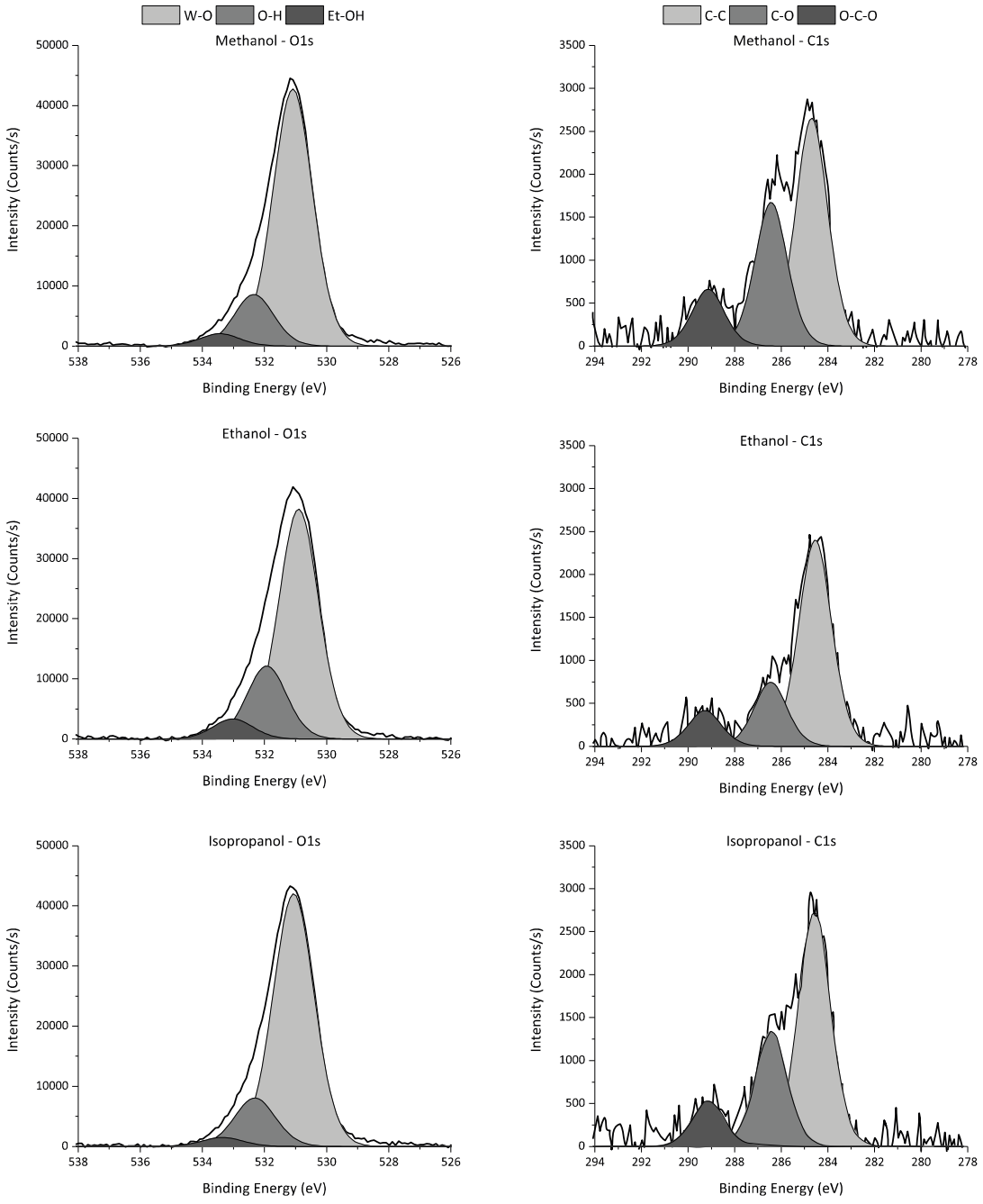

Figure 5.2: XPS spectra for the C1s (on the right) and the O1s (on the left) signal of WO_{3-x} films deposited from three different solvents and subject to a 150 °C post-deposition treatment.

Despite the presence of signals from the organic precursor, the intensity was very low, an indication that there was not much residuals left over. Analysis of films deposited directly from the precursor dispersion showed slightly higher amounts of carbon, especially for the C-O signal (Figure 5.3); nevertheless, the quantity was very small, confirming the suitability of ethoxide as an easily removed organic ligand in sol-gel routes to metal oxides synthesis.

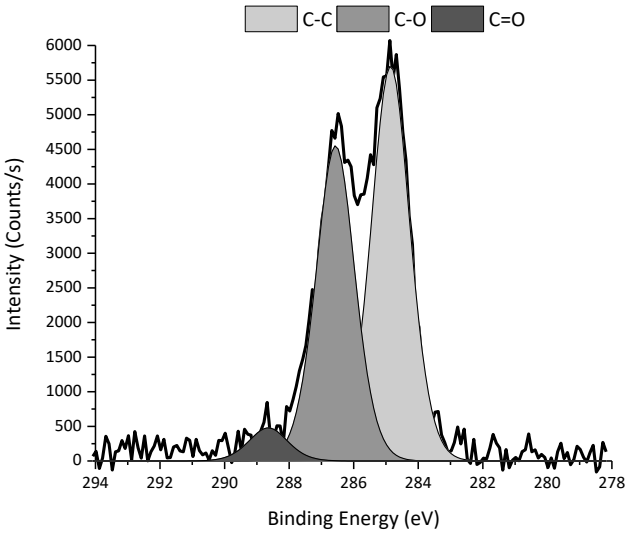

Figure 5.3: C1s signal from a film deposited by spin-coating of tungsten (V) ethoxide dispersion.

UV-Vis data was recorded for films deposited from isopropanol and subject to a 150 °C post-deposition treatment; different thicknesses were analysed, the same that were used in devices. The spectra (absorption, transmission, and reflection) are shown in Figure 5.4. The Tauc plot is shown only for the 13 nm film, as the very low α for the thinnest films resulted in a noisy curve from which no useful information could be extracted. At the thicknesses studied here, which were later implemented in devices, the material was very transparent over the visible range. It did not present any particular feature, such as the plasmonic absorption observed in MoO_{3-x}. The band gap was evaluated at 3.06 eV (Figure 5.4c), consistent with what is reported in the literature[73–75].

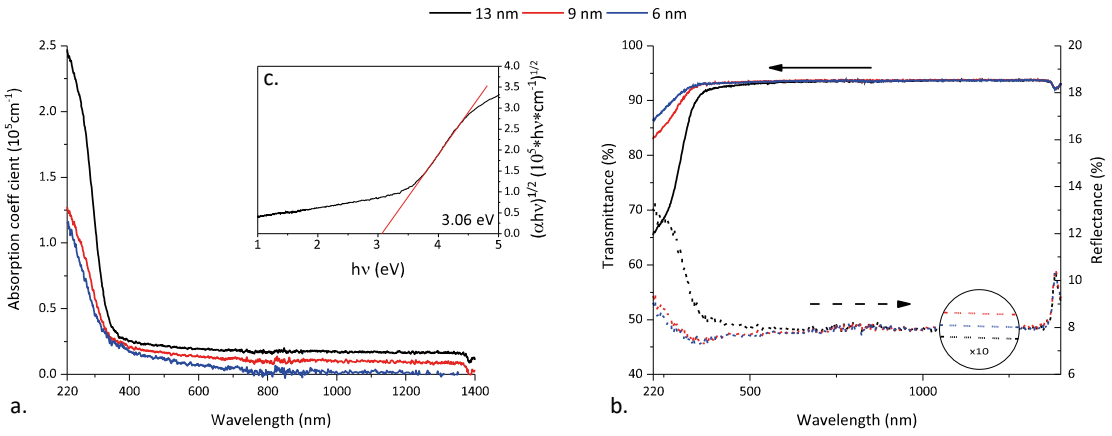

Figure 5.4: a. Absorption coefficient of WO_{3-x} films of different thickness. b. Transmission and reflection spectra for the same films are plotted. c. Tauc Plot for the 13 nm thick film.

After having evaluated composition and transparency of the interlayers, hybrid devices incorporating the WO_{3-x} films as HTL were fabricated. hyPV devices were fabricated first,

starting with the identification of the optimal WO_{3-x} thickness (Table 5.2). This was determined to be 9 nm; these films outperformed both thicker and thinner films in all the metrics apart from V_{oc}, which was constant for all of them. The FF especially was very interesting, because it showed that all films had excellent electrical properties. Having determined the best thickness, the next step was to compare the performances of WO_{3-x} films processed under different conditions: the results are shown in Table 5.1, together with those of devices incorporating PEDOT:PSS for comparison. Films deposited from methanol and treated at temperatures lower than 150 °C showed poor power conversion efficiencies. However, both V_{oc} and J_{sc} values were comparable with the other WO_{3-x} films; electrical losses were the cause of the loss in efficiency, as highlighted by the very low FF obtained from those devices. A post-deposition treatment at 150 °C dramatically improved things, with the FF going from 0.30 to 0.54 and the PCE overtaking that of devices incorporating PEDOT:PSS. It was observed in Figure 5.2 that the use of methanol as a solvent resulted in the highest amount of organic residue in the film, for films treated at 150 °C. It was therefore assumed that lower temperatures would result in a greater amount of organic impurities which were detrimental to the electrical behaviour of the devices.

Thickness	Measured parameter			
	V_{oc} (V, +/- 0.02)	J_{sc} (mA*cm^{-2}, +/- 0.05)	FF (+/- 0.01)	PCE (%, +/- 0.05)
13 nm	0.77	-8.18	0.55	3.43
9 nm	0.76	-8.72	0.60	3.95
6 nm	0.76	-8.53	0.57	3.65

Table 5.2: Results from hyPV devices incorporating WO_{3-x} films of different thickness as HTL. The films were deposited from isopropanol and subject to a 150 °C post-deposition treatment.

Sample		Measured parameter			
Solvent	Post-deposition treatment	V_{oc} (V, +/- 0.02)	J_{sc} (mA*cm^{-2}, +/- 0.05)	FF (+/- 0.01)	PCE (%, +/- 0.05)
PEDOT:PSS		0.73	-8.16	0.58	3.41
Methanol	V.A.S.R.	0.81	-8.05	0.30	1.94
	75 °C	0.80	-8.25	0.31	2.02
	150 °C	0.81	-8.49	0.54	3.67
Ethanol	V.A.S.R.	0.81	-8.72	0.58	4.01
	75 °C	0.82	-8.75	0.54	3.81
	150 °C	0.76	-8.26	0.56	3.45
Isopropanol	V.A.S.R.	0.84	-8.77	0.57	4.10
	75 °C	0.75	-8.26	0.59	3.62
	150 °C	0.76	-8.77	0.64	4.17

Table 5.1: Performance metrics of hyPV devices fabricated with different WO_{3-x} films as HTL. Also results from a PEDOT:PSS reference are shown.

Films deposited from either ethanol or isopropanol yielded high performing devices regardless of the post-deposition treatment the WO_{3-x} film was subject to. The worse performance,

obtained with films deposited from ethanol and subject to a 150 °C treatment, was still higher than the results achieved by PEDOT:PSS.

All films cast from ethanol and isopropanol showed high J_{sc} values, always higher than PEDOT:PSS. Fill factors were close to that of the reference, with one set of parameter delivering an excellent 0.64 which translated into a 4.17% PCE, 22% greater than the PEDOT:PSS devices. V_{oc} values are larger than PEDOT:PSS as well, with the highest being from films deposited from isopropanol and subject to a vacuum-assisted solvent removal step.

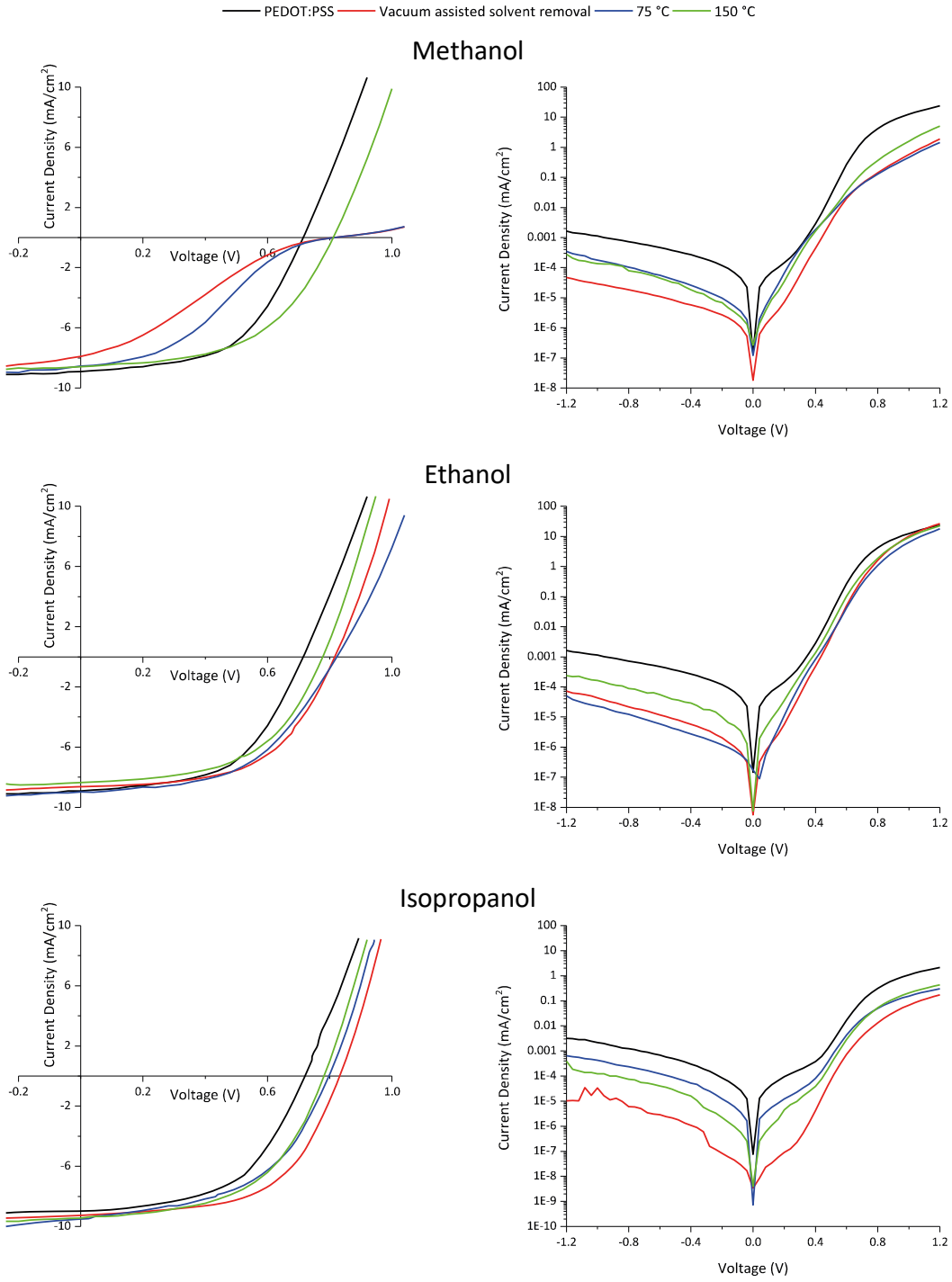

Figure 5.5: Representative J-V curves under light (left) and dark (right) for the devices in Table 5.1.

These films also showed the highest J_{sc} together with the champion films. They produced a 4.10% PCE, only slightly lower than the best performing set of parameters; this was caused by the lower fill factor, which albeit still very good at 0.57 was lower than the champion devices. This drop in fill factor could be due to the presence of an increased amount of residues; analysis of the characteristic resistances (listed in Table 5.3) seemed to support this as, while R_{sh} were the same for the two processing conditions, R_s was much lower for the films treated at 150 °C. This was a constant trend for the three different solvents, with the films treated at 150 °C always showing the lowest R_s of the set. A greater amount of impurities might result in an increased resistivity of the WO_{3-x} films, thus explaining the increase in the series resistance. Anyway, all the values apart from the first two in Table 5.3 were very good and close to PEDOT:PSS. Similarly, R_{sh} were excellent and mirrored the very high V_{oc} values observed. These two parameters together suggested that the energy level alignment at the interface was favourable and resulted in a minimal energy barrier to charge injection/extraction. The J-V plots are shown in Figure 5.5, under light and dark conditions. When tested under illumination, films deposited from methanol and treated at T<150 °C clearly showed the s-shape behaviour in the fourth quadrant typical of devices with high electrical losses, likely due to recombination of opposite carriers at the active layer/WO_{3-x} interface. Also, in dark conditions at positive biases (V>0.8 V) they showed lower currents than both PEDOT:PSS and films deposited from methanol but treated at 150 °C, a consequence of the very high R_s[40].

Sample		Measured parameter	
Solvent	Post-deposition treatment	R_{sh} (kΩ, +/- 1)	R_s (Ω, +/- 10)
PEDOT:PSS		17	380
Methanol	V.A.S.R.	8.0 (+/- 0.5)	8040
	75 °C	7.9 (+/- 0.5)	8180
	150 °C	20	500
Ethanol	V.A.S.R.	21	420
	75 °C	20	580
	150 °C	19	390
Isopropanol	V.A.S.R.	25	520
	75 °C	24	390
	150 °C	25	300

Table 5.3: Shunt and series resistances of the devices shown in Table 5.1.

Films deposited from the other two alcohols followed the trends highlighted in Table 5.1-Table 5.3. The plots under dark revealed the excellent electron blocking behaviour of WO_{3-x} films, whose reverse currents were 2 order of magnitudes lower than PEDOT:PSS-based devices. The slope of the dark curves in the region 0.5-0.8 V were similar to the reference, an indication that the recombination processes were analogous when PEDOT:PSS or WO_{3-x} films were used as HTL[37]. To understand and explain the excellent behaviour observed in solar cells, especially the high V_{oc} values, the injection behaviour of the ITO/WO_{3-x}/Active Layer junction was studied.

Single carrier (hole-only) devices were fabricated with either PEDOT:PSS or the champion WO_{3-x} film[nn] (Figure 5.6a).

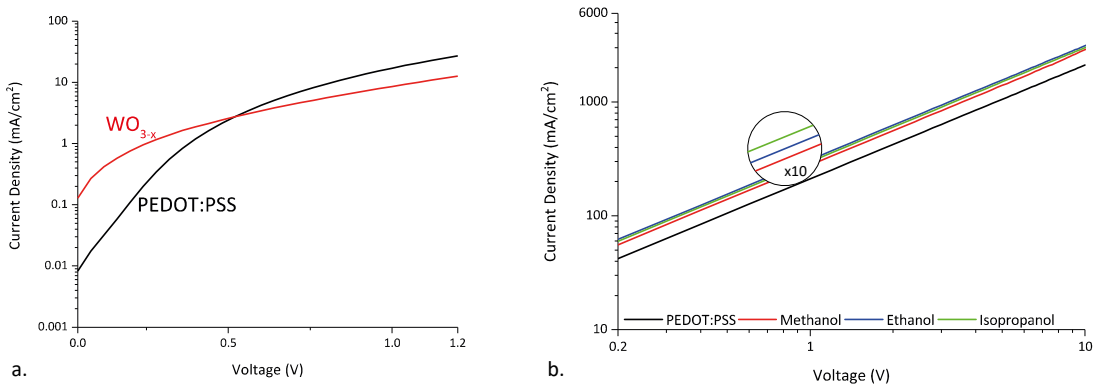

Figure 5.6: a. J-V plots of hole-only devices incorporating either PEDOT:PSS or the best performing WO_{3-x} film. b. J-V curves for 'sandwich' devices (ITO/HTL/Au, where HTL is either PEDOT:PSS or WO_{3-x} deposited from different solvents) in a log-log scale.

Current density values were higher for WO_{3-x} compared to PEDOT:PSS at low biases, while at V>0.5 V the two flipped with the PEDOT:PSS showing higher values. This was similar to what observed for V_2O_{5-x} and may help explain the poor performance recorded for hyLED (discussed later in this chapter).

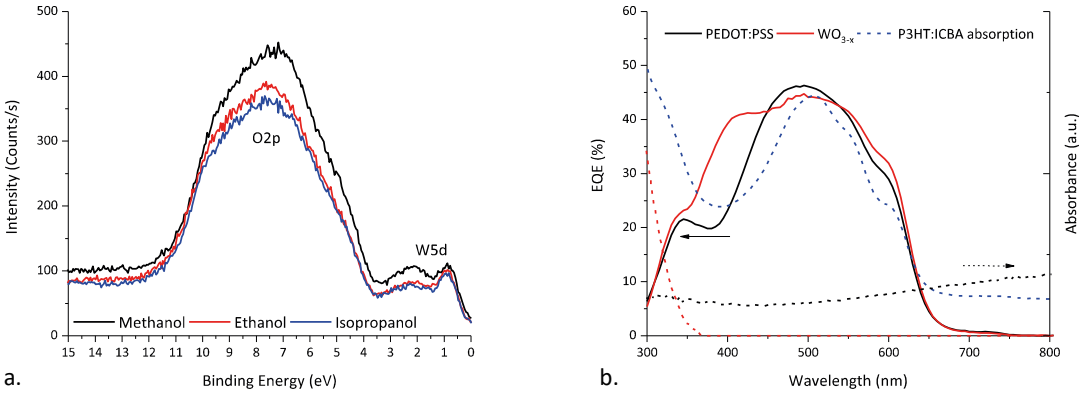

Figure 5.7: a. Valence band spectra for WO_{3-x} films deposited from different solvents. b. EQE spectra of the champion WO_{3-x} device and a PEDOT:PSS reference (also shown in dashed lines the absorption spectra of the two interlayers and of the P3HT:ICBA blend).

Charge transport across the ITO/HTL interface was probed as well, with the results shown in Figure 5.6b. Films deposited from different solvents all showed higher current density values than PEDOT:PSS. This, together with the high work function value expected from these films[73,74,173], was deemed to be the main factor in the recorded increase in V_{oc} with respect to PEDOT:PSS (it is worth noting that, similar to MoO_{3-x} and V_2O_{5-x}, it was impossible to determine the surface potential using Kelvin Probe because of sensitivity to air and moisture). The

[nn] Solvent: isopropanol. Post-deposition treatment: 150 °C

increased charge transport across the ITO/HTL/Active Layer junction was ascribed to intragap states induced by oxygen vacancies. This was similar to what observed for the other n-type oxides: hole injection/extraction was helped by the defect states formed by semi-occupied W5d orbitals, as seen in the valence band spectra of WO_{3-x} films deposited from different solvents (Figure 5.7a). Finally, the EQE spectrum of the champion WO_{3-x}-based device was measured and compared with that of a PEDOT:PSS-based reference device (Figure 5.7b). The combination of lower thickness and higher refractive index contribute to an optical spacing effect[33,195] which enhanced the photon to current conversion efficiency at low wavelengths. The integral of the WO_{3-x} curve was 6% greater than that of the PEDOT:PSS one, in excellent agreement with the data shown in Table 5.1. There were two windows of improvement over PEDOT:PSS, one between 350 and 450 nm and the other one between 540 and 660 nm. In the region between 450 and 540 nm the photocurrent was instead higher for the PEDOT:PSS device. The different contributions can be analysed individually:

a) 350-450 nm: the increase in photocurrent was 5% of the J_{sc} obtained with PEDOT:PSS;
b) 450-540 nm: the decrease in photocurrent was 1.3% of the J_{sc} obtained with PEDOT:PSS;
c) 540-660 nm: the increase in photocurrent was 2.5% of the J_{sc} obtained with PEDOT:PSS.

Therefore, by substituting PEDOT:PSS with a WO_{3-x} film a ~6% increase in J_{sc} was obtained.

hyLED devices were fabricated next. Similar to what observed with V_2O_{5-x}, despite the excellent behaviour in hyPV devices the WO_{3-x} films underperformed in light-emitting diodes. First, the optimal thickness of WO_{3-x} was identified at 6 nm (Table 5.4) using films deposited from isopropanol and subject to a 150 °C post-deposition treatment. It could be already observed that CE and L values were very low. Next, films deposited from different solvents and subject to three different post-deposition treatments were incorporated as HTL and their performances compared with those of PEDOT:PSS; the results are shown in Table 5.5. PEDOT:PSS clearly outperformed WO_{3-x} processed under all the different conditions. The best performing oxide HTL was obtained by depositing with methanol and processing at 75 °C, but even these devices had CE values less than half of PEDOT:PSS. Also, the luminance was very low, one order of magnitude less than the reference, and the current density was a quarter of that obtained with PEDOT:PSS. All other set of conditions yielded devices that were even less performing, with low luminances and current efficiencies. The current density values were at times higher than the reference, but only

Thickness	Max CE	L at max CE
	cd/A (+/ 0.02)	cd/m^2 (+/ 10)
13 nm	0.40	58
9 nm	0.80	103
6 nm	0.87	131

Table 5.4: Maximum CE and luminance at the maximum CE for hyLED incorporating WO3 x of different thicknesses.

because the values were recorded at very high biases. This poor show of performances was explained as non-radiative recombination processes induced by organic residues present at the interface. This was supported by the combined low luminance in hyLED and high performances in hyPV: recombination centres at the interface between the active layer and the HTL would be beneficial in solar cells because they prevent electrons from reaching the anode. However, being the recombination non-radiative, it would quench the luminance in light-emitting devices.

Sample		Measured parameter				
		Max CE	V at max CE	PE at max CE	L at max CE	J at max CE
Solvent	Post-deposition treatment	cd/A (+/- 0.02)	V (+/- 0.2)	lm/W (+/- 0.02)	cd/m² (+/- 10)	mA/cm² (+/- 0.05)
PEDOT:PSS Reference		5.57	6.2	2.80	1210	21.95
Methanol	V.A.S.R.	1.36	8.5	0.50	331	25.21
	75 °C	2.19	5.8	1.23	104	5.20
	150 °C	1.29	6.6	0.62	93	7.75
Ethanol	V.A.S.R.	0.94	10.0	0.30	239	26.32
	75 °C	0.04	12.8	0.01	24 (+/- 2)	54.60
	150 °C	1.06	6.2	0.59	69	6.94
Isopropanol	V.A.S.R.	0.73	7.8	0.30	191	26.20
	75 °C	0.85	10.0	0.26	776	89.97
	150 °C	0.64	7.3	0.27	73	11.06

Table 5.5: Performances of hyLED devices incorporating different WO_{3-x} films as HTL.

This was very similar to what observed with V_2O_{5-x}, where the cause of the low performances of hyLEDs was identified as defect states acting as recombination centres. With WO_{3-x} it was observed that a small amount of organic residues from the precursor was still present in the film, and the loss processes described were ascribed to these impurities. Interestingly, the hyPV performances obtained with V_2O_{5-x} were worse than those recorded with WO_{3-x}; on the contrary, hyLEDs results were better for V_2O_{5-x} than WO_{3-x}. It was therefore concluded that recombination processes were more efficient when caused by organic impurities rather than defect states. To conclude, the J-V-L plots were very noisy and did not add any useful information to the discussion, hence for the sake of clarity they were not shown here.

5.2 CoO_x

Cobalt oxide was synthesised from cobalt (III) acetylacetonate and a number of organic solvents (chlorobenzene, toluene and p-xylene); the precursor solution was spun in a fume hood. The films were subject to a post-deposition treatment at either 75 °C or 150 °C. Deposition was carried out in air because the absence of water or alcohol groups in the solvents required external sources of -OH groups for the hydrolysis of the precursor. In fact, deposition inside a glovebox did not seem to produce any usable film, with XPS analysis showing only the ITO signal from the substrate and a very low intensity contribution from cobalt. It is argued that the

absence of any source of oxygen or hydroxyl groups prevented oxide formation. Also, films deposited in air but subject to a vacuum assisted solvent removal step presented the same problems, therefore only the two temperature treatments stated above were selected.

XPS analysis was performed to understand the composition of the films. Because of the presence of the acetylacetonate ligand, analysis of the C1s signal becomes very important, unlike in the hydrogen bronze route where no organic ligands were present.

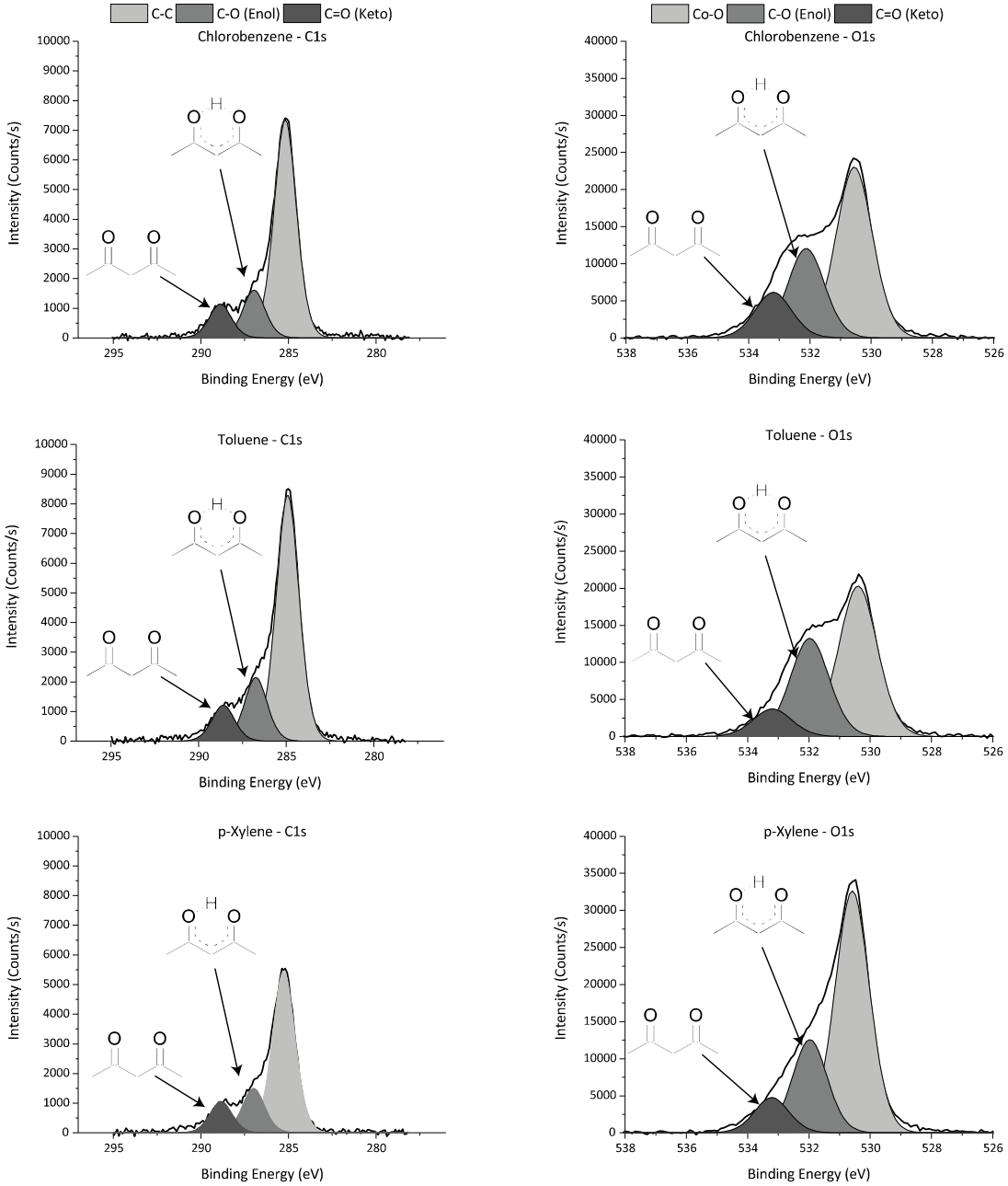

Figure 5.8: XPS spectra for the C1s (on the left) and the O1s (on the right) signal of CoO_x films deposited from three different organic solvents and subject to a 150 °C post-deposition treatment.

The C1s data is shown on the left column in Figure 5.8 for films deposited from different organic solvents and subject to a 150 °C post-deposition treatment. The main peak was ascribed to

aliphatic C-C bonds, due to both adventitious carbon impurities and C-C bonds in the acetylacetonate anion. The two peaks at higher binding energy were both ascribed to carbon-oxygen bonds: C-O centred at ~287 eV and C=O centred at ~288 eV. The presence of both signals is a consequence of the tautomerism of the acetylacetonate ion, which can be present in both the keto and the enol form. In toluene, the enol form is favoured ($K_{keto->enol}$ = 10)[226], possibly explaining the slightly stronger signal for this tautomer. The presence of the three C1s signals, albeit weak, was an indication that some residuals of the organic anion remained in the film. The signals were also stronger than those observed for WO_{3-x} films, suggesting that a greater quantity of residues was present here. This was confirmed by the O1s signals, shown on the right in Figure 5.8; again, both the keto and the enol signals were present, with higher intensity from the latter. The main peak was due to the metal-oxygen bond. The Co2p signal was also measured, with the data shown in Figure 5.9. The presence of satellite features due to electron correlation effects was an indication that Co(II) was present[91]; they were also a nuisance for the peak fitting process, therefore peak analysis was carried out only on the $^3/_2$ component of the Co2p signal.

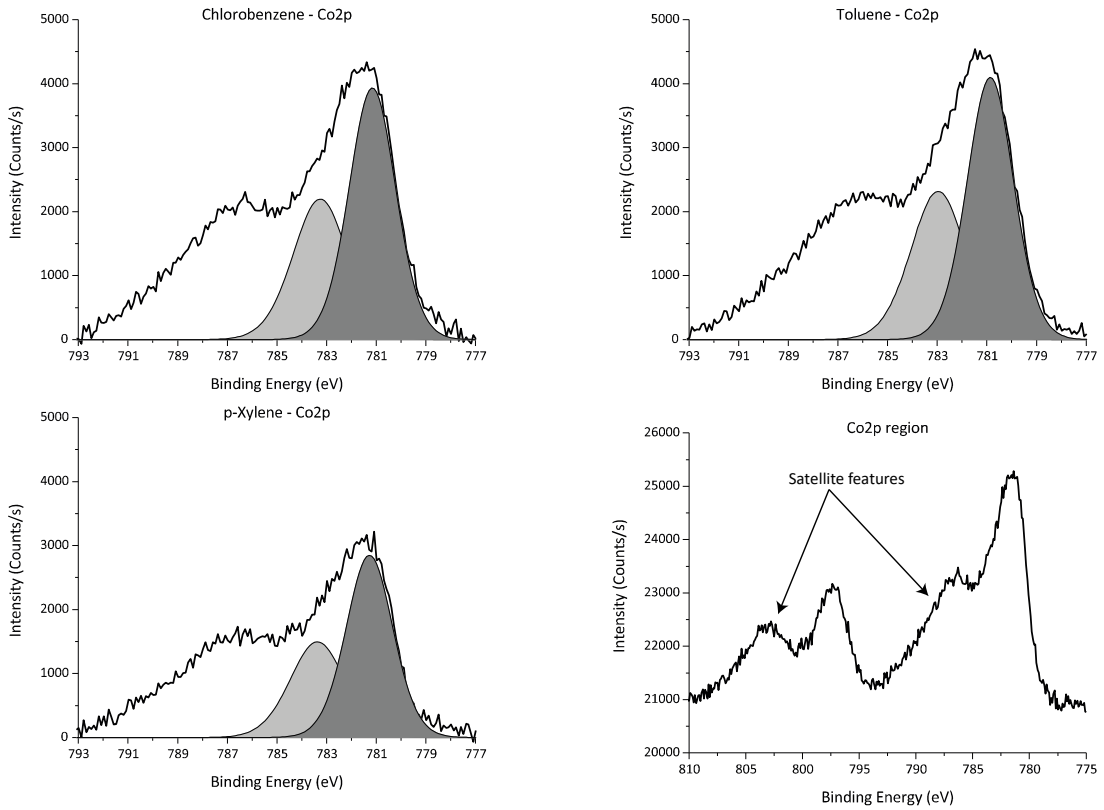

Figure 5.9: XPS spectra for the Co2p signal of CoO_x films deposited from three different organic solvents and subject to a 150 °C post-deposition treatment (satellite feature not fitted).

Correlation effects and substoichiometry were responsible for the presence of two separate peaks[76], shown in different shades of grey in Figure 5.9. The intensity of the signal was rather

low, as opposed to that obtained from oxygen; moreover, the survey spectra showed peaks from indium and tin (results in the Appendix, Figure 6.6) : these were indications that the films were possibly extremely thin and non-homogeneous.

The cobalt signal was not attributed to the precursor (Co(III) acetylacetonate), but entirely to the cobalt (II) oxide: the presence of cobalt in the form of the precursor was ruled out because Co(III) does not present the satellite features observed in the Co2p signal[226]. It was therefore concluded that, despite some organic impurities remaining from the acetylacetonate ligand, the films were composed of CoO_x. The presence of organic residues, while undesired, might however not be detrimental on devices' performance; for instance, beneficial effects were observed for sol-gel synthesised ZnO thin films with aminic residues from the precursor solution[227] when they were used as ETL in hyPV devices. It was therefore decided to keep the post-deposition temperatures below 150 °C instead of employing higher temperatures to try and completely remove the organic ligands.

Next, the optical properties of the films were analysed with UV-Vis spectroscopy measurements; the results are shown in Figure 5.10. The weak absorption, together with the very low thickness, affected the measurements: the data obtained was very noisy, especially when used to calculate the absorption coefficient and subsquently the optical band gap from the Tauc plot.

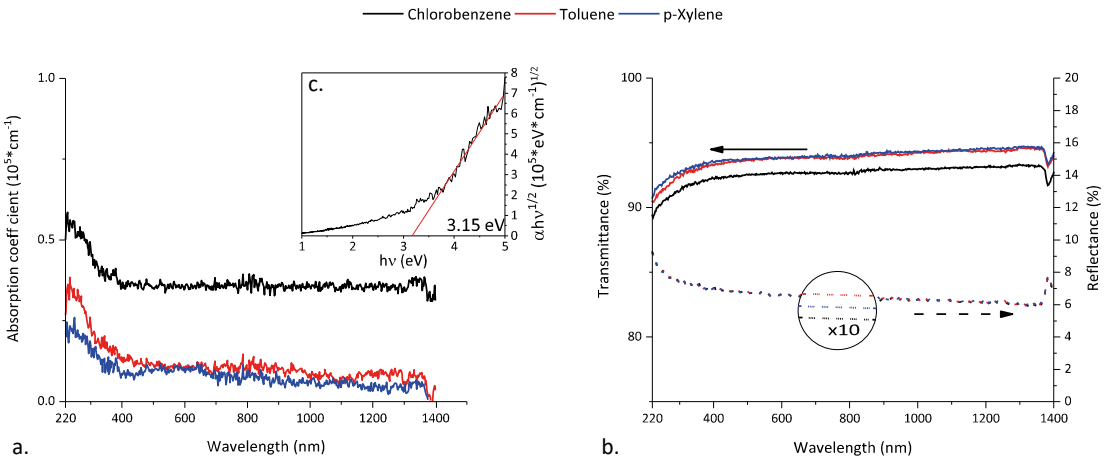

Figure 5.10: a. Absorption coefficient of CoO_x films deposited from different solvents and subject to a 150 °C post-deposition treatment. b. Transmission and reflection spectra for the same films. c. Tauc plot for the film cast from chlorobenzene.

The gap value obtained (3.15 eV) is much higher than the commonly reported value of 2.4 eV[14,76]: this was likely an artefact due to the low signal-to-noise ratio. Quantum confinement effects were ruled out because of the very high deviation from the literature observed. Nevertheless, from the transmission and reflection data it was observed that the films were highly transparent, a desired feature for anode interlayers in standard architecture devices.

Measurements of film thicknesses were more challenging than for MoO_{3-x} and V_2O_{5-x} films. Also, there seemed to be a variation with the different solvents and the XPS analysis showed the possible non-homogeneity of the films. Therefore, it was decided to analyse combinations of different spin speeds and post-deposition temperatures to account for the problems encountered in thickness determination. Three spin speeds were selected (2000, 4000, and 6000 rpm) and two post-deposition treatments (75 °C and 150 °C). hyLED devices were fabricated first, but the incorporation of CoO_x as anode interlayer did not result in viable devices. No parameters had a maximum current efficiency greater than 1 cd/A and all of them had their maximum CE at very high voltages, around 14 V. It was again speculated that organic residues acting as non-radiative recombination centres had hindered the hyLED performances, as observed for WO_{3-x}. The higher amount of organic residues in the CoO_x films was likely responsible for the complete failure of light-emitting devices as opposed to the low performances obtained with WO_{3-x}. A trend can be identified among the oxides that did not deliver good results in hyLEDs: V_2O_{5-x} performed slightly better than WO_{3-x}, which in return performed better than CoO_x. The former lacked presence of organic residues, with the recombination processes ascribed to defect states. On the other hand, there were organic impurities on the other two, more so in CoO_x films. It was concluded that, as speculated before for WO_{3-x}, organic residues provide a more efficient non-radiative recombination pathway, and that a relatively large amount of impurities would be enough to prevent the light emission process almost completely.

hyPV devices were then analysed, with improved results. The different performance metrics were divided in three tables for clarity; each table shows devices incorporating CoO_x deposited from a different solvent. All devices were compared with a reference incorporating PEDOT:PSS. Results for CoO_x deposited from chlorobenzene are shown in Table 5.6; films subject to a 75 °C post-deposition treatment resulted in poorly performing devices, with all metrics lower than the reference device. There was an improving trend with increasing spin speed, with thinner films performing slightly better, albeit still to an unsatisfactory level. Also, films treated at 150 °C showed much better performances. The lower post-deposition temperature might result in a greater number of organic residues on the films, which could be affecting the devices' performances. Thinner films would have less residues, resulting in the small increases observed. However, XPS analysis of films treated at different temperatures did not show any particular difference in the carbon content of the films: when all three C1s peaks were considered, the atomic percent ratio between the film treated at 75 °C and the one treated at 150 °C was 50.3:49.7, basically 1:1. When only the keto-enol signals were considered, it increased to

52.1:47.9, still very small and likely not enough to justify the large drop in performances observed. Treating the films at 150 °C improved the performances, with the best film (spun at 4000 rpm) reaching 3.00% PCE. This was still lower than the reference device: while FF and J_{sc} were comparable with the reference, as were the two characteristic resistances, there was a drop in V_{oc} affecting the PCE value. Thinner films showed a similar drop, while simultaneously losing on J_{sc}.

Chlorobenzene		Measured parameter					
Spin Speed	Post-deposition treatment	V_{oc} (V, +/- 0.02)	J_{sc} (mA*cm^{-2}, +/- 0.05)	FF (+/- 0.01)	PCE (%, +/- 0.05)	R_{sh} (kΩ, +/- 1)	R_s (Ω, +/- 10)
PEDOT:PSS		0.73	-8.16	0.58	3.41	17	380
2000	75 °C	0.31	-4.13	0.27	0.33	1.5 (+/- 0.2)	1400
4000		0.49	-6.89	0.38	1.28	3.5 (+/- 0.2)	770
6000		0.58	-7.41	0.45	1.90	6.5 (+/- 0.2)	690
2000	150 °C	0.63	-7.25	0.49	2.24	9.5	590
4000		0.69	-8.11	0.55	3.00	14	450
6000		0.68	-7.55	0.54	2.73	14	470

Table 5.6: Performance metrics of hyPV devices incorporating CoO_x films deposited from chlorobenzene.

Using toluene as a solvent resulted in some improvements (results in Table 5.7): the V_{oc} values remained lower than the reference, albeit closer to it than chlorobenzene-based devices. Both post-deposition treatments resulted in viable devices, with only the thickest film treated at 75 °C showing high electrical losses. These were observed in the simultaneous decrease in R_{sh} and increase in R_s, which combined in a very low fill factor. All devices showed J_{sc} value comparable with the reference, with the champion one showing a 7% increase which, coupled with a good FF of 55%, produced a PCE of 3.38%, extremely close to the 3.41% value observed for the reference. This device incorporated a CoO_x film spun at 2000 rpm and subject to a 150 °C post-deposition treatment.

Toluene		Measured parameter					
Spin Speed	Post-deposition treatment	V_{oc} (V, +/- 0.02)	J_{sc} (mA*cm^{-2}, +/- 0.05)	FF (+/- 0.01)	PCE (%, +/- 0.05)	R_{sh} (kΩ, +/- 1)	R_s (Ω, +/- 10)
PEDOT:PSS		0.73	-8.16	0.58	3.41	17	380
2000	75 °C	0.61	-7.61	0.40	1.84	5.7 (+/- 0.2)	830
4000		0.69	-8.07	0.53	2.92	12	510
6000		0.71	-7.96	0.54	3.00	13	470
2000	150 °C	0.71	-8.76	0.55	3.38	14	430
4000		0.70	-8.15	0.52	2.95	12	550
6000		0.70	-8.38	0.55	3.19	12	420

Table 5.7: Performance metrics of hyPV devices incorporating CoO_x films deposited from Toluene.

Finally, devices were fabricated using p-xylene as the CoO_x solvent (results in Table 5.8). As for toluene, all conditions resulted in working devices; in fact, all metrics were very similar, resulting

in only a 9% PCE difference between the best and worst performing interlayer. Fill factors were slightly lower than devices fabricated using toluene, mirroring the trends observed with R_{sh} and R_s, while J_{sc} values were similar between p-xylene and toluene and higher than chlorobenzene devices. The main difference was in the V_{oc}, which was higher than both other solvents and PEDOT:PSS for all thicknesses and post-deposition treatments.

p-Xylene		Measured parameter					
Spin Speed	**Post-deposition treatment**	**V_{oc} (V, +/- 0.02)**	**J_{sc} (mA*cm^{-2}, +/- 0.05)**	**FF (+/- 0.01)**	**PCE (%, +/- 0.05)**	**R_{sh} (kΩ, +/ 1)**	**R_s (Ω, +/- 10)**
PEDOT:PSS		0.73	-8.16	0.58	3.41	17	380
2000	75 °C	0.76	-7.89	0.49	2.85	9.7 (+/- 0.2)	600
4000		0.74	-8.49	0.50	3.13	9.8 (+/- 0.2)	510
6000		0.75	-8.03	0.50	2.98	10.2 (+/- 0.2)	560
2000	150 °C	0.75	-8.13	0.50	3.01	12	620
4000		0.74	-8.22	0.53	3.16	12	540
6000		0.74	-8.38	0.52	3.14	12	540

Table 5.8: Performance metrics of hyPV devices incorporating CoOx films deposited from p-xylene.

The resulting PCE were higher than those obtained using chlorobenzene, with the best one only 8% smaller than the reference. Even though none of the devices were close to the best ones obtained with toluene, the small variation observed between the different set of conditions suggested that the use of p-xylene may be beneficial in terms of reproducibility and sensibility to the processing, and be able to reduce the batch-to-batch variations observed in organic devices.

The J-V curves under light and dark for the best performing device for each solvent and a PEDOT:PSS reference cell are shown in Figure 5.11.

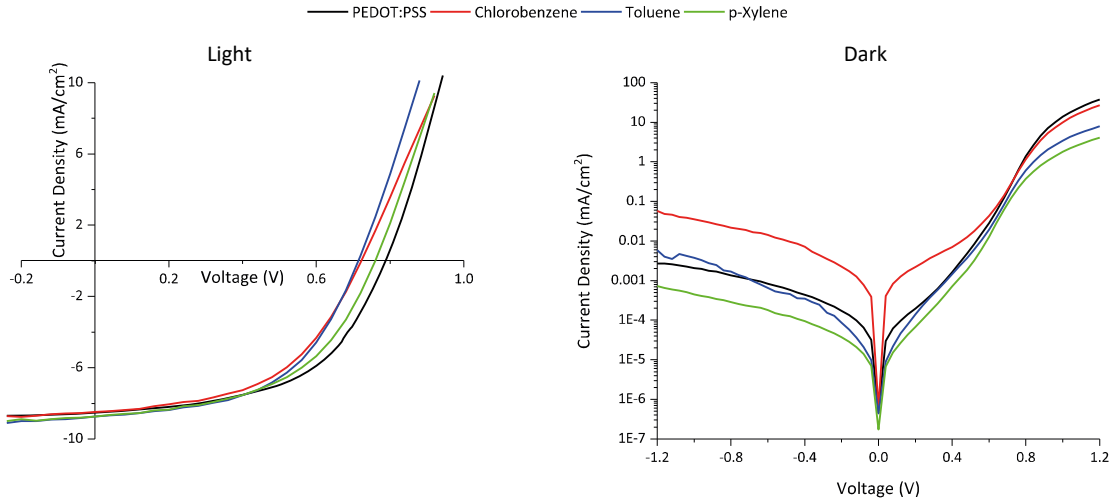

Figure 5.11: J-V curves under light and dark of the best performing device from each solvent and a PEDOT:PSS-based one.

The curves under illumination followed the trends observed in the performance metrics shown in Table 5.6, Table 5.7,Table 5.8. The reverse currents under dark suggested that the electron blocking behaviour for both toluene and p-xylene were excellent, with p-xylene devices showing reverse current almost one order of magnitude lower than PEDOT:PSS. Even the chlorobenzene devices, despite performing worse than both PEDOT:PSS and the other two solvents, displayed the electrical characteristic typical of a diode.

To better understand the behaviour observed in devices, a few analyses were carried out. First, Kelvin Probe measurements were performed on films deposited from different solvents and subject to either a 75 °C or a 150 °C post-deposition treatment. It was observed that films treated at lower temperature had a measured work function of 4.7 eV, while for films treated at 150 °C the value was 4.8 eV, regardless of the solvent used. The very similar values were consistent with the trend observed in toluene and p-xylene devices, where post-deposition temperature did not seem to have any effect on the V_{oc}. The measured value was lower than that of PEDOT:PSS, which explained the lower V_{oc} observed when toluene was used. The recorded increase with p-xylene can probably be ascribed to enhanced charge extraction and favourable morphology. The very low V_{oc} values observed when chlorobenzene was used, on the contrary, can be explained by a combination of poor energy level alignment at the interface (caused by the low work function) and possibly poor coverage by the CoO_x film, which may have resulted in the very low values observed for films treated at 75 °C and the thickest film treated at 150 °C. Charge injection/extraction from the ITO into the CoO_x films was probed by fabricating sandwich (ITO/HTL/Au) devices; the results are shown in Figure 5.12a, together with a PEDOT:PSS reference. The CoO_x films used were the best performing ones for each solvent.

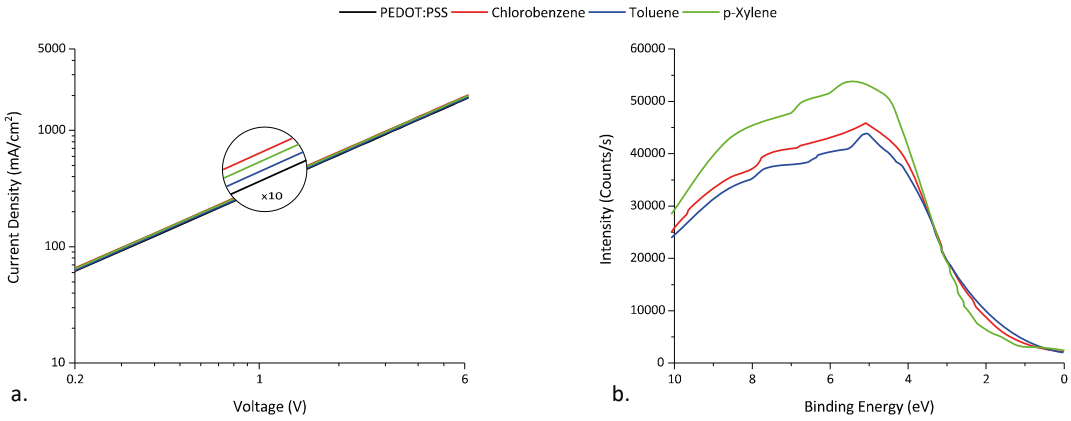

Figure 5.12: a. Sandwich devices (ITO/HTL/Au) fabricated using PEDOT:PSS or CoO_x deposited from different solvents. b. Valence band spectra of CoO_x films deposited from different solvents.

They all presented similar current densities when compared with each other and with PEDOT:PSS, suggesting that charge transport across the ITO/CoO_x interface was not the limiting

step in devices' performance. The valence band spectra for the same CoO_x films was also measured, to understand whether intragap states were present and responsible for the good charge transport between either the ITO and the HTL or the HTL and the active layer (Figure 5.12b). It is worth remembering that in oxides such as CoO and Co_3O_4, metal vacancies are responsible for the semiconducting behaviour (p-type). Unlike MoO_{3-x}, V_2O_{5-x}, and WO_{3-x}, however, CoO_x films did not have defects states within the band gap that could enhance charge transport. This, together with the non-ideal work function (i.e. less than 5 eV) could explain the poor electrical behaviour of these devices, especially the low V_{oc} and fill factor.

Finally, the best performing CoO_x film overall was compared with PEDOT:PSS with EQE and hole injection into the active layer. CoO_x deposited from toluene at 2000 rpm and treated at 150 °C was chosen because, in addition to having the highest PCE among the oxide HTLs, it also had the highest J_{sc}. Both EQE and single carrier device data are shown in Figure 5.13. The EQE spectrum for the device incorporating CoO_x presented a widened window of activity, similar to that observed for MoO_{3-x} and V_2O_{5-x}, with the extra contribution between 370 and 460 nm worth 2% of the J_{sc} obtained with PEDOT:PSS. As before, this improvement at lower wavelengths can be ascribed to the combined effect of low thickness and high refractive index, which redistributed the light intensity across the device[33,195]. The integral of the CoO_x curve was larger than that of the PEDOT:PSS device, by an amount similar to the increase observed in J_{sc}.

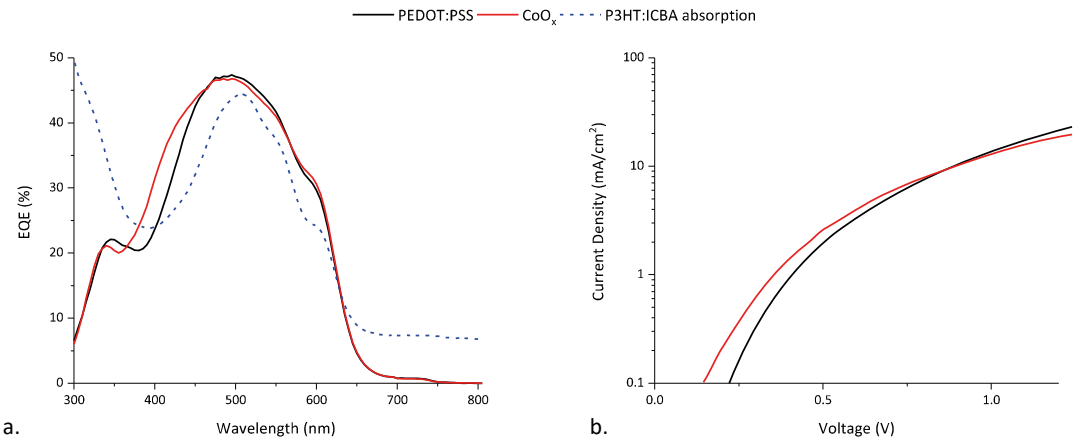

Figure 5.13: a. EQE data of devices incorporating either PEDOT:PSS or the champion CoO_x film as HTL. b. Hole-only device data from the same devices.

Single carrier devices showed that at low voltages CoO_x extracted charges more efficiently than PEDOT:PSS, but this changed at voltages higher than the V_{oc}, where the hole current in PEDOT:PSS- based devices became higher. However, these differences between the PEDOT:PSS and the CoO_x devices were very small at both low and high biases, suggesting that charge extraction efficiency was not a major issue influencing the solar cells' behaviour.

5.3 CONCLUSIONS

In this chapter, WO_{3-x} and CoO_x were synthesised from organometallic precursors and incorporated in optoelectronic devices. Unlike what observed when metallic precursors were used (for MoO_{3-x} and V_2O_{5-x}), organic residues were present on the oxide films after different low temperature post-deposition treatments. All films were nevertheless mainly composed of the oxide and transparent in the visible range. WO_{3-x} films performed exceptionally well in hyPV devices, achieving as much as a 22% increase in PCE over devices incorporating PEDOT:PSS. Improvements were all over the chart, with enhancements in J_{sc}, V_{oc} and fill factors. Optical spacing caused by WO_{3-x} films was the main cause of the increased photocurrent, while enhanced carrier extraction across the interfaces favoured the V_{oc} and lowered electrical losses. It was found that little amounts of organic impurities improved the behaviour of the HTL, and especially its electron blocking properties, by acting as recombination centres for electrons moving towards the anode. However, this was also the cause of the very low performances observed in hyLEDs, whose efficiencies were very underwhelming. It was speculated that these recombination centres quenched the luminance of hyLED devices because the recombination processes were non-radiative. Of all the systems analysed in this work, WO_{3-x} resulted in the best performing hyPV values, and it is therefore the best candidate to replace PEDOT:PSS in this kind of devices. On the contrary, if hyLEDs are the target, more work is needed to understand if the processing route can be adjusted to remove the organic impurities affecting the light-emitting performances. For instance, a solvent rinse of the deposited oxide film could help remove superficial residues. Also, higher temperatures could be employed for post-deposition treatments; this was however beyond the scope of this work, as the main purpose was to keep processing temperatures below 150 °C. Similarly, WO_{3-x}, CoO_x did not deliver viable hyLEDs; it was observed that more organic residues were present on these films as compared to WO_{3-x} films. Therefore, the depletion of luminance was higher, effectively preventing the hyLEDs from working. Similarly, the presence of a large quantity of impurities also affected hyPV devices. Albeit working devices were fabricated using CoO_x films as HTL, their performances did not quite match those of the PEDOT:PSS reference. Impurities especially influenced the V_{oc}, together with a lower work function than PEDOT:PSS (4.7-4.8 eV versus 5.1-5.2 eV). Nevertheless, a few set of parameters resulted in efficiencies close to that of the reference, with CoO_x films cast from toluene and subject to a 150 °C post-deposition treatment reaching PCE values of 3.38% (PEDOT:PSS devices at 3.41%). Even though the results from the reference could not be surpassed, the synthesis route could prove useful in situations where normal alcoholic solvents cannot be used and there is the need to employ different solvent systems.

6 CONCLUSIONS AND FURTHER WORK

Organic semiconductors can be combined with transition metal oxides to fabricate hybrid organic:inorganic photovoltaic and light-emitting devices (hyPVs and hyLEDs). The advantages of organic materials (possibility of solution processing/printing, low-cost, semi-transparency) are complemented by the superior stability and lifetime that the presence of inorganic materials provides (acting as oxygen/moisture barrier, for instance). To fully exploit all the benefits of these devices, the inorganic components must be solution processable and not require high temperature post-deposition treatments. Various routes have been explored to deposit transition metal oxides films while satisfying these requirements; a summary of the various processes was provided in Chapter 1, while more comprehensive reports can be found in the various literature reviews published over the years [47,61,75,98,228]. Usually, the focus of the research in this topic is the discovery of novel recipes or the optimisation of existing ones using additives and modifiers. Instead, the effects of different solvents on a particular recipe are seldom investigated. This work aimed at filling that knowledge gap by understanding the effect of solvo-thermal processing conditions on the performances of optoelectronic devices.

Conclusions

In Chapter 3, different metal oxides (MoO_{3-x}, V_2O_{5-x}) were deposited using a solution-based method that did not involve organometallic precursors, instead starting from a powder of the metal of interest. Using organic-free precursors simplifies the study of the effects of the processing conditions on the properties of the oxide films. It was shown how device performances are strongly influenced by the choice of solvent and post-deposition treatments carried out on the TMOs interlayers. While a few reports do compare films subject to different temperature treatments when exploring new routes, the choice of solvent is usually arbitrary; moreover, it is commonly assumed that similar solvents (like methanol/ethanol/isopropanol in this work) are interchangeable and do not influence the properties of the deposited films (examples of this can be found in refs. [134,145]). This work demonstrated that a complete assessment of the suitability of a wet-chemistry route cannot be performed without investigating different solvo-thermal conditions. For instance, it was shown that, by simply changing the solvent from isopropanol to methanol in the processing of MoO_{3-x} films, hyPV devices efficiency improved from 2.91% to 3.50% when the oxide was annealed at 150 °C. Additionally, when films cast from methanol were subject to a vacuum assisted solvent removal step instead of thermal annealing, the efficiency was further increased from 3.50% to 3.91%, which was 10% higher than the efficiency recorded using PEDOT:PSS. The same behaviour was

observed in hyLED devices, albeit with different solvo-thermal conditions. V_2O_{5-x} films showed the same dependence on processing parameters, with the additional interesting note that champion devices were obtained with solvo-thermal conditions different from those used in MoO_{3-x}. This dependence of device performance on the HTL processing condition was also recorded when the oxides films were synthesised from organometallic precursors, as seen in Chapter 5. The situation is complicated by the presence of residual organic impurities on the films, due to the low-temperature nature of the post-deposition treatments. Nevertheless, for both WO_{3-x} and CoO_x the solvo-thermal processing conditions influenced greatly the performances of the devices.

The comparison between the different oxides in Chapter 3 and 5 also highlighted another interesting point: the effect of organic impurities on the behaviour of the interlayer. The benefits provided by the presence of organics within an oxide-based charge transport layer had already been observed in a similar work involving electron transport layers[227]. Here, the evolution of device performances with an increasing amount of organic impurities was further clarified. To begin with, MoO_{3-x} deposited from a carbon-free precursor performed well in both hyPV and hyLED devices; XPS analysis of the C1s signal from these films showed that only adventitious carbon was present. WO_{3-x}, on the other hand, was processed form an alkoxide precursor, which left some organic residue after deposition and post-deposition treatment. These films performed exceptionally well in hyPV devices, showing simultaneous enhancements in both extraction of holes and blocking of electrons. This was ascribed to the presence of the organic impurities, which acted as charge recombination centres for electrons moving towards the anode. This was also supported by the poor performance obtained in hyLED, because of the non-radiative exciton recombination favoured by these impurities. Finally, CoO_x films deposited from an organometallic precursor presented the largest amount of impurities after deposition. This was found to be detrimental for both hyPV and hyLED. Therefore, it was concluded that the presence of organic residue, while not always undesirable for devices performances, must be carefully controlled in order to exploit its beneficial effects while at the same time mitigating the negative ones.

In both Chapter 3 and 5, the possibility of substituting PEDOT:PSS with transition metal oxides films was explored successfully. Champion devices incorporating TMOs showed efficiency improvements of 22% (hyPV[oo]) and 24% (hyLED[pp]) over PEDOT:PSS based references. However,

[oo] WO_{3-x} film cast from isopropanol and subject to a 150 °C post-deposition treatment.
[pp] MoO_{3-x} film cast from methanol and subject to a 75 °C post-deposition treatment.

the very low thickness at which oxide-based HTL must be deposited could be counterproductive, for example when very rough substrates must be used. For cases like this, PEDOT:PSS still remains the best candidate as HTL. The possibility of tuning the properties of PEDOT:PSS by blending it with a TMO such as MoO_{3-x} was investigated in Chapter 4. Hybrid PEDOT:PSS/MoO_{3-x} films were easily obtained by a two-step process: first, the precursors solutions of the two components were mixed in different volume ratios; after mixing, the resulting solution was spin-coated to deposit hybrid films. As opposed to what reported elsewhere for similar blends[205], the hybrid films obtained in this work were very smooth and the MoO_{3-x} well dispersed within the PEDOT:PSS matrix, resulting in uniform films. The presence of the oxide influenced some of the properties of PEDOT:PSS, such as its refractive index, the wetting of the active layer solution, and the valence band spectra (through the insertion of intragap defect states). These enhancements resulted in efficiency improvements of 10% (in hyPV) and 23% (in hyLED).

Further Work

Further work building up on the findings presented here can be broadly classified in terms of the timescale over which it could be carried out. The following applies to both TMOs interlayers and to TMO-modified PEDOT:PSS.

Immediate work would involve further characterisation of TMOs films and devices. For instance, ultraviolet photoemission spectroscopy (UPS) analysis could be performed to study the energy level alignment at the oxide/organic interface. Transient photovoltage and transient photocurrent measurements could be used to understand the processes at the core of the efficiency improvements observed when TMOs are used instead of PEDOT:PSS. At the same time, preliminary studies on stability and lifetime of oxide-based devices could be carried out, as an increase in both parameters over PEDOT:PSS-based devices is expected.

Fabrication of inverted-architecture devices would be the natural next step. This would start with a study on the wetting of the active layer by the oxide precursor solutions. Some preliminary work on this is shown in Appendix D. It is important to bear in mind that solution processing of TMOs interlayers on top of the device is likely to have an influence on the organic active layer materials underneath. Therefore, it would be paramount to confirm that the deposition of TMOs does not degrade the underlying active layer. Examples of possible techniques to employ for this are optical (e.g. UV-Vis) and morphological characterisation (e.g. using X-Ray diffraction) before and after TMO deposition; also, XPS and Secondary Ion Mass Spectroscopy (SIMS) could help in understanding whether the oxide infiltrates the active layer,

while cross-sectional electron microscopy[qq] could shed some light on the nature and structure of the interface between the organic and the oxide. This would then be followed by a systematic investigation into the effects of the different solvo-thermal conditions on the performances of devices, similar to the work presented here.

In the long run, two main paths can be followed. Research could focus on finding other wet-chemistry methods for TMOs deposition, and works similar to this one could be carried out with a variety of solution-based routes. For each of them, the combined effects of solvent and post-deposition treatments on devices performances could be assessed, ultimately building up a toolkit of hole transporting layers whose behaviour in devices can be tuned by adjusting the solvo-thermal processing conditions. In the case of TMO-modified PEDOT:PSS, different oxides can be considered for blending with PEDOT:PSS, mirroring the work presented in Chapter 4.

On the other hand, the present work could be brought even more forward by beginning to explore the possibility of fabricating large-area devices. This would include adjustments on the precursor solutions to allow for inkjet printing of the interlayers, while at the same time optimising the performances of devices on larger substrates. This would be followed by a study on different, possibly flexible, substrates, and would ultimately lead to the fabrication of printed, large area solar modules for household and industrial applications.

[qq] Both Scanning Electron Microscopy (SEM) and Transmission Electron Microscopy (TEM)

REFERENCES

1. Shirakawa, H., Louis, E. J., MacDiarmid, A. G., Chiang, C. K. & Heeger, A. J. Synthesis of electrically conducting organic polymers: halogen derivatives of polyacetylene, $(CH)_x$. *J. Chem. Soc. Chem. Commun.* 578 (1977). doi:10.1039/c39770000578
2. The Nobel Prize in Chemistry 2000. *Nobel Media AB 2014* Available at: http://www.nobelprize.org/nobel_prizes/chemistry/laureates/2000/. (Accessed: 21st June 2015)
3. Tang, C. W. Two-layer organic photovoltaic cell. *Appl. Phys. Lett.* **48,** 183 (1986).
4. Tang, C. W. & VanSlyke, S. A. Organic electroluminescent diodes. *Appl. Phys. Lett.* **51,** 913 (1987).
5. Burroughes, J. H. *et al.* Light-emitting diodes based on conjugated polymers. *Nature* **347,** 539–541 (1990).
6. Samsung OLED TV - You Won't Believe Your Eyes. Available at: http://www.samsung.com/us/oled-tv/#home. (Accessed: 21st June 2015)
7. OLED Display: The Ultimate TV Display | LG USA. Available at: http://www.lg.com/us/experience-tvs/oled-tv/oled-display. (Accessed: 21st June 2015)
8. Sharp: OLED Displays. Available at: http://www.sharpmicro.com/Page.aspx/americas/en/b3fad008-bf63-4e66-ab68-7a52cae8fa1e/OLED_Displays/. (Accessed: 21st June 2015)
9. Geoghegan, M. & Hadziioannou, G. *Polymer Electronics*. (OUP Oxford, 2013).
10. Augustin McEvoy, L. C. and T. M. (Eds. . *Solar Cells. Materials, Manufacture and Operation*. (Elsevier, 2012).
11. Nelson, J. Polymer: Fullerene bulk heterojunction solar cells. *Mater. Today* **14,** 462–470 (2011).
12. Janssen, R. A. J. & Nelson, J. Factors limiting device efficiency in organic photovoltaics. *Advanced Materials* **25,** 1847–1858 (2013).
13. Brabec, C. J., Dyakonov, V., Parisi, J. & Sariciftci, N. S. *Organic photovoltaics : concepts and realization*. (Spring, 2010).
14. Greiner, M. T. *et al.* Universal energy-level alignment of molecules on metal oxides. *Nat. Mater.* **11,** 76–81 (2011).
15. Granstrom, M. *et al.* Laminated fabrication of polymeric photovoltaic diodes. *Nature* **395,** 257–260 (1998).
16. Gilot, J., Wienk, M. M. & Janssen, R. A. J. Double and triple junction polymer solar cells processed from solution. *Appl. Phys. Lett.* **90,** 143512 (2007).

17. Forrest, S. R. Ultrathin Organic Films Grown by Organic Molecular Beam Deposition and Related Techniques. *Chem. Rev.* **97,** 1793–1896 (1997).
18. *Semiconducting Polymers: Chemistry, Physics and Engineering, Volume 2*. (Wiley-VCH, 2007).
19. Yu, G., Gao, J., Hummelen, J. C., Wudl, F. & Heeger, A. J. Polymer Photovoltaic Cells - Enhanced Efficiencies Via a Network of Internal Donor-Acceptor Heterojunctions. *Science (80-.).* **270,** 1789–1791 (1995).
20. Halls, J. J. M. *et al.* Efficient photodiodes from interpenetrating polymer networks. *Letters to Nature* **376,** 498–500 (1995).
21. Koehler, A. & Baessler, H. in *Electronic Processes in Organic Semiconductors* 1–86 (Wiley-VCH Verlag GmbH & Co. KGaA, 2015). doi:10.1002/9783527685172.ch1
22. Brabec, C. J. *et al.* Origin of the open circuit voltage of plastic solar cells. *Adv. Funtional Mater.* **11,** 374–380 (2001).
23. Vandewal, K., Tvingstedt, K., Gadisa, A., Inganäs, O. & Manca, J. V. On the origin of the open-circuit voltage of polymer–fullerene solar cells. *Nat. Mater.* **8,** 904–909 (2009).
24. Scharber, M. C. *et al.* Design rules for donors in bulk-heterojunction solar cells - Towards 10 % energy-conversion efficiency. *Adv. Mater.* **18,** 789–794 (2006).
25. Blakesley, J. C. & Greenham, N. C. Charge transfer at polymer-electrode interfaces: The effect of energetic disorder and thermal injection on band bending and open-circuit voltage. *J. Appl. Phys.* **106,** 1–7 (2009).
26. Steiner, F., Foster, S., Losquin, A., Labram, J. & Anthopoulos, T. D. Distinguishing the Influence of Structural and Energetic Disorder on Electron Transport in Fullerene Multi-Adducts. *Mater. Horizons* **2,** 113–119 (2014).
27. Faist, M. A. *et al.* Competition between the charge transfer state and the singlet states of donor or acceptor limiting the efficiency in polymer : fullerene solar cells Competition between the charge transfer state and the singlet states of donor or acceptor limiting the eff. *J. Am. Chem. Soc.,* **134,** 685–692 (2011).
28. Faist, M. A. *et al.* Effect of multiple adduct fullerenes on charge generation and transport in photovoltaic blends with poly(3-hexylthiophene-2,5-diyl). *J. Polym. Sci. Part B Polym. Phys.* **49,** 45–51 (2011).
29. Markvart, T. & Castañer, L. *Practical handbook of photovoltaics: fundamentals and applications*. (Elsevier, 2003). doi:10.1016/B978-0-12-385934-1.X0001-3
30. Winder, C. & Sariciftci, N. S. Low bandgap polymers for photon harvesting in bulk heterojunction solar cells. *J. Mater. Chem.* **14,** 1077 (2004).

31. Reilly, T. H., van de Lagemaat, J., Tenent, R. C., Morfa, A. J. & Rowlen, K. L. Surface-plasmon enhanced transparent electrodes in organic photovoltaics. *Appl. Phys. Lett.* **92,** 243304 (2008).
32. Shahin, S., Gangopadhyay, P. & Norwood, R. A. Ultrathin organic bulk heterojunction solar cells: Plasmon enhanced performance using Au nanoparticles. *Appl. Phys. Lett.* **101,** 53109 (2012).
33. Steim, R., Kogler, F. R. & Brabec, C. J. Interface materials for organic solar cells. *J. Mater. Chem.* **20,** 2499 (2010).
34. Han, S. *et al.* Improving performance of organic solar cells using amorphous tungsten oxides as an interfacial buffer layer on transparent anodes. *Org. Electron.* **10,** 791–797 (2009).
35. Yang, Y. & Li, G. *Progress in High-Efficient Solution Process Organic Photovoltaic Devices: Fundamentals, Materials, Devices and Fabrication*. (Springer Berlin Heidelberg, 2015).
36. Andersson, B. V., Huang, D. M., Moulé, A. J. & Inganäs, O. An optical spacer is no panacea for light collection in organic solar cells. *Appl. Phys. Lett.* **94,** 43302 (2009).
37. Servaites, J. D., Ratner, M. A. & Marks, T. J. Organic solar cells: A new look at traditional models. *Energy Environ. Sci.* **4,** 4410 (2011).
38. Servaites, J. D., Savoie, B. M., Brink, J. B., Marks, T. J. & Ratner, M. A. Modeling geminate pair dissociation in organic solar cells: high power conversion efficiencies achieved with moderate optical bandgaps. *Energy Environ. Sci.* **5,** 8343 (2012).
39. Lakhwani, G., Rao, A. & Friend, R. H. Bimolecular recombination in organic photovoltaics. *Annu. Rev. Phys. Chem.* **65,** (2014).
40. Servaites, J. D., Yeganeh, S., Marks, T. J. & Ratner, M. A. Efficiency enhancement in organic photovoltaic cells: Consequences of optimizing series resistance. *Adv. Funct. Mater.* **20,** 97–104 (2010).
41. Shinar, J. Organic light-emitting devices: a survey. 309 (2003).
42. Buckley, A. *Organic Light-emitting Diodes (OLEDs): Materials, Devices and Applications*. (2013).
43. Jasieniak, J. J., Seifter, J., Jo, J., Mates, T. & Heeger, A. J. A Solution-Processed MoO_x Anode Interlayer for Use within Organic Photovoltaic Devices. *Adv. Funct. Mater.* **22,** 2594–2605 (2012).
44. Choulis, S. A., Choong, V.-E., Mathai, M. K. & So, F. The effect of interfacial layer on the performance of organic light-emitting diodes. *Appl. Phys. Lett.* **87,** 113503 (2005).
45. Lin, H.-P. *et al.* Enhanced hole injection and improved performance in organic light-

emitting devices by utilizing a novel composite hole injection layer. *Solid State Commun.* **150,** 1601–1604 (2010).

46. Huh, Y. H., Kwon, O. E. & Park, B. Triple-stacked hole-selective layers for efficient solution-processable organic semiconducting devices. *Opt. Express* **23,** A625 (2015).
47. Sessolo, M. & Bolink, H. J. Hybrid organic-inorganic light-emitting diodes. *Adv. Mater.* **23,** 1829–1845 (2011).
48. Liu, J. *et al.* Low-temperature MoO 3 film from a facile synthetic route for an efficient anode interfacial layer in organic optoelectronic devices. *J. Mater. Chem. C* **2,** 158–163 (2014).
49. Li, X., Xie, F., Zhang, S., Hou, J. & Choy, W. C. MoOx and V2Ox as hole and electron transport layers through functionalized intercalation in normal and inverted organic optoelectronic devices. *Light Sci. Appl.* **4,** e273 (2015).
50. Kröger, M. *et al.* P-type doping of organic wide band gap materials by transition metal oxides: A case-study on Molybdenum trioxide. *Org. Electron.* **10,** 932–938 (2009).
51. Bolink, H. J. *et al.* Inverted Solution Processable OLEDs Using a Metal Oxide as an Electron Injection Contact. *Adv. Funct. Mater.* **18,** 145–150 (2008).
52. Griffits, D. J. *Introduction to Quantum Mechanics*. (1995).
53. Baldo, M. A., Thompson, M. E. & Forrest, S. R. Phosphorescent materials for application to organic light emitting devices. *Pure Appl. Chem.* **71,** (1999).
54. Forrest, S. R. The road to high efficiency organic light emitting devices. *Org. Electron. physics, Mater. Appl.* **4,** 45–48 (2003).
55. Uoyama, H., Goushi, K., Shizu, K., Nomura, H. & Adachi, C. Highly efficient organic light-emitting diodes from delayed fluorescence. *Nature* **492,** 234–238 (2012).
56. Suntivich, J. *et al.* Design principles for oxygen-reduction activity on perovskite oxide catalysts for fuel cells and metal–air batteries. *Nat. Chem.* **3,** 546–550 (2011).
57. Tao, S. & Irvine, J. T. S. A redox-stable efficient anode for solid-oxide fuel cells. *Nat. Mater.* **2,** 320–323 (2003).
58. Sawa, A. Resistive switching in transition metal oxides. *Mater. Today* **11,** 28–36 (2008).
59. Keppert, D. L. The Early Transition Metals. 499 (1972).
60. *Semiconducting Polymers*. (Wiley-VCH Verlag GmbH & Co. KGaA, 1999). doi:10.1002/3527602186
61. Pasquarelli, R. M., Ginley, D. S. & O'Hayre, R. Solution processing of transparent conductors: from flask to film. *Chem. Soc. Rev.* **40,** 5406 (2011).
62. Facchetti, A. & Marks, T. J. *Transparent Electronics*. (John Wiley & Sons, Ltd, 2010).

doi:10.1002/9780470710609

63. *Handbook of Transparent Conductors*. (Springer US, 2011). doi:10.1007/978-1-4419-1638-9

64. Jagadamma, L. K. *et al.* Solution-processable MoOx nanocrystals enable highly efficient reflective and semitransparent polymer solar cells. *Nano Energy* **28,** 277–287 (2016).

65. Scanlon, D. O. *et al.* Theoretical and Experimental Study of the Electronic Structures of MoO 3 and MoO 2. *J. Phys. Chem. C* **114,** 4636–4645 (2010).

66. Lee, Y. J., Wang, J., Cheng, S. R. & Hsu, J. W. P. Solution processed ZnO hybrid nanocomposite with tailored work function for improved electron transport layer in organic photovoltaic devices. *ACS Appl. Mater. Interfaces* **5,** 9128–9133 (2013).

67. Bolink, H. J., Coronado, E., Repetto, D. & Sessolo, M. Air stable hybrid organic-inorganic light emitting diodes using ZnO as the cathode. *Appl. Phys. Lett.* **91,** 223501 (2007).

68. Chai, L., White, R. T., Greiner, M. T. & Lu, Z. H. Experimental demonstration of the universal energy level alignment rule at oxide/organic semiconductor interfaces. *Phys. Rev. B* **89,** 35202 (2014).

69. A. D. McNaught and A. Wilkinson. *IUPAC. Compendium of Chemical Terminology*. (Blackwell Scientiic Publications, Oxford, 1997). doi:10.1351/goldbook

70. Meyer, J., Zilberberg, K., Riedl, T. & Kahn, A. Electronic structure of Vanadium pentoxide: An efficient hole injector for organic electronic materials. *J. Appl. Phys.* **110,** 33710 (2011).

71. Akande, S. O., Chroneos, A., Vasilopoulou, M., Kennou, S. & Schwingenschlö, U. Vacancy formation in MoO 3 : hybrid density functional theory and photoemission experiments. *J. Mater. Chem. C* **4,** (2016).

72. Kröger, M. *et al.* Role of the deep-lying electronic states of MoO_3 in the enhancement of hole-injection in organic thin films. *Appl. Phys. Lett.* **95,** 123301 (2009).

73. Choi, H. *et al.* Solution processed WO3 layer for the replacement of PEDOT:PSS layer in organic photovoltaic cells. *Organic Electronics* **13,** 959–968 (2012).

74. Vasilopoulou, M. *et al.* Hydrogenated under-stoichiometric tungsten oxide anode interlayers for efficient and stable organic photovoltaics. *J. Mater. Chem. A* **2,** 1738–1749 (2014).

75. Wang, F., Tan, Z. & Li, Y. Solution-processable metal oxides/chelates as electrode buffer layers for efficient and stable polymer solar cells. *Energy Environ. Sci.* **8,** 1059–1091 (2015).

76. Biesinger, M. C., Lau, L. W. M., Gerson, A. R. & Smart, R. S. C. Resolving surface chemical

states in XPS analysis of first row transition metals, oxides and hydroxides: Sc, Ti, V, Cu and Zn. *Appl. Surf. Sci.* **257,** 887–898 (2010).

77. Cox, P. A. *Transition Metal Oxides: An Introduction to Their Electronic Structure and Properties*. (OUP Oxford, 2010).
78. Henrich, V. E. & Cox, P. A. *The Surface Science of Metal Oxides*. (Cambridge University Press, 1996).
79. Greiner, M. T. & Lu, Z.-H. Thin-film metal oxides in organic semiconductor devices: their electronic structures, work functions and interfaces. *NPG Asia Mater.* **5,** e55 (2013).
80. Bailar, J. C. & Trotman-Dickenson, A. F. *Comprehensive Inorganic Chemistry*. **103,** (Pergamon Press; distributed by Compendium Publishers [Elmsford, N.Y.], 1972).
81. Asahi, R., Taga, Y., Mannstadt, W. & Freeman, A. Electronic and optical properties of anatase TiO2. *Phys. Rev. B* **61,** 7459–7465 (2000).
82. Hubbard, J. Electron Correlations in Narrow Energy Bands. *Proc. R. Soc. A Math. Phys. Eng. Sci.* **276,** 238–257 (1963).
83. Hubbard, J. Electron Correlations in Narrow Energy Bands. II. The Degenerate Band Case. *Proc. R. Soc. London A Math. Phys. Eng. Sci.* **277,** 237–259 (1964).
84. Mott, N. F. The Transitions to the Metallic State. *Philos. Mag.* **6,** 287–309 (1961).
85. Hubbard, J. Electron Correlations in Narrow Energy Bands. III. An Improved Solution. *Proc. R. Soc. A Math. Phys. Eng. Sci.* **281,** 401–419 (1964).
86. Zaanen, J., Sawatzky, G. A. & Allen, J. W. Band gaps and electronic structure of transition-metal compounds. *Phys. Rev. Lett.* **55,** 418–421 (1985).
87. Scanlon, D. O., Morgan, B. J., Watson, G. W. & Walsh, A. Acceptor levels in p-type Cu2O: Rationalizing theory and Experiment. *Phys. Rev. Lett.* **103,** 96405 (2009).
88. Tengstedt, C. *et al.* Fermi-level pinning at conjugated polymer interfaces. *Appl. Phys. Lett.* **88,** 1–3 (2006).
89. Fahlman, M. *et al.* Electronic structure of hybrid interfaces for polymer-based electronics. *J. Phys. Condens. Matter* **19,** (2007).
90. Greiner, M. T., Chai, L., Helander, M. G., Tang, W.-M. & Lu, Z.-H. Transition Metal Oxide Work Functions: The Influence of Cation Oxidation State and Oxygen Vacancies. *Adv. Funct. Mater.* **22,** 4557–4568 (2012).
91. Greiner, M. T. Transition Metal Oxides in Organic Electronics. *Thesis* (University of Toronto, 2012).
92. Greiner, M. T., Chai, L., Helander, M. G., Tang, W. M. & Lu, Z. H. Metal/metal-oxide interfaces: How metal contacts affect the work function and band structure of MoO3.

Adv. Funct. Mater. **23,** 215–226 (2013).

93. Helander, M. G., Wang, Z. B., Greiner, M. T., Qiu, J. & Lu, Z. H. Substrate dependent charge injection at the V2 O5 /organic interface. *Appl. Phys. Lett.* **95,** 83301 (2009).
94. Greiner, M. T., Helander, M. G., Wang, Z. Bin, Tang, W. M. & Lu, Z. H. Effects of processing conditions on the work function and energy-level alignment of NiO thin films. *J. Phys. Chem. C* **114,** 19777–19781 (2010).
95. Greiner, M. T. *et al.* A metallic molybdenum suboxide buffer layer for organic electronic devices. *Appl. Phys. Lett.* **96,** 213302 (2010).
96. Wang, Z. B., Helander, M. G., Greiner, M. T., Qiu, J. & Lu, Z. H. Analysis of charge-injection characteristics at electrode-organic interfaces: Case study of transition-metal oxides. *Phys. Rev. B - Condens. Matter Mater. Phys.* **80,** 235325 (2009).
97. Ley, L., Smets, Y., Pakes, C. I. & Ristein, J. Calculating the universal energy-level alignment of organic molecules on metal oxides. *Adv. Funct. Mater.* **23,** 794–805 (2013).
98. Meyer, J. *et al.* Transition metal oxides for organic electronics: Energetics, device physics and applications. *Adv. Mater.* **24,** 5408–5427 (2012).
99. Cao, Y., Yu, G., Zhang, C., Menon, R. & Heeger, A. . Polymer light-emitting diodes with polyethylene dioxythiophene–polystyrene sulfonate as the transparent anode. *Synth. Met.* **87,** 171–174 (1997).
100. Heithecker, D. *et al.* Low-voltage organic electroluminescence device with an ultrathin, hybrid structure. *Appl. Phys. Lett.* **82,** 4178 (2003).
101. Jørgensen, M. *et al.* Stability of polymer solar cells. *Adv. Mater.* **24,** 580–612 (2012).
102. Voroshazi, E., Verreet, B., Aernouts, T. & Heremans, P. Long-term operational lifetime and degradation analysis of P3HT:PCBM photovoltaic cells. *Sol. Energy Mater. Sol. Cells* **95,** 1303–1307 (2011).
103. Lee, Y.-J. *et al.* Low-Temperature Solution-Processed Molybdenum Oxide Nanoparticle Hole Transport Layers for Organic Photovoltaic Devices. *Adv. Energy Mater.* **2,** 1193–1197 (2012).
104. Meyer, J., Khalandovsky, R., Görrn, P. & Kahn, A. MoO_x Films Spin-Coated from a Nanoparticle Suspension for Efficient Hole-Injection in Organic Electronics. *Adv. Mater.* **23,** 70–73 (2011).
105. Stubhan, T. *et al.* High shunt resistance in polymer solar cells comprising a MoO_x hole extraction layer processed from nanoparticle suspension. *Appl. Phys. Lett.* **98,** 253308 (2011).
106. Li, N. *et al.* Inverted structure organic photovoltaic devices employing a low temperature

solution processed WO_x anode buffer layer. *Org. Electron.* **13,** 2479–2484 (2012).

107. Ryu, M. S. & Jang, J. Enhanced efficiency of organic photovoltaic cells using solution-processed metal oxide as an anode buffer layer. *Sol. Energy Mater. Sol. Cells* **95,** 3015–3020 (2011).
108. Dharmaraj, N. *et al.* Synthesis of nickel oxide nanoparticles using nickel acetate and poly(vinyl acetate) precursor. *Mater. Sci. Eng. B* **128,** 111–114 (2006).
109. Thota, S. & Kumar, J. Sol–gel synthesis and anomalous magnetic behaviour of NiO nanoparticles. *J. Phys. Chem. Solids* **68,** 1951–1964 (2007).
110. Tao, D. & Wei, F. New procedure towards size-homogeneous and well-dispersed nickel oxide nanoparticles of 30 nm. *Mater. Lett.* **58,** 3226–3228 (2004).
111. Habibi, M. H. & Karimi, B. Effect of the annealing temperature on crystalline phase of copper oxide nanoparticle by copper acetate precursor and sol–gel method. *J. Therm. Anal. Calorim.* **115,** 419–423 (2013).
112. Steirer, K. X. *et al.* Solution deposited NiO thin-films as hole transport layers in organic photovoltaics. *Org. Electron.* **11,** 1414–1418 (2010).
113. Jiang, F., Choy, W. C. H., Li, X., Zhang, D. & Cheng, J. Post-treatment-Free Solution-Processed Non-stoichiometric NiO_x Nanoparticles for Efficient Hole-Transport Layers of Organic Optoelectronic Devices. *Adv. Mater.* **27,** 2930–7 (2015).
114. Jayaprakash, J., Srinivasan, N., Chandrasekaran, P. & Girija, E. K. Synthesis and characterization of cluster of grapes like pure and Zinc-doped CuO nanoparticles by sol-gel method. *Spectrochim. Acta. A. Mol. Biomol. Spectrosc.* **136PC,** 1803–1806 (2014).
115. Venkatesan, A. *et al.* Luminescence and electrochemical properties of rare earth (Gd, Nd) doped V_2O_5 nanostructures synthesized by a non-aqueous sol–gel route. *RSC Adv.* **5,** 21778–21785 (2015).
116. Kim, M. G. *et al.* Delayed ignition of autocatalytic combustion precursors: Low-temperature nanomaterial binder approach to electronically functional oxide films. *J. Am. Chem. Soc.* **134,** 11583–11593 (2012).
117. Matijevic, E. Monodispersed metal (hydrous) oxides - a fascinating field of colloid science. (2002).
118. Livage, J., Henry, M. & Sanchez, C. Sol-gel chemistry of transition metal oxides. *Prog. Solid State Chem.* **18,** 259–341 (1988).
119. Sta, I., Jlassi, M., Hajji, M. & Ezzaouia, H. Structural, optical and electrical properties of undoped and Li-doped NiO thin films prepared by sol–gel spin coating method. *Thin Solid Films* **555,** 131–137 (2014).

120. Wheeler, S. *et al.* Influence of Surface Recombination on Charge-Carrier Kinetics in Organic Bulk Heterojunction Solar Cells with Nickel Oxide Interlayers. *Phys. Rev. Appl.* **4,** 24020 (2015).

121. Lin, M.-Y. *et al.* Sol–gel processed CuO_x thin film as an anode interlayer for inverted polymer solar cells. *Org. Electron.* **11,** 1828–1834 (2010).

122. Desai, J. D., Min, S. K., Jung, K. D. & Joo, O. S. Spray pyrolytic synthesis of large area NiO_x thin films from aqueous nickel acetate solutions. *Appl. Surf. Sci.* **253,** 1781–1786 (2006).

123. Pattanasattayavong, P., Thomas, S., Adamopoulos, G., McLachlan, M. a. & Anthopoulos, T. D. P-channel thin-film transistors based on spray-coated Cu_2O films. *Appl. Phys. Lett.* **102,** 163505 (2013).

124. Kim, K. H., Takahashi, C., Abe, Y. & Kawamura, M. Effects of Cu doping on nickel oxide thin film prepared by sol–gel solution process. *Opt. - Int. J. Light Electron Opt.* **125,** 2899–2901 (2014).

125. Liu, S., Ho, S., Chen, Y. & So, F. Passivation of Metal Oxide Surfaces for High-Performance Organic and Hybrid Optoelectronic Devices. *Chem. Mater.* **27,** 2532–2539 (2015).

126. De Jesus, J. C., González, I., Quevedo, A. & Puerta, T. Thermal decomposition of nickel acetate tetrahydrate: an integrated study by TGA, QMS and XPS techniques. *J. Mol. Catal. A Chem.* **228,** 283–291 (2005).

127. Lin, Z., Han, D. & Li, S. Study on thermal decomposition of copper(II) acetate monohydrate in air. *J. Therm. Anal. Calorim.* **107,** 471–475 (2011).

128. Mitzi, D. B. *Solution Processing of Inorganic Materials*. (John Wiley & Sons, Inc., 2008).

129. Jlassi, M., Sta, I., Hajji, M. & Ezzaouia, H. Optical and electrical properties of nickel oxide thin films synthesized by sol–gel spin coating. *Mater. Sci. Semicond. Process.* **21,** 7–13 (2014).

130. Garcia, A. *et al.* Improvement of interfacial contacts for new small-molecule bulk-heterojunction organic photovoltaics. *Adv. Mater.* **24,** 5368–5373 (2012).

131. Manders, J. R. *et al.* Solution-Processed Nickel Oxide Hole Transport Layers in High Efficiency Polymer Photovoltaic Cells. *Adv. Funct. Mater.* **23,** 2993–3001 (2013).

132. Ginley, D. S., Curtis, C. J., Miedaner, A., van Hest, M. F. A. M. & Kaydanova, T. Metal Inks. (2008).

133. Steirer, K. X. *et al.* Enhanced Efficiency in Plastic Solar Cells via Energy Matched Solution Processed NiO_x Interlayers. *Adv. Energy Mater.* **1,** 813–820 (2011).

134. Xie, F. *et al.* Low-temperature solution-processed hydrogen molybdenum and vanadium bronzes for an efficient hole-transport layer in organic electronics. *Adv. Mater.* **25,** 2051–

5 (2013).

135. Soultati, A. *et al.* Solution-Processed Hydrogen Molybdenum Bronzes as Highly Conductive Anode Interlayers in Efficient Organic Photovoltaics. *Adv. Energy Mater.* **4,** n/a-n/a (2014).

136. Girotto, C., Voroshazi, E., Cheyns, D., Heremans, P. & Rand, B. P. Solution-processed MoO_x thin films as a hole-injection layer for organic solar cells. *ACS Appl. Mater. Interfaces* **3,** 3244–7 (2011).

137. Vidmar, T., Topič, M., Dzik, P. & Opara Krašovec, U. Inkjet printing of sol–gel derived tungsten oxide inks. *Sol. Energy Mater. Sol. Cells* **125,** 87–95 (2014).

138. Alsawafta, M. *et al.* Electrochromic Properties of Sol-Gel Synthesized Macroporous Tungsten Oxide Films Doped with Gold Nanoparticles. *J. Electrochem. Soc.* **161,** H276–H283 (2014).

139. Brinker, C. J. & Scherer, G. W. *Sol-Gel Science: The Physics and Chemistry of Sol-Gel Processing*. (Elsevier Science, 2013).

140. Kololuoma, T. *et al.* Flexo printed sol-gel derived vanadium oxide films as an interfacial hole-transporting layer for organic solar cells. in *SPIE OPTO* (eds. Teherani, F. H., Look, D. C. & Rogers, D. J.) 93640K (International Society for Optics and Photonics, 2015). doi:10.1117/12.2079270

141. Zilberberg, K. *et al.* Inverted Organic Solar Cells with Sol-Gel Processed High Work-Function Vanadium Oxide Hole-Extraction Layers. *Adv. Funct. Mater.* **21,** 4776–4783 (2011).

142. Kim, J., Kim, H., Kim, G., Back, H. & Lee, K. Soluble transition metal oxide/polymeric acid composites for efficient hole-transport layers in polymer solar cells. *ACS Appl. Mater. Interfaces* **6,** 951–7 (2014).

143. Bao, X. *et al.* Simple O_x plasma-processed V_2O_5 as an anode buffer layer for high-performance polymer solar cells. *ACS Appl. Mater. Interfaces* **7,** 7613–8 (2015).

144. Chen, L., Xie, C. & Chen, Y. Optimization of the Power Conversion Efficiency of Room Temperature-Fabricated Polymer Solar Cells Utilizing Solution Processed Tungsten Oxide and Conjugated Polyelectrolyte as Electrode Interlayer. *Adv. Funct. Mater.* **24,** 3986–3995 (2014).

145. Guillain, F. *et al.* Annealing-free solution-processed tungsten oxide for inverted organic solar cells. *Sol. Energy Mater. Sol. Cells* **122,** 251–256 (2014).

146. Kim, M.-G., Kanatzidis, M. G., Facchetti, A. & Marks, T. J. Low-temperature fabrication of high-performance metal oxide thin-film electronics via combustion processing. *Nat.*

Mater. **10,** 382–388 (2011).

147. Kingsley, J. J. & Patil, K. C. A novel combustion process for the synthesis of fine particle α-alumina and related oxide materials. *Mater. Lett.* **6,** 427–432 (1988).
148. Aruna, S. T. & Mukasyan, A. S. Combustion synthesis and nanomaterials. *Curr. Opin. Solid State Mater. Sci.* **12,** 44–50 (2008).
149. Bai, S. *et al.* Low-Temperature Combustion-Synthesized Nickel Oxide Thin Films as Hole-Transport Interlayers for Solution-Processed Optoelectronic Devices. *Adv. Energy Mater.* **4,** n/a-n/a (2014).
150. Epifani, M., Melissano, E., Pace, G. & Schioppa, M. Precursors for the combustion synthesis of metal oxides from the sol–gel processing of metal complexes. *J. Eur. Ceram. Soc.* **27,** 115–123 (2007).
151. Lian, J. ., Zhang, X. ., Zhang, H. ., Jiang, Z. . & Zhang, J. Synthesis of nanocrystalline NiO/doped CeO_2 compound powders through combustion of citrate/nitrate gel. *Mater. Lett.* **58,** 1183–1188 (2004).
152. Yue, Z., Zhou, J., Li, L., Zhang, H. & Gui, Z. Synthesis of nanocrystalline NiCuZn ferrite powders by sol–gel auto-combustion method. *J. Magn. Magn. Mater.* **208,** 55–60 (2000).
153. Zhu, H. *et al.* Metal oxides modified NiO catalysts for oxidative dehydrogenation of ethane to ethylene. *Catal. Today* **228,** 58–64 (2014).
154. Pechini, M. P. Barium titanium citrate, barium titanate and processes for producing same. (1966).
155. Patil, K. C., Hedge, M. S., Rattan, T. & Aruna, S. T. *Chemistry of Nanocrystalline Oxide Materials: Combustion Synthesis, Properties and Applications*. (World Scientific, 2008).
156. Sarner, S. F. *Propellant Chemistry*. (Reinhold Publishing Corporation, 1966).
157. Yao, C., Xu, X., Wang, J., Shi, L. & Li, L. Low-temperature, solution-processed hole selective layers for polymer solar cells. *ACS Appl. Mater. Interfaces* **5,** 1100–7 (2013).
158. Spin Coating: A Guide to Theory and Techniques – Ossila. Available at: https://www.ossila.com/pages/spin-coating. (Accessed: 10th January 2017)
159. PEDOT:PSS | Ossila. Available at: https://www.ossila.com/products/pedot-pss?variant=22831509953#Al 4083. (Accessed: 10th January 2017)
160. Bannock, J. H. *et al.* Continuous synthesis of device-grade semiconducting polymers in droplet-based microreactors. *Adv. Funct. Mater.* **23,** 2123–2129 (2013).
161. Watts, J. F. & Wolstenholme, J. *An introduction to surface analysis by XPS and AES*. (J. Wiley, 2003).
162. Eaton, P. & West, P. *Atomic Force Microscopy*. (Oxford University Press, 2010).

163. Poruba, A. *et al.* Optical absorption and light scattering in microcrystalline silicon thin films and solar cells. *J. Appl. Phys.* **88,** 148–160 (2000).

164. Hong, W. Q. Extraction of extinction coefficient of weak absorbing thin films from special absorption. *J. Phys. D. Appl. Phys.* **22,** 1384–1385 (1989).

165. *Ullmann's Encyclopedia of Industrial Chemistry*. (Wiley-VCH Verlag GmbH & Co. KGaA, 2000).

166. Tauc, J. Optical properties and electronic structure of amorphous Ge and Si. *Mater. Res. Bull.* **3,** 37–46 (1968).

167. Tauc, J., Grigorovici, R. & Vancu, A. Optical Properties and Electronic Structure of Amorphous Germanium. *Phys. status solidi* **15,** 627–637 (1966).

168. Davis, E. A. & Mott, N. F. Conduction in non-crystalline systems V. Conductivity, optical absorption and photoconductivity in amorphous semiconductors. *Philos. Mag.* **22,** 0903–0922 (1970).

169. Livingston, J. D. *Electronic properties of engineering materials*. (Wiley, 1999).

170. C., K. *Introduction to solid state physics*. **Third,** (Wiley, 1953).

171. Lüth, H. *Solid Surfaces, Interfaces and Thin Films*. *Chemistry &* (2010). doi:10.1007/978-3-642-13592-7

172. Irfan *et al.* Energy level evolution of air and oxygen exposed molybdenum trioxide films. *Appl. Phys. Lett.* **96,** 243307 (2010).

173. Vasilopoulou, M., Soultati, A., Argitis, P., Stergiopoulos, T. & Davazoglou, D. Fast Recovery of the High Work Function of Tungsten and Molybdenum Oxides via Microwave Exposure for Efficient Organic Photovoltaics. *J. Phys. Chem. Lett.* **5,** 1871–9 (2014).

174. Ratcliff, E. L. *et al.* Investigating the Influence of Interfacial Contact Properties on Open Circuit Voltages in Organic Photovoltaic Performance: Work Function Versus Selectivity. *Adv. Energy Mater.* **3,** 647–656 (2013).

175. National Instruments. Part II – Photovoltaic Cell I-V Characterization Theory and LabVIEW Analysis Code - National Instruments. (2012). Available at: http://www.ni.com/white-paper/7230/en/. (Accessed: 22nd February 2017)

176. Pope, M. T. in *Progress in Inorganic Chemistry, Volume 39* 181–257 (John Wiley & Sons, Inc., 1991). doi:10.1002/9780470166406.ch4

177. Cotton, F. A. & Wilkinson, G. *Advanced inorganic chemistry.* (Wiley, 1999).

178. Grunert, W. *et al.* Analysis of Mo(3d) XPS Spectra of Supported Mo Catalysts: An Alternative Approach. *J. Phys. Chem.* **95,** 1323–1328 (1991).

179. Vasilopoulou, M. *et al.* The influence of hydrogenation and oxygen vacancies on molybdenum oxides work function and gap states for application in organic optoelectronics. *J. Am. Chem. Soc.* **134,** 16178–87 (2012).

180. Dupin, J.-C., Gonbeau, D., Vinatier, P. & Levasseur, A. Systematic XPS studies of metal oxides, hydroxides and peroxides. *Phys. Chem. Chem. Phys.* **2,** 1319–1324 (2000).

181. Alsaif, M. M. Y. A. *et al.* Tunable plasmon resonances in two-dimensional molybdenum oxide nanoflakes. *Adv. Mater.* **26,** 3931–7 (2014).

182. Fleisch, T. H. & Mains, G. J. An XPS study of the UV reduction and photochromism of MoO3 and WO3. *J. Chem. Phys.* **76,** 780 (1982).

183. Wang, G. *et al.* Preparation and characterization of MoO_3 hole-injection layer for organic solar cell fabrication and optimization. *Sol. Energy Mater. Sol. Cells* **120,** 603–609 (2014).

184. Zou, Y. & Holmes, R. J. Influence of a MoO_x interlayer on the open-circuit voltage in organic photovoltaic cells. *Appl. Phys. Lett.* **103,** 53302 (2013).

185. Sun, Y. *et al.* Efficient, air-stable bulk heterojunction polymer solar cells using MoO(x) as the anode interfacial layer. *Adv. Mater.* **23,** 2226–30 (2011).

186. Guo, Y. & Robertson, J. Origin of the high work function and high conductivity of MoO3. *Appl. Phys. Lett.* **105,** (2014).

187. Xie, F. Y. *et al.* XPS studies on surface reduction of tungsten oxide nanowire film by Ar+ bombardment. *J. Electron Spectros. Relat. Phenomena* **185,** 112–118 (2012).

188. Holm, R. & Storp, S. ESCA studies on changes in surface composition under ion bombardment. *Appl. Phys.* **12,** 101–112 (1977).

189. Kim, K. S., Baitinger, W. E., Amy, J. W. & Winograd, N. ESCA studies of metal-oxygen surfaces using argon and oxygen ion-bombardment. *J. Electron Spectros. Relat. Phenomena* **5,** 351–367 (1974).

190. Wang, F., Qiao, X., Xiong, T. & Ma, D. The role of molybdenum oxide as anode interfacial modification in the improvement of efficiency and stability in organic light-emitting diodes. *Org. Electron.* **9,** 985–993 (2008).

191. Jha, J. K., Santos-Ortiz, R., Du, J. & Shepherd, N. D. The influence of MoO_x gap states on hole injection from aluminum doped zinc oxide with nanoscale MoO_x surface layer anodes for organic light emitting diodes. *J. Appl. Phys.* **118,** 65304 (2015).

192. Blanquart, T. *et al.* Atomic layer deposition and characterization of vanadium oxide thin films. *RSC Adv.* **3,** 1179–1185 (2013).

193. Lu, Y., Liu, L., Mandler, D. & Lee, P. S. High switching speed and coloration efficiency of titanium-doped vanadium oxide thin film electrochromic devices. *J. Mater. Chem. C* **1,**

7380 (2013).

194. Warwick, M. E. A., Roberts, A. J., Slade, R. C. T. & Binions, R. Electric field assisted chemical vapour deposition-a new method for the preparation of highly porous supercapacitor electrodes. *J. Mater. Chem. A* **2,** 6115–6120 (2014).

195. Huang, J.-S. *et al.* Solution-processed vanadium oxide as an anode interlayer for inverted polymer solar cells hybridized with ZnO nanorods. *Org. Electron.* **10,** 1060–1065 (2009).

196. Campbell Scott, J. & Malliaras, G. G. Charge injection and recombination at the metal–organic interface. *Chem. Phys. Lett.* **299,** 115–119 (1999).

197. Choulis, S. A., Choong, V.-E., Patwardhan, A., Mathai, M. K. & So, F. Interface Modification to Improve Hole-Injection Properties in Organic Electronic Devices. *Adv. Funct. Mater.* **16,** 1075–1080 (2006).

198. Douvas, A. M. *et al.* Sol–gel synthesized, low-temperature processed, reduced molybdenum peroxides for organic optoelectronics applications. *J. Mater. Chem. C* **2,** 6290 (2014).

199. Lipomi, D. J. *et al.* Electronic properties of transparent conductive films of PEDOT:PSS on stretchable substrates. *Chem. Mater.* **24,** 373–382 (2012).

200. Tait, J. G. *et al.* Spray coated high-conductivity PEDOT:PSS transparent electrodes for stretchable and mechanically-robust organic solar cells. *Sol. Energy Mater. Sol. Cells* **110,** 98–106 (2013).

201. Sun, K. *et al.* Review on application of PEDOTs and PEDOT:PSS in energy conversion and storage devices. *Journal of Materials Science: Materials in Electronics* **26,** 4438–4462 (2015).

202. Vosgueritchian, M., Lipomi, D. J. & Bao, Z. Highly conductive and transparent PEDOT:PSS films with a fluorosurfactant for stretchable and flexible transparent electrodes. *Adv. Funct. Mater.* **22,** 421–428 (2012).

203. Shao, S. *et al.* In Situ Formation of MoO3 in PEDOT:PSS Matrix: A Facile Way to Produce a Smooth and Less Hygroscopic Hole Transport Layer for Highly Stable Polymer Bulk Heterojunction Solar Cells. *Adv. Energy Mater.* **3,** 349–355 (2013).

204. Wang, Y. *et al.* Solution-processed MoO3:PEDOT:PSS hybrid hole transporting layer for inverted polymer solar cells. *ACS Appl. Mater. Interfaces* **7,** 7170–7179 (2015).

205. Chen, L., Wang, P., Li, F., Yu, S. & Chen, Y. Efficient bulk heterojunction polymer solar cells using PEDOT/PSS doped with solution-processed MoO3 as anode buffer layer. *Sol. Energy Mater. Sol. Cells* **102,** 66–70 (2012).

206. Greczynski, G., Kugler, T. & Salaneck, W. R. Characterization of the PEDOT-PSS system by

means of X-ray and ultraviolet photoelectron spectroscopy. *Thin Solid Films* **354,** 129–135 (1999).

207. Kim, Y. H. *et al.* Highly conductive PEDOT:PSS electrode with optimized solvent and thermal post-treatment for ITO-free organic solar cells. *Adv. Funct. Mater.* **21,** 1076–1081 (2011).
208. Jönsson, S. K. M. *et al.* The effects of solvents on the morphology and sheet resistance in poly(3,4-ethylenedioxythiophene)-polystyrenesulfonic acid (PEDOT-PSS) films. *Synth. Met.* **139,** 1–10 (2003).
209. Deb, S. K. & Chopoorian, J. A. Optical properties and color-center formation in thin films of molybdenum trioxide. *J. Appl. Phys.* **37,** 4818–4825 (1966).
210. Busscher, H. J., van Pelt, A. W. J., de Boer, P., de Jong, H. P. & Arends, J. The effect of surface roughening of polymers on measured contact angles of liquids. *Colloids and Surfaces* **9,** 319–331 (1984).
211. Hong, K. T., Imadojemu, H. & Webb, R. L. Effects of oxidation and surface roughness on contact angle. *Exp. Therm. Fluid Sci.* **8,** 279–285 (1994).
212. Wenzel, R. N. Surface roughness and contact angle. *J. Phys. Colloid Chem.* **53,** 1466–1467 (1949).
213. Giebink, N. C. & Forrest, S. R. Quantum efficiency roll-off at high brightness in fluorescent and phosphorescent organic light emitting diodes. *Phys. Rev. B - Condens. Matter Mater. Phys.* **77,** 235215 (2008).
214. Baldo, M. A., Adachi, C. & Forrest, S. R. Transient analysis of organic electrophosphorescence. II. Transient analysis of triplet-triplet annihilation. *Phys. Rev. B - Condens. Matter Mater. Phys.* **62,** 10967–10977 (2000).
215. Murawski, C., Leo, K. & Gather, M. C. Efficiency roll-off in organic light-emitting diodes. *Adv. Mater.* **25,** 6801–6827 (2013).
216. Xu, Q. *et al.* High-performance polymer solar cells with solution-processed and environmentally friendly CuO_x anode buffer layer. *ACS Appl. Mater. Interfaces* **5,** 10658–64 (2013).
217. Vasilopoulou, M. *et al.* Tungsten oxides as interfacial layers for improved performance in hybrid optoelectronic devices. *Thin Solid Films* **519,** 5748–5753 (2011).
218. Lien, H.-T. *et al.* Effect of copper oxide oxidation state on the polymer-based solar cell buffer layers. *ACS Appl. Mater. Interfaces* **6,** 22445–50 (2014).
219. Wang, M. *et al.* Device lifetime improvement of polymer-based bulk heterojunction solar cells by incorporating copper oxide layer at Al cathode. *Appl. Phys. Lett.* **98,** 183304

(2011).

220. Höfle, S. *et al.* Tungsten Oxide Buffer Layers Fabricated in an Inert Sol-Gel Process at Room-Temperature for Blue Organic Light-Emitting Diodes. *Adv. Mater.* **25,** 4113–4116 (2013).

221. Oh, I. S., Kim, G. M., Han, S. H. & Oh, S. Y. PEDOT:PSS-free organic photovoltaic cells using tungsten oxides as buffer layer on anodes. *Electron. Mater. Lett.* **9,** 375–379 (2013).

222. Lee, J., Youn, H. & Yang, M. Work function modification of solution-processed tungsten oxide for a hole-injection layer of polymer light-emitting diodes. *Org. Electron. physics, Mater. Appl.* **22,** (2015).

223. Law, M. *et al.* Structural, Optical, and Electrical Properties of PbSe Nanocrystal Solids Treated Thermally or with Simple Amines. *J. Am. Chem. Soc.* **130,** 5974–5985 (2008).

224. Liu, Z. *et al.* Ambient pressure XPS and IRRAS investigation of ethanol steam reforming on Ni-CeO2(111) catalysts: an in situ study of C-C and O-H bond scission. *Phys. Chem. Chem. Phys.* **18,** 16621–16628 (2016).

225. Nadeem, A. M. *et al.* Ethanol photo-oxidation on a rutile TiO2(110) single crystal surface. *Phys. Chem. Chem. Phys.* **13,** 7637–7643 (2011).

226. Reichardt, C. & Welton, T. *Solvents and solvent effects in organic chemistry*. (Wiley-VCH, 2011).

227. Zhang, J. *et al.* Low-Temperature Solution-Processed Electron Transport Layers for Inverted Polymer Solar Cells. *Adv. Electron. Mater.* **2,** 1600008 (2016).

228. Zilberberg, K., Meyer, J. & Riedl, T. Solution processed metal-oxides for organic electronic devices. *J. Mater. Chem. C* **1,** 4796–4815 (2013).

229. Tan, W. C., Koughia, K., Singh, J. & Kasap, S. O. *Fundamental Optical Properties of Materials I*. *Optical Properties of Condensed Matter and Applications* (John Wiley & Sons, Ltd, 2006). doi:10.1002/0470021942.ch1

230. Jenkins, F. & White, H. *LSC Fundamentals of Optics*. (McGraw-Hill, 2001).

231. Poelman, D. & Smet, P. F. Methods for the determination of the optical constants of thin films from single transmission measurements: a critical review. *J. Phys. D. Appl. Phys.* **36,** 1850–1857 (2003).

232. Macleod, H. *Thin-Film Optical Filters, Third Edition*. **20010719,** (CRC Press, 2001).

233. Singleton, J. *Band theory and electronic properties of solids*. (Oxford University Press, 2001).

APPENDIX

A. APPENDIX TO CHAPTER 3

Some complementary data is hereby presented to support the discussion of the MoO_{3-x} results. XRD data from films subject to different post-deposition treatment (Figure 6.1) shows the absence of the characteristic MoO_3 peaks. However, crystallinity cannot be excluded as the films, at a thickness of about 50 nm, may have been too thin for the instrument. The deposition of thicker films was unsuccessful.

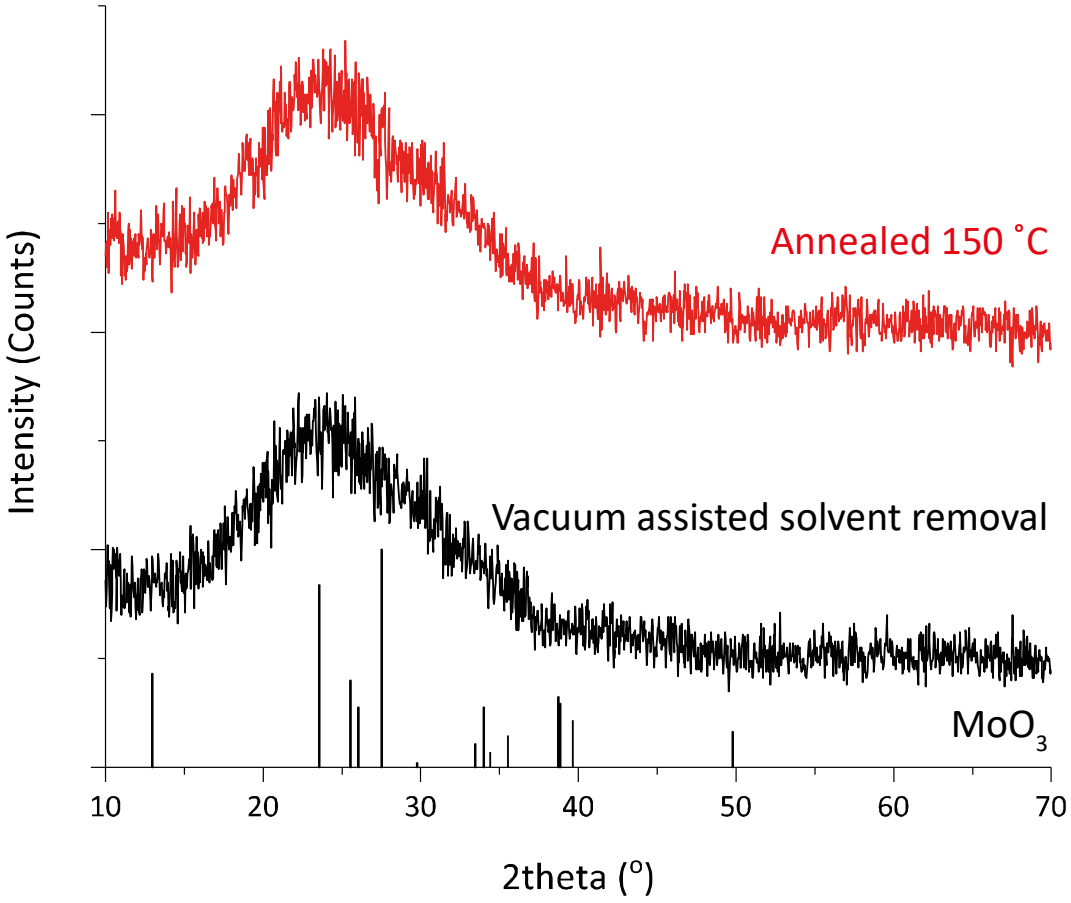

Figure 6.1: XRD data from MoO_{3-x} films subject to two different post-deposition treatments. The stick pattern ofMoO_3 is also shown.

Figure 6.2 shows the results obtained from an AC-Hall effect measurement on a MoO_{3-x} sample deposited from isopropanol and subject to a 150 °C post-deposition treatment[rr]. The very high resistivity of the film resulted in high uncertainties on carrier type, concentration, and mobility.

[rr] Thanks to Miss Becky Kilmurray for the measurement.

Lake Shore CRYOTRONICS 8400 Series

Hall measurement

Run-time operator

HMS User

Sample

ID:	
Type:	van der Pauw
Thickness t [nm]:	130
Other dimensions Lp [mm]:	
Hall factor:	1
Max voltage [V]:	20
Max current [mA]:	20
Gate bias voltage [V]:	0
Comment:	

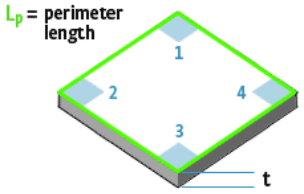

Low confidence

Final results

		Mean value	Limit
μ_H	Hall mobility [cm²/V·s]	3.43E-3	
	Carrier type	N	45 %
n	Carrier concentration [1/cm³]	8.02E13	
n_{sheet}	Sheet carrier concentration [1/cm²]	1.04E9	
R_H	Hall coefficient [cm³/C]	7.79E4	
R_{Hsheet}	Sheet Hall coefficient [cm²/C]	5.99E9	
ρ	Resistivity [Ω·cm]	2.27E7	
ρ_{sheet}	Sheet resistivity [Ω/□]	1.75E12	
V_H	Hall voltage [V]	3.2603E-6	
	Phase [deg.]	113.3	
	Worst case Ohmic check correlation (1-3)	9.9560E-1	

High resistivity

Figure 6.2: Copy of the results report of AC-Hall measurements performed on a MoO_{3-x} sample deposited from isopropanol and subject to a 150 °C post-deposition treatment. The high resistivity is pointed out, which lead to high uncertainty in the mobility and carrier concentration measurement.

To confirm the unsuitability of X-Ray diffraction for this work, different oxides films were deposited on a Si substrate and analysed (Figure 6.3). The results mirrored those of Figure 6.1, with no reflection observed apart from those of the silicon substrate.

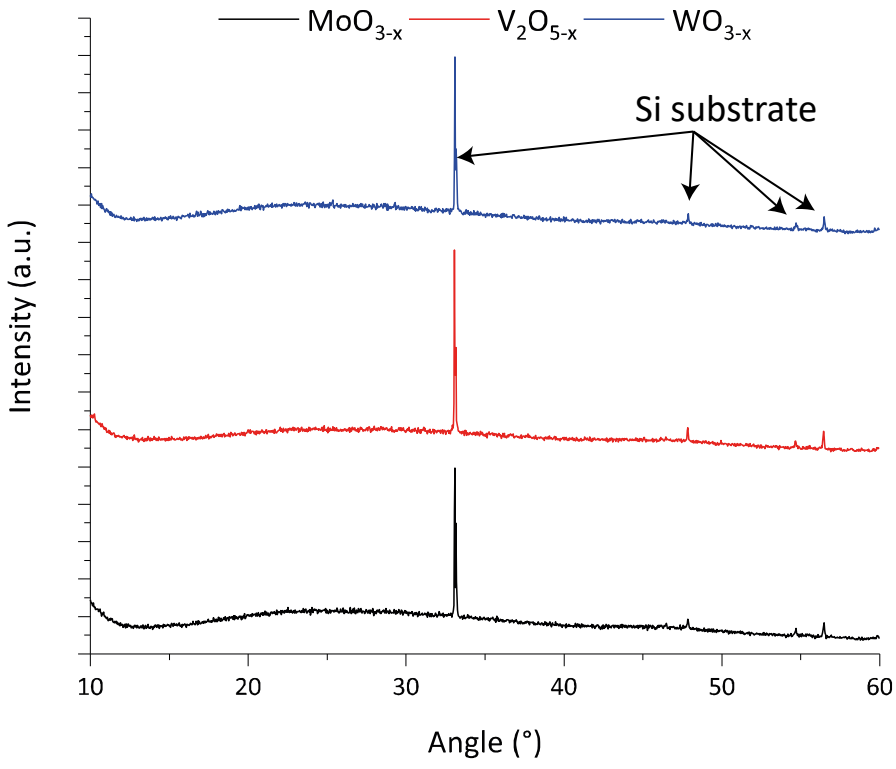

Figure 6.3: XRD data for films of different oxides cast from isopropanol and subject to a 150 °C post-deposition treatment. The films were deposited on Si substrates.

B. Appendix to Chapter 4

In thick films, multiple reflections produced within the thickness produce Fabry-Perot oscillations whose amplitude depends on the refractive index of the material. These oscillations can be used to calculate the refractive index of the material using the transfer matrix method. However, this procedure does not work in materials with a high absorption coefficient because the Fabry-Perot oscillations disappear. A solution to this problem was provided by Dr Paul Stavrinou's group[ss] and employs a thin film of the material of interest deposited over a Fabry-Perot optical cavity (1 µm thick SiO_2 on Si). The thin film perturbs the Fabry-Perot oscillations from the SiO_2, and changes in their amplitude and period can be used to evaluate the refractive index using the transfer matrix method and Cauchy and Sellmeier laws[229–232]. The experimental data used to calculate the refractive index of the PEDOT:PSS/MoO_{3-x} hybrid films is shown in Figure 6.4; the black line is the reflectance spectra from the SiO_2/Si substrate.

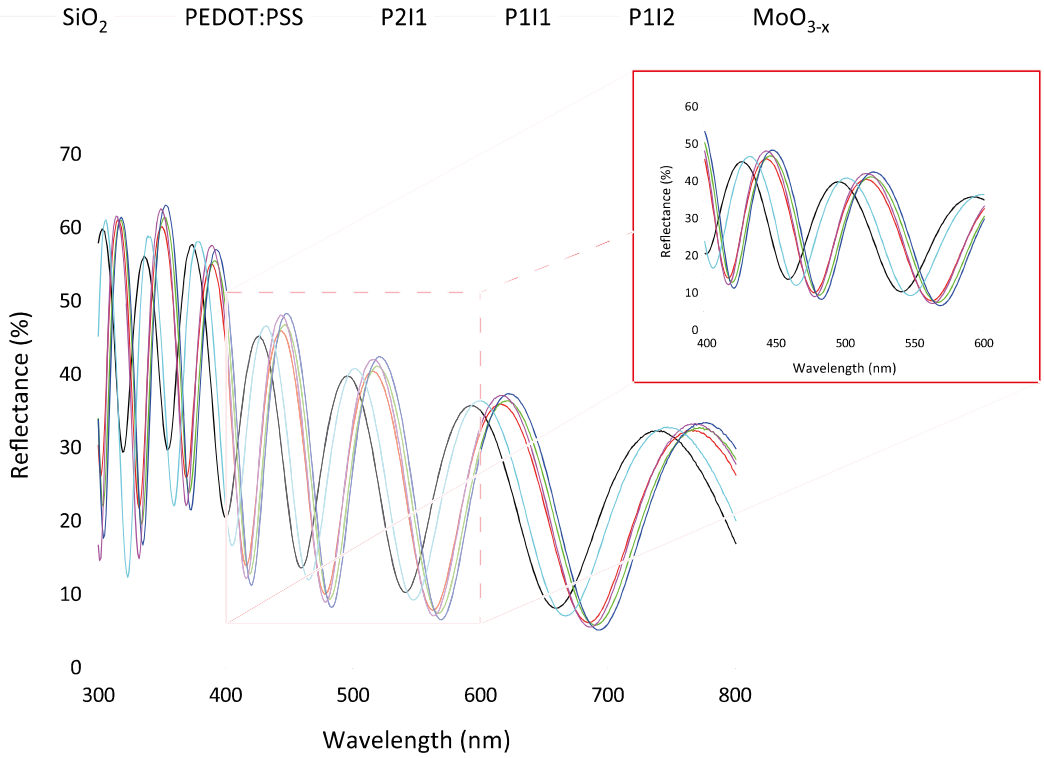

Figure 6.4: Experimental data from PEDOT:PSS, three different hybrids, and MoO_{3-x}, as well as the SiO_2 on Si substrate. The Fabry-Perot oscillations of the reflectance spectra are clearly visible, and the changes induced by the presence of the sample film on top of the substrate are clearly seen in the inset.

The calculations did not yield satisfactory results for the refractive index of plain MoO_{3-x}, but the signals from PEDOT:PSS and the hybrids were shifted enough from that of the substrate to allow for the calculations to be carried out successfully, producing the results shown in Chapter 4.

[ss] A special thanks to Luca Occhi, who helped with the experiments and carried out the simulations.

C. Appendix to Chapter 5

Supplementary data for the XPS analysis in Chapter 5.

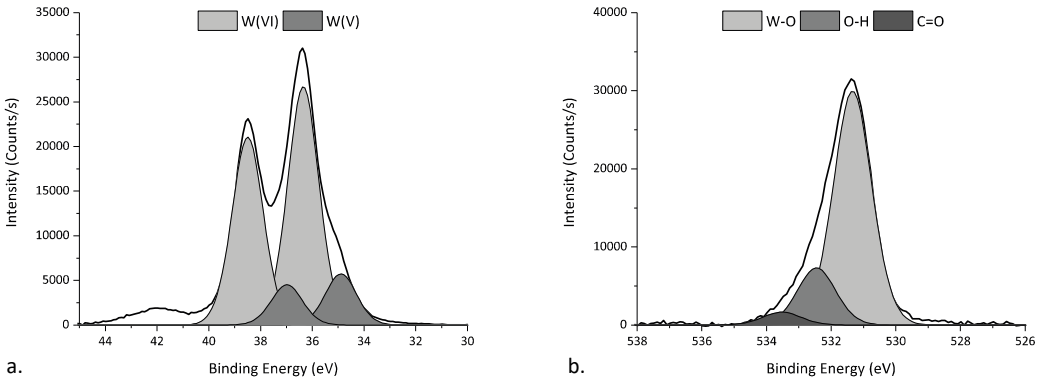

Figure 6.5: a. W4f signal of film cast from a tungsten (V) ethoxide dispersion in ethanol. b. O1s signal from the same film.

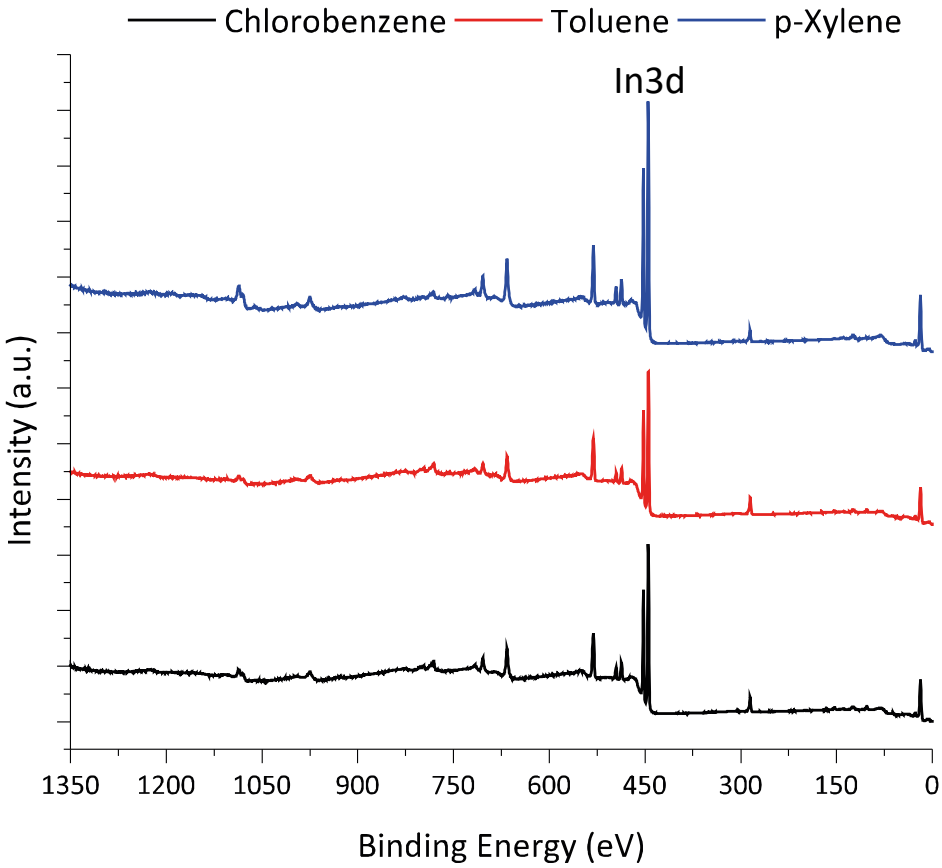

Figure 6.6: XPS survey spectra of CoO_x films cast from different solvents, showing a major contribution from In3d signal coming from the ITO substrate.

D. Appendix on Wetting Behaviour

The wetting of MoO_{3-x} solution in isopropanol on the P3HT:ICBA blend was analysed, and the possibility of different surface treatments on the blend were explored. The results are shown in Figure 6.7: preliminary studies on the annealing of the blend at 150 °C for 10 minutes and the rinsing of the surface with isopropanol were carried out. Combinations of the two were also taken into consideration.

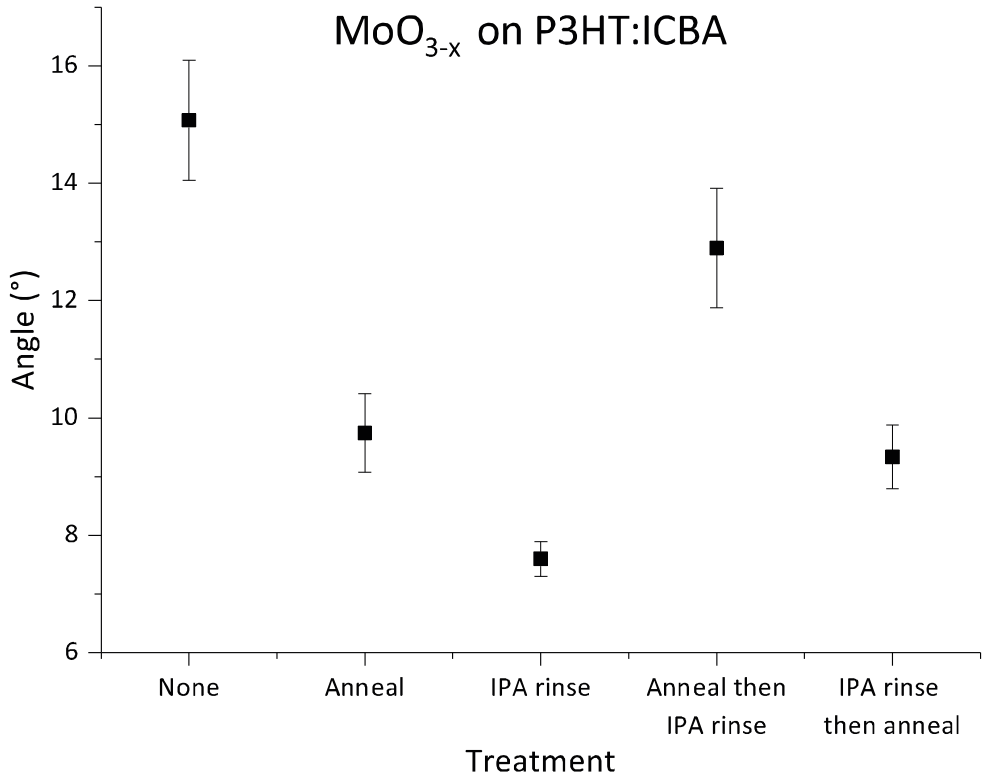

Figure 6.7: Contact angle of MoO_{3-x} solution in isopropanol on a P3HT:ICBA film subject to different surface treatments. IPA is here short for isopropanol, anneal indicates a post-deposition treatment at 150 °C.

An isopropanol rinse seemed to be the most suitable candidate to enhance the wetting of the MoO_{3-x} solution in the fabrication of an inverted architecture device.

Also, the wetting of isopropanol solutions of three different oxides on the same P3HT:ICBA blend was analysed; the organic active layer was subject to a 150 °C annealing step. All three solutions showed excellent wetting: this suggests the possibility of their implementation in inverted architecture devices. The wetting of CoO_x solutions because of the non-orthogonality of their solvents with the active layer materials, was not investigated here.

Oxide	Contact Angle
MoO_{3-x}	9.7 °C
V_2O_{5-x}	8.3 °C
WO_{3-x}	8.7 °C

Table 6.1: Contact angles of the different oxide solutions (in isopropanol) on P3HT:ICBA films subject to a 150 °C post-deposition treatment.